

# Nonlinear ultrasound for cancer diagnostics

***Citation for published version (APA):***

Panfilova, A. (2022). *Nonlinear ultrasound for cancer diagnostics*. [Phd Thesis 1 (Research TU/e / Graduation TU/e), Electrical Engineering]. Eindhoven University of Technology.

***Document status and date:***

Published: 18/01/2022

***Document Version:***

Publisher's PDF, also known as Version of Record (includes final page, issue and volume numbers)

***Please check the document version of this publication:***

- A submitted manuscript is the version of the article upon submission and before peer-review. There can be important differences between the submitted version and the official published version of record. People interested in the research are advised to contact the author for the final version of the publication, or visit the DOI to the publisher's website.
- The final author version and the galley proof are versions of the publication after peer review.
- The final published version features the final layout of the paper including the volume, issue and page numbers.

[Link to publication](#)

***General rights***

Copyright and moral rights for the publications made accessible in the public portal are retained by the authors and/or other copyright owners and it is a condition of accessing publications that users recognise and abide by the legal requirements associated with these rights.

- Users may download and print one copy of any publication from the public portal for the purpose of private study or research.
- You may not further distribute the material or use it for any profit-making activity or commercial gain
- You may freely distribute the URL identifying the publication in the public portal.

If the publication is distributed under the terms of Article 25fa of the Dutch Copyright Act, indicated by the "Taverne" license above, please follow below link for the End User Agreement:

[www.tue.nl/taverne](http://www.tue.nl/taverne)

***Take down policy***

If you believe that this document breaches copyright please contact us at:

[openaccess@tue.nl](mailto:openaccess@tue.nl)

providing details and we will investigate your claim.

# Nonlinear Ultrasound for Cancer Diagnostics

PROEFSCHRIFT

ter verkrijging van de graad van doctor aan de Technische Universiteit Eindhoven, op  
gezag van de rector magnificus prof. dr. ir. F. P. T. Baaijens, voor een commissie  
aangewezen door het College voor Promoties, in het openbaar te verdedigen op dinsdag  
18 januari 2022 om 13:30 uur

door

Anastasiia Panfilova

geboren te Ussuriysk, Rusland

Dit proefschrift is goedgekeurd door de promotoren en de samenstelling van de promotiecommissie is als volgt:

voorzitter:	prof.dr.ir. M.J. Bentum
1 <sup>e</sup> promotor:	prof.dr.ir. M. Mischi
2 <sup>e</sup> promotor:	prof.dr.ir. H. Wijkstra
copromotor:	dr.ir. R.J.G. Van Sloun
leden:	dr.ir. M.D. Verweij (Technische Universiteit Delft) dr.ir. R.G.P. Lopata dr. L. Demi (University of Trento)
adviseur:	prof.dr. M. Postema (Tampere University) dr. P.J. Zondervan (Amsterdam UMC)

Het onderzoek of ontwerp dat in dit proefschrift wordt beschreven is uitgevoerd in overeenstemming met de TU/e Gedragscode Wetenschapsbeoefening.

*“God would not be so unkind as to make the laws of nature nonlinear”*

(Stewart I., Does God play dice? The mathematics of chaos. 1990)

*“When life gives you lemons, make lemonade”*

(Common saying)



Посвящается моим родным и любимым людям, без чьей  
поддержки эта работа не увидела бы свет:

Самому любимому человеку моего раннего детства, бабушке  
Александре Александровне. Я мало знаю таких бескорыстных и  
добрых людей, как ты. Благополучие твоих детей и внуков для  
тебя всегда было выше собственного.

Моей маме Руслане Валерьевне, воспитавшей меня и давшей мне  
так много любви, внимания, и возможностей самореализоваться.

Моему отцу Вадиму Николаевичу. Я знаю, что ты рядом в  
трудную минуту.

Aan mijn lieve Aldo. Je warmte en liefde maken de wereld een betere  
plek voor mij.

Посвящается всей моей семье, моим друзьям и добрым  
людям, встретившимся мне в годы работы над диссертацией.

Dedicated to my family, my friends, and the kind and inspiring  
people I came across during the years of this work.

# Contents

---

<b>1</b>	<b>Introduction</b>	<b>15</b>
1.1	Cancer epidemiology . . . . .	16
1.2	Imaging biomarkers of cancer . . . . .	16
1.3	Cancer diagnostics and detection . . . . .	17
1.3.1	Magnetic resonance imaging . . . . .	18
1.3.2	X-ray and x-ray computer tomography . . . . .	19
1.3.3	Emission tomography . . . . .	19
1.3.4	Ultrasound . . . . .	19
1.4	Research questions and objectives of this thesis . . . . .	20
1.5	Outline . . . . .	22
<b>I</b>	<b>US imaging modalities</b>	<b>24</b>
<b>2</b>	<b>Ultrasound modalities and their use in cancer diagnostics</b>	<b>25</b>
2.1	Ultrasound generation and propagation . . . . .	26
2.2	Echography . . . . .	26
2.3	Ultrasound modalities . . . . .	27
2.3.1	Linear ultrasound . . . . .	27
2.3.2	Nonlinear ultrasound . . . . .	29
<b>II</b>	<b>CE-US imaging</b>	<b>38</b>
<b>3</b>	<b>The relationship between DCE-US parameters and the vascular architecture</b>	<b>39</b>
3.1	Introduction . . . . .	41
3.2	Materials and Methods . . . . .	42
3.2.1	Rat Models . . . . .	42
3.2.2	Image acquisition . . . . .	43
3.2.3	DCE-US bolus data processing . . . . .	43
3.2.4	AA data processing . . . . .	44

3.2.5	Statistical analysis . . . . .	45
3.2.6	Mapping of vascular properties on the bolus acquisition plane . . . . .	47
3.3	Results . . . . .	47
3.3.1	Statistical analysis . . . . .	47
3.3.2	Mapping of vascular properties on the bolus acquisition plane . . . . .	48
3.4	Discussion . . . . .	48
3.5	Conclusions . . . . .	51
<b>4</b>	<b>Experimental acoustic characterisation of an endoskeletal antibubble UCA</b>	<b>53</b>
4.1	Introduction . . . . .	55
4.2	Methods . . . . .	58
4.2.1	Scatter measurements . . . . .	58
4.2.2	Attenuation measurements . . . . .	61
4.2.3	Dynamic contrast-enhanced ultrasound measurement . . . . .	63
4.3	Results . . . . .	64
4.3.1	Scattering . . . . .	64
4.3.2	Attenuation . . . . .	67
4.3.3	Dynamic contrast-enhanced ultrasound . . . . .	67
4.4	Discussion . . . . .	68
4.5	Conclusions . . . . .	71
<b>III</b>	<b><i>B/A</i> imaging</b>	<b>74</b>
<b>5</b>	<b>A review on <i>B/A</i> measurement methods</b>	<b>75</b>
5.1	Introduction . . . . .	77
5.2	Theoretical background . . . . .	79
5.2.1	<i>B/A</i> origin . . . . .	79
5.2.2	Main wave equations . . . . .	83
5.3	Thermodynamic method . . . . .	84
5.3.1	Traditional thermodynamic technique . . . . .	85
5.3.2	Isentropic thermodynamic technique . . . . .	87
5.4	Method for aqueous solutions . . . . .	90
5.5	Finite amplitude methods (FAM) . . . . .	92
5.5.1	Wave shape. . . . .	92
5.5.2	Second harmonic measurements . . . . .	97
5.5.3	Fundamental nonlinear absorption . . . . .	110
5.6	Parametric array . . . . .	112
5.7	Pumping waves . . . . .	116
5.7.1	Classic pump wave technique . . . . .	117
5.7.2	Second order ultrasound field technique for echo-mode imaging . . . . .	120
5.8	Phase conjugate beams . . . . .	122
5.9	Conclusions . . . . .	124
<b>6</b>	<b>The gFAIS method for <i>B/A</i> measurement of tissues and liquids</b>	<b>133</b>
6.1	Section 1. <i>In – silico</i> validation . . . . .	134
6.1.1	Introduction . . . . .	135
6.1.2	Methods . . . . .	135
6.1.3	Results . . . . .	138

6.1.4	Discussion and Conclusions . . . . .	142
6.2	Section 2. <i>Ex – vivo</i> validation . . . . .	144
6.2.1	Introduction . . . . .	145
6.2.2	Materials and methods . . . . .	145
6.2.3	Results . . . . .	149
6.2.4	Conclusions . . . . .	152
<b>7</b>	<b><i>B/A</i> measurement of clear cell renal cell carcinoma versus healthy kidney tissue</b>	<b>155</b>
7.1	Introduction . . . . .	157
7.2	Materials and Methods . . . . .	157
7.2.1	Theoretical background . . . . .	157
7.2.2	Experimental Procedure . . . . .	157
7.2.3	Patient selection and sample preparation . . . . .	157
7.2.4	Data analysis . . . . .	159
7.3	Results . . . . .	160
7.4	Discussion . . . . .	160
7.5	Conclusion . . . . .	162
<b>IV</b>	<b>Epilogue</b>	<b>164</b>
<b>8</b>	<b>Discussion and future prospects</b>	<b>165</b>
<b>9</b>	<b>Conclusions</b>	<b>171</b>
	<b>Bibliography</b>	<b>173</b>
	<b>Acknowledgements</b>	<b>200</b>
	<b>Curriculum vitae</b>	<b>202</b>
	<b>List of author's publications</b>	<b>203</b>

## Summary

Compared to the typical imaging modalities employed for cancer diagnostics, such as magnetic resonance imaging, computer tomography and emission tomography, ultrasound has the advantages of being a real-time, portable, widely available and cost-effective modality. Adequate cancer diagnostics with ultrasound would have a global impact, giving access to clinical diagnostics even in low-income countries. Therefore, the development of ultrasonic modalities for the detection of various cancer markers is of societal relevance. This thesis aims at improving cancer diagnostics with ultrasound, focusing on two nonlinear ultrasound modalities: contrast-enhanced ultrasound (CE-US) and nonlinear parameter ( $B/A$ ) imaging. CE-US is already utilized in the clinic to aid cancer diagnostics.  $B/A$  imaging is still under development and the utility of  $B/A$  has been poorly studied for cancer diagnostics.

CE-US involves the intravenous injection of ultrasound contrast agents (UCAs). UCAs are gas bubbles, 1-10 micrometers in diameter, stabilized by a biocompatible shell. In contrast-specific imaging modes, the nonlinear signal generated by UCAs is visualized on CE-US images, reflecting tissue perfusion. Cancer growth requires angiogenesis, *i.e.*, the formation of new vessels, for the intake of nutrients. However, the formed vascular network is malfunctioning, with an irregular vessel hierarchy. As a result, tumors are often avidly perfused or heterogeneously perfused. Semiquantitative perfusion-related features like wash-in time of UCAs help identify tumor regions and can be assessed by the sonographer real-time.

Dynamic contrast-enhanced ultrasound (DCE-US) records the varying UCA concentration in time. Analysis of the DCE-US clips allows extracting the spatiotemporal distribution of quantitative perfusion-related features and, with a more recent approach, dispersion-related features. Currently, it is not yet fully understood what properties of the vascular architecture are highlighted by DCE-US perfusion and dispersion features to enable cancer detection. Identifying this link would favor a better understanding of cancer hemodynamics and, possibly, lead to the identification of more powerful features for cancer detection. This thesis explores the correlation between Acoustic Angiography (AA) vascular features (e.g. tortuosity, microvascular density) and DCE-US features in malignant and benign tissue. It shows perfusion to reflect microvascular density and the presence/absence of large feeding vessels. Dispersion was hypothesized to reflect properties of smaller vessels than those visible with AA.

This thesis also paves the way to improving CE-US and DCE-US image quality through the investigation of a new UCA prototype. Current UCAs do not always exhibit sufficient nonlinear behavior to eliminate image artefacts, leading to diagnostic misinterpretation. This issue may be overcome with a different UCA that shows augmented nonlinear behavior compared to current UCAs. Recent studies suggest that bubbles with incompressible cores in the gas phase, referred to as antibubbles, show augmented nonlinear behavior. In this thesis, one of the first experimental characterizations of antibubbles demonstrated that they generate high nonlinear signal, comparable to that of a commercial, clinically-approved UCA (SonoVue<sup>TM</sup>). To present solid experimental proof that an incompressible core enhances the nonlinear behavior of a bubble, further work is required. From a different perspective, antibubbles have the potential to become a new generation theragnostic agent, easily traceable and carrying large quantities of liquid medication in the core.

The parameter of nonlinearity  $B/A$  reflects tissue water, fat and protein content. Moreover, it is influenced by the tissue structure: in the absence of cellular adhesion, as in tumors,  $B/A$  of animal liver decreases.  $B/A$  acoustic tomography and single-value assessment of healthy and diseased livers has shown  $B/A$  to be capable of tissue differentiation. However, the literature on the utility of  $B/A$  for cancer diagnostics is limited to only few measurements on the human

breast and liver. From a technical perspective,  $B/A$  measurement is a complex task. The finite amplitude insert-substitution (FAIS) method is one of the most popular and relatively simple methods, requiring a through-transmission measurement and providing a single-value  $B/A$  of the investigated tissue sample. The original FAIS imposes limitations on the sample position between the source and receiver and makes an assumption about the frequency dependence of attenuation in the studied sample. The size of the source and receiver must also be chosen carefully, to ensure validity of the plane wave approximation. Echo-mode imaging proved to be much more difficult.

To improve the accuracy and practicality of the  $B/A$  measurement, a generalized FAIS is proposed, making no assumptions about the frequency dependence of the sample attenuation and allowing freedom in its positioning. To validate the measurement strategy and setup, simulations and experiments were conducted on tissues with well-known  $B/A$  values. Once the method was validated, it was demonstrated, on a limited data set, that clear cell renal cell carcinoma (ccRCC) has significantly higher  $B/A$  values than those of healthy tissue, indicating  $B/A$  as a potential diagnostic marker of ccRCC. Besides this, a literature review has been conducted to highlight the challenges of and the most promising strategies for  $B/A$  echo-mode imaging.

In conclusion, this thesis contributes to improving the current CE-US and DCE-US techniques, and brings the measurement of  $B/A$  a step closer to a practical implementation, demonstrating potential utility of  $B/A$  for ccRCC diagnostics and providing practical guidelines for  $B/A$  measurement and imaging.

## List of abbreviations

AA	Acoustic angiography
A-mode	Amplitude-mode
ARFI	Acoustic radiation force impulse
B-mode	Brightness-mode
CE-US	Contrast-enhanced ultrasound
ccRCC	Clear cell renal cell carcinoma
CTR	Contrast to tissue ratio
CT	Computer tomography
CUDI	Contrast ultrasound dispersion imaging
DCE-US	Dynamic contrast-enhanced ultrasound
DM	Distance metric
EFAM	Extended finite amplitude methods
ET	Emission tomography
FAMs	Finite amplitude methods
FAIS	Finite amplitude insert-substitution method
FALT	Finite amplitude loss technique
GFAIS	Generalized finite amplitude insert-substitution method
IDC	Indicator dilution curve
KZK	Khokhlov-Zabolotskaya-Kuznetsov
LDRW	Local Density Random Walk model
mLDRW	Modified Local Density Random Walk model
MI	Mechanical index
MRI	Magnetic resonance imaging
MR	Mean radius
MVD	Microvascular density
PET	Positron emission tomography
PRF	Pulse repetition frequency
SNR	Signal-to-noise ratio
SOAM	Sum of angles metric
SPECT	Single-photon emission computed tomography
SURF	Second order ultrasound field technique
TIC	Time intensity curve
UCA	Ultrasound contrast agents
US	Ultrasound
VEGF	Vascular endothelial growth factor
VL	Vessel length
VVD	Volume vascular density
WHO	World Health Organization

## 1.1 Cancer epidemiology

Cancer is the second leading cause of death worldwide, with 1 in 6 deaths occurring due to cancer in 2018, according to the World Health Organization (WHO). In 2018, 9.6 million people died due to cancer. This number has been growing in the past decades and this trend is expected to prevail, largely due to global population aging and population growth [404]. Besides its burden on human lives, cancer also requires costly healthcare solutions. The annual costs of cancer treatment were estimated to be € 199 billion in 2018 in Europe [173].

## 1.2 Imaging biomarkers of cancer

Cancer is induced by malfunctioning biological cells. Numerous biochemical cascades and pathways are disrupted in such cells, leading to great replicative potential and alterations of multiple cell and tissue properties. Below is a description of some alterations in cancerous tissue, which are exploited by various imaging modalities for cancer detection.

### Tissue structure and cell morphology

Cancerogenesis induces morphological changes in the cells, characterized by nuclear atypia [382], tubule formation, and mitotic activity [424]. The assembly and organisation of the cell cytoskeleton and the extracellular matrix that binds the cells together is altered in cancerous tissue [164], cell-to-cell adhesion is lost [186]. Moreover, solid tumors typically exhibit greater cellular density and irregular tissue structure [285].

### Biomechanical properties

The changes in the cytoskeleton and the extracellular matrix result in changes in the viscoelastic properties of the cells and tissue as a whole. These are defined by the type of cancer. Most solid tumors are stiffer than healthy tissue, sometimes exhibiting a stiffness 100 times greater than that of healthy tissue [420]. Other types, like cancerous bladder cells, have lower stiffness, compared to normal cells [365].

### Intersitial fluid

The lymphatic system also malfunctions in tumors. In a healthy environment, there is an influx of plasma from the vasculature into tissue, feeding it with nutrients and oxygen. Part of this fluid is drained through the lymphatic system, preventing its accumulation. In tumors, the fluid is poorly drained [267]. Consequently, cancerous tissue typically has higher water content, compared to healthy tissue [204, 267, 341].

### Angiogenesis and tumor vasculature

Vessel growth from existing vessels, referred to as angiogenesis, is required to satisfy the growing tumor's demand for nutrients [131]. High microvascular density is associated with cancer aggressiveness [275]. However, since the mechanisms of angiogenesis are impaired in cancer, the vasculature within cancer is characterized by irregular vessel hierarchy, heterogeneous microvascular density, tortuous vessels with leaky walls. This results in irregular blood flow supply, and, consequently, hypoxic and necrotic regions [38, 207].

## Molecular markers

The first identified metabolic alteration of cancer cells was aerobic glycolysis, discovered by Otto Warburg in 1920. Tumor cells utilize glycolysis to for ATP generation, leading to increased glucose uptake by tumor cells.

Tumor growth beyond a couple of  $\text{mm}^3$  requires angiogenesis [192]. The signalling molecule that induces new vessel growth (angiogenesis) is the vascular endothelial growth factor (VEGF) [253]. Overexpression of VEGF indicates active angiogenesis.

The vascular networks that grows to feed the tumors are usually malfunctional. Therefore, the provided blood supply is inadequate, and many regions within the tumor may stay hypoxic. Hypoxic tumors are associated with poor prognosis [2].

## 1.3 Cancer diagnostics and detection

Detection of cancer is often hindered by the asymptomatic course of the disease [18, 71, 187, 240, 358]. According to the WHO, only 25 to 44% of cases are diagnosed at a localized stage of the disease. Ovarian cancer, lung and bronchus cancers are extreme cases, mainly diagnosed at the distant stage of disease [158], associated with poor prognosis. Due to this, screening procedures are implemented for identified risk groups defined by age and patient history [355]. These procedures involve organ palpation [355], tests of biological material (*e.g.*, blood, urine) for cancer biomarkers [53, 355, 356, 358] and imaging examinations [53, 254, 355].

When experiencing characteristic symptoms, *e.g.*, haematuria (blood in urine) for renal cell carcinoma [236], or altered bowel habit for colorectal cancer (<https://radiopaedia.org/>) the patient is directed to a physical examination and laboratory test of biological material. When laboratory findings indicate a possible tumor, a medical imaging examination is prescribed. If a suspicious region is found, typically a biopsy is taken, *i.e.*, a tissue sample is extracted from that region with a needle. This tissue undergoes histopathological analysis [397], which is the golden standard of cancer diagnosis for most cancer types [113]. Histopathology involves the microscopic observation of the extracted cells, assessing cytomorphologic features, such as nuclei size and shape [382, 397]. If malignancy is confirmed by histopathology, imaging plays a pivotal role in tumor staging, survival prognosis, choice of treatment, image-guided therapy, *e.g.*, radiotherapy, and monitoring of the response to treatment [170]. In some cases, imaging is the golden standard for cancer diagnosis in itself. For instance, as indicated by the European association of urology guidelines, biopsies are not necessary for detection and assesment of renal tumours, due to the high diagnostic accuracy of imaging.

The most common imaging modalities utilized for cancer diagnostics are magnetic resonance imaging (MRI), x-ray computer tomography (CT), and emission tomography (ET). A schematic of these devices is provided on Fig. 1.1. These are bulky scanners that require a dedicated enviroment and where the patient is positioned in bore. Ultrasound is advised to aid cancer diagnostics in some organs, and is the most suitable imaging modality for biopsy guidance. A schematic of an ultrasound device is provided in Fig. 1.2. The basic principles, advantages and disadvantages of these imaging modalities are discussed hereafter.



Figure 1.1: Schematic illustration of an MRI, CT or Emission Tomography machines. The patient has to be positioned inside the circular structure that contains the signal sources and detectors.

### 1.3.1 Magnetic resonance imaging

MRI provides anatomical and morphological information about the body. For this purpose, it exploits the influence of tissue composition on the density and relaxation times of hydrogen protons, abundant in water-rich soft tissue. When subjected to a constant magnetic field, the spins of hydrogen nuclei align with this field. Further an alternating magnetic field is utilized to flip the spin orientation and induce precession of the hydrogen nuclei. The decay of the precession is characterized by the longitudinal  $T_1$  and transverse  $T_2$  relaxation times dependent on the macromolecular composition [417], specific for tissue types [298].  $T_1$  and  $T_2$ -weighted imaging visualize these relaxation times.  $T_1$  performs best at demonstrating anatomy and bone marrow architecture, whereas  $T_2$  grants high soft tissue contrast, identifying fluid and general pathology [423].

Alternative MRI modalities, based on  $T_1$  and  $T_2$ -weighted imaging, visualize other cancer markers. Dynamic contrast-enhanced MRI (also called perfusion MRI) visualizes tissue perfusion and vessel permeability [417]. It involves an intravenous injection of a contrast agent made of small molecules that extravasate and change the relaxation times ( $T_1$ ,  $T_2$ ) of water protons. Diffusion-weighted MRI visualizes the apparent water diffusion, *i.e.*, Brownian motion of water molecules [292]. Water diffusion is attenuated in high-density tissue, characteristic for solid cancers [128, 285]. Cell necrosis (*e.g.*, due to treatment) is, on the contrary, associated with high diffusion values [128, 292]. All MRI modalities provide high signal-to-noise ratio and contrast-to-noise ratio [129, 284]. Since the technique utilizes strong magnetic fields to alter the proton spin orientation, it is incompatible with metal devices. In addition to this, it is a very expensive technology: about two thirds of the global population can not afford MRI [26].

### 1.3.2 X-ray and x-ray computer tomography

X-ray and x-ray CT involve the transmission of x-rays and their measurement after propagation through the body. The resulting images represent the absorption of x-rays that varies for substances with significant differences in atomic number and density [162]. In conventional plain chest x-ray, the patient is positioned between an x-ray source and a flat x-ray film. The more common X-ray CT incorporates the source and the detectors in a circular structure (Fig. 1.1). X-ray imaging grants anatomical information with excellent contrast for soft tissue versus *e.g.* bone structures, lungs and much lower contrast for discrimination of soft tissue types [407]. Because of rather weak soft tissue contrast [162], cancer diagnostics does not typically rely on x-ray CT alone. To increase the soft tissue contrast, contrast-enhanced CT can be utilized, where a radiopaque contrast medium with a high atomic number is injected intravenously [236]. Depending on the type of contrast agent, it can extravasate through leaky vessels and accumulate in tissue or stay in the blood pool. Contrast-enhanced CT assesses vasculature, perfusion and angiogenesis. It is the primary imaging modality utilized for diagnosis of renal cancer [236].

Since CT reflects x-ray absorption, it is an indispensable technique for radiotherapy planning [84], allowing to predict the radiation dose delivered to the malignant and the surrounding healthy tissues after propagation through tissue structures close to the source.

Due to the short wavelength of x-rays, x-ray CT images have high resolution. The disadvantages of CT are weak soft tissue contrast [162] and the use of ionizing radiation, known for its ability to induce cancer. The high cost of the equipment is an additional limiting factor [26].

### 1.3.3 Emission tomography

ET visualizes tissue metabolism. It involves the intravenous injection of a radioactive tracer that after 1-2 hours accumulates in tissue regions with higher uptake [57, 176]. Typically it is the glucose uptake that is imaged [33], but other molecular processes like oxygen uptake can also be visualized [57, 170]. Emission tomography registers the photons emitted due to radioactive decay of a radioactive tracer (F-18 fluorodeoxyglucose for glucose). It can be stratified in two techniques, positron emission tomography (PET) and single-photon emission computed tomography (SPECT). In SPECT, photons are detected as independent events; in PET, two diverging photons are registered resulting from the positron annihilation with an electron [170]. The emitted photons are registered by the detectors that surround the patient.

Since ET visualizes metabolic information, it may identify cancer at early stages, before structural changes in tissue are appreciable [249]. On the other hand, its accuracy is limited due to *e.g.* increased glucose uptake in inflammatory tissue and poor consumption of glucose in some tumors [127]. The main weaknesses are low spatial resolution (4–10 mm) [127], the use of radioactive tracers, and a lengthy in-take procedure since the tracer needs to be processed by the body.

### 1.3.4 Ultrasound

Conventional B-mode Ultrasound (US) imaging grants anatomical information. When an ultrasound probe transmits an US wave into tissue, as the wave propagates, it is scattered back by tissue scatterers and reflected at interfaces of tissues with different acoustic properties. The backscattered signal is registered by the same ultrasound probe to form an image, where tissue interfaces appear bright and different tissue types are of different brightness, determined



by their echogenicity. Echogenicity is the ability to scatter US, determined by scatter density. Conventional B-mode ultrasound imaging does not provide high soft-tissue contrast and, therefore, is not accurate enough to perform reliable cancer diagnostics. However, it grants anatomical information that indirectly (*e.g.*, through organ dimensions), along with other clinical information, aids cancer diagnostics. Ultrasound modalities like contrast-enhanced ultrasound, reflecting blood perfusion, and elastography, reflecting tissue stiffness, have shown more diagnostic power. They are utilized in the clinic to aid cancer diagnostics [98, 319].

At diagnostic frequencies of several MHz, US imaging provides sufficient resolution, below 1 mm. Unlike the previously described techniques, it is a real-time modality compatible with metal, and, therefore, particularly suitable for biopsy guidance and intraoperative use [239]. US scanners are relatively low cost and portable (Fig. 1.2), producing no ionizing radiation.

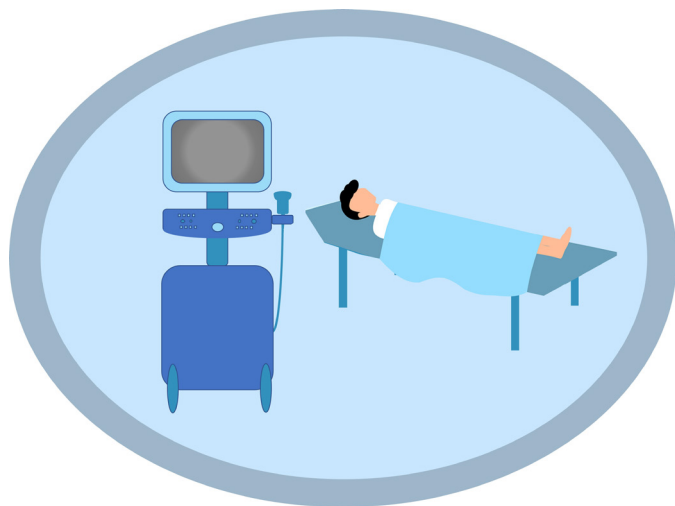


Figure 1.2: Schematic illustration of an US scanner. The patient lays by the US scanner that can be easily moved due to its compact size.

## 1.4 Research questions and objectives of this thesis

Compared to MRI, CT and Emission Tomography, Ultrasound has a number of advantages: it is a real-time, portable and cost-effective modality. Adequate cancer diagnostics with ultrasound would have a global impact, giving access to clinical diagnostics even in poor countries. Therefore, it is of societal impact to develop this technique and exploit its multiple modalities to visualize various cancer markers. This thesis aims to improve cancer diagnostics with ultrasound, focusing on two nonlinear ultrasound modalities: contrast-enhanced ultrasound (CE-US) and nonlinear parameter ( $B/A$ ) imaging.

Nonlinear ultrasound refers to modalities that exploit the sonic wave shape alterations: when transmitting a monochromatic sinusoidal wave, the wave shape is altered in the course of its propagation through tissue or ultrasound contrast agents (UCAs). The degree of the wave shape alteration (or higher harmonic generation) can be quantified with the parameter of nonlinearity  $B/A$ . Tissue is characterized by a much lower parameter of nonlinearity compared to UCAs.

CE-US is an established nonlinear US modality, advised to assess bladder, ovarian and liver cancer [100, 351, 356]. Ultrasound contrast agents (UCAs) are encapsulated gas-filled bubbles that travel through the smallest capillaries and do not extravasate into tissue. When sonicated, these bubbles oscillate in a nonlinear fashion. As the UCA nonlinear signal is much greater than that of tissue, CE-US visualizes predominantly UCA signal from the vasculature. Dynamic CE-US (DCE-US) records the UCA passage over time, capturing its wash-in and wash-out from the vasculature [95]. Signal processing allows analyzing the received nonlinear signals in time and space to extract features like perfusion [95] and dispersion [262, 391] from DCE-US recordings, shown to differ for cancerous and healthy tissue. However, it is still not fully understood what properties of the vascular architecture these DCE-US features highlight to enable cancer detection. Identifying this link would bring us to a better understanding of hemodynamics and, possibly, inspire new analyses, extracting new, more powerful features for cancer detection. In connection with this, the following question is posed in this thesis:

- **What is the relationship between vascular features and DCE-US dispersion and perfusion?**

Despite the recognized utility of CE-US and DCE-US in cancer detection [95, 98], the current UCAs do not always exhibit sufficient nonlinear behavior to eliminate clutter and image artefacts, leading to diagnostic misinterpretation [125]. Cumulative nonlinear effects occurring in tissue can reduce the contrast-to-tissue ratio, especially at greater depth [125]. This issue may be overcome if another UCA was developed, demonstrating augmented nonlinear behavior compared to current UCAs. Recent studies suggest that antibubbles, *i.e.*, encapsulated gas bubbles with incompressible cores in the gas phase, exhibit augmented nonlinear behavior. Experimental proof of augmented nonlinear behavior, and simply nonlinear behavior of antibubbles is scarce. Therefore, the aim is to experimentally characterize the antibubble nonlinear response and answer the question:

- **Do antibubbles exhibit augmented nonlinear behavior compared to current-generation UCAs?**

The parameter of nonlinearity  $B/A$  of tissue reflects its structure and content. Zhang et al. [435] has demonstrated that in the absence of cellular adhesion,  $B/A$  of animal liver decreases. Moreover, increased tissue water content also reduces  $B/A$  [435], whereas lipid content increases  $B/A$  [153].  $B/A$  imaging has not (yet) found its way to the clinic, since  $B/A$  measurement and, to a greater extent,  $B/A$  imaging proved to be challenging tasks, and the diagnostic capabilities of  $B/A$  have not been fully explored. However, single-value assessment of healthy and diseased livers in transmit and echo-mode, as well as  $B/A$  acoustic tomography have shown  $B/A$  to be capable of tissue differentiation [141, 153, 401]. Echo-mode imaging, being the most valuable modality for clinical diagnostics, has been implemented only by a few groups, imaging tissue-mimicking phantoms rather than real biological tissue [225, 390, 394]. To assess the potential of  $B/A$  to aid cancer diagnosis from the implementation point of view, the following is required:

- **Which are the most promising  $B/A$  measurement and imaging strategies and what are the challenges on the way to  $B/A$  imaging?**

The finite amplitude insert-substitution (FAIS) method was identified as one of the simplest single-value  $B/A$  measurement methods, however, it makes the assumptions of a nearly linear frequency dependence of the attenuation coefficient and of a sample position close to the receiver. These assumptions result in a limited range of tissues that can be studied with this



method and impose additional requirements on the measurement setup. In connection with this, the following is inquired:

- **Can a more practical and applicable version of the FAIS method be developed?**

The utility of  $B/A$  for cancer diagnostics has not yet been established, with only two works measuring  $B/A$  of liver carcinoma [341] and multiple myeloma in the breast [340], demonstrating similar values for healthy and malignant tissues. However, the loss of cellular adhesion [186] and increased water content [267], typical for cancer, are expected to result in a lower  $B/A$  for cancerous tissue than that of healthy tissue. On the other hand, high lipid content tumors, e.g., clear cell renal cell carcinoma (ccRCC) may exhibit greater  $B/A$  values than healthy tissue [153]. To broaden the scope of our knowledge about  $B/A$  of cancerous tissue and assess its utility for cancer diagnostics, this thesis aims to answer the question:

- **Does  $B/A$  differ for healthy kidney tissue and ccRCC?**

## 1.5 Outline

To address all the research questions, the rest of this thesis is structured in four main parts. Each part contains chapters. The thesis outline is presented below.

### Part 1. US imaging modalities

**Chapter 2** provides an introduction on US imaging modalities, with emphasis on nonlinear imaging.

### Part 2. CE-US

**Chapter 3** aims to identify the link of vascular features with perfusion and dispersion, extracted from DCE-US clips. Perfusion, and especially dispersion, have been shown effective for cancer localization. However, it is not completely understood which altered features of the vascular architecture are reflected by the estimated perfusion and dispersion. Acoustic angiography (AA) enables imaging of the vasculature, with a resolution up to 100-200  $\mu\text{m}$ , by registering high frequency content, centered at 30 MHz, from UCAs. This thesis attempts to clarify the influence of the vascular network on the hemodynamics by comparing AA-extracted vascular features and DCE-US features in tumor and healthy regions. It demonstrates that regions with high microvascular density and large vessels appear as highly perfused. However, no link between dispersion and vascular features was identified. It is hypothesized that dispersion reflects properties of smaller vessels than those visible with AA. In alignment with previous studies [215, 216, 217, 391], dispersion has shown a higher discrimination capability between malignant and healthy tissue, especially for larger tumors.

**Chapter 4** characterizes a new UCA referred to as endoskeletal antibubbles. It is demonstrated that endoskeletal antibubbles generate high nonlinear signal, comparable to that of a commercial, clinically approved contrast agent SonoVue. To present solid experimental proof that the addition of an incompressible core enhances the nonlinear behavior of a bubble, it is necessary to manufacture bubbles of analogous size and shell composition as the studied antibubbles. From a different perspective, this work demonstrates that antibubbles have the potential to become a new generation therapeutic agent, easily traceable and carrying large quantities of liquid medication in the core.

### Part 3. $B/A$ imaging

**Chapter 5** provides a review on the  $B/A$  measurement and imaging methods with a clinical perspective. It presents the theoretical  $B/A$  origin, current evidence of  $B/A$ 's clinical relevance, and summarizes the progress and typical challenges in the field of  $B/A$  measurement and imaging.

**Chapter 6** describes the generalized FAIS method (gFAIS) for  $B/A$  measurement and presents an *in-silico* and an experimental validation procedure for the chosen strategy. The current work introduces a more practical strategy to measure  $B/A$  that is appropriate for a wider range of studied samples than the original FAIS.

**Chapter 7** is devoted to  $B/A$  measurement in healthy and malignant human kidney tissue, with the gFAIS. The aim of this work is to identify whether  $B/A$  can be utilized as a marker for diagnostics of ccRCC. A significant difference between ccRCC and healthy tissue has been identified in a limited data set, indicating that  $B/A$  may be a potential diagnostic marker for cancer diagnostics.

### Part 4. Epilogue

**Chapter 8** summarizes the findings of this thesis, discusses the limitations of the conducted research and gives recommendations for future work in the domain of nonlinear US for cancer diagnostics.

**Chapter 9** summarizes the main conclusions derived in this thesis.

## **Part I**

# **US imaging modalities**

# **2**

## **Ultrasound modalities and their use in cancer diagnostics**

---

## 2.1 Ultrasound generation and propagation

In 1880 Pierre and Jacques Curie discovered the reverse piezoelectric effect: when a rapidly changing electric potential is applied to a piezoelectric crystal, it vibrates [273]. Piezoelectric elements are the main components of ultrasonic transducers, which perform the electromechanical conversion. Their mechanical vibration displaces particles adjacent to their surface, giving rise to longitudinal compressional waves. These waves are a propagating series of density compressions (regions with high density) and rarefactions (regions with low density), accompanied by variations of excess pressure  $P'$  and particle velocity  $u$ . We can describe the variation of these variables in space,  $z$ , and time,  $t$ , with the wave equation, assuming the simplest model of a lossless 1D propagation medium [263]

$$\frac{\partial^2 u(z, t)}{\partial z^2} - \frac{1}{c_0^2} \frac{\partial^2 u(z, t)}{\partial t^2} = 0, \quad (2.1)$$

where  $u$  is the particle velocity and  $c_0$  is the speed of sound. The real part of the solution describes the particle velocity variation in space and time:

$$u = u_0 \cos(k(c_0 t - z)), \quad (2.2)$$

where  $u_0$  is the particle velocity at the source of US, at  $z = 0$  and  $t = 0$ , and  $k$  is the wave number, defined as

$$k = \frac{2\pi f}{c_0}, \quad (2.3)$$

where  $f$  is the frequency of the wave.

At small acoustic amplitudes, the excess pressure  $P'$  and particle velocity are connected through

$$P' = u \rho_0 c_0 \quad (2.4)$$

where  $\rho_0$  is the equilibrium density of the propagation medium. The speed of sound  $c_0$  is defined by the bulk modulus  $\kappa_0$  and density of the medium

$$c_0 = \sqrt{\frac{\kappa_0}{\rho_0}}, \quad (2.5)$$

where the bulk modulus reflects tissue stiffness, *i.e.*, quantifies the tissue's capacity to resist normal inward pressure [352].

US refers to acoustic waves with a frequency  $f$  above 20 kHz, above the human hearing range [52]. Diagnostic sonographic devices typically operate at frequencies between 2 MHz and 18 MHz [52].

## 2.2 Echography

Echography is defined by the Free Dictionary, as “a radiologic technique in which deep structures of the body are visualized by recording the reflections (echoes) of ultrasonic waves directed into the tissues”. It refers to clinical US imaging as a whole, since US modalities predominantly register and analyze the backscattered echoes to form acoustic images, with few tomographic applications. In an ultrasonic examination, the transducer is positioned above the investigated organ of the patient. The transducer emits an ultrasound pulse and registers the backscattered signals at various depths. When tissue scatterers are smaller than

the sonic wavelength, they produce scattering in all directions (Rayleigh scattering) [263]. Highly scattering tissue types are called echogenic, while weakly scattering regions are called hypoechoic [123, 247]. When the scattering structures are larger than the sonic wavelength, reflection takes place at acoustic impedance discontinuities [263]. Assuming normal incidence of the US wave on the interface between two media, the ratio of the amplitudes of the reflected pressure wave  $P_r'$  to that of the incident wave  $P_i'$  (or amplitude of the particle velocity  $u_r$  of the reflected wave to that of the incident wave  $u_i$ ) is

$$\frac{P_r'}{P_i'} = \frac{u_r}{u_i} = \frac{Z_2 - Z_1}{Z_2 + Z_1}, \quad (2.6)$$

where  $Z_1$  and  $Z_2$  are the acoustic impedances of the first and second medium, respectively. The acoustic impedance of a medium is the product of its speed of sound  $c_0$  and density  $\rho_0$ :

$$Z = \rho_0 c_0. \quad (2.7)$$

Equation 2.6 illustrates that the greater the difference between the acoustic impedances,  $Z_1$  and  $Z_2$ , the stronger the reflection. This motivates the use of a water-based gel on the patient's skin, to couple the transducer to tissue [52], since tissue and air have very different acoustic impedances.

As the sonic wave propagates it is attenuated by tissue in the following manner

$$P'(z) = P'(0)e^{-\alpha z}, \quad (2.8)$$

where  $P'(0)$  is the transmitted pressure amplitude and  $\alpha$  is the attenuation coefficient. For most tissues, the attenuation coefficient is nearly linearly dependent on the frequency  $f$ :

$$\alpha = \alpha_0 f^{1.1}, \quad (2.9)$$

where  $\alpha_0$  is the power law prefactor that differs among tissues [263]. This way, even though higher frequencies grant higher resolution images, they are attenuated more and achieve a limited penetration depth. To compensate for attenuation, echography utilizes a depth-dependent gain, with greater gain for signals received from deeper structures.

## 2.3 Ultrasound modalities

### 2.3.1 Linear ultrasound

The varying quantities of excess density and pressure, and particle velocity are connected. The adiabatic equation of state describes the relation between excess pressure and excess density in an ultrasound wave. Linear acoustics makes the assumption of an infinitesimal amplitude of the propagating disturbance. At low excess pressures, this assumption is realistic and allows neglecting second order effects, yielding the following adiabatic equation of state

$$P - P_0 = \rho_0 \left( \frac{\partial P}{\partial \rho} \right)_{0,s} \frac{\rho - \rho_0}{\rho_0} = c_0^2 (\rho - \rho_0). \quad (2.10)$$

Here  $P$  and  $P_0$  are the instantaneous and hydrostatic pressures,  $\rho$  and  $\rho_0$  are the instantaneous and equilibrium densities of the medium under investigation, and the partial derivatives are taken about the equilibrium state (indicated by the subscript 0) and constant entropy (indicated

by subscript  $s$ ). Linear acoustics views excess pressure  $P' = P - P_0$  as linearly dependent on excess density  $\rho' = \rho - \rho_0$ . The speed of sound  $c_0$  is considered constant for all phases of the transmitted wave, and often referred to as the small-signal speed of sound. The connection between instantaneous excess pressure  $P'$  and the particle velocity  $u$  can be described with:

$$P' = u\rho_0c_0 = uZ, \quad (2.11)$$

where  $Z$  is the acoustic impedance of the medium.

### 2.3.1.1 B-mode

B-mode imaging registers the amplitude of backscattered echoes. The arrival time of the signal allows inferring the depth of the echo origin, since the speed of sound in soft tissues exhibits little variation, and is known to be around 1540 m/s [263]. The A(amplitude)-mode is the predecessor of B(brightness)-mode imaging. In A-mode, a single piezoelement is utilized as an acoustic source and receiver. Therefore, the reflection properties are captured along one line, resulting in a 1D depth profile of the echo amplitudes. Current ultrasound probes typically consist of 64 or 128 piezoelements, providing reconstruction along several lines and resulting in 2D images, where greyscale brightness is proportional to the amplitude of the echoes after demodulation (envelope).

B-mode imaging provides anatomical information [280], highlighting boundaries between different tissue types and tissue-bone interfaces (Eq. 2.6). Anatomical information is utilized to aid cancer diagnostics, *e.g.*, patients with an increased blood level of the prostate specific antigen are much more likely to have cancer if they have a small prostate, than those with a large prostate [345]. Besides this, cancerous tissue can differ in echogenicity from surrounding healthy tissue [273], visualizing suspicious lesions.

B-mode imaging of the prostate, breast, ovaries and liver are typically advised when a suspicion for cancer arises [123]. B-mode sonography in conjunction with mammography improves cancer detection rate by 5.3 times [22]. However, B-mode images alone still miss many tumors. For instance, the sensitivity of prostate cancer detection is very low, around 11–35% [247].

### 2.3.1.2 Doppler

Doppler sonography allows imaging blood flow and tissue movement, exploiting the Doppler effect. The Doppler effect is the change in the frequency of an ultrasound signal for an observer moving relative to the ultrasound source. When the observer moves towards the source, the frequency of the signal increases, when it moves away it is the contrary [4]. The amplitude of the frequency shift (or Doppler shift) is proportional to the velocity of the moving object, allowing to infer the velocity amplitude and direction (projected onto the line of ultrasound propagation) through the frequency shift in the signal reflected by the moving object (*e.g.*, red blood cell) [4]. In color Doppler, the color-coded velocity is overlaid on the grayscale B-mode image [416]. Doppler sonography is typically used for cardiovascular applications [4]. It is also utilized to assess tissue perfusion and vascularity [20] to diagnose and stage cancer in several organs, such as the thyroid [232], the breast [416] and cervix [20]. Further, Doppler can be helpful to avoid puncture of large vessels during biopsy [239].

### 2.3.1.3 Elastography

Elastography visualizes tissue stiffness and, this way, provides a more objective substitute to tissue palpation. Besides the bulk modulus (Eq. 2.5), tissue stiffness can be quantified with Young's modulus, and the shear modulus that reflect the resistance of tissue to normal and shear deformation, respectively [352]. The former moduli offer much greater contrast between tissue types compared to the bulk modulus.

Two types of elastography exist. The quasistatic method visualizes tissue displacement and strain in response to a static stress, induced by the operator through manually pushing the US probe against the tissue [97, 352]. Here, the Young's modulus is inferred. Dynamic methods are operator-independent; they involve the application of a time-varying force. Acoustic radiation force impulse (ARFI) strain imaging displaces tissue with a high amplitude short-duration acoustic “push-pulse” [352]. The tissue displacement in the direction of beam propagation is then registered to estimate the Young's modulus. Shear wave imaging utilizes either mechanical stress or an acoustic “push-pulse”, as ARFI, but registers shear wave speed [352]. Shear wave elastography is the only US technique that analyzes shear waves, rather than longitudinal US waves. Such waves are characterized by particle motion, perpendicular to the wave propagation direction [145, 352]. The shear modulus and an approximation of the Young's modulus are inferred from the shear wave speed.

On ultrasound examinations, the stiffness is often visualized by overlaying tissue stiffness distribution, displayed in color, on the grayscale B-mode image [99, 247]. Elastography is widely used to assess liver fibrosis and portal hypertension [96]; it is also seen by the European Federation of Societies for Ultrasound in Medicine and Biology as an optional imaging modality that can aid tumor staging of rectal cancer, differentiation between benign and malignant lymph nodes, and identify suspicious regions for prostate cancer biopsy; and as a possible complementary imaging modality for classification of pancreatic and breast lesions [319].

### 2.3.2 Nonlinear ultrasound

When linear US modalities form images based on signal/envelope amplitude, those of nonlinear ultrasound quantify alterations of the US wave shape. Changes in the wave shape can not be expressed with linear models, granting these modalities the name “nonlinear”. In the frequency domain, wave shape alteration results in the generation of higher harmonics, which can also be used to form US images.

Nonlinear effects grow with the amplitude of the transmitted pressure. One of the indicators assessing US safety at greater pressures is the mechanical index (MI):

$$MI = \frac{P_-}{f}, \quad (2.12)$$

where  $P_-$  is the peak negative pressure in MPa and  $f$  is the frequency expressed in MHz. “The mechanical index (MI) quantifies the likelihood that exposure to diagnostic ultrasound will produce an adverse biological effect” as a result of inertial cavitation, *i.e.*, a large expansion of an air bubble in blood “followed by a rapid, violent collapse. Such a collapse can radiate damaging shock waves and cause the gas within the bubble to attain a very high temperature,” “thereby producing large numbers of potentially highly destructive free radicals.” [70]. The maximum MI allowed on US devices is 1.9, set by the Food and Drug Administration [263].

This section provides a description of cumulative nonlinear effects, occurring when a sonic wave propagates through tissue, and of local nonlinear effects, occurring in UCA microbubbles.

### 2.3.2.1 Cumulative nonlinear effects

Cumulative nonlinear effects play a role when the acoustic pressures are too high to neglect higher-order terms in the adiabatic equation of state (Eq. 2.10). Limiting the analysis to second order effects, the adiabatic equation of state reads

$$P = P_0 + \rho_0 \left( \frac{\partial P}{\partial \rho} \right)_{0,s} \frac{\rho - \rho_0}{\rho_0} + \frac{\rho_0^2}{2} \left( \frac{\partial^2 P}{\partial \rho^2} \right)_{0,s} \left( \frac{\rho - \rho_0}{\rho_0} \right)^2. \quad (2.13)$$

The equation above may also be written as

$$P = P_0 + A \frac{\rho - \rho_0}{\rho_0} + \frac{B}{2} \left( \frac{\rho - \rho_0}{\rho_0} \right)^2, \quad (2.14)$$

where

$$A = \rho_0 \left( \frac{\partial P}{\partial \rho} \right)_{0,s} = \rho_0 c_0^2, \quad (2.15)$$

and

$$B = \rho_0^2 \left( \frac{\partial^2 P}{\partial \rho^2} \right)_{0,s}. \quad (2.16)$$

As stated in [25, 166], one may differentiate Eq. (2.13) by  $\rho$  and by substituting the speed of sound  $c^2 = \left( \frac{\partial P}{\partial \rho} \right)_s$  obtain

$$\frac{c}{c_0} = 1 + \frac{B}{2A} \left( \frac{\rho - \rho_0}{\rho_0} \right) = 1 + \frac{B}{2A} \frac{u}{c_0} \quad (2.17)$$

for a plane progressive wave. This illustrates that the local speed of sound  $c$  is dependent on  $B/A$  and  $u$ , the particle velocity. This leads to waveform distortion: the compressional part of the wave, with positive particle velocity  $u$  travels faster than the rarefactional part with negative particle velocity (Fig. 2.1). The distortion of the wave continuously grows as the wave propagates, granting the name ‘‘cumulative’’ to these nonlinear effects.

In the frequency domain, wave deformation is analogous to energy transfer from the fundamental harmonic to higher harmonics. The 2nd harmonic amplitude can be described by the Fubini solution for a plane wave in a lossless medium [140] as

$$P_2(z) = \left( \frac{B}{A} + 2 \right) \frac{\pi f z P_1^2(0)}{2 \rho_0 c_0^3}, \quad (2.18)$$

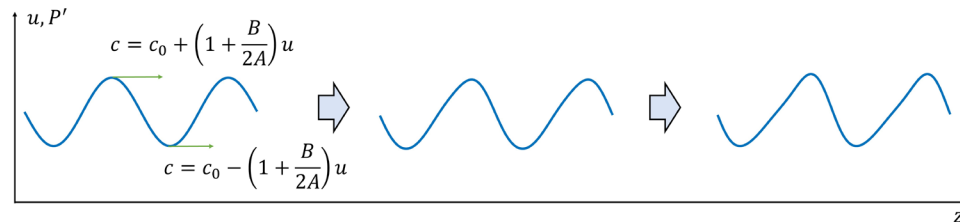


Figure 2.1: Schematic illustration of the cumulative distortion of the US wave, illustrated in particle velocity  $u$  and pressure perturbation  $P'$ . The greater the travelled distance  $z$ , the greater the distortion.

where the 2nd harmonic amplitude  $P_2(z)$  is proportional to excess pressure at the source  $P_1^2$  at the fundamental frequency  $f$ , and grows with distance from the source  $z$ . The dependence on the source pressure  $P_1^2(0)$  shows nonlinear effects to be more prominent for greater transmitted pressures. Harmonics higher than the 2nd harmonic are rarely exploited to form images due to their small amplitudes. In fact, when generated, these frequencies are attenuated fast due to the linear frequency dependence of tissue attenuation (Eq. 2.9).

**Harmonic B-mode imaging** Harmonic imaging constructs B-mode images by recording echoes at higher harmonic frequencies. Most clinical US systems implement harmonic imaging by recording the backscatter at the 2nd harmonic frequency [6]. The advantages of 2nd harmonic imaging are improved signal to noise ratio, border delineation and spatial resolution. Moreover, the second harmonic beam forms gradually as the transmitted wave propagates (Eq. 2.18), allowing better visualization of deep structures compared to linear imaging at the 2nd harmonic. Today tissue harmonic imaging is routinely used in clinical practice, and is reported to represent a valuable solution especially in obstetrics, abdominal imaging and cardiology [11, 107].

**$B/A$  imaging** As shown in Eq. 2.17, the degree of wave shape distortion is proportional to  $B/A$ , the parameter of nonlinearity.  $B/A$  expresses the relative contribution of second-order nonlinear effects to linear effects and is specific to the propagation medium [393].  $B/A$  has been investigated for multiple reasons. This parameter reflects tissue content [8, 340]. Water has low  $B/A$  of 5.2, whereas  $B/A$  of proteins and lipids is in the range 9-11. Due to this, water-rich tissues exhibit low  $B/A$ . Moreover,  $B/A$  is affected by the molar fractions of bound ( $B/A=0.4$ ) and free water ( $B/A=8.0$ ) [435], bringing hope that  $B/A$  could be an ultrasound alternative to diffusion-weighted MRI. Besides this,  $B/A$  reflects tissue structure: it decreases when cell-cell contacts are dissociated and varies depending on the cellular and molecular structure [435].  $B/A$  has been shown useful for distinguishing healthy from diseased tissues [153, 430]. However, it has been barely investigated for cancer diagnostics, with only two studies involving  $B/A$  measurement in malignant tissues [340, 341].  $B/A$  seems promising for cancer detection since malignant tissue exhibits altered water content [204, 267], altered lipid content [264], and a higher level of bound water compared to healthy tissue [128, 285], and lack of cell-to cell adhesion [186].

Already for several decades, researchers have been working on the development of a new echo-mode ultrasound modality that would allow  $B/A$  imaging [43, 141, 153, 179, 268, 378, 390, 394]. Tomographic  $B/A$  imaging has already been demonstrated in several works [153, 430]; however, tomographic examinations are limited to few organs, such as the breast. Echo-mode imaging, on the contrary, has multiple potential applications, but poses difficult challenges, elaborated on in Chapter 5. Due to this, echo-mode imaging has only been implemented on tissue-mimicking phantoms [122, 225, 378, 390, 394].

Several phenomena can be potentially observed to construct  $B/A$  images. The most common are finite amplitude methods that exploit 2nd harmonic generation [153, 430] and enhanced attenuation of the fundamental beam due to energy transfer from the fundamental into higher harmonics [122].

### 2.3.2.2 Local nonlinear effects of radial bubble motion

Ultrasound contrast agents (UCA) are gas bubbles, stabilized by a biocompatible shell. Their size is close to that of red blood cells and, therefore, they travel through the whole vascular



system, including the smallest capillaries. At the same time, they are larger than endothelial gaps and, unlike most MRI and PET contrast agents, do not extravasate from the vascular bed. Once injected in the patient's blood stream, UCAs are imaged with an US probe at the site of interest. Contrast-specific imaging modes allow nearly exclusive imaging of the blood flow.

Since gas is highly compressible, the alternating pressure of the US wave causes the bubbles to oscillate: positive excess pressure contracts the bubbles, negative pressure expands them. This way, these bubbles become secondary scatterers of US due to the induced oscillation. Typically the bubble oscillation is nearly linear at  $MI < 0.1$  [214, 304, 338]. However, at low MIs greater than the mentioned threshold ( $0.1 < MI < 0.4$ ), the radial bubble motion is already nonlinear, containing harmonics of the sonicating frequency [110, 202, 343] (Fig. 2.2). Several theoretical models have been introduced to model the radial motion of bubbles with different shell types, *e.g.*, thick solid shells [69, 171, 383], thin lipid monolayer shells [250, 383]. Below the model of Marmottant et al. [250], is presented, developed for lipid coated bubbles.

The radial bubble motion  $R(t)$  is determined by the properties of the surrounding liquid, the bubble gas and shell, and the incident US wave  $P_{drive}(t)$ , expressed as

$$\rho_L \left( R \frac{d^2 R}{dt^2} + \frac{3}{2} \left( \frac{dR}{dt} \right)^2 \right) = (P_0 + 2 \frac{\sigma_w}{R_0}) \left( \frac{R_0}{R} \right)^{3\gamma} \left( 1 - \frac{3\gamma}{c} \frac{dR}{dt} \right) - 2 \frac{\sigma_w}{R} - 4\chi \left( \frac{1}{R_0} - \frac{1}{R} \right) - 4\eta_L \frac{1}{R} \frac{dR}{dt} - 4 \frac{\kappa_s}{R^2} \frac{dR}{dt} - P_0 - P_{drive}(t), \quad (2.19)$$

where  $R_0$  is the equilibrium bubble radius at ambient pressure  $P_0$ ;  $\rho_L$  and  $\eta_L$  are the density and the viscosity of the surrounding Newtonian liquid, respectively;  $\chi$  and  $\kappa_s$  the shell elasticity and dilatational viscosity, respectively;  $P_v$  and  $\gamma$  the vapor pressure and the polytropic exponent of the gas; and  $\sigma$  the surface tension, *i.e.*, the force acting to collapse the bubbles. The second order solution of this equation for low sonicating pressures  $P_{drive}(t)$ , transmitted at frequency  $f = \frac{\omega}{2\pi}$  has the form

$$R(t) = R_0(1 + A_0 + A_1 \cos(\omega t + \phi) + A_2 \cos(2\omega t + \phi_2)), \quad (2.20)$$

where  $\omega$  is the angular frequency of the sonicating pressure  $P_{drive}(t)$ ,  $A_0$  is the average change of the bubble radius during pulsation,  $A_1$  the first harmonic amplitude of radial motion, and  $A_2$  the second harmonic amplitude [87, 250]. The amplitudes  $A_1$  and  $A_2$  are maximal when the frequency of the sonicating wave is equal to the resonance frequency of the bubble. This frequency can be expressed as

$$f_0 = \left( \frac{3}{2\pi\rho_L R_0^2} \left( \gamma P + \frac{4}{3} \frac{\chi}{R_0} \right) \right)^{\frac{1}{2}}, \quad (2.21)$$

where the first term of on the right-handside is the resonance frequency of a free bubble [297], defined by the bubble size and the gas. The second term reflects the influence of the shell on the resonance frequency.

The advantage of the Marmottant's model is in that it can also describe bubble motion at higher pressures by introducing a radius-dependent surface tension  $\sigma$ . Based on experimental findings for lipid-coated bubbles, the surface tension nearly vanishes for highly compressed (buckled) bubbles and is equal to that of a gas-water interface for greatly expanded bubbles, when shell rupture occurs. This difference in surface tension introduces an asymmetry in the bubble oscillation: the bubble is able to contract freely, but when expanding to a critical volume,

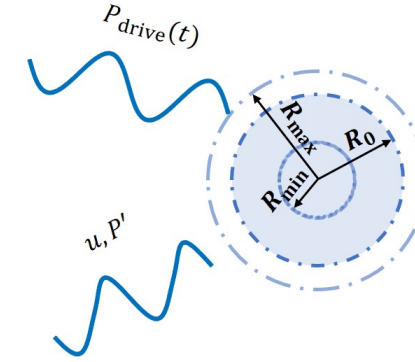


Figure 2.2: Illustration of an oscillating encapsulated gas bubble. The sonicating wave with pressure  $P_{drive}(t)$  induces the bubble oscillation. As a result, the bubble becomes a secondary source of sound. The asymmetry in the radial oscillation ( $|R_0 - R_{max}| < |R_0 - R_{min}|$ ) gives rise to nonlinear content in the scattered sonic signal.

it faces great surface tension (Fig. 2.2). This behavior was demonstrated experimentally by a high speed framing camera recoding oscillations of lipid coated bubbles, including Sonovue [250]. This asymmetry in the oscillation gives rise to higher harmonics and subharmonics.

## Contrast-enhanced ultrasound

**Imaging schemes** UCAs are mainly utilized to visualise blood flow. The acoustic signal scattered by UCAs is proportional to the UCA bubble concentration in the low range of bubble concentrations, utilized for medical examinations [85, 161, 215, 226]. The quality of contrast-enhanced ultrasound (CE-US) images can be characterized by the signal-to-noise ratio (SNR) and the ability to separate microbubbles from tissue, measured by the contrast to tissue ratio (CTR) [280]. The latter quantifies the magnitude of nonlinear effects occurring in bubbles in comparison to those in tissue.

The solution expressing radial bubble motion, presented in Eq. 2.20, is limited to second order effects. In reality, besides the fundamental and the 2nd harmonic, bubbles also scatter superharmonics ( $3f_0$ ,  $4f_0$  and  $5f_0$ ) and subharmonic ( $0.5f_0$ ) or ultraharmonic ( $1.5f_0$ ) components [280] of the sonicating frequency  $f_0$ . These effects grant opportunities for multiple UCA imaging strategies.

Fundamental imaging of UCA can provide greater image clarity, compared to conventional fundamental B-mode images [88]. However, this modality has low CTR, since the echoes from tissue scatterers can easily mask the signal from UCAs in smaller vessels. To tackle this limitation, 2nd harmonic imaging was proposed [12]. The 2nd harmonic is typically the strongest among the scattered higher harmonics [280]. At the same time, cumulative nonlinear effects are weak in tissue for low pressures ( $MI < 0.2$ ), resulting in a much better CTR, compared to fundamental imaging. This modality is still widely used, since 2nd harmonic imaging is available on the majority of US scanners.

Alternatively, subharmonics have the potential to provide high CTR, since these frequencies are not generated in tissue [112, 346]. Moreover, a lower frequency gives the advantage of imaging at greater depth, due to reduced attenuation in tissue. However, the subharmonic is generated at relatively high pressures and in a specific frequency range determined by the

bubble shell. Due to this, obtaining a strong SNR in a subharmonic image may be challenging [82, 280]. This modality is available on some scanners [82, 112]. Ultraharmonic imaging, on the other hand, had little success, demonstrating low image quality [82]. Imaging of superharmonics has the potential to provide high CTR, since superharmonics are greatly attenuated in tissue and, therefore, barely present. However, it is difficult to implement this imaging modality, since current commercial probes have a frequency bandwidth which is typically limited to 2nd harmonic imaging. Transducers composed of piezoelements with different center frequency were proposed as a solution, whose feasibility was demonstrated in several studies [34, 389].

Several contrast-specific imaging schemes exploiting nonlinear alterations in the wave shape were proposed, such as pulse inversion [178] and power modulation [37]. They involve the transmission of two pulses, where the second pulse  $P_{2s}$  has the opposite phase of the first pulse  $P_{1s}$  ( $P_{2s} = -P_{1s}$ ) for pulse inversion, and a lower amplitude ( $P_{2s} = \frac{1}{2}P_{1s}$ ) for amplitude modulation. The echoes from both pulses are summed up according to

$$PS = P_{1s} + P_{2s} \quad (2.22)$$

for pulse inversion, and according to

$$PS = P_{1s} - 2P_{2s} \quad (2.23)$$

for power modulation [110]. For linear propagation the sum  $PS$  equals zero, while for nonlinear propagation it produces a residual related to the nonlinear part of the signal. Power modulated pulse inversion and cadence contrast pulse sequence are schemes that involve both: transmission of pulses with altered phase and amplitude [110].

Contrast-specific imaging schemes are widely used in current ultrasonic scanners [280, 353]. Nonlinear imaging is often utilized in combination with grey-scale B-mode imaging, together providing anatomical and (micro)vascular information [112, 409].

**Clinical relevance** Tumors often manifest themselves as highly perfused, underperfused or heterogeneously perfused regions: highly perfused regions correspond to feeding vasculature and regions with high microvascular density, whereas necrotic regions are underperfused [36, 288]. It has also been noticed that contrast agent arrival time to tumors is shorter [161, 283, 288] and the washed out can be later [283] or earlier [283], compared to healthy tissue. This atypical behavior, compared to surrounding tissue, can be assessed in real-time by the sonographer.

Currently, the European Federation of Societies for Ultrasound in Medicine and Biology recommends to utilize CE-US in the following cases, relevant to cancer care: detection of malignant lesions in liver, bladder and brain tumors (intravascular examination). It is also recommended for differentiation between renal tumor and “pseudotumors”, to exclude malignancy in testicles, distinguish pancreatic tumor types, assess vascularity of gastrointestinal tumors, differential gallbladder carcinoma from cholecystitis. CE-US is also recognized to be valuable when performing biopsies: it helps avoid necrotic areas in percutaneous biopsy of intra-abdominal tumors [239] and identify abnormal blood flow patterns, improving cancer detection rates [247].

**Dynamic contrast-enhanced ultrasound** Dynamic contrast-enhanced ultrasound (DCE-US) clips are recordings of the UCA passage through the organ. Every pixel in the image provides a corresponding time intensity curve (TIC) that demonstrates the changing intensity of the acoustic signal generated by the UCA passage. DCE-US clips give the opportunity to

process and extract quantitative time- and space-related parameters [78]. Injection of UCA in the patient’s blood stream can be performed instantaneously, referred to as a bolus injection, or at a constant rate for a period of time, referred to as a constant infusion.

**Constant infusion** A constant infusion is performed when the disruption replenishment technique is adopted [403]. It involves the transmission of a high-amplitude US pulse to destroy the bubbles present in the imaging plane. Thereafter, the vascular bed slowly refills up with UCA bubbles, returning to the original plateau concentration. The TIC can be fit to extract blood volume, reflected with the plateau, and mean blood velocity reflected by the wash-in slope. Their product is the relative blood flow, referred to as perfusion [161]. The destruction-replenishment technique is typically used to assess myocardial perfusion, with limited application to cancer diagnostics [263].

**Bolus injection** When a bolus injection is performed, the UCA passage through the vasculature is captured, including its washin and washout (Fig 2.3). Heuristic features such as peak intensity, wash-in/wash-out time can be quantified on DCE-US clips, making diagnostics less operator-dependent. To eliminate errors due to noise, these features can also be extracted from the curves fit to the TICs. Several models exist for this purpose [386]. Below we describe the evolution of UCA concentration  $C(\vec{r}, t)$  as a convective dispersion process, modelled by the convective diffusion equation as

$$\frac{\partial C(\vec{r}, t)}{\partial t} = \nabla[D\nabla C(\vec{r}, t) - \vec{v}C(\vec{r}, t)], \quad (2.24)$$

where  $\vec{r}$  and  $t$  are the spatial coordinate and time, respectively; and  $D$  and  $\vec{v}$  are the diffusion coefficient and UCA velocity, respectively [260].

A modified Local Density Random Walk model (mLDRW) solution has been presented by Kuenen et al. [215] for the 1D convective diffusion equation. Assuming a constant velocity of the contrast agent  $\vec{v}$ , an isotropic dispersion coefficient  $D$  and a Gaussian distribution of the

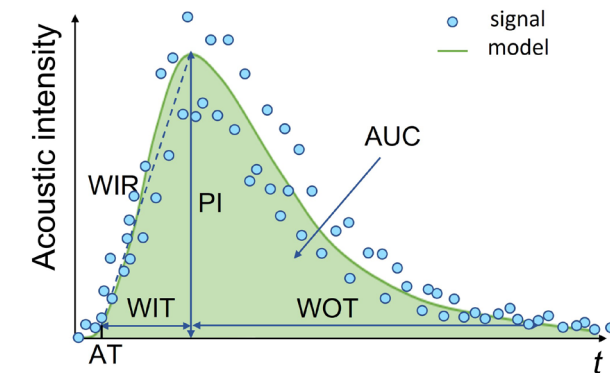


Figure 2.3: Schematic illustration of a time intensity curve and the fit curve with the semiquantitative parameters that are extracted to characterize it [386].  $PI$  refers to the peak intensity,  $AT$  to appearance time,  $WIT$  to the washin time, i.e., the time from UCA appearance to peak intensity,  $WIR$  to the washin rate, calculated as the slope of the rising acoustic signal,  $WOT$  to washout time and  $AUC$  to the area under the time intensity curve.

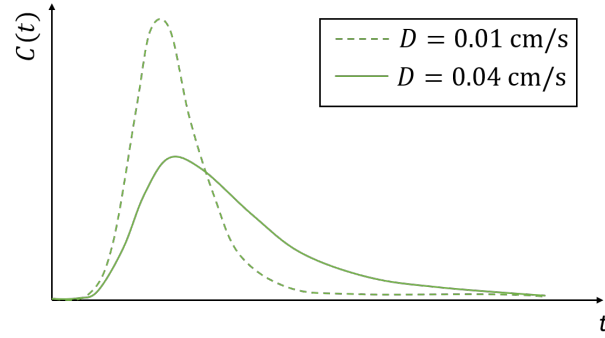


Figure 2.4: Schematic illustration of two TIC profiles at a distance  $z$  away from the injection site. Identical initial UCA concentration distributions at the injection site are assumed, as well as identical convective speed  $v$  while the propagation media are characterized by two different dispersion coefficients.

UCA concentration, the UCA concentration at time  $t$  since injection time is :

$$C(t) = \alpha \sqrt{\frac{\kappa}{2\pi(t)}} e^{-\frac{\kappa(t-\mu)^2}{2t}}, \quad (2.25)$$

where  $\mu$  is the mean time taken by the bubbles to travel from the injection site to the region of interest [95],  $\kappa = \frac{v^2}{2D}$  and  $\alpha$  a scaling coefficient, related to the injected UCA dose to blood flow.

When this model is fit to a TIC, multiple perfusion-related features, like wash-in-time, wash-in rate, peak intensity, area under the curve and wash-out time can be extracted (Fig. 2.3). Moreover, the parameter  $\kappa$ , characterizing the skewness of the TICs, can also be estimated [215, 262].  $\kappa$  is an indirect measure of diffusion. When all other parameters kept alike, TICs at greater diffusion are broader, with a lower peak concentration (Fig. 2.4). Since diffusion typically refers to Brownian motion, UCA diffusion occurring due to multi-path trajectories in the vascular network is typically referred to as dispersion [217, 262].

It was observed that the degree of TIC similarity of neighboring pixels was influenced by dispersion and spatiotemporal analyses were proposed to quantify dispersion in terms of correlation [262], spectral coherence [216, 217], or mutual information [333]. These measures do not require TIC fitting, which may be unreliable at low SNR. They compute the spatiotemporal similarity of the TIC in each pixel with the surrounding TICs in a ring-shaped kernel, presented in Fig. 2.5. The inner dimensions of the kernel are defined by the resolution of the imaging system, while the outer corresponds to the minimal size a tumor can grow without angiogenesis [274]. The proposed dispersion-related parameters demonstrated superior classification performance, compared to perfusion-related features, with improved sensitivity and specificity [216, 217].

**Clinical relevance** The distribution of DCE-US parameters in an organ can be depicted with color maps. DCE-US is finding its way to the clinic, demonstrating encouraging results in the clinical prediction of prostate cancer [248].

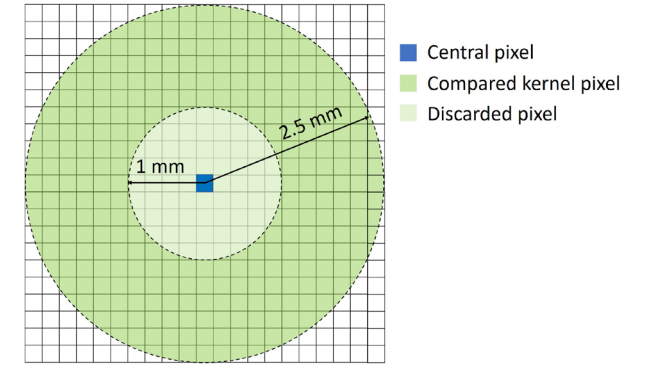


Figure 2.5: Illustration of the kernel which contains pixels, whose spatiotemporal similarity with the central pixel is computed. A mean is computed for every pixel in the DCE-US recording.

**Ultrasound molecular imaging** Ultrasound molecular imaging utilizes UCA bubbles with a shell decorated with binding ligands [280]. These ligands bind to molecular markers of diseases. In the context of cancer, VEGF receptor 2-targeting microbubbles have been developed. After UCA bolus wash-out some bubbles stay attached to VEGF receptor 2, indicating places of active angiogenesis [384]. First clinical human studies show the capacity of such UCAs to identify cancer lesions [354, 410].



**Part II**  
**CE-US imaging**

**3**  
**The relationship between DCE-US  
parameters and the vascular architecture**

## Abstract:

Dynamic contrast-enhanced ultrasound (DCE-US) has been proposed as a powerful tool for cancer diagnosis by estimation of perfusion and dispersion parameters reflecting angiogenic vascular changes. This work aims at identifying which vascular features are mainly reflected by the estimated perfusion and dispersion parameters through comparison with Acoustic Angiography (AA). AA is a high resolution technique that allows quantification of vascular morphology. 3D AA and 2D DCE-US bolus acquisitions monitored growth of fibrosarcoma tumors in 9 rats. AA-derived vascular properties were analyzed along with DCE-US perfusion and dispersion in order to investigate the differences between tumor and control, and their evolution in time. AA-derived microvascular density and DCE-US perfusion showed good agreement, confirmed by their spatial distributions. No vascular feature was correlated with dispersion. Yet, dispersion provided better cancer classification than perfusion. We therefore hypothesize that dispersion characterizes vessels that are smaller than those visible with AA.

From: A. Panfilova, S. E. Shelton, C. Caresio, R. J. G. van Sloun, F. Molinari, H. Wijkstra, P. A. Dayton, and M. Mischi, "On the relationship between dynamic contrast - enhanced ultrasound parameters and the underlying vascular architecture extracted from acoustic angiography", *Ultrasound Med. Biol.*, vol. 45, pp. 539-548, 2019, doi: <https://doi.org/10.1016/j.ultrasmedbio.2018.08.018>

## 3.1 Introduction

Malignant tissue shows a set of alterations from benign tissue that can be used as markers to detect it [207]. Of particular interest for cancer imaging are the altered vascular architecture and the consequent changes in blood supply. Angiogenic vessels grow to nourish the tumor and support its proliferation. These vessels have been found to be tortuous, to grow chaotically, without the typical vessel hierarchy, and with a high occurrence of arteriovenous shunts. Many of these properties can be recognized with contrast-enhanced ultrasound techniques, which have shown promising results for distinguishing malignant tissue from benign [36, 147, 215, 216, 261, 312, 347].

Dynamic contrast-enhanced ultrasound (DCE-US) captures the contrast-agent passage through the vascular bed after its injection in the patient's bloodstream. Specifically, it registers the local evolution of gray-level intensity at each pixel, referred to as the time intensity curve (TIC), which reflects the varying ultrasound contrast agent (UCA) concentration. The recorded intensities are then converted into UCA concentration with a linearization function specific to the employed ultrasound scanner [315], yielding an indicator dilution curve (IDC) for every pixel in the video. Various characteristics of IDCs have been proven to be useful for distinguishing malignant from benign tissue [261].

Several approaches have been adopted to extract information from IDCs derived from DCE-US bolus acquisitions. Some heuristic features of the IDCs, such as the wash-in time and the peak intensity, are related to cancer [261, 436]. Multiple other techniques employ IDC fitting by analytical models, such as the lognormal, gamma, and local density random walk (LDRW) model [362]. Functional parameters of the curves (*e.g.*, area-under-the-curve) are extracted and displayed in colormaps, aiming to obtain a clearly distinguishable malignant region. All these approaches mainly attempt to quantify perfusion, which is motivated by the presence of ample arteries feeding the tumor, increased microvascular density (MVD), and presence of arteriovenous shunts. Despite this, clinical evidence has shown that cancerous lesions in the prostate can also be iso- or hypo-perfused [36]. Indeed, it is known that tumor tissue has higher resistance to blood flow [270]. This induces a counterbalancing factor that complicates predictions about the level of blood supply within the tumor, as compared to surrounding tissue [78]. Furthermore, the MVD inside the tumor can be strongly heterogeneous, creating highly perfused regions as well as hypoxic, avascular regions. Therefore, assessment of perfusion alone is insufficient for reliable cancer diagnostics. These findings have motivated the development of contrast ultrasound dispersion imaging (CUDI), a method which enables assessment of UCA dispersion, in addition to quantification of perfusion [215, 261].

CUDI aims at quantifying the UCA dispersion due to the architecture of the vascular tree and complex multipath trajectories available for UCA transport. The main hypothesis that lies in the foundation of the method states that dispersion reflects structural vascular changes induced by angiogenesis. The first CUDI approach involved modelling of the IDCs in time domain with a LDRW model and extraction of a dispersion-related parameter from the fit model [215]. An important complication associated with this approach was poor signal to noise ratio, hindering the fitting procedure and decreasing its reliability. This problem has been mitigated by spatiotemporal similarity analysis [217, 261]. In a promising implementation, this approach involves calculation of an average correlation coefficient measuring the similarity of a TIC at a pixel and its surrounding pixels [216]. A theoretical description of the problem within the framework of the LDRW model has shown that the correlation coefficient between IDCs is monotonically related to the dispersion coefficient [217]. Moreover, this approach has demonstrated its superior performance compared to perfusion-related param-

ters at localizing prostate cancer in a clinical setting [216]. This method has been validated against cell differentiation reflected with the Gleason score for prostate cancer [334]. Another study identified that regions of low dispersion correlated with those of high MVD, quantified by immunohistology [320]. However, in this study detailed characterization of the vascular architecture (*e.g.*, tortuosity and vessel size) was not available.

Acoustic angiography (AA) can provide accurate characterization of the vascular architecture: it is a high-resolution technique, capable of imaging individual microvessels [147, 347]. AA permits imaging vessels at a high resolution of 100-200  $\mu\text{m}$  at 2 cm depth with minimal signal from tissue. While transmitting ultrasonic waves at frequencies in the order of a few MHz, close to the UCA bubble resonance frequency, it records the nonlinear response of the contrast agents in a high frequency range centered at 30 MHz. This technique grants the possibility to quantify vessel density and morphology measures such as the sum of angles metric (SOAM) and distance metric (DM) [313, 347]. These parameters have been reported to be significantly different for malignant and benign tissue [147, 347]. Thereby, AA gives the opportunity to validate whether these features are reflected in DCE-US due to the different character of UCA perfusion and dispersion in these vessels.

The aim of this work is to determine whether DCE-US is able to characterize the underlying vascular architecture. It involves DCE-US and AA imaging of fibrosarcoma tumors and control regions in a longitudinal study of 9 rats. AA and DCE-US acquisitions were performed every 3 days, at 4 time points, starting with the day when the tumors could be palpated. An overall comparison of the tumor's and control's vascular properties was performed. Additionally, a longitudinal study of these properties was conducted, aiming to find similar trends in features extracted from the two different techniques of DCE-US and AA.

## 3.2 Materials and Methods

### 3.2.1 Rat Models

Fibrosarcoma tumor implantation was performed in rats according to a previously applied protocol [360]. The tumor models were established from propagated tumor tissue provided by the Dewhirst Lab at Duke University. Before surgery the (Fischer 344) rats were anesthetized with isoflurane; their left flank was then shaved and disinfected. An incision ( $\sim 2$  mm) was made above the quadriceps muscle, and a sample of tumor tissue ( $\sim 1$  mm<sup>3</sup>) was positioned under the skin. The incision was closed with 1-2 staples. This procedure was performed at 3 different time points with 9 rats in total. Rats belonging to the same series were operated on the same day.

On day 8 after implantation, the first ultrasound acquisition was performed if the tumors were palpable. Otherwise, we waited for 2-3 days for subsequent assessment. When the tumors were palpable, UCA was injected in the rats' tail vein through a 24 gauge catheter while the animals were anesthetized with vaporized isoflurane in oxygen. DCE-US was performed on the tumor-bearing flank for assessment of perfusion and dispersion. The AA acquisition protocol immediately followed the DCE-US acquisition to minimize the amount of time each animal spent under anesthesia. The beginning of the DCE-US and AA acquisitions were different between the series, starting with day 8, day 11, and day 13, respectively. For all but one animal, subsequent imaging acquisitions were performed with an interval of 3 days, amounting to 4 time points in total. One rat was an exception since we were not able to inject the contrast (for both modalities) in its tail vein, and managed to image only at the first and third time points. All experiments were performed at the University of North Carolina at

Chapel Hill, approved by the Institutional Animal Care and Use Committee at the University of North Carolina at Chapel Hill.

### 3.2.2 Image acquisition

#### 3.2.2.1 DCE-US bolus injection protocol

A UCA bolus of  $2 \times 10^8$  microbubbles was injected in the rats' tail vein. The contrast agent used in this study was made in-house; it has a lipid shell and perfluorocarbon core, similar to Definity® (Lathes Medical Imaging/U.S.A, N. Billerica). A 15L8-S probe was utilized with a Siemens Sequoia scanner in Cadence Pulse Sequencing mode at an insonifying central frequency of 7 MHz. The acquired DCE-US recordings were stored in DICOM format.

#### 3.2.2.2 AA continuous infusion protocol

A continuous infusion of microbubbles was administered using a syringe pump (PHD 2000, Harvard Apparatus) at a rate of  $1.5 \times 10^8$  microbubbles per minute. AA imaging was performed with a dual-frequency single-element transducer transmitting at 4 MHz, and receiving around 30 MHz. The 3D AA images were acquired plane by plane, with a step size of 100  $\mu\text{m}$ .

### 3.2.3 DCE-US bolus data processing

#### 3.2.3.1 Preprocessing

All the bolus recordings were filtered with a Gaussian filter, as previously performed in [261], using a kernel of 0.13 mm equal to 1.6 pixels. This value improved the signal-to-noise-ratio at the cost of additional spatial correlation between TICs at neighbouring pixels. The TIC power of every pixel was evaluated as the root mean square of the TIC after the baseline was removed. Regions with a level of TIC power below -22 dBs of the maximum TIC power over all images were excluded from further analysis (shown in black in Fig. 3.1 a.). This limited the effect of random noise on the parameters of interest [218]. Characteristic of DCE-US is multiplicative noise: noise proportional in its power to the signal amplitude. By eliminating regions with low TIC power, we avoided erroneous parameter estimation from regions with low signal power where random noise dominates. After this, the intensity values of the remaining regions were linearized by inverting the logarithmic compression function implemented in the adopted scanner, yielding the IDCs.

#### 3.2.3.2 Assessment of dispersion

An average correlation coefficient was calculated for every pixel between its own IDC and those at its surrounding pixels within a ring-shaped kernel [261] with an inner radius of 0.6 mm and an outer radius of 2 mm. The inner radius was chosen equal to the lateral resolution of the preprocessed bolus recordings at  $\sim 2$  cm depth as identified with local autocorrelation analysis. Details about the latter procedure can be found in [261]. The lateral resolution was taken as a reference since it was worse than the axial resolution. The outer radius of the kernel was set equal to the size of 2 mm, which a tumor can usually reach without neovascularization [130]. The time window over which the IDCs were correlated to each other was selected to maximize the area under the receiver operating characteristic curve for tumor classification, resulting in a value of 17 seconds as proposed in previous work [286]. This is the only informative segment of the IDC (Fig. 3.2) due to early recirculation, as often observed in small animals

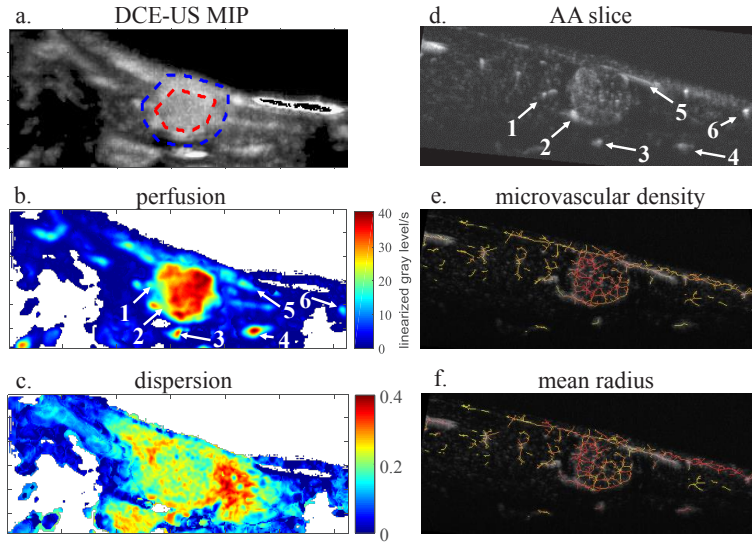


Figure 3.1: DCE-US and AA images of the same plane, and maps of the extracted features. a: maximum intensity projection of the DCE-US video. The tumor is encircled by a red contour, while the region outside the blue contour belongs to the control, separated by a margin which was not included in the analysis. Regions with power below the threshold of -22 dBs of the maximum intensity are displayed in black. b-c: perfusion and dispersion colormaps, respectively. Regions with power below -22 dBs of the maximum intensity are displayed in white. d: Selected AA slice. e-f: vascular skeleton, colorcoded according to the values of the microvascular density, and mean radius, respectively (yellow indicates low values, while red indicates high values). The numbers in b and d illustrate the vessels identified in the perfusion maps, used as markers to locate the right plane in AA volumes.

[359]. In this work, the beginning of the analyzed time window was set with 3 seconds before the appearance time, ensuring the wash-in phase to be entirely captured.

### 3.2.3.3 Assessment of perfusion

Wash-in-rate was adopted to assess perfusion and computed as the slope of a line fitted to the IDC in the 2-second interval after appearance time, as illustrated in Fig. 3.2. The value of 2 seconds was chosen to reflect the rise of UCA concentration in the initial part of the IDCs in all acquired clips.

### 3.2.4 AA data processing

The AA volumes were interpolated to reduce the inter-plane distance to 50 microns and make the pixels isotropic. Visible vessels were manually segmented and characterized in terms of vessel dimensions: vessel length (VL) and mean radius (MR). VL was computed as the length of the vessel segment identified between successive branching points, and MR was computed as the mean radius of this vessel segment along its length. Vessel tortuosity was assessed with the distance metric and the sum of angles metric (SOAM) [40]. The DM was computed as the ratio of vessel length to the Euclidean distance between its beginning and end. The SOAM

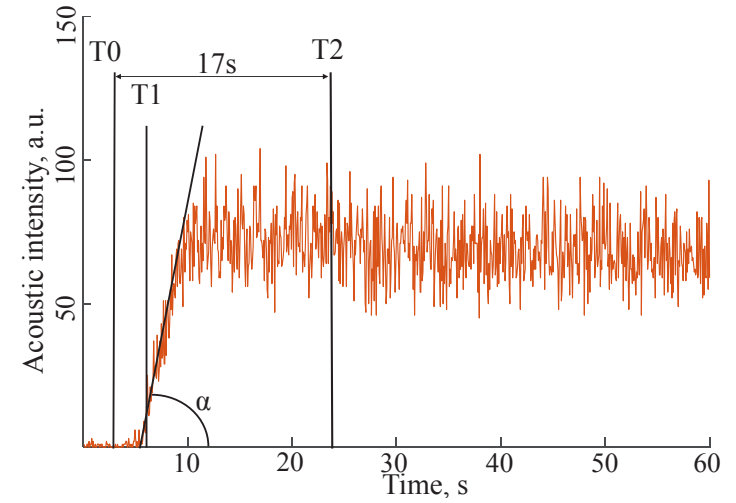


Figure 3.2: A typical preprocessed indicator dilution curve.  $T1$  shows the appearance time,  $T0$  is taken 3 seconds before appearance time. The interval from  $T0$  to  $T2$  shows the interval of the IDC used for dispersion analysis. The tangens of the angle  $\alpha$  of the line fitted to the indicator dilution curve in the 2 seconds after appearance time is the wash-in-rate.

was calculated as the sum of angles between successive points on the vessel centerline divided by VL, using the same formula as in [40], but excluding the torsional angle. Besides these individual vessel properties, MVD was calculated as a global characteristic of the tumor at a given timepoint, defined as the number of visible vessel segments divided by tumor volume. The volume vascular density (VVD) was computed with a moving 3D isotropic kernel in the central slice of the tumor ( $\sim 1$  mm in thickness). Otsu's method [388] was used to select a threshold to separate noise from vessel signal within the central slices; the percentage of pixels with vessel signal from the overall number of pixels in the 3D kernel was calculated.

### 3.2.5 Statistical analysis

The DCE-US parameters were spatially downsampled by a factor 7 in both directions, equal to the resolution of the preprocessed images. This was performed to exclude spatial correlation and prepare the data for the statistical tests that require sample independence.

#### 3.2.5.1 Comparison between tumor and control

Dispersion and perfusion values were divided into two groups. The tumor group was composed of the manually selected tumor regions (inside the red contour, Fig. 3.1 a.) from all rats at all time points binned together. The control group was taken from pixels outside the tumor contour, dilated by  $\sim 1$  mm (in blue, Fig. 3.1 a.). The region between the red and blue contour was excluded from analysis to avoid pixel assignment to the wrong group, since DCE-US information was not considered sufficiently accurate for tumor delineation as required by e.g. ablation therapy and surgery. The AA parameters were extracted in a similar fashion: vessels were taken from within the tumor region and outside it in the same flank (Fig. 3.3). Vessel segments on the border of the selected contour, whose belonging to a tumor or control group was debatable were disregarded from analysis.



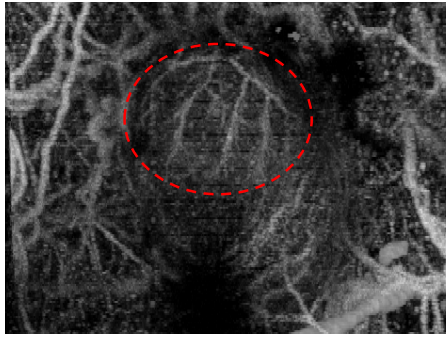


Figure 3.3: AA maximum intensity projection. The tumor region is indicated by the red contour, surrounded by the control region.

An Anderson-Darling goodness of fit hypothesis test was performed on all the parameter distributions to check for data normality. Since all the distributions were identified as non-Gaussian, a Mann Whitney non-parametric test was performed to establish the significance ( $p$ -value) of the difference between tumor and control. No additional subsampling or upsampling was performed to make the control and tumor data sets balanced, since the Mann Whitney test can be applied to data sets with distributions of different size [246].

The Cohen's  $d$  was used as a measure of the 'effect size' [363] that the tumor has on the underlying vasculature, calculated as the difference between the means of two distributions divided by the standard deviation of the control. The values of the Cohen's  $d$  term allow to classify the difference between two distributions according to 4 categories: small, medium, large, and very large for values of 0.2, 0.5, 0.8, 1.3, respectively.

### 3.2.5.2 Longitudinal study of tumor and control

A longitudinal study of the tumor evolution was performed with the Kruskal-Wallis post hoc test, evaluating the differences among the distributions of dispersion and perfusion, and vascular features of tumor and control at 4 time points. The Kruskal-Wallis test [212] does not require equal sample sizes, which is an advantage considering that our data set is unbalanced and incomplete: data is missing for one tumor at two time points as well as control at several time points for the large tumors. Moreover, the number of visible vessels is different for every image acquisition. For all rats, all parameter values were binned together according to the time point of the acquisition.

The statistic test calculation is influenced by the number of observations and can result in different outcomes for different sample sizes [212]. Since the number of pixels provided more samples for dispersion and perfusion compared to the number of vessels extracted with AA, these pixels were randomly subsampled to yield the same number of samples as vessels per each representative dataset of tumor and control at each time point. The only parameter that remained different in terms of group size is the MVD; being a global parameter that characterizes the entire tumor and control at a specific time point.

After the post-hoc tests were performed, the Pearson correlation coefficient was computed between the medians of the parameters showing similar longitudinal trends.

### 3.2.6 Mapping of vascular properties on the bolus acquisition plane

During the DCE-US bolus acquisitions the operator always tried to image the largest cross-section of the tumor, and keep the same orientation of the probe as used for AA. However, it was noticed that these precautions were not sufficient to reliably identify the DCE-US plane within AA: even a movement of the order of  $\sim 1$  mm alters the imaged vascular pattern of a tumor. It was noticed that the perfusion maps highlight larger vessels, clearly visible in the AA (Fig. 3.1 b. and d.). These vessels were used as markers to locate the bolus recording plane in the AA volume. For this, a dedicated tool was developed, allowing to freely scroll through the AA volume planes and change their orientation.

The selection of the plane was performed by visual inspection, choosing an image containing as many as possible vessel markers present in the perfusion maps. A slice in the AA volume of  $\sim 1$  mm thickness was selected and an extension of the skeletonization algorithm described in [252] was applied to extract MVD (Fig. 3.1 e.), MR (Fig. 3.1 f.), VL, and SOAM. This slice thickness was chosen to be of the order of the elevational resolution in the bolus recordings and sufficiently large to register vessel segments. This allowed a qualitative comparison of the spatial distribution of the vascular features with those of dispersion and perfusion in the same plane.

All the image processing and statistical analysis was performed with Matlab software (the MathWorks, Natick, MA).

## 3.3 Results

### 3.3.1 Statistical analysis

#### 3.3.1.1 Comparison between tumor and control

For all the extracted parameters, tumor and control have significantly different distributions ( $p < 0.001$ ). However, the magnitude of the differences, expressed in Cohen's  $d$ , spans a wide range (Fig. 3.4), showing a marginal effect size for the DM (Fig. 3.4 c.), and small to very large differences for the rest of the parameters.

#### 3.3.1.2 Longitudinal study of tumor and control

Since the DM showed almost no difference between tumor and control, it was excluded from the longitudinal analysis. Boxplots with all parameter values binned according to the time points are shown in Fig. 3.4, while Fig. 3.5 illustrates the results of the post hoc Kruskal-Wallis test, color-coded according to the significance level of the intra-distribution differences.

The dispersion median is relatively constant in time for both tumor and control, showing a significant difference for control and tumor distributions (Fig. 3.4 a., Fig. 3.5 a.). Tumor perfusion is significantly different from the control at all time points (Fig. 3.4 b., Fig. 3.5 b.), peaking for the tumors at the second time point. Interestingly, the longitudinal trend of the control's perfusion seems to mimic the tumor's trend in time, however, at a smaller magnitude, not identified as significant with the post hoc test.

The VVD is stably higher for tumor, while the MVD seems to follow a similar trend to that of perfusion, peaking for tumors at the second time point. However, the result of the MVD post hoc test is difficult to compare to others since the number of samples is different: only one value of MVD per time point is available, while the other parameters were subsampled according to the number of segmented vessels in the AA volume at a given time point.

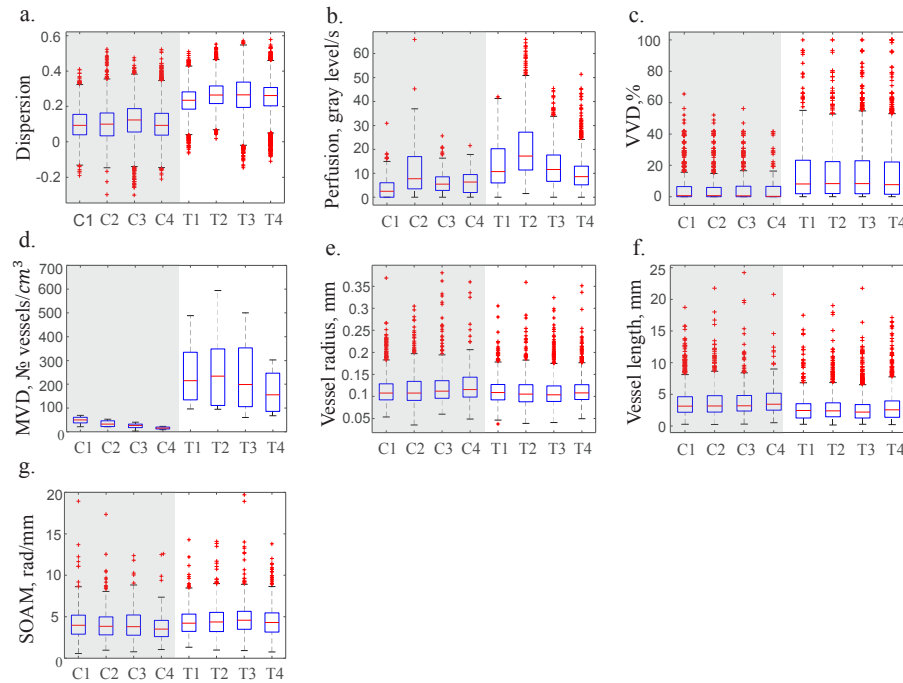


Figure 3.4: Boxplots of tumor and control parameters, binned together from all time points. *a*: dispersion, *b*: perfusion, *c*: distance metric, *d*: sum of angles metric, *e*: vessel length, *f*: vessel radius, *g*: microvascular density, *h*: volume vascular density. Cohen's *d* measure is indicated above the plots.

The post hoc results, illustrated by colormaps in Fig. 3.5, are comparable for dispersion, the VVD, the VL, and the SOAM. However, no significant correlation between the medians of the dispersion levels and the mentioned AA parameters has been identified. As for perfusion, the mean perfusion in tumors and their MVD showed a significant correlation coefficient of 0.572 ( $p < 0.001$ ) and inclusion of both control and tumor values resulted in a Pearson correlation coefficient of 0.67 ( $p < 0.001$ ).

### 3.3.2 Mapping of vascular properties on the bolus acquisition plane

The spatial parametric maps of the AA skeleton confirmed our observation that there is a correlation between regions of high perfusion and elevated MVD (Fig. 3.1 b. and f.). No spatial correspondance was found between dispersion and the other AA - derived parameters.

## 3.4 Discussion

Dispersion shows a large difference (Cohen's  $d = 1.68$ ) between tumor and control, exhibiting stable performance at tumor detection as it develops. Perfusion shows a lower discrimination power than dispersion, that is high for younger tumors, peaking at time point 2, and decreases

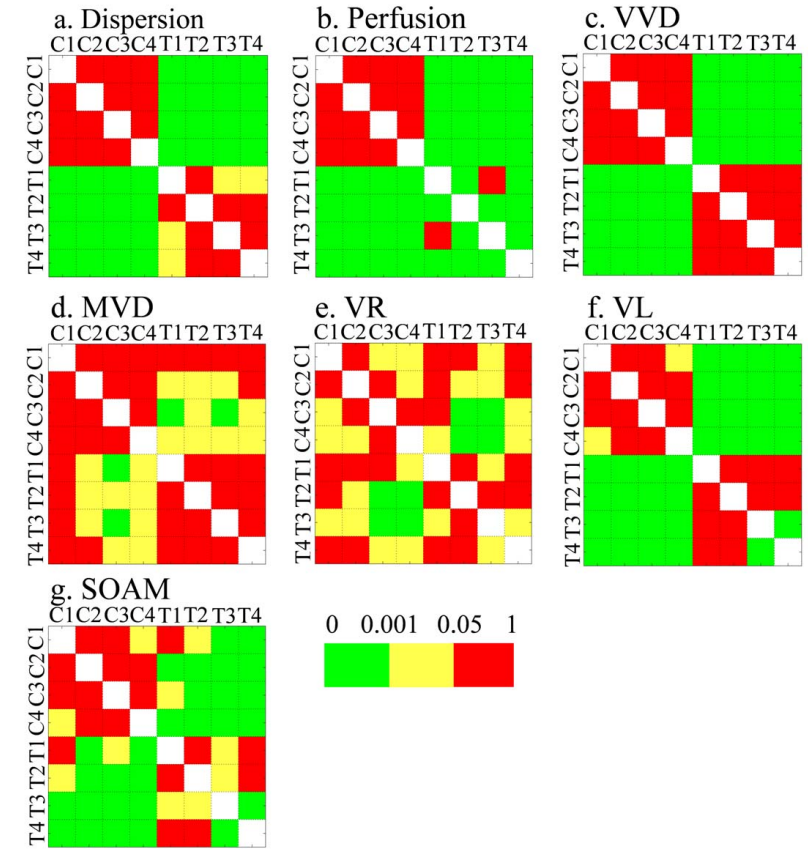


Figure 3.5: Results of the post hoc Kruskal-Wallis test performed on tumor and control parameters at four time points (indicated by T1, T2, T3, T4 and by C1, C2, C3, C4, respectively). The colors of the rows indicate whether the distribution is significantly different from the others, green and yellow representing different significance levels. *a*: dispersion, *b*: perfusion, *c*: volume vascular density, *d*: microvascular density, *e*: vessel radius, *f*: vessel length, *g*: sum of angles metric.

with tumor growth. Interestingly, the perfusion level in the control around the tumor is also elevated (Fig. 3.4 b.), showing a similar trend as in the tumor itself. This may reflect that the overall perfusion of tissue around the tumor is increased and influenced by the tumor. This effect has been shown for the SOAM, which exhibits intermediate values between that of tumor and control in tissue adjacent to the tumor [313]. Moreover, it has been shown for the fibrosarcoma model that the vascular source is often located in the periphery of the tumor [299, 379, 398].

Dispersion of the control stays stable over time, indicating that dispersion-related changes mainly occur within the tumor itself, and not in the surroundings. The spatial perfusion and dispersion maps are complementary, showing different patterns of highlighted regions (Fig. 3.1 b. and c.). Perfusion highlights large vessels, as well as regions with high MVD.

The SOAM indicates that the tumor has more tortuous vessels, exhibiting a similar trend

to that of dispersion (Fig. 3.4 a., g.) and comparable results for the post-hoc test (Fig. 3.5 a., g.). Nevertheless, the effect size difference, as indicated by Cohen's  $d$ , is much lower for the SOAM than for dispersion. In general, the control regions in this experiment show a higher tortuosity than we previously observed for these rats, expressed by the DM in [347]. Direct comparison of the SOAM in this work and in [347] is not available since the calculation of the SOAM has been adjusted since then. The unusually high tortuosity for control may be caused by the presence of the bowel region in some of the AA images, which was excluded from analysis in earlier studies, and may have elevated tortuosity. Previous data also shows that the SOAM exhibited an intermediate level of tortuosity in tissue up to 1 cm away from a tumor, with a mean tortuosity between that of tumors and non tumor-bearing animals [313]. The discrimination power of the SOAM in our data set increases for smaller vessels (Cohen's  $d=0.14$  for vessels with a radius  $> 0.11$  mm, 0.28 with an intermediate radius, and 0.43 with a radius  $< 0.09$  mm). Therefore, its relation with the extracted DCE-US features can not be fully appreciated due to the finite resolution of AA. Similarly, a previous study has shown that the difference in MVD between tumor and control increases for smaller vessels [337]. Therefore, it may be that the SOAM, MVD, and other metrics extracted in this study are related to dispersion; however, mainly smaller vessels' properties have a significant influence on it. Supporting this hypothesis is the former observation that regions with increased MVD correspond to those with low dispersion [320], as derived from immunohistology. The immunohistology derived MVD was based on evaluation of tomato lectin binding to the endothelial cells and therefore characterized the presence of vessels of all sizes.

Spots of increased vascular density or large vessels were detected with perfusion colormaps. The correlation between median perfusion level and MVD is the only significant inter-parameter agreement found in this work.

The Kruskal-Wallis test is ideally constructed for a study design when subjects are randomly assigned to different groups, so that each subject appears in one group only [212]. Moreover, the subjects within the group must be independent. We realize that these assumptions are not strictly valid in this study, since we observe the tumor evolution in the same rats over time and since the vessels selected from the same rat are, strictly speaking, not independent. However, we do not expect these limitations to be crucial for deriving a meaningful conclusion about the significant trends in time.

Imaging initialization was different among 3 series of experiments, starting with day 8, 11, and 13 after tumor implantation, as explained before. We consider that combining all the rats together according to the number of the acquisition is justified as the imaging was initialized according to the same strategy: when the tumors became palpable. However, since we waited for 2-3 days for subsequent assessment if tumors were not palpable on day 8, in future work it may be beneficial to assess the tumors every day or evaluate all tumors in a single cohort. This would ensure that the development of the imaged tumors is more consistent.

It is often observed that the wash-out phase is masked by recirculation in small animals. [359] shows that for a range of administered UCA doses the wash-out phase is more prominent in mice. Different UCA doses should therefore be investigated in our future work, since a prominent wash-out phase, in our experience, enhances the performance of CUDI [216]. A clear wash-out would also allow evaluating the wash-out as a complementary perfusion parameter.

An important limitation of this study is the 2D character of the extracted parameters of dispersion and perfusion. The results of the post hoc tests, therefore, must still be taken with caution since it was performed for 3D vascular features evaluated in the whole tumor volume and 2D dispersion and perfusion that leave us blind to out of plane information and restrict us

to the central tumor slice, which is not always representative of the whole tumor [360]. We mitigated this limitation by performing an additional spatial comparison of the parameter maps in the same plane, matched with the help of large vessels identified in the perfusion maps. The agreement between perfusion and MVD, noticed in the longitudinal trends, was also identified in the spatial distribution of these parameters in the same plane, raising more confidence to the finding that perfusion and MVD are correlated.

An improved study design should either include 3D DCE-US [332], giving more accurate overall tumor characteristics, or a registration procedure, allowing to fix the orientation of the probes and identify the location of the DCE-US plane within the AA volume. The finding that perfusion highlights large vessels can be used to further improve registration.

The absence of any parameters correlated with dispersion may pinpoint to the limitation of AA as a validation method for CUDI: while enabling very high resolution ultrasound imaging, it may not be sufficient to find out which vascular properties substantially influence dispersion, since dispersion may be mainly defined by properties of subresolution vessels. In this respect, it is possible to direct our attention to superlocalization methods that overcome the limit of diffraction: they are able to track single bubbles and determine their exact positions by finding the centers of their point spread functions [79, 118]. Another possible reason for the absence of vascular parameters that correlate with dispersion is that the adopted dispersion parameter, is in fact related to both dispersion and flow velocity [217]. Different vascular parameters may contribute to the separate terms of dispersion and flow velocity, while we assessed their combination. In this regard, it would also be of interest to apply another analysis to the DCE-US bolus recordings that allows to separate dispersion and velocity contributions [391].

### 3.5 Conclusions

In this work, dispersion demonstrated its superior performance at tumor classification compared to perfusion, as previously found for prostate cancer [216, 217, 261]. Perfusion colormaps highlight large vessels and regions of elevated MVD. The vascular factors that determine the dispersion level remain yet to be found, as well as the role of vessels with a diameter below 100-200  $\mu$  in defining perfusion levels.

### Acknowledgements

This work was supported by the European Research Council Starting Grant (#280209) and the Impulse2 programme within TU/e and Philips. This work was also supported by R01CA170665, R43CA165621, and R01CA189479 from the National Institutes of Health. Disclosure: P.A. Dayton declares that he is an inventor on a patent enabling the acoustic angiography technology and a co-founder of SonoVol, Inc, a company which has licensed this technology.

# 4

## **Experimental acoustic characterisation of an endoskeletal antibubble UCA**

---

4



## Abstract:

**Purpose:** An antibubble is an encapsulated gas bubble with an incompressible inclusion inside the gas phase. Current-generation ultrasound contrast agents are bubble-based: they contain encapsulated gas bubbles with no inclusions. The objective of this work is to determine the linear and nonlinear responses of an antibubble contrast agent in comparison to two bubble-based ultrasound contrast agents, *i.e.*, reference bubbles and SonoVue<sup>TM</sup>.

**Methods:** Side scatter and attenuation of the three contrast agents were measured, using single-element ultrasound transducers, operating at 1.0 MHz, 2.25 MHz and 3.5 MHz. The scatter measurements were performed at acoustic pressures of 200 kPa and 300 kPa for 1.0 MHz, 300 kPa and 450 kPa for 2.25 MHz, and 370 kPa and 560 kPa for 3.5 MHz. Attenuation measurements were conducted at pressures of 13 kPa, 55 kPa and 50 kPa for 1.0 MHz, 2.25 MHz, and 3.5 MHz, respectively. In addition, a dynamic contrast-enhanced ultrasound measurement was performed, imaging the contrast agent flow through a vascular phantom with a commercial diagnostic linear array probe.

**Results:** Antibubbles generated equivalent or stronger harmonic signal, compared to bubble-based ultrasound contrast agents. The 2nd harmonic side-scatter amplitude of the antibubble agent was up to 3 dB greater than that of reference bubble agent and up to 4 dB greater than that of SonoVue<sup>TM</sup> at the estimated concentration of  $8 \times 10^4$  bubbles/mL. For ultrasound with a center transmit frequency of 1.0 MHz, the attenuation coefficient of the antibubble agent was 8.7 dB/cm, whereas the attenuation coefficient of the reference agent was 7.7 dB/cm and 0.3 dB/cm for SonoVue<sup>TM</sup>. At 2.25 MHz the attenuation coefficients were 9.7 dB/cm, 3.0 dB/cm and 0.6 dB/cm, respectively. For 3.5 MHz, they were 4.4 dB/cm, 1.8 dB/cm and 1.0 dB/cm, respectively. We hypothesize that the antibubble agent attenuation is greater than that of the reference agent due to the solid cores in the antibubble agent. A dynamic contrast-enhanced ultrasound recording showed the nonlinear signal of the antibubble agent to be red 31% greater than for reference bubbles and 23% lower than SonoVue<sup>TM</sup> at a high concentration of  $2 \times 10^6$  bubbles/mL.

**Conclusion:** Endoskeletal antibubbles generate comparable or greater higher harmonics than reference bubbles and SonoVue<sup>TM</sup>. As a result, antibubbles with liquid therapeutic agents inside the gas phase have high potential to become a traceable therapeutic agent.

From: A. Panfilova, P. Chen, R. J. G. van Sloun, H. Wijkstra, M. Postema, A. T. Poortinga, and M. Mischi, "Experimental acoustic characterisation of an endoskeletal antibubble contrast agent: first results", *Med. Phys.*, vol. 48, pp. 6765-6780, 2021, doi: <https://doi.org/10.1002/mp.15242>

## 4.1 Introduction

Ultrasound contrast agents (UCA) are utilized in the clinic in order to visualize the blood pool and assess organ perfusion and dispersion, aiding cancer detection [215, 280, 385, 391]. In some cases, the current UCAs do not exhibit sufficient nonlinear behavior to eliminate clutter and image artefacts, leading to diagnostic misinterpretation [125]. Augmenting UCA nonlinear behavior improves image contrast and diagnostic confidence. To this end, we propose antibubbles as a new UCA. Endoskeletal antibubbles [214, 300] have been shown to oscillate significantly more asymmetrically than reference bubbles with no cores and, therefore, are hypothesized to demonstrate enhanced nonlinear behavior compared to bubble-based UCAs.

UCAs are gas microbubbles stabilized by a shell composed of lipids, cross-linked polymers or denatured proteins [344, 361]. With a size comparable to that of the red blood cells, they are able to pass through the smallest capillaries. At the same time, they are bigger than endothelial gaps and therefore do not extravasate into tissue [194]. When insonified at sufficient pressure, gas microbubbles oscillate in a nonlinear fashion, generating higher harmonics [69, 87]. This effect is generally more pronounced when the sonicating frequency is close to the resonance frequency of the microbubbles. The generation of higher harmonics in tissue is much weaker compared to that in UCAs. This enables the implementation of contrast-specific imaging solutions for visualization of the blood pool, and therefore analysis of blood flow and vasculature by contrast-enhanced ultrasound (CE-US) [98] and dynamic contrast-enhanced ultrasound (DCE-US) [147, 385, 391]. Despite the recognized utility of CE-US and DCE-US in the clinic [98, 238], cumulative nonlinear effects occurring in tissue can reduce the contrast-to-tissue ratio, especially at greater depth [125]. Several contrast-specific imaging schemes, such as power modulation [75, 280] and subharmonic imaging [132, 281] can significantly suppress the nonlinear signal generated by tissue. In this work, we investigate the possibility of using a contrast agent with augmented nonlinear behavior for this purpose, enabling imaging at lower pressure amplitudes and causing weaker higher harmonic generation in tissue.

A droplet entrapped in a gas bubble has been referred to as an antibubble [105, 305]. This term has also been used for UCAs with microbubbles containing incompressible inclusions in the gas phase [206, 300]. Encapsulated microbubbles that contain incompressible inclusions and a solid supporting skeleton that suspends the inclusion have been referred to as endoskeletal antibubbles [214]. Figure 4.1 presents a schematic of an endoskeletal antibubble with a 2% volume inclusion. Theoretical work [206] demonstrated antibubbles to show an increased nonlinear behavior, compared to reference gas bubbles without incompressible cores. This was attributed to non-symmetric oscillation in the US field, where the antibubble showed larger expansion than contraction because of the incompressible core. Experimental evidence of this effect was acquired with a high-speed camera for endoskeletal antibubbles [214]. These studies [206, 214] suggest that antibubbles have a high potential to improve CE-US image quality, generating greater higher harmonics, compared to conventional UCAs. Besides this, antibubbles incorporating therapeutic agents in the gas phase can deliver larger doses of therapeutic agents, compared to alternative strategies [302, 344]. This way, antibubbles may offer clinicians a traceable and highly effective therapeutic agent. Currently no clinically approved antibubble contrast agent exists. Moreover, experimental proof of greater higher-harmonic generation is scarce [306]. The current experimental study investigated the potential of antibubbles for imaging purposes. To this end, nonlinear side scatter and linear attenuation measurements of endoskeletal antibubbles, reference bubbles and SonoVue<sup>TM</sup> were performed in the clinically diagnostic frequency range at frequencies of 1.0, 2.25 and 3.5 MHz. The

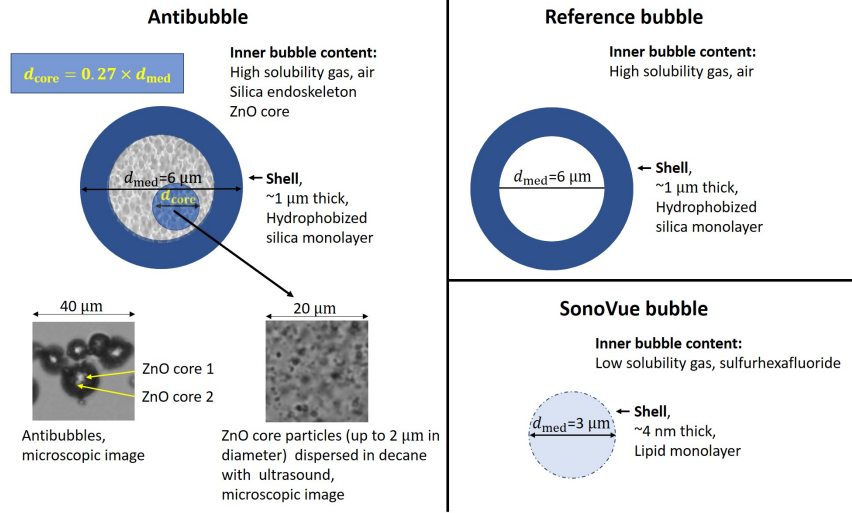


Figure 4.1: Schematic illustration of antibubbles, reference and Sonovue bubbles. The median antibubble diameter was estimated to be  $6 \mu\text{m}$  [5]. The incompressible core(s) comprises, on average, 2% volume, equivalent to an inclusion radius constituting 27 % of the bubble radius. Surrounding the core is the endoskeleton in air, encapsulated by a silica shell, whose thickness was estimated to be around  $1 \mu\text{m}$ , estimated from microscopic images in [214]. The median reference bubble diameter was estimated to be  $6 \mu\text{m}$  [5]. Reference bubbles are filled with air, encapsulated by a silica shell. Sonovue bubble, with hexafluoride ( $\text{SF}_6$ ) gas, encapsulated by a thin phospholipid shell [172, 383] and a mean diameter of  $3 \mu\text{m}$  [335, 383].

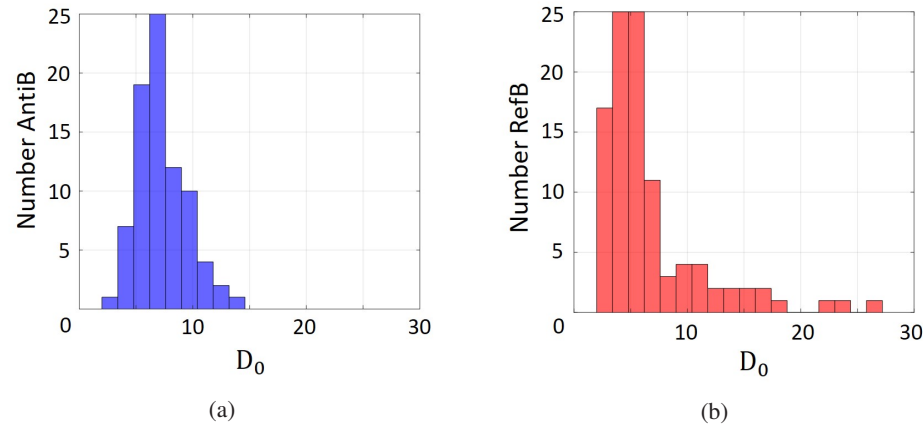


Figure 4.2: The size distributions of (a) antibubble and (b) reference bubble in the studied dispersions. The data was taken from (Anderton, 2020) [5].

scatter and attenuation parameters quantify UCA efficacy: the amplitude of the nonlinear scatter signal defines the signal-to-noise ratio in DCE-US imaging, while attenuation defines

the visible image depth [35]. The endoskeletal antibubbles have a median diameter of  $6 \mu\text{m}$ , with 93% smaller than  $10 \mu\text{m}$  [5] (Fig. 4.2a). They are stabilized by a silica shell and contain solid ZnO inclusions in the air gas phase. These inclusions take up 2% of the antibubble volume, while the rest of the gas phase contains silica nanoparticles, forming the endoskeleton [214] (Fig. 4.1). The studied endoskeletal antibubbles are somewhat bigger than those typically utilized in the clinic and, therefore, are currently only a UCA prototype. Reference bubbles have no core inclusions and no endoskeleton but, like antibubbles, have a silica shell [214] (Fig. 4.1). The median diameter of reference bubbles is  $6 \mu\text{m}$ , with 81% below  $10 \mu\text{m}$  [5] (Fig. 4.2b). The endoskeletal antibubbles and reference bubbles have not been clinically approved. Endoskeletal antibubbles are currently only an antibubble prototype, while reference bubbles give the opportunity to compare higher harmonic generation of endoskeletal antibubbles to that of a UCA with the same shell. SonoVue<sup>TM</sup> is a clinically approved UCA, used as a benchmark in this study. SonoVue<sup>TM</sup> microbubbles contain a low-solubility gas ( $\text{SF}_6$ ) encapsulated in a phospholipid shell, with a mean diameter of  $3 \mu\text{m}$ , with more than 90% of the bubbles below  $8 \mu\text{m}$  [335, 383] (Fig. 4.1). Its size distribution leads to a resonance frequency around 3 MHz [89, 155]. The resonance frequencies of endoskeletal antibubbles and reference bubbles have not yet been identified.

The scatter measurement was performed at acoustic pressures comparable to those employed clinically at mechanical indexes (MIs) of 0.2 and 0.3, often utilized for DCE-US [94, 202, 251]. Signals at these MIs are sufficiently strong to trigger nonlinear bubble oscillation and, at the same time, low enough not to induce damage to biological tissue and bubble bursting [77, 301]. A hydrophone was utilized as a receiver to enable registration of a broad spectrum of the scattered signal, including higher harmonics and subharmonics. The attenuation measurement was performed for  $\text{MI} < 0.04$ . Low pressures are typical for attenuation measurements [425], they avoid depletion of the fundamental signal due to generation of higher harmonics, which is especially prominent in case of UCAs. Moreover, at greater pressures UCA bubbles may generate a strong fundamental component, interfering with the transmitted pulse and introducing further error in the measurement. This way, we measured attenuation as a result of energy absorption [35] and energy scattering in a nearly linear low-amplitude regime of bubble oscillation [138], as demonstrated for antibubbles, reference bubbles and other contrast agents at greater pressures than those utilized in this work [214, 226, 338]. For both scatter and attenuation measurement pulses of 10-20 cycles were transmitted, providing a sufficiently narrow bandwidth to avoid overlap between the harmonics in the received spectra.

To demonstrate antibubbles' performance in a nearly clinical setting, a DCE-US measurement was performed: the flow of endoskeletal antibubbles, reference bubbles and SonoVue<sup>TM</sup> was imaged through a porous phantom [62] with a linear array US transducer. The spaces between the acoustically transparent beads composing the vascular phantom simulated a vascular network. The transmitted pulses consisted of 3 cycles at 3.5 MHz, granting sufficient resolution for phantom visualization, and with an  $\text{MI} = 0.2$ .

## 4.2 Methods

### 4.2.1 Scatter measurements

#### 4.2.1.1 Contrast agent fabrication and preparation

Endoskeletal antibubbles were produced as described by Poortinga [300] with some modifications. The antibubbles were stabilized using pharmaceutical grade Aerosil<sup>®</sup> 972 Pharma hydrophobized silica particles (Evonik Industries AG, Essen, Germany). The aqueous cores were replaced by 2 vol% (sample 1) of hydrophobically modified Zano 10 Plus ZnO nanoparticles (Umicore, Brussels, Belgium). Reference bubbles containing no cores were produced in the same way but without adding core material. As compared to the procedure in [300], the mixing speed of the high-shear mixer (IKA T18 Ultra Turrax equipped with an S18N-19G rotor-stator) was increased to 12,000 rotations per minute to produce smaller antibubbles with a size comparable to that of conventional UCAs.

All UCAs were maintained at room temperature before activation. The concentrations of investigated UCA dispersions were chosen in the low range, where a linear dependence of the scattered energy [32, 35, 137, 226] and attenuation [35, 86] on bubble concentration has been reported. The adopted concentration was in the order of  $10^5$  bubbles/mL for all studied UCAs, yielding a sufficient signal-to-noise ratio of the received signals. Preparation of reference bubble and antibubble dispersions was identical. 10 mg of dried material was diluted with 12 mL of saline in a vial. The resulting dispersions were manually gently agitated for 10 seconds, 0.35 mL was taken out and diluted in 3.35 mL of saline, giving a concentration of 0.08 mg per 1 mL. This corresponded to  $10^5$  bubbles/mL, based on the calculation of the overall gas volume corresponding to 0.08 mg of powder material and the average bubble volume. SonoVue<sup>TM</sup> was prepared according to the manufacturer instructions. The vial was gently agitated, and 0.4 mL of the dispersions was extracted right before the measurement and diluted to the concentration of 1  $\mu$ g per 1 mL which corresponds to  $8 \times 10^4$  bubbles/mL. For all UCAs the final dispersions were gently shaken manually for 10 seconds right before the measurement.

#### 4.2.1.2 Experimental procedure

The center of the cuvette with UCA dispersions was always positioned a few millimeters beyond the focal point of an US source (Fig. 4.3). A source holder and a cuvette holder were fixed on a rail system, providing alignment of the source and the cuvette. The utilized sources were all single-element focused US circular transducers with a diameter of 2.5 cm, and a focal distance of  $6.4 \pm 0.1$  cm. Transducers of type V302-SU-F, V304-SU-F and V380-SU-F (Olympus Nederland B.V., Leiderdorp, the Netherlands), were excited at their center frequencies of 1.0, 2.25 and 3.5 MHz, respectively. The omnidirectional secondary field created by the UCAs was recorded with a 1.0 mm needle hydrophone (Precision Acoustics Ltd., Dorchester, UK), oriented perpendicular to the source (Fig. 4.3). This is a typical configuration of the source and the receiver, utilized for scatter measurements [87, 115, 137, 338].

Gelatin cuvettes were prepared to contain the contrast agents during the experiments. Their advantage is a similar acoustic impedance to that of water and, therefore, low reflection. For cuvette fabrication, a hollow form and a ceiling top were 3D printed. The black cubic form was hollow, with inner dimensions of 12 by 3 by 3 cm. A lid was printed to seal the top of the cuvette once the liquid gelatin mixture was inside. This lid had a long cubic stick in the center with dimensions 10 by 1 by 1 cm. This construction shaped cubic gelatin cuvettes

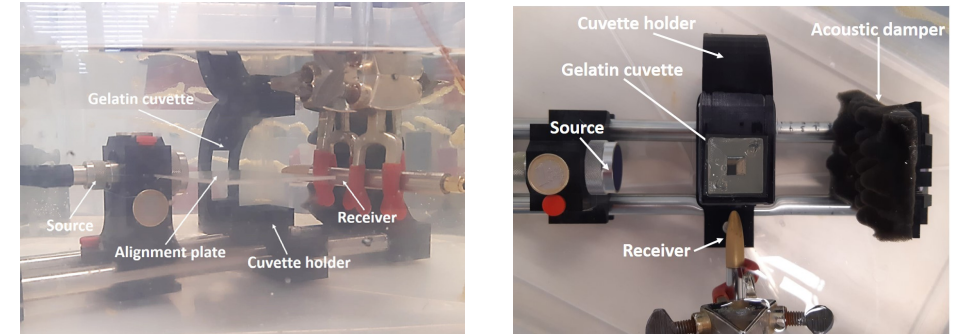


Figure 4.3: The setup for scatter measurements. (a) Side view. (b) Top view.

with 1 cm thick sides, and a hollow cubic void (with the dimensions of the cubic stick), where contrast material could be poured in. When preparing the gelatin mixture, 8 sheets of animal-based gelatin (Dr. Oetker, Amersfoort, The Netherlands) were diluted in 100 mL of water, corresponding to a concentration of 13 grams of gelatin per 100 mL. The mixture was poured in the hollow form, smeared with vaseline from the inside. The form was sealed with the lid and put in the fridge.

Prior to the scatter measurements, the voltage amplitudes of the driving signals were identified for each transducer in order to generate MIs of 0.2 and 0.3. These mechanical indexes are often used in clinical practice since they do not induce either bubble bursting or damage to biological tissue [77, 301]. Nevertheless, such signals are sufficiently strong to trigger nonlinear bubble oscillation. In the MI measurement, the gelatin cuvette was modified to position the hydrophone in the center of the cuvette. The generated pressures were recorded for various voltage amplitudes of the signals driving the source. The initial placement of the hydrophone in the center of the cuvette was visually aided, further adjustments were performed with the help of an oscilloscope, identifying the angular orientation of the hydrophone with the maximum signal amplitude.

Before the scatter measurement, the setup was submerged in a degassed water bath and left for a half an hour, allowing the gelatin phantom extracted from the fridge to reach room temperature. Two sides of the water tank, facing the source, were lined with foam to reduce possible reflections. The first measurement was always conducted for the reference liquid of saline. Additional acquisitions with a needle on the inside borders of the cuvette, were acquired to identify the region where the UCA signal was expected to originate. Further, the cuvette was emptied, the contrast-agent dispersions gently shaken and slowly injected in the cuvette. The UCA was shaken to ensure a homogeneous dispersion, *i.e.*, with a homogeneous spatial distribution of bubbles/antibubbles, filling the whole inner cavity of the cuvette. The measurement was performed right after injection not to allow the larger bubbles with more gas to rise. Two driving voltages were used one after another, corresponding to  $MI = 0.2$  and  $MI = 0.3$ , in an ascending order. The whole measurement lasted for a couple of seconds. This procedure was repeated 15 times for each UCA, with different batches of the contrast-agent dispersions being injected in the cuvette.

Labview (National Instruments Corp., Austin, TX, USA) was used to control the US acquisition of the acoustic response generated by UCAs. A 33220A arbitrary wave generator (Agilent Technologies, Santa Clara, California, USA) was connected to a desktop and con-



trolled by dedicated Labview software to generate the driving signals. The driving signals were transmitted to a 50-dB 2100L RF Power amplifier (Acquitek, Massy, France) connected to the source transducer. The received signals were displayed on a TDS2014 oscilloscope (Tektronix U.K. Limited, Bracknell, UK) and were further sampled throughout an NI-5122 (National Instruments Corp.) acquisition board which was connected back to the desktop and controlled by the Labview software. Sinusoidal tone bursts with a rectangular window, were transmitted by 3 sources driven at their center frequencies of 1.0, 2.25 and 3.5 MHz. A length of 20 cycles was chosen for 2.25 MHz and 3.5 MHz, and 10 cycles for 1.0 MHz. These pulse lengths provided a sufficiently narrow bandwidth of the transmitted signals and, therefore, allowed avoiding overlap between the harmonics in the received spectrum. The silence period between the pulses was always set to 250 microseconds, chosen to prevent interference of any possible reflection of the preceding pulse with the following pulse. A total of 92-95 pulses was transmitted at every acquisition. The signals were recorded at a sampling frequency of 25 MHz and stored for analysis.

#### 4.2.1.3 Data analysis of scatter measurements

All data analysis was performed with MATLAB<sup>®</sup> (The MathWorks, Inc., Natick, MA, USA). In the scatter measurement, the analyzed segment of the signal, generated by the UCAs was identified manually, confirmed by the acquisitions with the needles inside the cuvette (Sec. 4.2.1.2). A window of 9 microseconds was chosen for the analysis, defined by the shortest signal generated by the UCAs. The length of the time window was fixed for all sonicating frequencies. For each acquisition, an average Fourier amplitude spectrum was calculated based on 92 acquisitions, radiated by the UCAs, using Matlab's Fast Fourier Transform function. A Hanning window was used in all cases to reduce spectral leakage [157]. The nonlinear scatter spectra were represented in two ways. First, using

$$S_{nl}(f) = 10 \log_{10} \left( \frac{A_{CA}(f)}{A_{sal}(f)} \right), \quad (4.1)$$

where  $A(f)_{CA}$  is the amplitude of the signal generated by the UCA at frequency  $f$  and  $A(f)_{sal}$  the amplitude of the signal at frequency  $f$  acquired with saline in the cuvette, representing the noise level at that frequency [306]. In the second representation, the spectra were normalized by the amplitude of the fundamental frequency  $A_{CA}(f_0)$  in these spectra, using

$$S_{nl}(f) = 10 \log_{10} \left( \frac{A_{CA}(f)}{A_{CA}(f_0)} \right). \quad (4.2)$$

For each medium studied, the responses of 15 acquisitions, calculated with Eqs 4.1 and 4.2, were averaged, and their standard deviation was assessed.

Equation 4.1 allows comparison of the UCA efficacy at the concentrations used. However, this concentration is significantly lower than that used in the clinic [314, 414]. Since in the low concentration range all the generated harmonic amplitudes are proportional to the bubble concentration [137, 226], we normalized the UCA responses at all frequencies by the corresponding responses at the fundamental frequency, as shown in de Jong et al. [89]. Besides this, the scattered energy for every harmonic is also proportional to the squared bubble radius [137]. Therefore, it is hypothesized that this normalization reduces the influence of bubbles size and concentration on the scattered spectra.

Assessment of the significance of the differences between the higher harmonics of the UCAs was performed with the two-tailed Student's t-test, assuming a Gaussian distribution of

the higher harmonic amplitudes among the 15 acquisitions. A p-value below 0.05 is considered to indicate a statistically significant difference between the distributions.

#### 4.2.2 Attenuation measurements

The attenuation measurement was performed with a transmission setting (Fig. 4.4). The same source transducers as for the scatter measurement (Sec. 4.2.1) were employed, resulting in attenuation coefficients at 3 frequencies for all studied UCAs. The sources, the receivers and the cuvette with UCAs were fixed on the same rail system as for the scatter measurement. The center of the cuvette was positioned in the focal region of the sources. The opening in the gelatin cuvette containing UCA was 1.6-cm wide, ensuring that the whole beam passed through the studied dispersions. The length of the cuvette, corresponding to the path in the UCA dispersion, was 1 cm. Varying greatly among other experimental studies, from 2 cm to 8 cm, [121, 338, 371, 372], this cuvette length was chosen to ensure a sufficient signal-to-noise ratio after propagation through all studied UCAs at all frequencies. The receiver was fixed in a holder located 85 mm away from the cuvette (Fig. 4.4). A plane piston V306 transducer (Panametrics-NDT, Olympus NDT Inc., Waltham, MA, USA), centered at 2.25 MHz was used as the receiver for measurements at 1.0 and 2.25 MHz, and a plane piston V309 (Panametrics-NDT, Olympus NDT Inc., Waltham, MA, USA) was used for 3.5 MHz. The same system and control software was used for the attenuation measurement (Sec. 4.2.1.2), transmitting 20-cycle tone bursts for all frequencies. For every source, transmitted pressure amplitudes were below 60 kPa, measured in the center of the cuvette by the hydrophone, as for the scatter measurement (Sec. 4.2.1.2). At such low pressures, the bubble oscillation is mostly linear, as demonstrated in (Kudo et al., 2020) [214] for antibubbles and reference bubbles. SonoVue<sup>TM</sup>, on the other hand, exhibited an initiation of 2nd harmonic growth at pressures of 24 to 50 kPa [89, 339], depending on the transmit frequency. Therefore, a preliminary experiment was conducted, assessing the higher harmonic amplitudes for the chosen settings, demonstrating the higher harmonics to be below 5% of the fundamental signal. This way, it was concluded that the chosen settings primarily corresponded to the linear regime of bubble oscillation. Contrast-agent dispersions were prepared as for the scattering measurement (Sec. 4.2.1.1). They were injected in a gelatin cuvette right before the measurement. Attenuation was estimated based

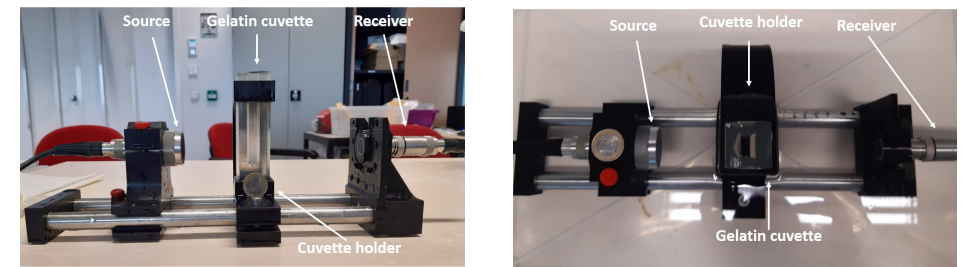


Figure 4.4: The setup for attenuation measurements. (a) Side view of the setup taken out of the water bath. (b) Top view.

on two measurements: when the cuvette contained 7 mL of saline and 7 mL of UCA. The Fast Fourier Transform was performed on all the received pulses in the acquisitions and the average amplitude at the fundamental frequency was extracted for saline  $A_{sal}$  and UCA  $A_{CA}$ .

The attenuation coefficient was computed using

$$\alpha(f) = \frac{20}{d} \log_{10} \left( \frac{TA_{\text{sal}}(f)}{A_{\text{CA}}(f)} \right), \quad (4.3)$$

where  $d$  is the length of the US path in the UCA medium defined by the inner dimensions of the cuvette and  $T$  is the transmit coefficient [338, 372]. For every UCA, 15 acquisitions were performed, yielding 15 values of the attenuation coefficient. The mean and standard deviation among these acquisitions were assessed.

In our measurement in Eq. 4.3,  $d = 1$  cm and  $T$  was approximated to 1, neglecting all reflection losses and possible acoustic impedance differences of UCAs with respect to water. In an experiment designed to verify this assumption for our gelatin cuvettes, it was identified that the amplitude of the transmitted pulse decreased by 1% only per 1 cm of the path in gelatin. These losses include reflection loss (defined by the difference in acoustic impedance) and attenuation. As for UCAs, the density was assumed identical to that of water due to the low concentration of bubbles used. The arrival times of the pulses transmitted through UCAs were compared to that in water. A maximum delay among all UCAs corresponded to 0.6 microseconds, indicating a maximum difference of 8 % in the speed of sound compared to water. For the three investigated frequencies, an attenuation measurement was conducted for corn oil, utilizing the same setup and making the same assumptions. The attenuation coefficients were in agreement with literature values [58], within a  $\pm 0.1$  dB/cm error.

To verify the measured attenuation values, another attenuation measurement was conducted with a different set up for 3.5 MHz, at the same acoustic pressure amplitude as for the through-transmission measurement, corresponding to  $MI = 0.03$ . 20-cycle pulses were transmitted, with a Gaussian window. An L11-4v linear array probe, controlled by a Verasonics US system (Vantage 128, Verasonics Inc.), was utilized to construct echo-mode videos, consisting of 100 frames. The image gain was set constant throughout depth and no log compression was performed, therefore, the graylevels of the videos represented the envelopes of the signals. The probe was positioned to provide normal incidence of the sonicating beam on the cuvette, while an aluminium plate behind the cuvette served as the reflector, as in [205]. A reference measurement with saline in the cuvette was performed, where  $A_{\text{sal}}$  was the grayvalue of the aluminium plate (Eq. 4.3), averaged over the 100 frames. Then the saline was taken out with a syringe and the UCA suspension was injected in the cuvette, resulting in a mean graylevel of the aluminium plate  $A_{\text{CA}}$ . The difference in the grayscale intensity of the aluminium plate in these two measurements allows to compute the attenuation coefficient (Eq. 4.3), accounting for the longer path through the UCA dispersion due to forward and backward directions. For all UCAs, the attenuation coefficient of 6 or 7 analogous dispersions was measured.

Besides this, the ratio of the pressures backscattered by the UCA suspensions to the transmitted pressure amplitudes was estimated for 3.5 MHz. For this estimation, the cuvette was removed from the acoustic path. The graylevel intensity of the aluminium plate divided by the reflection coefficient of the water-aluminium interface represented the sonicating amplitude  $A_{\text{transmit}}$ . The mean graylevel inside the cuvette represented the backscattered energy  $A_{\text{backsc}}$ . The ratio was computed as

$$S_{\text{lin}}(f) = \frac{A_{\text{backsc}}(f)}{A_{\text{transmit}}(f)} \times 100\%. \quad (4.4)$$

$S_{\text{lin}}$  represents the linear scatter at the fundamental frequency, since higher harmonic generation at these pressures was demonstrated to be negligible for antibubbles, reference bubbles and SonoVue<sup>TM</sup> [115, 137, 214].

### 4.2.3 Dynamic contrast-enhanced ultrasound measurement

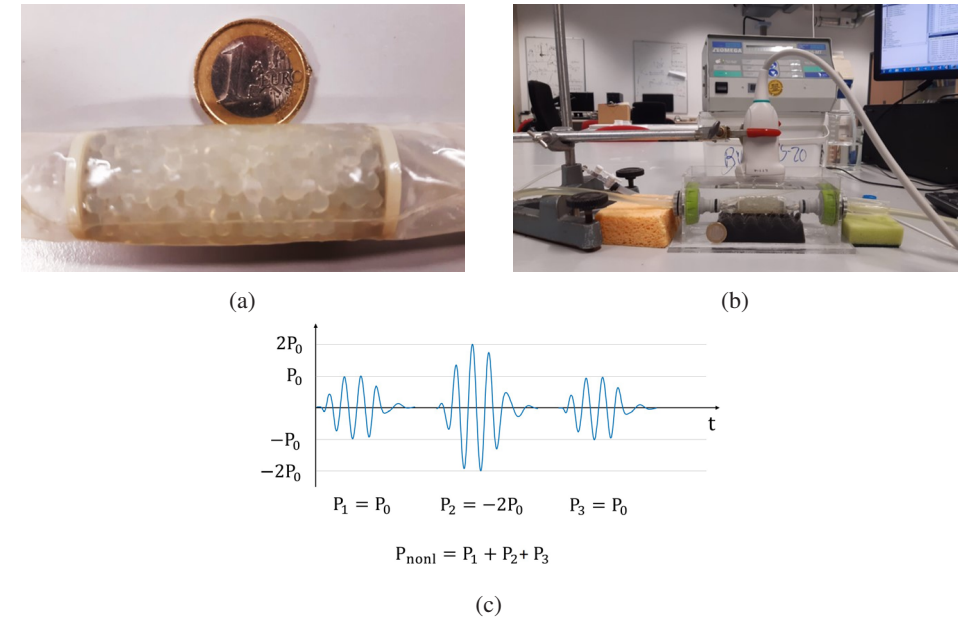


Figure 4.5: The setup for the dynamic contrast-enhanced ultrasound measurement. (a) A close-up view of a vascular phantom made of beads. (b) The probe is mounted on top of the vascular phantom, in a water bath. (c) The utilized pulse scheme, where three pulses were transmitted ( $P_1$ ,  $P_2$ , and  $P_3$ ) to form a DCE-US clip, reflecting the intensity of the nonlinear signal  $P_{\text{nonl}}$ .

To investigate the efficacy of UCAs in a near to clinical setting, a DCE-US measurement was performed. In this measurement, the UCAs were separately injected into a perfusion system, flowing through a porous phantom that mimicked a microvascular network. Degassed water flow through the phantom was supplied with an FPU5-MT peristaltic pump (Omega Engineering Ltd., Manchester, UK) at a rate of 36 mL/min. The utilized flow was in the range of expected physiological values, ranging from  $10^{-7}$  mL/min for capillaries [336] to  $10^3$  mL/min for large arteries [311, 336]. The porous phantom (Fig. 4.5a) was built by packing alginate beads with a diameter of 3.1 mm in a polyurethane tube, whose shape was fixed by two circular nets at the two sides of the phantoms. The phantom was gently squeezed and shaken after packing to achieve a more homogeneous structure [62]. The spaces between the beads simulated a microvascular network with porosity of 43%. Since the phantom consisted of identical beads, the simulated microvascular network did not exhibit the vessel/capillary topology typical for biological tissue [231, 336]. The water resistant alginate beads did not permit simulating tissue-water exchange observed in biological tissue [193]. This way, the phantom provided a simplified model of a microvascular network. The phantom used in the experiments was about 4.5 cm long, comparable to the length of the utilized US transducer, and 2 cm in diameter. Before the experiment, the phantom was submerged in a water bath and connected to the input and output flow paths (Fig. 4.5b). A linear array L11-4v probe, controlled by a Verasonics US system, was mounted above the



phantom. DCE-US plane wave imaging was performed in contrast-specific mode following the manual injection of a UCA bolus into the flow stream towards the vascular phantom. The utilized pulse scheme is illustrated in Fig. 4.5c, consisting of one high-amplitude pulse and two pulses, twice as low in amplitude and shifted in phase by  $180^\circ$ . The high-amplitude pulse pressure was 370 kPa, corresponding to  $MI = 0.2$  (the probe was calibrated with the same hydrophone). The transmitted pulses consisted of 3 cycles at 3.5 MHz, granting sufficient resolution for visualization of the beads composing the phantom. The contrast-specific mode was a combination of pulse inversion and amplitude modulation schemes, since it was shown to be the most sensitive imaging strategy to microbubble nonlinearities [110].

When injecting the contrast-agent bolus, we aimed to have the same concentrations at the peak of the time-intensity curves (TICs) as in the static measurement. A few preliminary measurements were conducted where 1 mL of reference bubble and antibubble dispersions (0.5 mg/mL) was injected. The water volume where the UCA was diluted [215, 391] before its arrival to the middle of the vascular phantom was assessed with the measured TICs in the middle of the phantom. A simple triangular model [237, 258] was used to correlate the concentration at the peak of the TIC and the identified mixing volume. For SonoVue<sup>TM</sup>, two greater concentrations were also used. Since the SonoVue<sup>TM</sup> bubbles are smaller, greater number densities were used to reach a volume fraction comparable to that in the reference and antibubble boluses. In these cases the concentration of SonoVue<sup>TM</sup> at the peak of the TIC was estimated to be 10 and 30 times greater than the concentration used in the static measurement.

For every UCA 4 DCE-US acquisitions were performed. For every acquisition, a 1-mL bolus with the calculated concentrations was injected. 40-second dynamic contrast-enhanced US clips recorded the flow through the porous phantom including the complete wash-in and wash-out. The TICs were extracted from the middle of the phantom (Fig. 4.5a) and compared, with the aim to identify the UCA producing the highest peak signal.

## 4.3 Results

### 4.3.1 Scattering

The average spectra of the signals generated by UCAs, normalized to the saline spectrum are presented in Fig. 4.6. The frequencies of the sonicating signals are stated above the plots. The thick vertical straight lines on the plots indicate this sonicating frequency and, therefore, the fundamental component of the signal scattered by UCAs. The thinner lines indicate integers of the fundamental frequency, representing the scattered higher harmonics. The error bars next to these lines demonstrate the mean and the standard deviation of the higher harmonic amplitudes among the 15 acquisitions for antibubbles (to the left of the harmonic line, in blue), reference bubbles (on the harmonic line, in red) and SonoVue<sup>TM</sup> (to the right of the harmonic line, in magenta). For the top plots, demonstrating the UCA response to sonication at an MI of 0.2, for 1.0 MHz and 2.25 MHz the nonlinear responses of antibubbles and reference bubbles are equivalent: the mean higher harmonic amplitudes differ no more than by 2 dB, with no significant differences in the higher harmonic distributions ( $p > 0.05$ ). For 3.5 MHz, the antibubbles scatter a 2nd harmonic 2 dB greater than the reference bubbles, with a significant ( $p < 0.001$ ) difference in the distributions. The 3rd harmonic content is equivalent. For SonoVue<sup>TM</sup>, at 1.0 MHz, all higher harmonics are up to 2 dBs weaker than those of antibubbles with a significant difference in the higher harmonic distributions ( $p < 0.05$ ). For 2.25 MHz and 3.5 MHz, SonoVue<sup>TM</sup> exhibits an analogous nonlinear response to antibubbles, with barely a difference in higher harmonic amplitudes

and complete or great overlap of the confidence intervals ( $p > 0.05$ ). For an MI of 0.3, all higher harmonics generated by antibubbles are significantly ( $p < 0.01$ ) greater than for the reference bubbles, at all the sonicating frequencies. In comparison to SonoVue<sup>TM</sup>, at 1.0 MHz the higher harmonic amplitudes of antibubbles are 2 to 4 dB greater ( $p < 0.001$ ). At 2.25 MHz, the nonlinear responses are equivalent ( $p > 0.05$ ), while for 3.5 MHz the 2nd and 3rd harmonic of antibubbles are significantly ( $p < 0.001$ ) greater (up to 2 dB) than those of SonoVue<sup>TM</sup>.

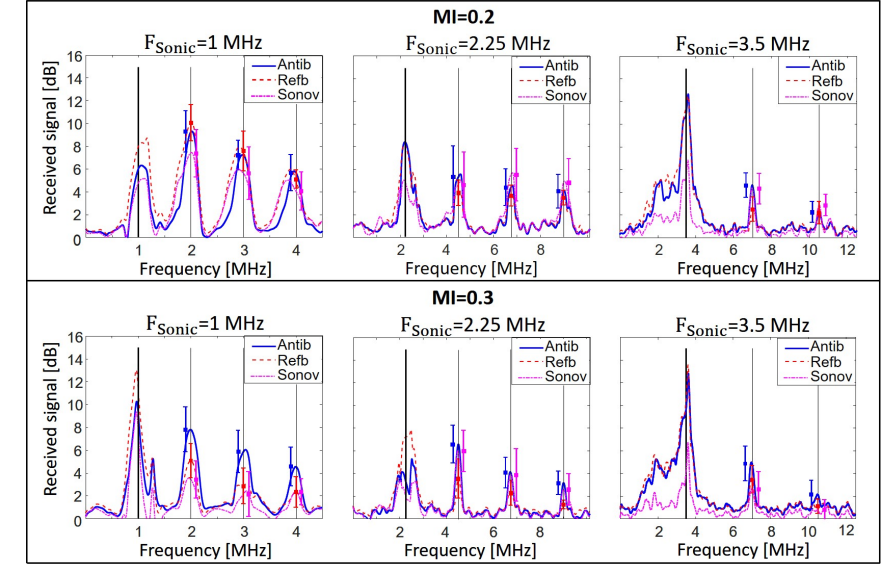


Figure 4.6: Mean spectra of the signals generated by antibubbles (Antib), reference bubbles (Refb) and SonoVue<sup>TM</sup> (Sonov) at frequencies of 1.0, 2.25 and 3.5 MHz for MIs of 0.2 (top) and 0.3 (bottom). The amplitude of the responses is presented in dB, normalized with respect to the responses in a reference acquisition with saline in the cuvette. The thick vertical lines indicate the fundamental frequency, while the thin vertical lines indicate higher harmonics. The error bars represent the standard deviations of the higher harmonic amplitudes.

The spectra normalized to their corresponding fundamental signals are shown in Fig. 4.7. Theoretical analysis predicts that all the harmonic amplitudes scattered by a UCA dispersion are proportional to the bubble concentration, in the low concentration range, and the bubble radius [69, 137, 226]. Normalizing the spectrum to the fundamental harmonic amplitude is hypothesized to mitigate to some extent the impact of the different bubble sizes and concentrations. This way, the provided normalized plots facilitate comparing the nonlinear behavior of the investigated bubbles/antibubbles. Analysis of the scatter spectra at pressures corresponding to an  $MI = 0.2$  follows below. At 1.0 MHz, antibubbles generated mean higher harmonic amplitudes equivalent to those of SonoVue<sup>TM</sup>, with nearly complete overlap of the confidence intervals ( $p > 0.05$ ). The mean higher harmonic amplitudes of reference bubbles are somewhat lower than those of antibubbles, with the greatest significant ( $p < 0.01$ ) difference of 3 dB in the 4th harmonic. At 2.25 MHz, higher harmonics of antibubbles are up to 5 dB weaker (3rd harmonic) than those of SonoVue<sup>TM</sup>, with a significant difference between the harmonic distributions ( $p < 0.05$ ), and equivalent to reference bubbles ( $p > 0.05$ ), with the

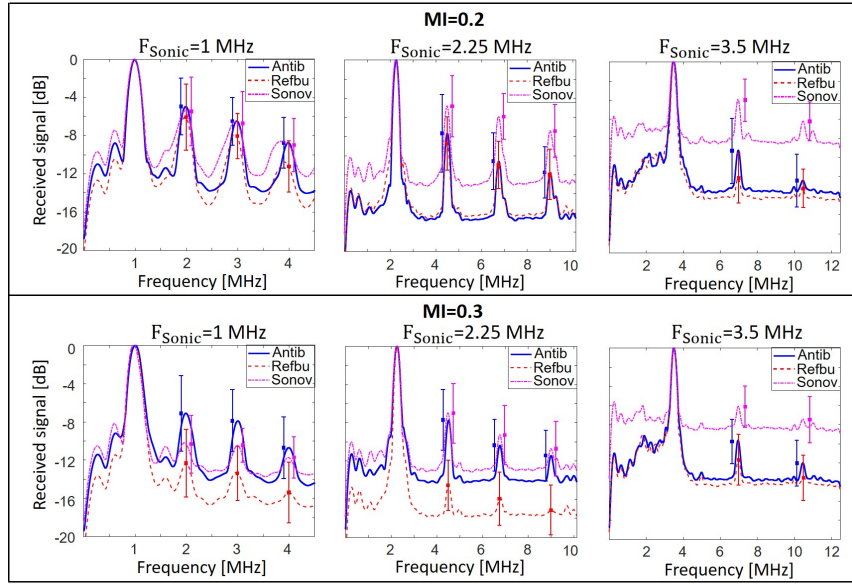


Figure 4.7: Spectra of the signals generated by UCAs at frequencies of 1.0, 2.25 and 3.5 MHz for MIs of 0.2 and 0.3. The amplitude of the responses is presented in dB, normalized with respect to the fundamental component in these responses.

antibubble signal up to 1 dB greater than that of reference bubbles. At 3.5 MHz, antibubble higher harmonics are significantly ( $p < 0.001$ ), up to 6 dB weaker than those of SonoVue<sup>TM</sup>. At the same time, they are up to 3 dB greater than those of reference bubbles with a significant difference between the scattered higher harmonics ( $p < 0.01$ ).

Analysis of the scatter responses at pressures corresponding to an MI = 0.3 follows below. For 1.0 MHz, antibubble higher harmonics are up to 3 dB greater ( $p < 0.05$ ) than those of SonoVue<sup>TM</sup> and up to 6 dB greater than those of reference bubbles ( $p < 0.001$ ). At 2.25 MHz, antibubble higher harmonics are equivalent to those of SonoVue<sup>TM</sup>, with a maximum difference of 1 dB and a p-value above 0.05. Antibubble higher harmonics are up to 7 dB greater than those of reference bubbles, with no overlap of the confidence intervals ( $p < 0.001$ ). At 3.5 MHz, antibubbles scatter higher harmonics that are significantly different from those of reference bubbles and SonoVue<sup>TM</sup>: they are up to 2 dB greater than those of reference bubbles ( $p < 0.05$ ) and up to 5 dB weaker than those of SonoVue<sup>TM</sup> ( $p < 0.001$ ).

Comparing plots at MI = 0.2 and MI = 0.3, in several cases the higher harmonic amplitudes decrease for higher pressures, compared to lower pressures. At 1.0 MHz, we observe this for all contrast agents ( $p < 0.05$ ). For 2.25 MHz this is observed for SonoVue<sup>TM</sup> and reference bubbles ( $p < 0.05$ ), while the signal scattered by antibubbles is equivalent for both sonicating pressures ( $p > 0.05$ ). At 3.5 MHz, SonoVue<sup>TM</sup>'s higher harmonics decrease for the higher pressure ( $p < 0.05$ ), while those of antibubbles and reference bubbles stay equivalent ( $p > 0.05$ ).

### 4.3.2 Attenuation

Figure 4.8 illustrates the mean attenuation of antibubbles, reference bubbles and SonoVue<sup>TM</sup>, with the corresponding standard deviations. For all frequencies, the mean attenuation coefficient is greater for antibubbles, compared to reference bubbles and SonoVue<sup>TM</sup>. At 1.0 MHz, antibubbles' attenuation coefficient is slightly higher than that of the reference bubbles, with a mean and significant difference of 1 dB/cm ( $p < 0.05$ ). For other measurements, all the differences in UCA attenuation are significant as well ( $p < 0.001$ ). At 1.0 MHz, the antibubble mean attenuation coefficient is 8.4 dB/cm greater than that of SonoVue<sup>TM</sup>. For 2.25 MHz, it is 6.7 dB/cm greater than that of reference bubbles and 9.1 dB/cm than that of SonoVue<sup>TM</sup>. At 3.5 MHz, it is 2.6 dB/cm greater than that of reference bubbles and 3.4 dB/cm greater than of SonoVue<sup>TM</sup>. The antibubbles attenuation coefficients are 8.7 dB/cm, 9.7 dB/cm and 4.4 dB/cm for 1.0 MHz, 2.25 MHz and 3.5 MHz, respectively.

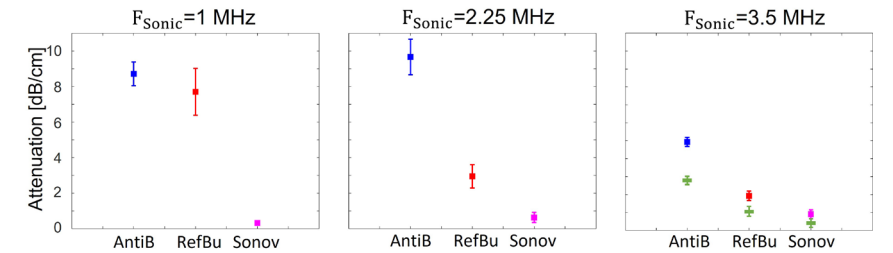


Figure 4.8: Attenuation coefficients measured for antibubbles (Antib), reference bubbles (Refbu) and SonoVue<sup>TM</sup> (Sonov) at sonicating frequencies of 1.0, 2.25 and 3.5 MHz (left to right). The square symbols indicate the mean attenuation coefficients measured with the piston source and receiver (Fig. 4.4). The rectangular (green) symbols indicate the mean attenuation measured in echo-mode with the Verasonics probe for 3.5 MHz.

The attenuation measurement conducted in echo-mode with the Verasonics system yielded attenuation values of 2.8 dB/cm, 1.1 dB/cm and 0.4 dB/cm for antibubbles, reference bubbles and SonoVue<sup>TM</sup>, respectively, illustrated with rectangular symbols in Fig. 4.8. The portion of the backscattered pressures  $S_{lin}$  (Eq. 4) constituted 4%, 6% and 2% of the transmitted pressures for antibubbles, reference bubbles and SonoVue<sup>TM</sup>, respectively.

### 4.3.3 Dynamic contrast-enhanced ultrasound

Figures 4.9a-4.9d demonstrate the maximum intensity projections of the DCE-US clips recording antibubble, reference bubble and SonoVue<sup>TM</sup> passage through the employed porous phantom. These images simulate potential clinical images of tissue, when imaging a UCA bolus passage in contrast-specific mode at pressures inducing nonlinear bubble oscillation. Figure 4.10 demonstrates the mean linearized TICs of the UCAs, normalized to the maximum mean peak intensity among the UCAs. From the measured TICs, one can observe that antibubbles generate a peak nonlinear signal 31% greater than that of the reference bubbles, 224% greater than that of SonoVue<sup>TM</sup> at the concentration studied in the static measurements, 53% greater than SonoVue<sup>TM</sup> at 10 times the concentration studied in the static measurements and 23% lower than that of SonoVue<sup>TM</sup> at the highest studied concentration.

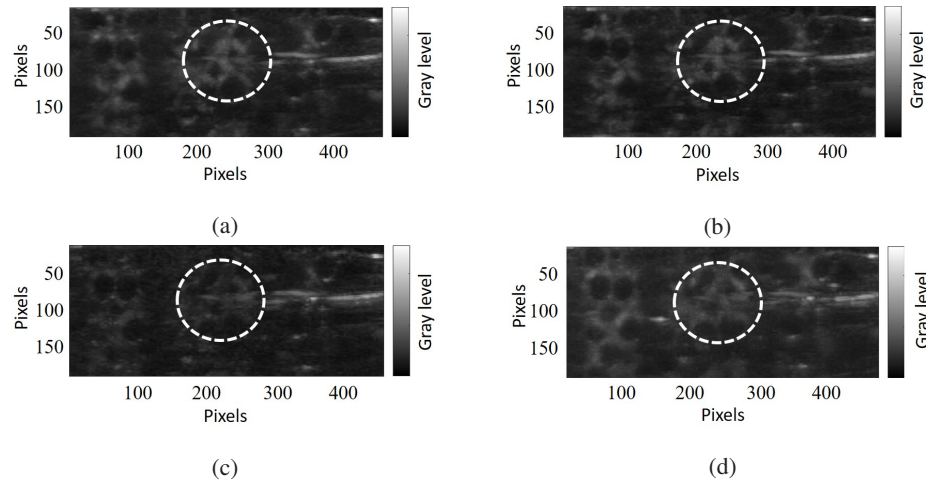


Figure 4.9: Maximum intensity projection based on the DCE-US recordings of UCAs passing through the porous phantom. The white contour indicates the region of interest where the TICs were extracted. (a) Antibubbles. (b) Reference bubbles. (c) SonoVue<sup>TM</sup> with a peak concentration as in the static measurement. (d) SonoVue<sup>TM</sup> with a peak concentration 30 times higher than in the static measurement.

## 4.4 Discussion

The scatter spectra normalized to the saline spectrum (Fig. 4.6) show antibubble higher harmonics to be equivalent or slightly greater, compared to reference bubbles and SonoVue<sup>TM</sup> in the studied frequency range. On the scatter spectra of SonoVue<sup>TM</sup> across all frequencies, we can not appreciate the expected growth in harmonic amplitude for the frequencies of 2.25 MHz and 3.5 MHz, close to its reported resonance frequency [89], in comparison to 1.0 MHz. This underlines that the scatter plots for separate sonicating frequencies do not demonstrate the frequency dependence of the UCA response. The sonicating field is different for every studied frequency, with different dimensions of the focal spot for each source.

For every sonicating frequency, comparing the spectra at  $MI = 0.2$  and  $MI = 0.3$ , we could not appreciate any marked growth of the nonlinear components of the scattered signals with increasing pressure amplitude. Markedly, at frequencies of 1.0 MHz and 3.5 MHz, at  $MI = 0.3$ , unlike at  $MI = 0.2$ , antibubbles scatter a higher nonlinear signal, compared to both other UCAs ( $p < 0.01$ ). The spectrum corresponding to 1.0 MHz and  $MI = 0.3$  exhibits an increase of broadband noise between the 2nd and 3rd harmonic, compared to  $MI = 0.2$ , possibly indicating the onset of bubble cavitation [64, 303]. It is also possible that the lower harmonic amplitudes at  $MI = 0.3$  are attributed to the rise of larger bubbles to the surface, since the scatter acquisitions at  $MI = 0.3$  were performed 2-5 seconds after those at  $MI = 0.2$ . Interestingly, antibubbles, the heaviest bubbles, exhibit the lowest difference in harmonic amplitudes for both  $MI$ s, while SonoVue<sup>TM</sup>, the lightest bubbles, exhibit the greatest difference. This indicates that for future characterization, the acquisition at all studied pressures should be performed right after injection of the contrast agents in the cuvette. Alternatively, a thickener can be added to increase the viscosity of the saline, slowing down the rise of larger bubbles to the surface of the dispersion, or a magnetic stirrer could be utilized to keep the dispersion uniform,

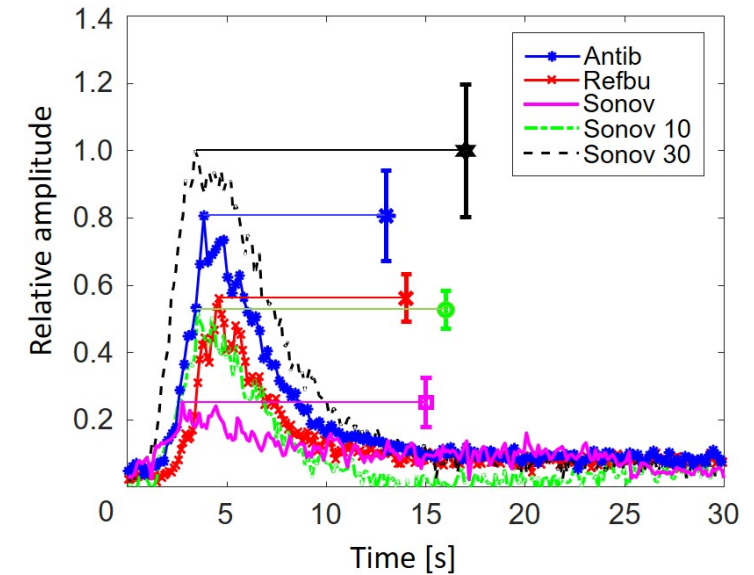


Figure 4.10: Linearized TICs of the middle region of the vascular phantom, averaged among 4 acquisitions for all studied dispersions. The peak amplitude for antibubbles, reference bubbles and SonoVue<sup>TM</sup> is generated by the same concentration of contrast agents as in the static measurement. The peak concentrations of Sonov10 and Sonov30 are 10 and 30 times higher than that in the static measurement. The error bars illustrate the standard deviation at the point of maximum intensity of the averaged curves.

as in [371].

The scatter spectra, normalized to the corresponding fundamental signal in the spectrum (Fig. 4.7), shows antibubble higher harmonics to be equivalent or up to 3 dB greater than those of reference bubbles. At frequencies of 2.25 MHz and 3.5 MHz, and pressures corresponding to  $MI = 0.2$ , SonoVue<sup>TM</sup> scattered the greatest higher harmonic amplitudes among the studied UCAs. This may indicate that, in the given experimental configuration, SonoVue<sup>TM</sup> has a greater capacity to scatter higher harmonics, compared to antibubbles and reference bubbles. At equivalent bubble size and bubble concentration, SonoVue<sup>TM</sup> may generate a stronger nonlinear signal. This might not have been appreciated on Fig. 6 due to the smaller size of SonoVue<sup>TM</sup> bubbles or a somewhat lower concentration. On the other hand, the provided normalization cannot fully compensate for the influence of the size distribution, as the energy scattered by a certain UCA dispersion is the energy integrated over the bubble size distribution through a complex nonlinear process. Experiments involving other bubble/antibubble size distributions are needed to confirm the observations in Fig. 7."

The attenuation measurement is an important indicator of UCA efficacy [35] since lower attenuation allows avoiding shadowing and imaging at further depth. Endoskeletal antibubbles exhibit the greatest attenuation among the studied UCAs. Given that the attenuation coefficient of most studied dispersions of clinically-approved UCAs does not exceed 4.5 dB/cm in the whole diagnostic frequency range [115, 149, 155, 370], and that most soft tissue types have an attenuation coefficient below 0.5 dB/(cm MHz) [153, 373], endoskeletal antibubbles exhibit remarkably high attenuation at 1.0 and 2.25 MHz. The high attenuation of antibubbles



may be caused by the endoskeleton that may add a viscous behavior to the inner gas phase. Alternatively, the hydrophobic ZnO particles forming the endoskeleton were observed to be surrounded by a thin gaseous layer [307]. These tiny air pockets are acoustically active at low acoustic amplitudes, absorbing acoustic energy and cavitating [307].

The attenuation measurement at 3.5 MHz, conducted with a Verasonics probe in echo-mode, yielded somewhat lower attenuation values for all UCAs than the through-transmission measurement with piston transducers. However, both measurements point out the same qualitative differences among UCAs. The discrepancy in the measurement results may be due to different pulse shapes: in the through-transmission acquisition a rectangular pulse was utilized, while a Gaussian pulse was transmitted in the echo-mode measurement.

The attenuation measurement is independent of the source pressure field [89]. The frequency of maximal attenuation of UCAs indicates the resonance frequency of the bubble population [89, 115]. At this frequency, the bubbles transfer a greater portion of energy to higher harmonics. A resonance frequency close to 3.5 MHz is in line with studies that report a resonance frequency close to 3 MHz for SonoVue<sup>TM</sup> [89]. Based on the attenuation measurements, the resonance frequency of reference bubbles is hypothesized to be close to 1.0 MHz, the frequency of maximum attenuation. Following the same reasoning, the resonance frequency of antibubbles is hypothesized to be between 1.0 and 2.25 MHz, closer to 2.25 MHz. This is in line with a smaller size of antibubbles compared to the largest reference bubbles [89, 155]. The presence of an incompressible core also increases the resonance frequency of a bubble [214]. However, it must be noted that the sonicating pressures differed for the studied frequencies and an additional measurement with equivalent pressures is advisable for future work.

At low acoustic pressures, where mainly linear low-amplitude bubble oscillation takes place [115, 137, 214], endoskeletal antibubbles backscatter less energy than reference bubbles and more than SonoVue<sup>TM</sup> at the studied concentration, expressed in  $S_{lin}$  (Eq. 4.4). It is theoretically predicated that the backscattered energy is proportional to the gas volume in the UCA dispersions [69, 137, 155]. The same weight of dried contrast material was diluted in saline for antibubbles and reference bubbles, whereas antibubbles contain an endoskeleton and solid cores. This may have resulted in a greater number of reference bubbles than antibubbles, as shown in Fig. 4.2 (81 antibubbles versus 101 reference bubbles). At the same time, the reference bubble dispersion contains a small percent of reference bubbles almost twice as large as the largest antibubbles (Fig. 4.2). These bubbles have a greater scattering cross-section [69, 137]. The SonoVue<sup>TM</sup> dispersion clearly contains a smaller gas volume with a comparable number of much smaller bubbles (Fig. 4.1).

The linearized TICs of the DCE-US acquisition exhibited periodic fluctuations (Fig. 4.10). These can be attributed to the pulsatile flow of the utilized peristaltic pump and to reverberation between the surfaces of the probe and the porous phantom. The TICs showed antibubbles to backscatter a nonlinear signal 31% greater than that of the reference bubbles, 224% greater than that of SonoVue<sup>TM</sup> at the concentration studied in the static measurements. This difference in the scattered signal is not present in the scatter measurement at the corresponding MI of 0.2, where antibubbles and SonoVue<sup>TM</sup> generate equivalent higher harmonics (Fig. 4.6). This finding may indicate that the scatter measurement was masked by the high attenuation of antibubbles surrounding the focal spot. Previous work [306] and preliminary work support this hypothesis. In preliminary scatter experiments (unpublished data), increasing the concentration of antibubbles and reference bubbles in homogeneous dispersions augmented the scattered nonlinear signal. However, the signal growth with concentration was greater for reference bubbles than for antibubbles. This way, the difference between the amplitudes of the scattered

nonlinear signal of reference bubbles and antibubbles decreased with growing concentration. At the same time, in previous work [306], a small quantity of antibubbles at a concentration 100 times greater than that in the studied homogeneous dispersions, injected in the very center of the cuvette filled with saline (the location of the peak pressure), generated a 2nd harmonic 10 dB greater than that generated by reference bubbles in the same setting. These findings support the conclusion that, in our scatter measurement configuration, where homogeneous dispersions were used and the US field was focused, attenuation affected the scatter measurement: the advantage of antibubbles over reference and SonoVue<sup>TM</sup> bubbles in Fig. 4.6 and Fig. 4.7 was masked proportionally to their attenuation. Since this evidence is indirect, additional experiments, imaging the fundamental pressure field and the generated 2nd harmonic in the DCE-US setting would help clarify whether the affect of attenuation was negligible on the generated and received 2nd harmonic signal. Scatter measurements in a wider/narrower cuvette may identify what role attenuation played in the scatter measurement.

At concentrations 10 and 30 times higher than that utilized in the scatter measurement, the nonlinear response of SonoVue<sup>TM</sup> grows, and at the highest SonoVue<sup>TM</sup> concentration the antibubble response is 23% lower than that of SonoVue<sup>TM</sup>. It is important to note that SonoVue<sup>TM</sup>'s resonance frequency is close to 3 MHz, while antibubbles have been shown to have a resonance frequency between 1.0 MHz and 2.25 MHz. Therefore, at lower frequencies, when sonicating with plane waves, antibubbles may perform better than SonoVue<sup>TM</sup>. Moreover, if made smaller for a clinical application, the antibubble resonance frequency is expected to increase, leading to even greater higher harmonic generation at 3.5 MHz. Figure 4.9 also illustrates that in cases when small quantities of contrast agent are distributed in a vascular network, in contrast to the scatter measurement, antibubble attenuation of 4.4 dB/cm does not degrade the images in a perceivable manner.

In comparison to commercial UCAs, the studied endoskeleton antibubbles are larger [77, 280]. A size below 7  $\mu\text{m}$  in diameter is recommended for UCA bubbles [77], about half the size of the largest endoskeleton antibubbles in the studied suspensions (Fig. 4.2). The shell thickness of commercial UCAs ranges from 2 to 200 nm [75, 136, 280, 383], with SonoVue<sup>TM</sup> having a particularly thin and compliant shell of about 4 nm [383]. The silica shell of antibubbles is stiff and about 1  $\mu\text{m}$  thick, based on brightfield microscopy images of antibubbles with the same shell [214]. The shell properties greatly contribute to UCA attenuation [69, 86], suggesting a study of alternative compliant materials for the antibubble shell that would reduce shadowing effects associated with high antibubble attenuation. Current generation contrast agents such as SonoVue<sup>TM</sup> and Definity<sup>TM</sup> typically contain low solubility gas, providing a longer bubble lifetime. The studied endoskeleton bubbles contain highly soluble air. No endoskeleton or core structures are present in any of the currently approved contrast agents.

## 4.5 Conclusions

Based on previous work, antibubbles, *i.e.*, encapsulated gas bubbles with incompressible cores, are expected to demonstrate augmented nonlinear behavior compared to encapsulated gas bubbles. This opens the door to improving CE-US image quality and to a traceable therapeutic agent with large amounts of therapeutic compounds in the core. This work aimed at characterizing the nonlinear behavior of endoskeletal antibubbles, an antibubble UCA prototype, and comparing it to reference bubbles and a commercially available and clinically approved UCA, SonoVue<sup>TM</sup>, in the range of diagnostic frequencies from 1.0 to 3.5 MHz and pressures comparable to those employed clinically at MI = 0.2 and MI = 0.3.

We demonstrated that the studied dispersions of endoskeletal antibubbles generate comparable or greater higher harmonic content than those composed of reference bubbles with an equivalent median diameter and smaller SonoVue<sup>TM</sup> bubbles. Higher harmonics comparable to that of SonoVue<sup>TM</sup> at a high concentration may be attributed to a larger antibubble size, a different shell and gas. Figure 4.7 mitigates the influence of bubble concentration and bubble size on the scattered spectra. However, the signals scattered by the UCAs in the focal spot may have been attenuated by the surrounding UCA. Therefore, the advantage of antibubbles over other contrast agents may have been masked in Fig. 4.7 by their higher attenuation. The plane-wave DCE-US measurement, simulating clinical imaging at 3.5 MHz, demonstrated that antibubbles have comparable performance to SonoVue<sup>TM</sup> at a high concentration at a frequency close to its resonance frequency, and superior performance, compared to the reference bubbles.

Based on this work, it is difficult to draw the solid conclusion that the incompressible core leads to greater higher harmonic generation, due to the differences in the size distributions (Fig. 4.2) and inner bubble content of the studied antibubbles and reference bubbles (Fig. 4.1). The stronger higher harmonics of antibubbles, compared to reference bubbles may also be attributed to the lower resonance frequency of the reference bubble dispersion. To present proof that antibubbles have an advantage over bubble-based contrast agents for imaging purposes, other reference bubbles are required, identical to antibubbles in all aspects, except for the core. Such an agent is currently not available. Nevertheless, we present evidence that endoskeletal antibubbles demonstrate strong nonlinear behavior at frequencies from 1.0 to 3.5 MHz. These results are encouraging and suggest that antibubbles hold high potential to serve as traceable therapeutic agents. For this purpose, the solid core would have to be replaced by a liquid inclusion with medication.

## Acknowledgements

This work was supported by eMTIC collaboration and partly by the National Research Foundation of South Africa, Grant Number 127102. We thank Anton Nikolaev for the design of the molds utilized for the cuvette preparation.

### **Part III**

## ***B/A* imaging**

# 5

## **A review on *B/A* measurement methods**

**Abstract:** The nonlinear parameter of ultrasound  $B/A$  has shown to be a useful diagnostic parameter, reflecting medium content, structure and temperature. Despite its recognized values,  $B/A$  is not yet used as a diagnostic tool in the clinic due to the limitations of current measurement and imaging techniques. This review presents an extensive and comprehensive overview of the techniques developed for  $B/A$  measurement of liquid and liquid-like media (*e.g.*, tissue), identifying the methods that are most promising from a clinical perspective. This work summarizes the progress made in the field and the typical challenges on the way to  $B/A$  estimation. Limitations and problems with the current techniques are identified, suggesting directions that may lead to further improvement. Since the basic theory of the physics behind the measurement strategies is presented, it is also suited for a reader who is new to nonlinear ultrasound.

From: A. Panfilova, R. J. G. van Sloun, H. Wijkstra, O. Sapozhnikov, and M. Mischi, “A review on  $B/A$  measurement methods with a clinical perspective”, *J. Acoust. Soc. Am.*, vol. 149, 2021, doi: 10.1121/10.0003627

## 5.1 Introduction

In the last several decades, ultrasound propagation has been treated as a nonlinear phenomenon [107]. The importance of nonlinear propagation effects has been recognised in medical ultrasound for predicting/modelling heat deposition in tissue, relevant for safety regulations, as well as defining optimal settings for high-intensity focused ultrasound therapy [54, 55, 108, 126, 148, 156, 183, 265] and lithotripsy [72]. In addition, tissue harmonic imaging has found wide application, improving the resolution of images with respect to those obtained in fundamental mode [42, 244, 348, 429]. Furthermore, stemming from a different underlying mechanism, contrast agents have become a useful tool in the clinic, generating strong nonlinear signal when isonified and allowing to extract information about vascular perfusion and dispersion [288, 391].

Apart from the established medical applications of nonlinearity, new ultrasound modalities for the quantification of the parameter of nonlinearity [245]  $B/A$  have been continuously developed for the last few decades in the effort to bring it to the clinic. This parameter characterizes the degree of nonlinearity of a medium. Studies of aqueous solutions have concluded that  $B/A$  is influenced by the chemical composition and molecular structure of the solutes [154, 329, 341], found useful to assess the structure of silicone oil used in eye surgery [439]. It has also been shown to be useful for tissue characterization, demonstrating distinct values for fatty [230], malignant, healthy and cirrhotic tissue in the liver [117, 154, 340, 341]. Since these different tissue conditions are also associated with different composition, several papers have developed models defining  $B/A$  depending on the constituents of the studied substance [7, 120], leading to works estimating tissue content from its  $B/A$  value combined with additional parameters (*e.g.*, speed of sound, compressibility) [8, 116, 154, 341].

In studies with the same chemical composition, it was shown that  $B/A$  increases with structural hierarchy of tissue (*e.g.*, intact liver vs homogenized liver) [227, 229, 435] and that  $B/A$  was sensitive to structural changes in tissue, caused by disease [154, 428]. Moreover, there have been indications that  $B/A$  reflects the quasilattice structure of water, i.e., the ratio of bound to unbound water molecules [342, 419], altered in malignant tissues [68, 276] and skin disease [369].

$B/A$  has also been used to quantify the nonlinear scattering properties of ultrasound contrast agents [395, 412, 413]. From a different perspective,  $B/A$  is sensitive to temperature, increasing for most liquids as the temperature increases [199, 243] and increasing as tissue is heated [66, 184, 235, 241, 341]. Even though some works show a small  $B/A$  increment when tissue is coagulated [184, 324], others state the contrary [66, 241]. Several works demonstrated that the  $B/A$  profile in tissue follows the temperature profile, generating images of the temperature distribution through  $B/A$  [179, 235, 241] and suggesting  $B/A$  as a tool for HIFU treatment monitoring [104, 394]. Besides this, there is evidence that some tumors exhibit an increased temperature, compared to surrounding parenchyma [124], and that glucose administration is able to raise their temperature by 7 °C [185], suggesting that the temperature distribution may help to identify tumor location. This body of evidence fortifies the motivation to develop  $B/A$  measurement methods, whether it is for assessment of biological liquids or for nonlinear imaging aimed at tissue diagnosis or temperature monitoring.

It was demonstrated that  $B/A$  is proportional to the change of sound speed accompanied by an adiabatic change in pressure (Eq. (5.4)). This dependency forms the basis of the thermodynamic method for measuring  $B/A$  [24, 119, 242, 340, 434, 441]. In this framework, one records speed of sound changes in the substance when it is subjected to different static pressures. This method is considered to be accurate [119, 166, 434]; however, it is also the

most cumbersome, requiring a temperature controlled environment and a special cell, where the pressure can be varied. This technique can only yield a single, averaged  $B/A$  value for the whole bulk of the studied medium.

The method for aqueous solutions observes the subtle  $B/A$  changes for varying solute concentration of biological compounds [56, 329]. Modifying the setup for the thermodynamic method, the inventors of the aqueous solution method enabled accurate velocity measurement for a small sample volume of 1 mL, and derived an equation with differential parameters between the solution and the solvent, rather than absolute values. Keeping the main disadvantages of the thermodynamic method, this technique is the most accurate of all  $B/A$  measurement methods.

The finite amplitude method exploits the dependency of the speed of sound on  $B/A$  and the excess medium density (or particle velocity, or excess pressure). Due to this dependency (Eq. (5.5)), the peaks of the sinusoidal US wave travel faster than the valleys. This leads to nonlinear distortion of the wave, equivalent to the generation of higher harmonics in the frequency spectrum. Consequently, nonlinear attenuation of the wave increases due to energy transfer from the fundamental component to the higher harmonics, which experience stronger attenuation than the fundamental. This way, the energy of a nonlinear wave is attenuated to a higher extent than that of a small-signal linear wave. Finite amplitude methods (FAMs) exploit all these alterations, quantifying distortion through direct observation of the wave profile [177, 256, 368], through harmonic content [1, 24, 141, 152, 230, 235, 349, 394, 400, 428, 433] or by observing nonlinearly induced attenuation [46, 169, 195, 277]. This family of methods counts the largest number of publications of all. Even though FAMs are less accurate than the thermodynamic method, they require a much simpler measurement setup and have high potential for a clinical application, enabling  $B/A$  tomography for in-transmit measurements and a few echo-mode imaging strategies.

The parametric array method requires transmission of two, typically collinear, beams that generate secondary waves at the sum and difference frequencies. The amplitude of these waves is proportional to the medium  $B/A$  [16, 21, 268, 431]. The secondary beams are narrow, less prone to diffraction than those observed with FAM, and do not have side lobes. Parametric array tomography allows for higher resolution, compared to finite amplitude amplitude tomography [153, 401]. No echo-mode imaging has been performed with this method.

The pump wave method registers the speed of sound change of a low-amplitude high-frequency wave, when another high-amplitude low-frequency wave modulates the pressure in the medium [179, 197, 331]. Uniquely, this method allows for a reconstruction of the  $B/A$  profile along the path of the low-amplitude high-frequency wave from a through-transmission measurement. A particular case of this method, the second order ultrasound field technique (SURF), has been utilized to acquire echo-mode images representing the  $B/A$  distribution [143, 225].

The method of phase conjugated beams [213, 308] utilizes a wave phase conjugator to reverse the beam insonating it and reradiate its amplified version back to the source. The amplitude of the harmonics of the reradiated beam reflects the  $B/A$  of the propagation medium. Phase conjugation provides the unique capability to compensate for phase distortion of the wave and achieves high-quality retrofocusing. Only C-scan images of isoechogetic phantoms have been acquired with this method. The possibility of echo-mode imaging is excluded.

The vast body of literature devoted to nonlinear ultrasound has already provided material for several review papers. [25, 107, 166, 265] discuss the origins of nonlinearity and the way it manifests itself with further consequences in practical applications. Some of these [25, 166] introduce separate equations for different states of matter: gas, liquid and solids. Hamilton and

Blackstock [166], Naugolnykh [271] wrote historical reviews on the evolution of nonlinearity in ultrasound. Zheng et al. [440] wrote a review on material characterization with the help of nonlinear acoustics, devoting a significant portion of it to solids. [27, 28, 29, 166, 429] are review papers that summarize the progress in  $B/A$  measurement methods either over a short time span, or devote their attention mainly to a specific measurement strategy, or provide a brief general overview of the main concepts of the existing methods. A concise review of most techniques for  $B/A$  measurement has been given by Sato and Yamakoshi more than 30 years ago [330]. Varray et al. [393] has presented a review of finite amplitude methods that have the potential to be extended to echo-mode, regarding the parametric array and pump wave method as one of the above.

This review aims at presenting an extensive and comprehensive up to date overview of  $B/A$  measurement and  $B/A$  imaging methods of liquids and liquid-like media (*e.g.*, tissue). Importantly, it gives more focus to methods that are relevant for a medical application and discusses the most common pitfalls in this context. By identifying blind spots and limitations we aim at suggesting directions of research that may bring  $B/A$  to the clinic. This review paper is further separated into the following sections:

- 5.2 Theoretical background
- 5.3 Thermodynamic method
- 5.4 Method for aqueous solutions
- 5.5 Finite amplitude method
- 5.6 Parametric array
- 5.7 Pumping waves
- 5.8 Phase conjugate beam
- 5.9 Conclusion.

Section 5.2 explains the origin of  $B/A$ , presents the most utilized wave equations of nonlinear acoustics and gives an short overview about the main  $B/A$  measurement groups of methods. The sections devoted to various methods (Sec. 5.3-5.8) start with a short introduction of the governing equations and the first published works, followed by the resulting developments, subdivided depending on the adopted measurement strategies. In cases where this has been accomplished, the sections are concluded with studies that presented  $B/A$  images. Since the review introduces the basic theory required to understand the physics behind the presented measurement strategies, it is also suited for a reader, who is new to nonlinear ultrasound.

## 5.2 Theoretical background

### 5.2.1 $B/A$ origin

An ultrasound wave consists of a series of compressions and rarefactions. Linear acoustics views density as linearly dependent on pressure. However, this is an approximation, and ultrasound propagation in general is a nonlinear process. The adiabatic equation of state expresses the pressure-density relation with the Taylor expansion series [24, 74, 166]:

$$P = P_0 + \rho_0 \left( \frac{\partial P}{\partial \rho} \right)_{0,s} \frac{\rho - \rho_0}{\rho_0} + \frac{\rho_0^2}{2} \left( \frac{\partial^2 P}{\partial \rho^2} \right)_{0,s} \left( \frac{\rho - \rho_0}{\rho_0} \right)^2 + \dots \quad (5.1)$$

Here  $P$  and  $P_0$  are instantaneous and hydrostatic pressures,  $\rho$  and  $\rho_0$  are instantaneous and equilibrium densities of the medium under investigation, and the partial derivatives are taken



about the equilibrium state (indicated by the subscript 0) and constant entropy (indicated by subscript s). One can define:

$$A = \rho_0 \left( \frac{\partial P}{\partial \rho} \right)_{0,s} = \rho_0 c_0^2, \tag{5.2}$$

where  $c_0$  is the small-signal speed of sound, and

$$B = \rho_0^2 \left( \frac{\partial^2 P}{\partial \rho^2} \right)_{0,s}, \tag{5.3}$$

making

$$\frac{B}{A} = \frac{\rho_0}{c_0^2} \left( \frac{\partial^2 P}{\partial \rho^2} \right)_{0,s} = \frac{\rho_0}{c_0} \left( \frac{\partial c}{\partial \rho} \right)_{0,s} = 2\rho_0 c_0 \left( \frac{\partial c}{\partial P} \right)_{0,s}. \tag{5.4}$$

The relative importance of second-order nonlinear effects to linear effects can be expressed with the nonlinear parameter  $B/A$  or the alternative nonlinear coefficient [393], expressed as  $\beta = 1 + \frac{B}{2A}$  for liquid and liquid-like media (*e.g.*, tissue).

As stated in [25, 166], one may differentiate Eq. (5.1) by  $\rho$  and by substituting the speed of sound  $c^2 = \left( \frac{\partial P}{\partial \rho} \right)_s$  obtain

$$\frac{c}{c_0} = 1 + \frac{B}{2A} \left( \frac{\rho - \rho_0}{\rho_0} \right) = 1 + \frac{B}{2A} \frac{u}{c_0} \tag{5.5}$$

for a plane progressive wave, illustrating that the local speed of sound  $c$  is dependent on  $B/A$  and  $u$ , the particle velocity. The former is an oscillating disturbance, induced by ultrasound propagation. This explains the origin of accumulating wave distortion, leading to saw-tooth waves: the compressional part of the wave (the high density region, with positive particle velocity and positive excess pressure) travels faster than the rarefractional part, contributing to wave distortion proportionally to  $B/A$ .

Tables 5.1 and 5.2 summarize the measured  $B/A$  values for liquids and animal tissues. As one can see, at atmospheric pressure and room temperature  $B/A$  is in the range of 5-11 for most liquids and liquid-like media.

Table 5.1: *Liquids.*

Medium	$B/A$	Studies
water	5.1	[24, 83, 441]
1-3 methanol	9.7	[242]
ethylene glycol	9.9	[434]
ethanol	10.4	[242]
carbon tetrachloride	8.3	[83, 441]
glycerol	10.1	[167, 199, 426]
methanol	9.6	[74, 242, 294]
glycerine	9.4	[257]
corn oil	11.4	[167, 220]
linseed oil	9	[220]
silicone oil	11	[368]
olive oil	10.7	[324]
hyper-branched silicone oil	8.5	[439]

Table 5.1: *Liquids.*

Medium	$B/A$	Studies
linear silicone oil	9.7	[439]
1-propanol	9.5	[14]
1-butanol	9.7	[14, 324, 325]
benzyl alcohol	10.4	[3, 321, 325]
1-pentanol	10.0	[14]
1-hexanol	10.2	[14]
1-heptanol	10.6	[14]
1-octanol	10.7	[14]
1-nonanol	10.8	[14]
1-decanol	10.7	[14]
n-butanol	11.2	[242, 294, 349]
1-propanol	10.3	[143]
n-propanol	10.7	[74, 242]
1,2-propanediol	11.5	[442]
acetone	9.2	[74]

This table presents  $B/A$  values of some pure liquids at atmospheric pressure and in a temperature range of 20-30 °C. When several studies are stated, all of them were included in the column “*Studies*” and only one value was chosen to be stated in the column “ $B/A$ ”.

Table 5.2: *Animal tissues and fluids.*

Medium	$B/A$	Studies
bovine liver	7.8	[109, 227, 228]
	6.2-8	[230]
	8.1	[321]
homogenized bovine liver	6.8	[109, 227, 228]
	7.2	[184]
beef brain	7.6	[230]
beef heart	6.7-7.4	[230]
homogenized porcine liver	6.5	[220]
	6.6	[152]
porcine liver	7	[321]
	7.6	[66]
	6.9	[154]
	7.1, 6.9	[152]
	7.2	[235, 241]
	6.5	[153]
	6.8	[428]
porcine liver	6.3	[430]
	6.5	[401]
	7.3	[432]
pathologic porcine liver	7.4-10.3	[153, 154, 401, 428, 430, 432]
porcine whole blood	6.3	[109, 227, 228]
	6.3	[152]
	6	[220]
porcine fat	10.9-11.3	[230]
	9.6	[321]



Table 5.2: Animal tissues and fluids.

Medium	$B/A$	Studies
porcine fat	10.8, 10.9	[152]
	9.7	[235]
	10.7	[432]
	11	[153]
	9.1	[430]
	11	[401]
porcine muscle	7.5-8.1	[230]
porcine muscle	5.8	[241]
porcine heart	7.1, 6.8	[152]
porcine kidney	6.9, 6.3	[152]
porcine kidney	7.1	[428]
pathologic porcine kidney	7.1-8.1	[428]
porcine spleen	6.9, 6.3	[152]
	6.9	[428]
porcine tongue	6.5, 6.8	[152]
<i>in vivo</i> cat liver	6.5-7.0	[433]
cat liver	6.4-6.9	[433]
human liver	6.5	[340]
human breast fat	9.2	[340]
human multiple myeloma	5.6	[340]
fresh human blood	6.0	[152]
different kinds of body fats	9.6-10.8	[116]
human liver	6.3	[341]
pathologic human liver	5.7-8.7	[341]
human whole blood	6.3	[415]
bovine serum albumin solutions (various concentrations)	5.2-7.4	[109, 227, 228, 230, 441]
hemoglobin solutions (various concentrations)	5.2-7.7	[109, 227, 228]
milk	5.1, 5.9	[152]
egg yolk	8.9	[430]
	8.3	[432]
	9.1	[116]
	9.5	[321]
egg white	5.8	[321]
	6.4	[430]
	6.3	[432]
	5.2	[116]

$B/A$  values of animal tissues and liquids at atmospheric pressure in a range of temperatures 20-30 °C. All studies performed *ex vivo*  $B/A$  measurements, unless otherwise mentioned. All tissues were studied in their regular form, unless specified that they were *homogenized*. When several studies were identified, measuring  $B/A$  of the same substance, all of them were included in the table. In some cases, the  $B/A$  value was taken from a graph, allowing for some error.

## 5.2.2 Main wave equations

To obtain the equations governing the propagation of ultrasound waves in fluid homogeneous media one may refer to the equation of motion, the continuity equation, the heat transfer equation and the equation of state (Eq. (5.1)) [272]. For an ultrasound wave, together these equations describe the relationship between the spacially varying quantities of pressure, particle velocity and density; as well as heat transfer, related to loss. When these equations model ideal fluid (lossless fluid) and only linear terms are kept, one may derive the well-known wave equation [80]:

$$\frac{\partial^2 P(z, t)}{\partial z^2} - \frac{1}{c_0^2} \frac{\partial^2 P(z, t)}{\partial t^2} = 0 \quad (5.6)$$

in 1D space, where we chose to describe the pressure variation  $P$ , dependant on the coordinate  $z$  and time  $t$ . When second order nonlinear effects are considered (*e.g.*, equation of state given in the form of Eq. (6.3)) and propagation in 3D space is addressed, one can obtain the Westervelt equation [406]:

$$\nabla^2 P - \frac{1}{c_0^2} \frac{\partial^2 P}{\partial t^2} = -\frac{\beta}{\rho_0 c_0^4} \frac{\partial^2 P^2}{\partial t^2}, \quad (5.7)$$

where  $\nabla^2 = \frac{\partial^2}{\partial x^2} + \frac{\partial^2}{\partial y^2} + \frac{\partial^2}{\partial z^2}$  is the Laplacian. The term on the right-hand of Eq. (5.7) models cumulative nonlinear effects, while local nonlinear effects are neglected here [166, 189], implying that the Westervelt equation is valid at propagation distances further than a few wavelengths from the source. Eq. (5.7) models sound propagation of plane waves or quasi-plane waves, like directional beams [93, 166] in homogeneous lossless media. It was further expanded to include loss in a weakly thermoviscous fluid [166, 272, 326, 366, 375]:

$$\nabla^2 P - \frac{1}{c_0^2} \frac{\partial^2 P}{\partial t^2} = -\frac{\delta}{c_0^4} \frac{\partial^3 P}{\partial t^3} - \frac{\beta}{\rho_0 c_0^4} \frac{\partial^2 P^2}{\partial t^2}, \quad (5.8)$$

where  $\delta = \frac{2c_0^3 \alpha}{\omega^2}$  is sound diffusivity, proportional to  $\alpha$ , the attenuation coefficient. Importantly, loss in a weakly thermoviscous fluid assumes attenuation to be proportional to the squared frequency of the wave  $f^2$  [166, 272, 366, 375]. This is valid for some liquids (*e.g.*, water, certain oils [59, 60, 272, 367]), however, most biological media exhibit a nearly linear attenuation-frequency dependence [47, 106, 282, 310]. Alternative time-domain equations exist, incorporating arbitrary attenuation [47, 366], more appropriate for *e.g.*, tissues. No exact analytical solution to the Westervelt equation exists. However, expressions in the form of integrals have been obtained in [189] for the case of weak nonlinearity with the help of the Green's function and when approximating the source pressure as a sum of Gaussian beams [405].

A somewhat simpler description of nonlinearity and attenuation was provided by Khokhlov, Zabolotskaya [422] and Kuznetsov [223]. Derived from the same original equations as the Westervelt equation, the Khokhlov-Zabolotskaya-Kuznetsov (KZK) equation (Eq. (5.9)) makes the additional assumption of the parabolic approximation that holds for “acoustic sources which are many wavelengths across and for field points that are not too close to the source or too far off axis” [189]:

$$\frac{\partial^2 P}{\partial \tau \partial z} = \frac{\delta}{2c_0^3} \frac{\partial^3 P}{\partial \tau^3} + \frac{\beta}{2\rho_0 c_0^3} \frac{\partial^2 P^2}{\partial \tau^2} + \frac{c_0}{2} \nabla_{\text{tr}}^2 P. \quad (5.9)$$

Here  $\nabla_{\text{tr}}^2 = \frac{\partial^2}{\partial x^2} + \frac{\partial^2}{\partial y^2}$  is the transverse Laplacian and  $\tau$  is the retarded time  $\tau = t - \frac{z}{c_0}$ . The terms on the right side of the equation from left to right represent wave attenuation,

nonlinearity and diffraction effects [438]. The diffraction effect describes the deviation of the field from a plane wave, due to finite source geometry and is somewhat elaborated on in Sec. 5.5.2.1. An explicit solution to the KZK equation for the case of weak nonlinearity has been derived in [139, 188, 191].

The simplest equation, describing combined effects of nonlinearity and thermoviscous loss is the Burgers equation [41]:

$$\frac{\partial P}{\partial z} - \frac{\beta}{\rho_0 c_0^3} P \frac{\partial P}{\partial \tau} = \frac{\delta}{2c_0^3} \frac{\partial^2 P}{\partial \tau^2}. \quad (5.10)$$

It considers only plane progressive waves, and therefore, doesn't account for the diffraction effects. Just as for the Westervelt equation, another form of Eq. (5.10) can be adopted for biological tissues and liquids, accounting for an arbitrary frequency dependence of attenuation [30, 60, 63]. The lossless Burgers equation is derived by setting the attenuation coefficient  $\alpha = 0$  (and therefore  $\delta = 0$ ) to zero:

$$\frac{\partial P}{\partial x} - \frac{\beta}{\rho_0 c_0^3} P \frac{\partial P}{\partial \tau} = 0. \quad (5.11)$$

The exact solutions to the lossy and lossless Burger's equations are known, derived by Fubini-Ghiron [140] and [198], respectively. These solutions are presented further in this review (Sec. 5.5.2). Unlike the Burger's equation, the Westervelt and KZK equations are mainly solved numerically, providing much more accurate predictions of the pressure field [91, 101, 310, 437]. At the same time, solutions of the Burger's equation provide simple formulas for the fundamental and higher harmonic pressures. Diffraction affects can be accounted for in the solutions in a *post hoc* manner.

### 5.3 Thermodynamic method

It has been shown in Eq. (5.4) that  $B/A$  is proportional to the change in sound velocity occurring with an isentropic (adiabatic) change of hydrostatic pressure. The term isentropic refers here to a process where no heat or matter is abstracted or conveyed to the system from outside. Once the derivative in Eq. (5.4) is expanded, as demonstrated in [24, 166, 317]

$$\frac{B}{A} = 2\rho_0 c_0 \left( \frac{\partial c}{\partial P} \right)_{0,T} + \frac{2c_0 T q}{\rho_0 C_P} \left( \frac{\partial c}{\partial T} \right)_{0,P} \quad (5.12)$$

$B/A$  can be expressed through the change in sound velocity caused by isothermal pressure and isobaric temperature ( $T$ ) changes. The parameter  $q = (1/V)(\partial V/\partial T)_P$  is the isobaric volume coefficient of thermal expansion and  $C_P$  is the specific heat at constant pressure.  $B/A$  is sometimes referred to in the literature as the adiabatic nonlinear parameter, while the first term on the right-hand side of Eq. (5.12) is referred to as the isothermal nonlinear parameter [117, 392]  $\left( \frac{B}{A} \right)'$ :

$$\left( \frac{B}{A} \right)' = 2\rho_0 c_0 \left( \frac{\partial c}{\partial P} \right)_{0,T}. \quad (5.13)$$

The remaining term in Eq. (5.12) is referred to as the isobaric nonlinear parameter:

$$\left( \frac{B}{A} \right)'' = \frac{2c_0 T q}{\rho_0 C_P} \left( \frac{\partial c}{\partial T} \right)_{0,P}. \quad (5.14)$$

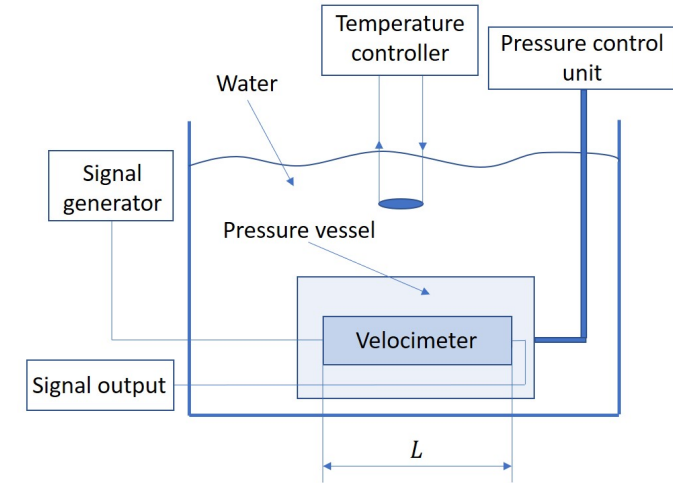


Figure 5.1: Schematic simplified diagram of the typical setup used for a thermodynamic  $B/A$  measurement. More detailed representations can be found in [174, 230].

In general, the thermodynamic methods can be classified in two groups, where  $B/A$  is determined either from Eq. (5.12), as it was initially done, or from Eq. (5.4). Within these groups, the strategies to measure the speed of sound  $c$  differ. All studies carried out with the thermodynamic method require a velocimeter: a vessel of known length  $L$ , comprising the test liquid and the transmitter - receiver equipment, inserted in a liquid-filled pressure vessel (e.g., water [229, 230], oil [159, 160, 411]) that is in turn submerged in a bath with controlled temperature (Fig. 5.1).

#### 5.3.1 Traditional thermodynamic technique

The traditional thermodynamic technique determines  $B/A$  via Eq. (5.14). The required speed of sound measurement can be performed with different techniques, allowing to infer the travel time (time of flight)  $t_{tr}$  of the wave through the velocimeter of known length  $L$  (Fig. 5.1). All the identified works utilizing the traditional thermodynamic technique are summarized in Table 5.3, stating the utilized technique and the parameter directly measured, as well as the specified measurement uncertainty and the investigated media.

The first paper reporting the determination of  $B/A$  by the thermodynamic method [24] used thermodynamic data previously acquired by other scientists [159, 160, 411] for several liquids. In [159, 160, 411]  $t_{tr}$  was inferred with the help of a sing-around circuit [144, 443]. This circuit allows to trigger the generator to send a pulse once the preceding pulse is received and, therefore, to infer  $t_{tr}$  through the pulse repetition frequency (PRF). In this work, to improve the accuracy of the measurement Greenspan and Tschiegg [159, 160], Wilson [411] adjusted the PRF of the generator so that a new pulse was transmitted when the echoes of the previously transmitted pulse were superimposed on the receiver. This way, the device allowed determining the speed of sound from the pulse transit time  $t_{tr}$ , inferred from the PRF and the distance travelled by the pulse ( $L$ ) equal to twice the length of the vessel:

$$c = 2L/t_{tr}. \quad (5.15)$$

Table 5.3: Summary of works that measured  $B/A$  with the traditional thermodynamic technique.

Study	Measured parameter	Uncert., %	Investigated media
[24, 159, 160, 411]	PRF, sing-around circuit	-	water, ethyl alcohol
[74]	PRF, sing-around circuit	<3 (liquid)	organic liquids, water-alcohol mixtures
[163, 174]	$t_{tr}$ , pulse-echo m.	-	water
[245]	PRF, sing-around circuit	-	fluorocarbon fluids
[229]	$t_{tr}$	3 (liquid), 5 (tissue)	biological solutions, soft tissues
[230]	$t_{tr}$	3 (liquid), 5 (tissue)	biological solutions, soft tissues
[442]	$t_{tr}$ , pulse echo-overlap m.	3 (liquid)	lower alkanediols
[444]	PRF, sing-around circuit, pulse-echo-overlap m.	3 (liquid)	ionic liquid

The indicators *liquid* and *tissue* refer to measurement uncertainties for liquids and tissues, respectively. Uncertainty (Uncert.,%) is stated in percent of the measured values.

Hagelberg et al. [163], Holton et al. [174] performed the speed of sound  $c$  measurement in water with the pulse-echo method: using one transducer as the source and receiver, where  $t_{tr}$  was inferred from the interval between echoes reflected from an acoustic mirror positioned at the other end of the vessel. Law et al. [229] measured the coefficient of nonlinearity of biological solutions and soft tissues. To this end, the original apparatus in Coppens et al. [74], including the velocimeter and electronics, was adjusted for measurements with biological specimens. Since for the studied substances, values of  $q$  and  $C_p$  in Eq. (5.12) were not known, the authors used the well-known values for water: the values for tissues measured in former studies showed a difference with water up to 30 %, and as previously discovered, the term  $\left(\frac{B}{A}\right)''$  contributed only 3 % to the  $B/A$  value. The speed of sound was inferred from a direct measurement of the time of flight based on the display of the oscilloscope, showing the driving and received signals. Law et al. [230] observed no dependence of  $B/A$  on solute molecular weight in dextran solutions and a linear dependency on solute concentration. The authors postulated that nonlinearity is a result of solute-solvent interactions. The authors also identified that homogenization of tissue reduced  $B/A$  and, in general,  $B/A$  showed an increasing trend with the specimen's structural hierarchy. It is worth mentioning that this paper presents a comprehensible diagram and description of the apparatus used.

Zorebski and Zorebski [442] utilized the pulse-echo-overlap method [159, 443] to determine the speed of sound in lower alkanediols by extracting the PRF at conditions of overlapping echoes coming back from a reflector. The authors acquired  $B/A$  at pressures up to 100 MPa and temperatures from 21 to 46 °C. Zorebski et al. [444] extended the range of studied temperatures, measuring  $B/A$  from 16 to 46 °C.

The accuracy of the traditional thermodynamic techniques, taking into account further measurement uncertainties (e.g., temperature and pressure), resulted in a global uncertainty of the  $B/A$  estimation within 3% for liquid, and 5% for tissue (Table 5.3). The higher uncertainty for tissue samples accounts for inhomogeneous speed of sound [230]. The studies conducted with the traditional thermodynamic method revealed that  $B/A''$  is much smaller compared to  $B/A'$  (constituting less than 5 % for fluorocarbon fluids [245], 9 % of  $B/A$  for the liquids studied in [442] and 12 % of the pressure-dependent term for methanol-water mixtures [74]). Besides this,  $B/A'$  has shown to be always positive, while  $B/A''$  can exhibit positive and negative values depending on the studied material. Hagelberg et al. [163], Holton et al. [174] illustrated that for a range of temperatures up to 80 °C and a very wide range of pressures  $B/A$  of water has small variability (from 4.1 to 6.8), and increases monotonically with temperature

for a pressure value of 1 atm. Coppens et al. [74] demonstrated that  $B/A$  of alcohol mixtures show low variability with temperature. Madigosky et al. [245] reported fluorocarbon fluids to have the highest nonlinearity reported so far ( $B/A=13$ ). Law et al. [229, 230] demonstrated the dependence of  $B/A$  on chemical composition of biological solutions as well as structural hierarchy of biological material.

### 5.3.2 Isentropic thermodynamic technique

The isentropic thermodynamic technique, also referred to as the improved thermodynamic method [152, 242, 295], makes use of Eq. (5.4) rather than Eq. (5.12). It requires a rapid (1-3 s) change of pressure to eliminate significant heat transfer with the test vessel. This way, the pressure change can be regarded as an isentropic process. As noted by Zhu et al. [441], this technique is simpler than its predecessor, since it eliminates the need for measurements at different temperature points. Moreover, as Sehgal et al. [340] indicated, the traditional thermodynamic method requires knowledge of  $q$  and  $C_p$ , which are “not known with great precision for most soft tissues”. The uncertainty of the early isentropic phase method is estimated to be 4 % [119]. However, the development of this method is connected to the improvement in the techniques measuring the speed of sound, permitting to reduce the uncertainty to < 1 % (Table 5.4, below). It is velocity measurement techniques that account for the variability of the isentropic phase methods. Therefore, the following section is divided into subsections according to the measured parameter through which the speed of sound is inferred, that being phase  $\phi$ , voltage  $U_p$ , frequency  $f$ , or the time of flight  $t_{tr}$  of a pulse. A summary of the identified works, utilizing the isentropic thermodynamic technique, is presented in Table 5.4. This table the measured parameter, the indicated measurement uncertainty and the studied media.

The most frequently used are phase measurement techniques, providing more accurate speed of sound estimations compared to earlier methods used in the framework of the traditional thermodynamic technique (Table 5.3). A few others, deriving speed of sound from frequency information, or estimating the time of flight of a pulse, are also used. A detailed explanation follows below.

#### 5.3.2.1 Phase measurements

Among the first publications using the isentropic thermodynamic technique are [114, 441], measuring  $B/A$  of liquids. The authors considered the measurement isentropic, as the applied pressure changes were small (varying from 1 to 2 atm) and too fast ( $\approx 2.0$  s) for a significant heat exchange. The speed of sound change is connected to the wave's transit time  $t_{tr}$  and the distance between transducers  $L$  via Eq. (5.16) [441]:

$$\left(\frac{\partial c}{\partial P}\right) = -\frac{L}{t_{tr}^2} \left(\frac{\partial t_{tr}}{\partial P}\right). \quad (5.16)$$

Eq. (5.16) allows us to determine  $B/A$  based on Eq. (5.4) as:

$$\frac{B}{A} = -\frac{2\rho_0 c_0^2}{t_{tr}} \left(\frac{\Delta t_{tr}}{\Delta P}\right)_s. \quad (5.17)$$

To detect the change in transit time  $t_{tr}$ , Zhu et al. [441] chose to conduct phase measurements: they compared the phase of the received tone burst to that of a reference signal with a phase



Table 5.4: Summary of strategies to measure  $B/A$  with the isentropic thermodynamic technique.

Measured parameter	Studies	Uncert., %	Investigated media
Phase $\phi$	[441]	2.5 (liquid)	liquids, <i>e.g.</i> , water, bovine serum albumin solution
	[152]	4 (liquid), 7 (tissue)	biological solutions and soft tissues
	[340, 341]	3 (tissue)	normal and malignant human tissues
	[342]	1 (liquid)	monohydric alcohol-water solutions
	[116]	-	livers, fat, egg, oils
	[117]	3	human and animal fats, simple mixtures ( <i>e.g.</i> , skim milk)
Voltage $\Delta U_p$	[242]	2.2 (liquid)	water, organic liquids
	[295]	2 (liquid)	water
	[294]	2 (liquid)	primary alcohols
	[296]	<2.2 (liquid)	alkanes
	[199]	2 (liquid)	glycerol
	[439]	<2 (liquid)	silicone oils
Transmit time $\Delta t_{tr}$	[434]	0.7 (liquid)	water, dextrose, ethylene glycol
	[435]	tissues not assessed separately	cat and rat livers, liver suspensions
Frequency $f$	[119]	0.85 (liquid)	aqueous buffers, protein solutions, lipid oils, emulsions
	[83]	1 (liquid)	liquids

The uncertainty (*Uncert.*, %) of the  $B/A$  measurement is stated in percent of the measured value for tissues and liquids.

mixer, and acquired  $\Delta t_{tr}$  with the help of a delay line. Since  $\Delta\varphi = \omega\Delta t_{tr}$  and  $t_{tr} = \frac{L}{c_0}$ ,  $B/A$  was determined according to

$$\frac{B}{A} = -\frac{2\rho_0 c_0^3}{\omega L} \left( \frac{\Delta\varphi}{\Delta P} \right)_s, \quad (5.18)$$

where  $L$  is the length of the ultrasound path through the liquid. Eq. (5.16) forms the basis of all phase measurement techniques, which in general produced more accurate results compared to earlier strategies. A follow-up paper [152] of one of the authors of [441] used the same version of the method to measure  $B/A$  of biological solutions and soft tissues. Gong et al. [152] confirmed the results obtained by Law et al. [230] for homogenized liver versus whole liver, as well as biological solutions, observing that  $B/A$  increases with structural hierarchy of the specimen.

**Pressure-jump method** Sehgal et al. [340] presented the pressure jump method. During the pressure increase, the phase of the received signal was monitored. The speed of sound was inferred from Eq. (5.18). After the pressure change, the system was allowed to equilibrate to the ambient temperature and the authors could also measure the isothermal nonlinear parameter  $\left(\frac{B}{A}\right)'$ . Sehgal et al. [340, 341] used the method described above, transmitting ultrasound in continuous-wave mode. This configuration was “most suitable for attenuating media” [340] as tissue, since high attenuation avoided the formation of standing waves. Sehgal et al. [340] measured  $B/A$  of several human tissues. They demonstrated that fatty breast tissue had a substantially higher value than parenchymal liver tissue, and that multiple myeloma had a

substantially lower  $B/A$  compared to normal parenchymal liver tissue. Sehgal et al. [341] showed that  $B/A$  of fatty liver is higher compared to normal, while cirrotic and tumorous  $B/A$  is lower than for normal liver. [340, 341] are the only papers, to the best of our knowledge, reporting  $B/A$  for malignant tissues.

In [116, 117, 342], the adiabatic nonlinear parameter and the isothermal nonlinear parameter were measured with the pressure-jump method, detecting the phase change (Eq. (5.18)) of a shock-excited pulse. Sehgal et al. [342] reported  $B/A$  of alcohol-water mixtures. Since alcohols have smaller speed of sound and larger  $B/A$ , their addition to water was expected to increase  $B/A$ . This was not the case for low concentrations of alcohol. Such an effect on  $B/A$  was attributed to the effects of solvent-solute interactions, and alteration in the water-molecule structure due to addition of alcohol. The authors speculated that since tissue is composed of 60-80 % of water, changes in the state of tissue due to the change in unbound-bound water ratio must have been reflected in its  $B/A$ , creating another opportunity for determining tissue properties based on  $B/A$ . Errabolu et al. [117] demonstrated that human and animal fat tissues are highly nonlinear, with  $B/A$  values ranging between 10 and 12. Moreover, in the range of temperatures from 20 to 37 °C,  $B/A$  vs. temperature exhibits a positive or flat trend. Errabolu et al. [116] proposed a two-component model (fat and nonfat), able to predict the fat percentage based on the measured  $B/A$  and speed of sound. The model was tested for livers, fats, oil and egg mixtures.

**Phase derivation from output voltage** Lu et al. [242] utilized a highly sensitive phase comparison technique by transmitting a tone-burst signal and producing small pressure changes below 2 atm to liquids. This technique, like [441] also utilizes a phase mixer. However, different from other methods, the phase change is inferred from the amplitude of the phase detector rather than with a delay line. The measurements are done for small phase changes (below  $\pi/20$ ), where the output voltage of the phase detector (mixer)  $U$  is linearly dependent on signal phase  $\phi$ . Therefore, the phase change of the detector signal,  $\Delta U$ , can be described through the phase change  $\Delta\phi$  as

$$\Delta U = k A_1 A_2 \Delta\phi, \quad (5.19)$$

where  $A_1$  and  $A_2$  are the amplitudes of the received and the reference signal that are mixed in the phase detector, and  $k$  is a constant characterizing the phase detector. This way,  $\Delta U$  can be utilized to estimate  $B/A$  as

$$\frac{B}{A} = -\frac{2\rho c^3}{\omega L} \frac{1}{k A_1 A_2} \left( \frac{\Delta U}{\Delta P} \right)_s. \quad (5.20)$$

The maximum pressure change was adjusted to maintain a linear relation between voltage and phase. Lu et al. [242] report the technique to have an uncertainty of 2.2 %.

This strategy was used to measure  $B/A$  of several liquids [199, 242, 294, 295, 296, 439]. A few of these studies [199, 294, 295, 296] enabled  $B/A$  measurement at pressures up to 100 MPa and temperatures up to 100 °C.

### 5.3.2.2 Transmit time

[434] developed an isentropic thermodynamic method capable of measuring  $B/A$  of 4-mL sample volumes. This system is important for situations when samples are products of biochemical reactions with small yields or pathological tissue areas which may be of limited locus/size. The distance between the source and receiver in the velocimeter was only 1 cm.

The speed of sound was determined with Eq. (5.17) by calculating the time delay from cross-correlation of the transmitted and received pulses. Since the receiver was in the near field, an error was introduced in the velocity measurements; however, the authors stated that their system was nevertheless able to measure within an error of 0.7 %, confirmed by measurement of 3 mixtures.

Zhang et al. [435] used the above described setup [434] to determine the influence of structural parameters on  $B/A$ . Performing measurements of cat and rat liver tissue as well as suspensions acquired from these livers, the authors altered their structure physically and biochemically, and reached the conclusion that structural dependence of  $B/A$  “exists at all three levels of biological structure, viz., the tissue level, the cellular level and the molecular level. The relative contributions due to structural features is 26 % at the tissue level, 20 % at the cellular level, and 15 % at the macromolecular level.”

### 5.3.2.3 Frequency measurement

Everbach and Apfel [119] automated the measurement of speed of sound, allowing to perform thousands of acquisitions on a sample in a reasonable time. The utilized interferometer consisted of a receiving and source transducer. A phase-locked loop circuit was used to correct for the frequency of the transmitted pulse by  $\Delta f$  so that a constant phase relationship was kept at the receiver transducer as the speed of sound changed in the medium. Since,  $\Delta f$  required to keep the phase constant can be defined by

$$\Delta f / f_0 = \Delta c / c_0, \quad (5.21)$$

$\frac{B}{A}$  can be expressed as

$$\frac{B}{A} = 2\rho_0 c_0^2 \left( \frac{\Delta f}{f_0 \Delta P} \right)_s, \quad (5.22)$$

where  $f_0$  and  $\rho_0$  are the initial frequency and density. A pressure of 180 kPa (1.85 atm) was generated in the measurement cell and then released. During this release (3 s) the source transducer transmitted 20-cycle tone bursts at 11 frequencies. Contrary to [340, 341], attenuation was an undesired effect for an interferometer, as the measurements were performed for a range of organic and aqueous solutions. The presented method is reported to have an accuracy of about 1 %.

Davies et al. [83] also measured the change in frequency associated with the pressure change (Eq. (5.22)). Contrary to [119], they performed continuous wave phase locking since the continuous wave approach avoids the uncertainty of pulse onset identification. As the system was developed for small-volume samples, the authors encountered near-field problems [434] in an early setup when using phase locking in double-disk interferometers. To overcome this problem, they utilized a cylindrical piezoelectric cavity resonator which, coupled with the developed electronic system, “provided a real-time measurement of the change in speed of sound as function of frequency”. The authors applied a 2-s pressure sweep from 0 to 200 kPa during which 100 data frequencies  $f = f_0 + \Delta f$  were acquired. This system was reported to produce uncertainty of less than 1 % for  $B/A$ .

## 5.4 Method for aqueous solutions

Sarvazyan et al. [329] noted that the  $B/A$  errors were too large to study solute-solvent mixtures with a small amount of solvent. Most biological compounds cannot be diluted

in high concentrations in aqueous solutions due to the low solubility. The  $B/A$  change in the possible range of concentration is estimated to be approximately 1 % [329], within the error span of the most accurate thermodynamic techniques (Tables 5.4, 5.3). For this reason, [329] developed a differential method that rather than measuring absolute values, estimated the differences between the solute and the solution, which is a common approach in chemical relaxation kinetics [111]. The accuracy of the relative measurements of the nonlinearity parameter achieved by this method was 0.3 %.

The theory was derived by differentiating Eq. (5.12) for the traditional thermodynamic method, resulting in the following expression:

$$\frac{\Delta B/A}{C} \frac{1}{2\rho_0 c_0} = \frac{1}{C} \Delta \left( \frac{\partial c}{\partial P} \right)_T + ([c] + [\rho]) \left( \frac{\partial c}{\partial P} \right)_{T_0} + \frac{\gamma_0 T_0}{\rho_0 C_p} \left[ \frac{1}{C} \Delta \left( \frac{\partial c}{\partial T} \right)_{P_0} + ([c] + [\gamma] - [C_p]) \left( \frac{\partial c}{\partial T} \right)_{P_0} \right], \quad (5.23)$$

where capital  $C$  is the solute concentration, values attributed to the solvent are denoted by subscript 0, and  $\Delta$  refers to the difference between the solution and the solvent for the corresponding expressions.  $[c]$ ,  $[\rho]$ ,  $[\gamma]$ ,  $[C_p]$  are relative specific increments of speed of sound, solution density, thermal expansion coefficient, and heat capacity at constant pressure, respectively:

$$[c] = \frac{\Delta c}{c_0 C}, \quad [\rho] = \frac{\Delta \rho}{\rho_0 C}, \quad [\gamma] = \frac{\Delta \gamma}{\gamma_0 C}, \quad [C_p] = \frac{\Delta C_p}{C_{P_0} C} \quad (5.24)$$

Parameters  $[\rho]$ ,  $[\gamma]$ ,  $[C_p]$  are known from literature, leaving  $[c]$ ,  $\Delta \left( \frac{\partial c}{\partial P} \right)_T$ , and  $\Delta \left( \frac{\partial c}{\partial T} \right)_P$  as the values to be measured, given that the solvent parameters with subscript 0 are known.

The setup used in [327] is typical for the thermodynamic method (Sec. 5.3). However, several important modifications were made. The measurement cell was represented by a four-channel resonator cell, each with a volume as small as 0.2 mL, all filled with the test liquids. Simultaneous velocity measurements in these chambers were made by the resonator method with an acoustic interferometer. Standing waves form in the cells at resonance frequencies at which the distance between transducers is equal to a whole number of half-wavelengths. This results in amplitude peaks at these frequencies (amplitude frequency characteristic), as well as a particular phase dependence of the received signal on the frequency (phase-frequency characteristic). The authors inferred  $\Delta c$  from the phase frequency characteristic, identifying the shift in resonance frequency  $\Delta f$  to keep the phase constant, at its inflection point (Eq. (5.21)). The resonator method is the only technique that can be applied for such small-volume samples [328]. Different from previous thermodynamic studies (Sec. 5.3), the authors introduced a reference cell with the solvent, placed in the same thermostated volume as the solution. This lowered the requirement for the temperature stability of the system.

The above work was employed to assess the acoustic properties of solutions of amino acids and proteins, giving insight into the molecular origins of  $B/A$ . For instance, the authors discovered that an increase of the number of charged groups that favor bonds with water molecules augments  $B/A$ , while  $\text{CH}_2$  groups decrease it due to decreased accessibility of water to such molecules. The authors also noted a strong sensitivity of  $B/A$  to a replacement of a single atomic group within a molecule, compared to ultrasound velocity and density. These observations demonstrated that  $B/A$  may be a useful indicator of molecular structure and hydration of biomolecules in solutions. This method enables measurement of the smallest amounts of sample reported and provides the highest measurement accuracy (0.3 %) reported



until now (Sec. 5.9, Table 5.8). A follow-up paper studied temperature dependencies of  $B/A$  of aqueous amino acid solutions [56].

## 5.5 Finite amplitude methods (FAM)

As demonstrated in Sec. 5.2, the speed of an ultrasound wave at a point in space and time is dependent on  $B/A$  (or  $\beta$ ) and the excess density (or particle velocity) at that point and time. Due to this, as the wave propagates it distorts, which was shown to be equivalent to the generation of higher harmonics (integers of the transmitted frequency) in the frequency domain [140, 198, 210]. As higher harmonics grow, the fundamental component is depleted due to the energy transfer from the fundamental harmonic to the higher harmonics.

All FAMs register the wave after a certain propagation distance in a medium (*e.g.*, Fig. 5.2) and derive  $B/A$  from cumulative nonlinear effects observed in the registered signal. The finite amplitude methods can be classified in three main groups: deriving  $B/A$  directly from the wave's shape, from the second harmonic component and from the fundamental component. Detailed description of each family of methods follows below. The theory presented in the introductory sections (Sec. 5.5.3.1, Sec. 5.5.2.1) of the FAM groups concerns only weak nonlinearity (the shock parameter  $\sigma = \frac{2\pi f P_1(0) z \beta}{\rho_0 c^3} \leq 1$ ), since the pressure amplitudes that demonstrate strong nonlinearity are above the safety regulations for assessment of biological media. Table 5.5, presented below, summarized all the identified FAM works and the utilized strategies to measure  $B/A$ .

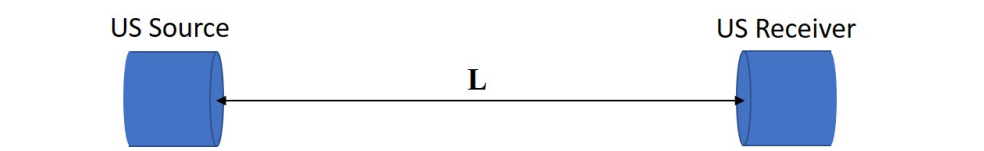


Figure 5.2: Schematic of the most common through-transmission setup used to measure  $B/A$  with many FAMs. Here  $L$  is the path in the studied medium. In reflection-mode imaging, the receiver is substituted by a reflector plate, and the source transducer acts as the receiver.

### 5.5.1 Wave shape.

#### 5.5.1.1 Light diffraction method

The earliest works observing the wave shape to infer  $B/A$  were performed with optical methods (Fig. 5.3). When an optical wave propagates in a direction perpendicular to the ultrasonic beam, the initially flat wave front of the optical wave is modulated in phase according to the velocity profile of the US wave, possibly distorted due to nonlinear propagation.

Table 5.5: Intercomparison of finite amplitude methods.

Main Groups	Subgroup	Main principle	Advantages	Disadvantages	Uncert., %	Images
Wave shape	Light diffraction. Sec. 5.5.1.1	Assessment US wave shape through diffraction of light	<ul style="list-style-type: none"> <li>- accurate,</li> <li>- no <i>per se</i> assumptions about the harmonic content of the signal is needed</li> </ul>	<ul style="list-style-type: none"> <li>- complicated setup that includes a laser and an optical receiving system</li> </ul>	7-8 (liquid) [257] <8 (liquid) [195]	-
	Modelling of the wave profile. Sec.5.5.1.2	Fit pulse waveforms to nonlinear models	<ul style="list-style-type: none"> <li>- no <i>per se</i> assumptions about the harmonic content of the signal is needed</li> </ul>	<ul style="list-style-type: none"> <li>- requires <math>P_1(0)</math> (calibration)</li> <li>- broadband receiver needed</li> </ul>	10 (liquid, tissue) [60, 177, 184], 5 (liquid) [189]	-
2nd harmonic measurement	2nd harmonic maximum. Sec. 5.5.2.2	Experimentally identifying the distance from the source of $P_2$ maximum	<ul style="list-style-type: none"> <li>- no clear advantages identified</li> </ul>	<ul style="list-style-type: none"> <li>- only for viscous liquids</li> <li>- measurements at several distances</li> </ul>	-	-

The table discusses the main principle, advantages and disadvantages, and accuracy of FAM variations in their initial form, developed for  $B/A$  estimation as a global parameter. In the column  $Uncert.$ , %, the measurement error is stated for liquids, tissues, or phantoms (tissue-mimicking or layers of liquid), respectively. The column *Images* states whether or not any experimental works presented  $B/A$  images, therefore, visualizing  $B/A$  distribution rather than a single global  $B/A$  value.  $P_1(0)$  indicates source pressure,  $P_2$  - 2nd harmonic pressure.

Main Groups	Subgroup	Main principle	Advantages	Disadvantages	Uncert., %	Images
2nd harmonic measurement	Extrapolation scheme. Sec. 5.5.2.2	Extrapolating $\left[\frac{P_2(x)}{xP_1(0)^2}\right]$ to zero distance from the source	- does not need any attenuation measurement	- requires transducer calibration to estimate $P_1(0)$ - measurements at several distances	10 (liquid) [1], 8 (liquid, tissue) [230] 2-11 (liquid) [400], 10 (liquid) [227, 228]	-
	Single measurement. Sec. 5.5.2.2	Measuring the 2nd harmonic amplitude at a distance	- one measurement at one distance is sufficient for $B/A$ estimation	- requires transducer calibration to estimate $P_1(0)$ and an extra $\alpha$ measurement	4 (liquid) [73], <8 (tissue) [433]	echo-mode: [390]
	Source $P_1(0)$ - $P_2$ characteristic. Sec. 5.5.2.2	Fitting a line to $P_2$ depending on the source pressure	- requires measurements at only one distance	- requires transducer calibration to estimate $P_1(0)$ , $\alpha$ (unless can be neglected)	7.5 (liquid) [65], 3 (liquid) [291], 12 (liquid) [287]	-
	Comparative method. Sec. 5.5.2.2	Comparing $P_2$ in the sample to that in a reference medium at a fixed distance from the source	- requires measurements at only one distance - no source calibration needed - potential to mitigate diffraction effects	- source pressure in the studied medium may be altered, compared to the reference medium (due to different acoustic impedances of the media)	< 3 (tissue) [421], 8 (liquid) [151], 3 (liquid) [435]	echo-mode: [378, 394]

Main Groups	Subgroup	Main principle	Advantages	Disadvantages	Uncert., %	Images
2nd harmonic measurement	FAIS. Sec. 5.5.2.2	Extracting $\beta$ from the ratio $\frac{P_{20}}{P_{20}}$ (with the sample in the path between the source and the receiver and without)	- as for the comparative method - requires little sample volume	-	8 (liquid) [151], <8 (liquid, phantom) [102], < 10 (liquid) [167], <5 (tissue, liquid) [220]	tomography: [430], [428], reflection to-mography and echo-mode C-scans: [153]
	Transmission line method. Sec.5.5.2.2	Measuring the fundamental saturation as source pressure is increased	- no transducer calibration required	- acquisitions at several source-receiver separation distances	20 (liquid) [222], <2 (liquid) [103]	-
Fundamental	- Sec.5.5.3	Measuring the fundamental saturation as source pressure is increased	- one measurement distance - transmit and reception at the same frequency	- transducer calibration required, - for tissue may require high $P_1(0)$ for an accurate $B/A$ estimation	10 (liquid) [195],	echo-mode: [278])

This way, measurement of the diffraction of light allows for reconstruction of the US wave's velocity profile and quantification of distortion by extracting  $w_0$  or  $w_1$  from its shape (Fig. 5.4), and thereby derivation of  $B/A$ .

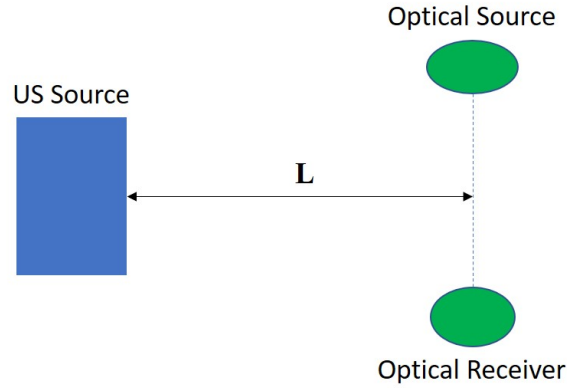


Figure 5.3: Schematic illustration of the setup used in optical methods/light diffraction methods for  $B/A$  measurement (top view). Detailed representations of such setups can be found in [1, 256].

This method was implemented by Mikhailov and Shutilov [257], Shutilov [350], and yielded  $B/A$  for water and several other optically transparent liquids. More recently, Takahashi [368] also utilized the waveshape to quantify  $B/A$  through assessment of  $w_0$  or  $w_1$ . In this case, the signal was received with a hydrophone, while the source pressure was determined from the diffraction pattern of light emitted by a laser. This way, the setup was hybrid of those presented in Fig. 5.2 and Fig. 5.3. Other works are also known [279], using the diffraction of light to capture the nonlinear distortion of ultrasound waves and extract  $B/A$ .

#### 5.5.1.2 Modelling of the wave profile

Chavrier et al. [60], Hunter et al. [177], Jackson et al. [184], Jeong et al. [189] utilized the setup presented in Fig. 5.2, where the signal passed through a medium of length  $L$  and was received by a hydrophone or a transducer. Chavrier et al. [60], Hunter et al. [177], Jackson et al. [184] fit nonlinear waveforms of the received pulses with the Burger's equation, where  $B/A$  (and  $\alpha$ ) was the fit parameter. These works use large source transducers (*e.g.*, 10 cm in diameter [184]) to avoid edge diffraction effects, eliminating the need for diffraction correction and justifying the use of the Burger's equation which cannot account for diffraction. Conversely, Jeong et al. developed multi-Gaussian beam models based on a quasilinear approximation of the Westervelt equation [189] and the KZK equation [188], including both diffraction and attenuation effects. This allowed describing the pressure fields of the fundamental and 2nd harmonic with no restrictions for the source size or the distance range. From a single measurement set at distances from 2 to 20 cm, the authors extracted the attenuation coefficients at the fundamental  $\alpha_1$  and 2nd harmonic frequency  $\alpha_2$ , as well as the  $\beta$  value by fitting a model to the observed pressure profiles. A calibration procedure for  $P_1(0)$  was required. Works inferring  $B/A$  through the wave profile require broadband receivers, able to capture the wave shape accurately.

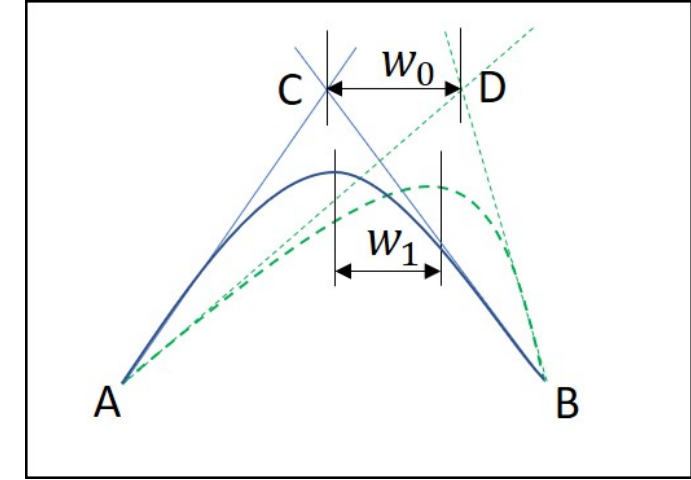


Figure 5.4: Illustration of the waveform deformation. The image shows the positive half-cycles of an undistorted sinus wave (solid line), and of a distorted wave (dashed line), where the distance  $w_1$  is the distance between the maxima of these waves.  $w_0$  is the distance between points C and D, which are the intersections of the tangents at points A and B.

### 5.5.2 Second harmonic measurements

#### 5.5.2.1 Basic theory

The amplitudes of the higher harmonics in the preshock region ( $\sigma \leq 1$ ) of a plane wave in a lossless medium are given by [133, 140, 166]:

$$P_n(\sigma) = \left[ \frac{2P_1(0)}{n\sigma} \right] J_n(n\sigma), \quad (5.25)$$

where  $n$  is a positive integer indicating the number of the harmonic: the fundamental  $P_1(0)$  at the source and higher harmonics  $P_{2,3,\dots}$ ; and  $\sigma$  is the shock parameter  $\sigma = \frac{2\pi f P_1(0) z \beta}{\rho c^3}$ . Eq. (5.25) is the Fubini solution [140] of the lossless Burgers equation (Eq. (5.11)). By expanding the Bessel function as a power series and neglecting the high order terms, the amplitude of the 2nd harmonic can be expressed as

$$P_2(z) = \left( \frac{B}{A} + 2 \right) \frac{\pi f z P_1^2(0)}{2\rho_0 c_0^3}. \quad (5.26)$$

This equation illustrates that the amplitude of the 2nd harmonic increases proportionally to  $B/A$ , to the distance  $z$  from the source, and the frequency of the transmitted signal  $f$ . It also shows a quadratic dependence on the transmitted pressure amplitude  $P_1(0)$  at the source.

Later this theory was further developed to include losses in two alternative ways. The first one was based on the assumption that the attenuation of the fundamental and higher harmonics are independent of each other. Furthermore, the change of the 2nd harmonic amplitude was ascribed to its harmonic generation due to nonzero  $B/A$  value and its small-signal absorption (neglecting energy transfer to higher harmonic components) [374]. The following expression is the solution to the equation describing the change of the 2nd harmonic

$$P_2(z) = \frac{(2 + B/A)\pi f}{2\rho_0 c_0^3} P_1^2(0) \frac{e^{-\alpha_2 z} - e^{-2\alpha_1 z}}{2\alpha_1 - \alpha_2}, \quad (5.27)$$

where  $\alpha_1$  and  $\alpha_2$  are the attenuation coefficients of the fundamental and its harmonic. Here no assumption about the frequency dependence of attenuation has been made, therefore the formula is valid for liquids and tissues. This expression can be further simplified [109] when assuming  $(\alpha_2 - 2\alpha_1)z$  to be small:

$$P_2(z) = \frac{(2 + B/A)\pi f z}{2\rho_0 c_0^3} P_1^2(0) e^{-(\alpha_1 + \frac{\alpha_2}{2})z}. \quad (5.28)$$

The previous simplification leads to an error of 1% when the value  $(\alpha_2 - 2\alpha_1)z$  is  $< 1/2$  [109]. Eq. (5.28) is particularly applicable to tissue, since tissue attenuation exhibits a nearly linear frequency dependence [106, 282].

An alternative way to take attenuation into account was proposed by Keck and Beyer [31, 198] when solving the Burgers equation (Eq. (5.10)) for the weakly nonlinear case characterized by a Goldberg number  $G = \frac{2\pi f P_0 \beta}{\rho c_0^3 \alpha} < 1$  [166].

$$P_2(z) = \left(\frac{B}{A} + 2\right) \frac{\pi f P_1^2(0)}{2\alpha \rho_0 c_0^3} (e^{-2\alpha z} - e^{-4\alpha z}), \quad (5.29)$$

where  $\alpha$  is the attenuation coefficient of the fundamental wave. The Golberg number reflects the balance between the nonlinear processes and the absorption processes [107]. Eq. (5.29) applies to weakly thermoviscous fluids (Sec. 5.2.2).

The theory above, as already mentioned, was developed for plane waves. Due to this, most studies use a plane piston source as a signal transmitter and perform the measurements in the near field at distances closer than the Rayleigh distance  $F_d$  ( $F_d = \frac{\pi r^2}{\lambda}$ , where  $r$  is the source radius and  $\lambda$  is the signal wavelength [221]). In reality, however, even the near field of a plane piston source differs from an ideal plane wave, due to interference of signals originated from different locations of the source (Huygens principle). These effects are diffraction effects [107] and result in a complicated diffraction pattern of pressure amplitude oscillations, demonstrated in Fig. 5.5. Only a very small triangular region of the near field remains truly a plane wave: in the proximity of the source the plane wave and the edge wave do not yet interfere [209]. It is also worth mentioning that the second harmonic beam is somewhat narrower than the fundamental beam. This can be fully appreciated at greater distances in [107], where the pressure distributions are presented up to the far field.

The deviation from plane wave theory can be accounted for by the diffraction correction term. For example, Dunn et al. [109] considered both attenuation and diffraction effects, leading to the following expression for the 2nd harmonic,

$$P_2(z) = \frac{(2 + B/A)\pi f z}{2\rho_0 c_0^3} P_1^2(0) e^{-(\alpha_1 + \frac{\alpha_2}{2})z} F(z), \quad (5.30)$$

where  $F(z)$  is the diffraction correction factor, described in detail in [182, 408]. Alternatively, the diffraction corrections developed using Multi-Gaussian beams have also been utilized [168, 188, 189, 190].

The theory above serves the basis of the FAMs. Numerous works have estimated  $B/A$  through 2nd harmonic measurement (Eq. (5.26-5.30)). In most of these methods the 2nd harmonic is measured in the near field of a plane piston source, enabling the plane-wave approximation. Therefore, these conditions are implied throughout this section (Sec. 5.5.2) unless otherwise stated. These methods are presented in two sections: measurements of homogeneous media (Sec. 5.5.2.2) and heterogeneous media (Sec. 5.5.2.3).

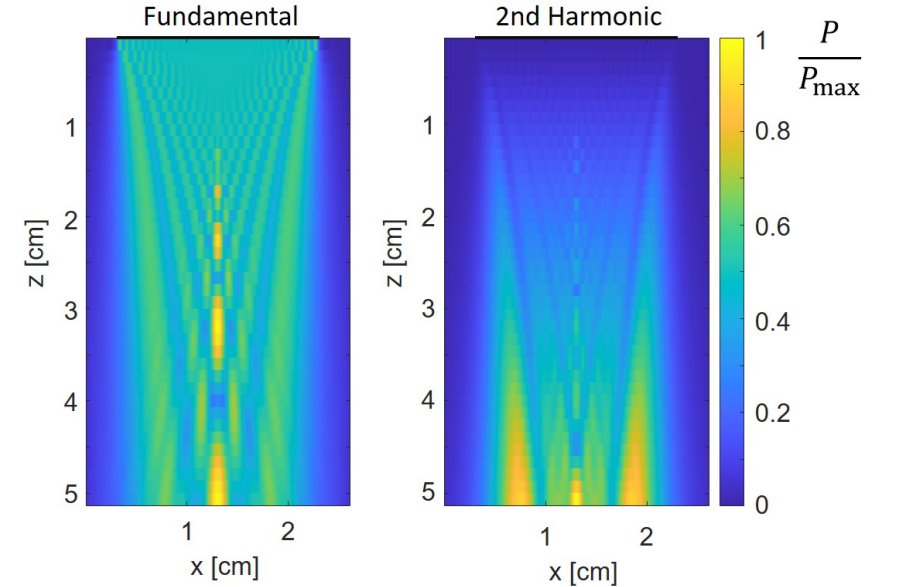


Figure 5.5: Simulated pressure distributions along the diagonal of a circular plane piston source up to 5 cm away from the source. The fundamental and the 2nd harmonic pressure amplitudes are normalized to their maximum amplitude values, the position of the source is indicated by the black line. The simulation was performed in *k-Wave*, Matlab<sup>®</sup> [380] for a source with a radius of 10 mm, transmitting a Gaussian 10-cycles pulse at 2.25 MHz with an amplitude of 0.1 MPa, in 3D space.

### 5.5.2.2 $B/A$ measurement of homogeneous media

The studies discussed in this section assume invariant  $B/A$  along the beam path in the medium, yielding a single  $B/A$  value. All the strategies suitable for bulk estimation of  $B/A$  through 2nd harmonic measurement are presented below. All the presented works, unless otherwise mentioned, utilized the setup as in Fig. 5.2. Unlike the wave shape method, in this case the receiver has to be responsive at the 2nd harmonic of the fundamental signal, transmitted by the source.

**Second harmonic maximum** Eq. (5.29) formed the basis for one of the early  $B/A$  measurement approaches [24, 198]. One can find the distance to the source where the 2nd harmonic reaches its maximum value by differentiating Eq. (5.29) with respect to  $z$  and finding the zero crossing. Once the coordinate of the 2nd harmonic maximum is determined experimentally,  $B/A$  can thus be calculated.

**Extrapolation scheme** Other strategies utilized the lossless formulation in Eq. (5.26). It has been experimentally verified [210], that at distances close to the source the dependance of the 2nd harmonic on the distance  $z$  and the pressure at the source  $P(0)$  follows the lossless model described by Eq. (5.26) also in a dissipative medium. Therefore, one can derive  $B/A$



by extrapolating the 2nd harmonic amplitude at zero distance from the source:

$$\frac{B}{A} = \frac{2\rho_0 c_0^3}{\pi f} \left[ \frac{P_2(z)}{z P_1(0)^2} \right]_{z P_1(0)=0} - 2. \quad (5.31)$$

For this purpose, Adler and Hiedemann [1] utilized the optical setup (Fig. 5.3) to measure the transmitted fundamental signal  $P_1(0)$  and the 2nd harmonic at different distances from the source transducer. Extrapolation of  $\left[ \frac{P_2(z)}{z P_1(0)^2} \right]$  to  $z=0$ , as in Fig. 5.6, yielded  $B/A$  for water and m-Xylene.

Law et al. [227, 228] utilized a much simpler setup (Fig. 5.2), measuring the 2nd harmonic amplitude  $P_2$  and  $P_1(0)$  with an additional planar transducer, also employed in all the following studies unless otherwise mentioned. For this purpose, a calibration procedure of the receiver is required, allowing to convert measured voltage to pressure values and to determine  $P_1(0)$ . Extrapolating  $\left[ \frac{P_2(z)}{z P_1(0)^2} \right]$  to zero distance from the source, they obtained  $B/A$  for several biological solutions as well as whole liver. When comparing their values to glycerol and glycerin, previously obtained by the thermodynamic method [74], they concluded that this technique has an uncertainty of 10%.

Dunn et al. [109] introduced attenuation in the expression for the 2nd harmonic (Eq. (5.28)), showing that  $\left[ \frac{P_2(z)}{z P_1(0)^2} \right]$  decreases exponentially with distance in the proximity of the transducer. Moreover, they were the first ones to consider diffraction effects (Eq. (5.30)) that manifested themselves in the calibration procedure [408] of the receiver as well as in the quantification of the 2nd harmonic [182]. Law et al. [230] followed the same procedure as Dunn et al. [109] to measure  $B/A$  of tissues, requiring the tissue sample to be sliced in order to obtain measurements at several distances.

The extrapolation scheme has an important advantage: it avoids measurements of the attenuation coefficient of the medium. As illustrated in Fig. 5.6, even if the attenuation value of the medium under study changes, the curves intersect at the same point, provided that the other acoustic parameters are equivalent. This method is sometimes referred to as the pullback method [400].

**Single measurement** Eqs. (5.27-5.30) also enable measuring  $B/A$  from a single measurement once the attenuation coefficients at the fundamental  $\alpha_1$  and harmonic  $\alpha_2$  frequencies are known. After first estimating the attenuation coefficients, Cobb [73] estimated  $B/A$ , taking diffraction of the 2nd harmonic [182] into account (for the case of transducers of equal size, Eq. (5.27)). The authors noted that the approximation given by Eq. (5.28), justifying the extrapolation scheme, may lead to errors of 7% in samples such as water and glycerin [109]. Zhang and Dunn [433] utilized Eq. (5.30) to estimate  $B/A$  from a single acquisition, finding that there is no significant difference between  $B/A$  of *in vivo* and *ex vivo* cat livers. In [168], the second harmonic was measured after its reflection from an aluminium plate that replaced the receiver in a typical through-transmission setup (Fig. 5.2). The reflection mode method increased the propagation path of the signal in the studied medium. This way an accurate  $B/A$  measurement could be acquired for a reduced amount of the investigated liquid. Li et al. [233] presented a through-transmission method for  $B/A$  measurement of fluids, utilizing focused transducers to transmit and receive acoustic signals. Diffraction corrections were derived for focused receiver and source and a simple calibration procedure of the receiver was proposed. This enabled estimating  $B/A$  of water within an 8% error for multiple distances.

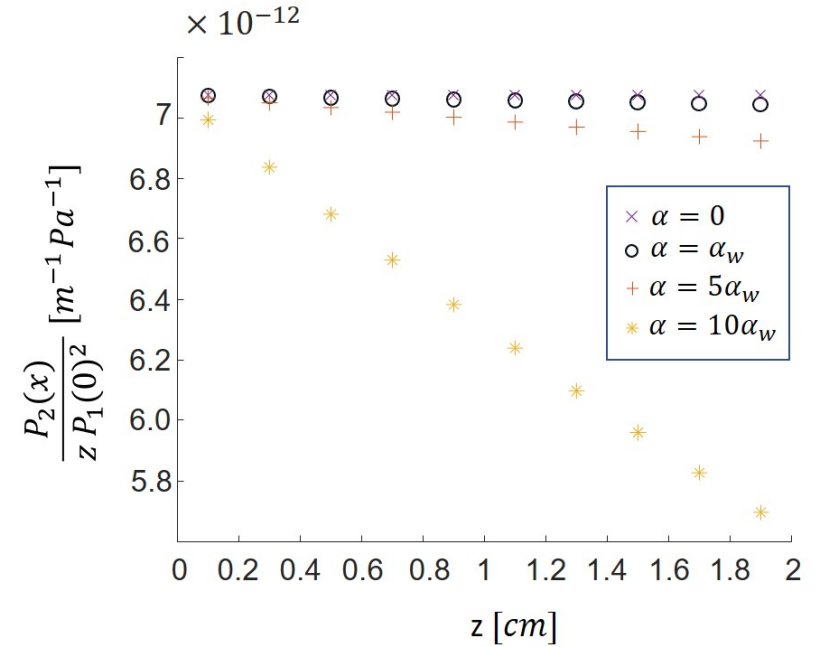


Figure 5.6: Simulated curves for media with the same acoustic parameters as for water but different attenuation. The graph illustrates the dependence of  $\left[ \frac{P_2(z)}{z P_1(0)^2} \right]$  on  $z$  for a lossless medium, a medium with an attenuation coefficient as that of water  $\alpha_w$ , and media with much higher attenuation than that of water ( $5\alpha_w$  and  $10\alpha_w$ ). The curves simulate Eq. 5.27 at close distances from the source, when transmitting a frequency of 2 MHz and a pressure of 0.5 MPa.

**Source pressure-harmonic characteristic** Panfilova et al. [287], Pantea et al. [291] determined  $B/A$  of water based on Eqs. (5.27-5.28) by fitting a line to the dependence of the 2nd harmonic amplitude on the fundamental pressure  $P_1(z)$ . They require no attenuation measurement, since they account for attenuation by using the fundamental and 2nd harmonic values at the measurement point. Pantea et al. [291] reported more extensive work, performing the fit for a larger range of distances and making use of the extrapolation scheme or pullback method (Sec. 5.5.2.2).

Meulen and Haumesser [255] implemented this method in echo-mode by employment of a reflector, concluding that the reflector must have an impedance higher than that of the studied fluid. This ensures that the 2nd harmonic components generated during forth and back propagation interfere constructively, and  $B/A$  quantification is possible. Otherwise, these components add out of phase.

Similarly, Chitnalath et al. [65] recorded the 2nd harmonic in reflection mode at different source pressures, but reflected from the interface of 2 liquids. They took into account attenuation and diffraction correction, decomposing the source function into a series of Gaussian beams.

## Comparative method



**Transmission mode comparative method** The first record of the comparative method was found in [150]. Its aim is to avoid absolute pressure measurements and therefore a receiver calibration procedure. The idea of the method is to compare the 2nd harmonic signal relative to that generated in a medium with a known  $B/A$  when the measurements are performed at the same source pressure and distance  $L$  from the source (Fig. 5.2). This way, when describing the 2nd harmonic component with Eq. (5.26) for both media, and taking their ratio, one can derive that

$$\left(\frac{B}{A}\right)_m = \frac{P_{2m}}{P_{20}} \frac{(\rho_0 c^3)_m}{(\rho c^3)_0} \left[\left(\frac{B}{A}\right)_0 + 2\right] - 2, \quad (5.32)$$

where the subscripts  $m$  and  $0$  denote the medium under study and the reference medium, respectively. In this first study, the reference liquid was acetone, with a density and speed of sound close to that of the studied nitrogen. However, most studies use water as the reference medium, as its  $B/A$  is well known and attenuation can be neglected. Gong et al. [151] and Zhang et al. [435] utilized the same technique, with the latter work also accounting for diffraction effects.

Wallace et al. [400] used a hybrid of the extrapolation and comparative methods. The authors compared the ratio  $\left[\frac{V_2(z)}{zV_1(0)^2}\right]_{zV_1(0)=0}$  of isopropanol to that of water, where  $V_1$  and  $V_2$  are the voltages associated with the fundamental and the 2nd harmonic. Differently from previous works, the authors took into account the fact that the generated source pressure actually depends on the medium where the source is immersed (also explained in [184]), defined by the transmission coefficient between the transducer material and the medium (see also Eq. (5.34)). Besides this, they introduced a steel delay line in front of the transmitting transducer. Since steel has a speed of sound that is approximately 4 times higher than in water, the resulting diffraction pattern is compressed compared to that in water. This allowed positioning the natural focus inside or right after the path in steel. As a result, Wallace et al. [400] satisfy the plane-wave approximation by measuring in the far field, requiring no further diffraction corrections.

Yu et al. [421] performed an evaluation of the comparative technique, including simulations and a phantom experiment for homogeneous tissue. The simulation study utilized a linear probe as the source and measured  $\beta$  for 3 tissue types at different distances. The experiment showed that the estimated  $\beta$  did not depend significantly on the measurement distance, demonstrating the method's robustness. The authors took into account tissue attenuation (Eq. (5.28)). In this work, the formula for  $B/A$  was derived from the special case of the comparative method: the finite amplitude insert substitution technique explained below in Sec. 5.5.2.2). This resulted in an erroneous formula. However, since the transmission coefficients of the studied tissues were close to unity, the introduced error was very small. The authors assessed their technique to be within 3 % of uncertainty.

**Reflection mode comparative method** Kourtiche et al. [208] used the same transducer to transmit the fundamental and receive the 2nd harmonic reflected from a reflector plate. In this case, the 2nd harmonic generation occurs both ways. The authors also performed an analysis of the electromechanical behavior of the transducer at different transmit frequencies. A transducer generates a “clean” and strong fundamental around its resonance frequency. At the same time, it must be sensitive enough to detect the 2nd harmonic of the transmitted signal. Therefore, a favorable trade off frequency region must be determined for  $B/A$  estimation. Besides this, a transducer usually shows different sensitivities in transmission and in receive.

These are influenced by the impedance of the transducer, which varies with signal frequency and the impedance of the medium. The authors showed that neglecting these effects can lead to errors in  $\beta$  estimation, and that there is a frequency range where  $B/A$  can be estimated most accurately. This work is relevant for all echo-mode developments as well as transmission mode measurements utilizing identical transducers as source and receiver.

### Finite amplitude insert substitution method

**Transmission mode FAIS** The finite amplitude insert substitution (FAIS) method was motivated by the idea of avoiding absolute pressure measurements, similar to the comparative method. Some authors classify the comparative method (Sec. 5.5.2.2) as a particular case of FAIS [421], which in reality was developed later. In light of this, it should be noted that the equation utilized for the comparative method should not be derived as a general case of the FAIS. With FAIS, the medium under study is inserted in a water path and does not have the same length as the reference medium (water), in most cases resulting in 2 reflection interfaces (Fig. (5.7)). Initially, Shklovskaya-Kordi [349] developed this method based on the Fubini solution (Eq. (5.26)) for measurement of internal pressure through  $B/A$ . When the source pressure and distance between the source and receiver ( $L$ ) are fixed (in this work kept within the near field distance to adhere to the plane wave approximation), the amplitude of the 2nd harmonic in a water path  $P_{20}$ , whose  $B/A$  is known, is compared to that when a sample of thickness  $d$  is inserted in this path  $P_{2m}$ . Through the ratio  $\frac{P_{2m}}{P_{20}}$ , we can calculate  $\frac{B}{A}$  as [151]:

$$\left(\frac{B}{A}\right)_m = \left(\frac{P_{2m}}{P_{20}} \frac{L}{dD'D''} - \frac{L}{d} + 1\right) \frac{(\rho_0 c_0^3)_m}{(\rho c^3)_0} \frac{1}{D''} \left[\left(\frac{B}{A}\right)_0 + 2\right] - 2, \quad (5.33)$$

where  $D'$  and  $D''$  are the sound transmission coefficients from water to the sample and from the sample to water, respectively:

$$D' = \frac{2(\rho_0 c_0)_0}{(\rho_0 c_0)_0 + (\rho_0 c_0)_m}; D'' = \frac{2(\rho_0 c_0)_m}{(\rho_0 c_0)_0 + (\rho_0 c_0)_m}. \quad (5.34)$$

Eq. (5.33) is only valid when the investigated medium is nearly lossless. Moreover, the formula was derived merging the 2nd harmonic contribution from water before the sample and after it, which is justified if the acoustic impedance of the medium is close to water. Alternatively, the medium can be placed very close to the receiver, making the 2nd harmonic generation in the water path after the sample negligible. Because of this, the sample is conventionally positioned close to the receiver in all FAIS modifications. As for the comparative method, FAIS does not require transducer calibration for recovery of the absolute pressure values, since the pressure ratio term is equivalent to the received voltage ratio. [152] built on this method, introducing an attenuation correction in Eq. (5.28) aimed at measuring  $B/A$  of tissue, making the assumption that  $(\alpha_2 - 2\alpha_1)z$  is small, valid for most tissues as they have a nearly linear frequency dependence [106, 282]. The resulting expression is

$$\left(\frac{B}{A}\right)_m = \left[\frac{P_{2m}}{P_{20}} \frac{L}{d} e^{(\alpha_1 + \frac{1}{2}\alpha_2)d} - \left(\frac{L}{d} - 1\right) e^{(\alpha_1 - \frac{1}{2}\alpha_2)d} D'D''\right] \frac{(\rho_0 c_0^3)_m}{(\rho_0 c_0^3)_0} \frac{1}{D''^2 D'} \left[\left(\frac{B}{A}\right)_0 + 2\right] - 2. \quad (5.35)$$

Here one can see that a measurement of the attenuation coefficient at the fundamental  $\alpha_1$  and the harmonic  $\alpha_2$  is required for  $B/A$  determination. Besides this, [152] also introduced a diffraction correction which for most biological tissues (speeds of sound: 1400-1600 m/s) they

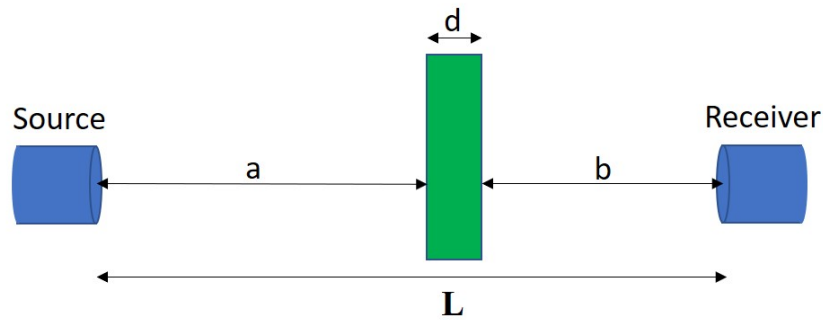


Figure 5.7: Setup for the FAIS method.

quantified to be within 2 %. However, it must be noted that, in general, for liquids with a speed of sound further away from that of water, the diffraction correction can introduce significant errors (*e.g.*, 5 % error for ethanol).

Wu and Tong [412] measured  $B/A$  of contrast agents. Since  $B/A$  of contrast agents can be in the order of hundreds and thousands, the harmonic component generated in water can be neglected for the configuration in Fig. 5.7. This resulted in a simpler expression. No diffraction correction was used, possibly due to the assumption of a similar speed of sound in contrast agents to that of water (not stated).

Dong et al. [102] derived a formula analogous to Eq. (5.35), however, they utilized the general expression for attenuation in Eq. (5.27). Dong et al. [102] positioned the sample and the receiver in the extreme far field of the source, another region of the piston field where the plane-wave approximation may be considered valid. The authors removed all harmonic content generated in the near field by placing an acoustic absorber before the sample. Yet, due to the absorber, the insonifying amplitude is expected to have been low, and the resulting distortion weak. Cortela et al. [76], King et al. [203] utilized the same configuration as Dong et al. [102] to measure  $B/A$  of gellan gum-based tissue-mimicking phantoms. Choi et al. [66] utilized the same formula as Dong et al. [102] in a setup where no acoustic absorber was used. They presented the temperature dependence of  $B/A$  of porcine liver.

Harris et al. [167] proposed another setup which allowed avoiding diffraction correction. Their solution was a large source transducer (8 cm in diameter), which provided a broad plane wave region, without diffraction effects. Fig. 5.5 demonstrates such a triangular region in the proximity of the transducer, where the field is stable.

Kujawska et al. [220] introduced a modified FAIS method. A model of the ratio  $\frac{P_{2m}}{P_{20}}$  depending on sample thickness  $d$  was fit to experimental data, when using a small receiver (0.4 mm in diameter). The best fit of the data provided an estimate  $B/A$  for liquids and homogenized tissue. The current approach required no plane-wave assumption.

Zeqiri et al. [426] conducted a detailed analysis of the influence of several factors on the accuracy of  $B/A$  measurement with the FAIS, *e.g.*, sample positioning with respect to the receiver, source pressure amplitude, and sample thickness.

**Reflection mode FAIS** Lu et al. [241] utilized FAIS in reflection mode, transmitting and receiving with the same compound transducer whose inner ring served as the source, and outer ring received the signal from a reflector plate. In this case, the authors needed to

take into account 2nd harmonic generation in the forward and backward path, making the calculations more complex. It is of notice that for FAIS the transducer sensitivity is not altered by the studied medium. The authors showed a strong dependence of  $B/A$  in porcine liver and muscle on temperature, suggesting the possibility of temperature monitoring through  $B/A$  during HIFU.

**Nonlinear acoustic microscopy** Acoustic microscopy allows studies of small-volume samples (*e.g.*, 0.1 ml [323]). It utilizes high frequency sources (14-19 MHz) in conjunction with acoustic lenses that provide a short focal distance (*e.g.*, 2.3 mm [146]). Altogether this produces appreciable nonlinear effects in the focal spot already at such short distances. All the studies in this field have adapted the comparative and FAIS techniques using water as a reference medium and either completely filling the space by the sample, or positioning it only in the focal region, surrounded by water.

Banchet and Cheeke [13], Banchet et al. [14], Germain et al. [146] developed an acoustic microscope for measurement of  $B/A$ . The 2nd harmonic was detected by a planar transducer. Its generation was assumed to be confined to the focal region and was described with plane-wave theory utilizing Eq. (5.28). This system also allowed measuring sound velocities; however, parameters like density and attenuation needed to be measured beforehand to enable calculations with Eq. (5.28).

Additional work in this direction was performed in [321, 322, 323, 324, 325]. The final setup of the developed system utilized the source as a receiver, detecting the signal from a reflector. The authors made use of Gaussian beam theory that models the field as a series of beams whose spatial pressure distribution is described by the Gaussian function [201]. This system allowed measurement of  $B/A$  as well as linear acoustic parameters, including sample density. At the latest stage of development, Saito and Kim [324] generated 2D images of  $B/A$  and linear acoustic parameters by mechanically translating the samples of biological tissues (*e.g.*, fat vs. nonfat; coagulated vs. normal), showing that tissue  $B/A$  was variable on a microscale and exhibited different variation patterns than the linear parameters (*e.g.*, attenuation, density). In [323, 324] the authors observed good reproducibility of their measurements (within 1%) and stated the measurement error to be within 10 %, typical for finite amplitude methods.

**Transmission line method** Dong et al. [103], Kushibiki et al. [222] introduced a novel method utilizing frequencies as high as 100-200 MHz. The specimen was positioned between two SiO<sub>2</sub> buffer rods with transducers at their outer ends. SiO<sub>2</sub> has a negative  $\beta$ : its 2nd harmonic shows an opposite phase compared to that generated in liquid. This way, when acquiring  $P_2$  for different sample lengths, at a certain point the 2nd harmonic was cancelled out completely. The authors utilized plane-wave theory (Eq. (5.27)), incorporating diffraction and dispersion in [222], showing that this gives more stable  $B/A$  estimates. The major advantage of this method is in that no pressure measurement is needed. However, the observed  $\beta$  for water was 20% higher than the value reported in literature. This was ascribed by the authors to uncertainties in the properties of SiO<sub>2</sub>.

### 5.5.2.3 $B/A$ imaging

The studies discussed in this section consider  $B/A$  estimation in heterogeneous media. First, the section performing through-transmission measurements is presented. In this case, the

image is reconstructed with computer tomography (CT) once the through-transmission measurement is repeated for several sample rotation and translation configurations (Fig. 5.8). The reconstruction is obtained by use of the Radon transform, with the resulting image resolution being determined by the number of employed rotation angles. Reflection-mode measurement follow the same scheme, however, utilize the source as the receiver. After transmission through the tissue, the signal is reflected from a reflective plate on the opposite side of the sample. Echo-mode imaging is the last family of methods presented in this section. In this case the signal is received by the source transducer as it is reflected along its propagation path in tissue, due to tissue inhomogeneities. This distinction between reflection-mode and echo-mode imaging will be further used in this review.

**B/A tomography** Zhang and Gong [427, 428], Zhang et al. [430] implemented B/A tomography based on the FAIS method. When considering a heterogeneous medium, the received 2nd harmonic amplitude at a distance  $L$  from the source is the result of its propagation path where different values of  $\beta$ ,  $\alpha_1$ ,  $\alpha_2$  correspond to every  $z$ :

$$P_{2m}(L) = \frac{\pi f_2 P_1(0)^2}{2\rho_m c_m^3} \int_0^L \beta_m(z) \exp\left(\int_0^z -2\alpha_1(z)dz - \int_z^L \alpha_2(z)dz\right) dz, \quad (5.36)$$

where the indice “m” refers to the medium under investigation. In order to avoid conversion to absolute pressure values, the authors also measure the amplitude of the 2nd harmonic  $P_2(L)$  in a homogeneous reference medium with a known  $\beta$ . The reference medium was water, making it possible to apply the lossless Fubini solution (Eq. (5.26)):

$$P_{20}(L) = \frac{\pi f_2 P_1(0)^2}{2\rho_0 c_0^3} L \beta_0. \quad (5.37)$$

This way, when the sample is placed in the water path between the source and the receiver, the ratio of the received 2nd harmonics is defined by

$$P = \frac{P_{2m}(L)}{P_{20}(L)} = \frac{\rho_0 c_0^3}{\rho_m c_m^3 \beta_0} \int_0^L \beta_m(z) \exp\left(\int_0^z -2\alpha_1(z)dz - \int_z^L \alpha_2(z)dz\right) dz. \quad (5.38)$$

The implemented CT system allowed for rotation of the sample and translation of the source and receiver (hydrophone) along the sample length (Fig. 5.8). The receiver was positioned in the near field of the transmitting transducer. The obtained projection images of the ratio  $P$  (Eq. (5.38)) were transferred to the  $\beta$  domain by the filtered convolution method and then corrected for by multiplying with the attenuation matrix describing the sample’s attenuation in space (estimated by attenuation tomography with the same setup). This work showed promising results; however, the authors concluded that attenuation and velocity estimates required further improvement. Yu et al. [421] also simulated B/A tomography based on Eq. (5.38), modified for the case of an attenuating reference medium and utilizing a filtered back projection algorithm.

**$\beta$  tomography in reflection mode** Gong et al. [153] extended their previous work [430] to reflection tomography. The tissue sample was positioned in water between the source and a reflective plate, where the reflective plate replaced the receiver in Fig. 5.8. Equation (5.38) was extended, now containing nonlinear generation and attenuation terms for the forward and backward path. Fig. 5.9 presents an example of an image acquired in this work. On this image we can see a two-layered tissue structure with porcine liver surrounded by porcine fat, submerged in water.

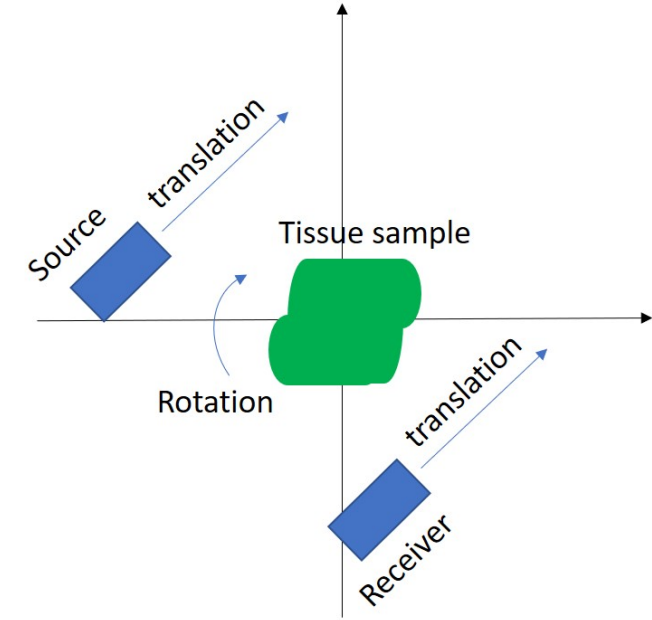


Figure 5.8: Top view of the typical CT scanning system. Multiple signal acquisitions are performed for various sample rotation configurations and multiple source-receiver translations.

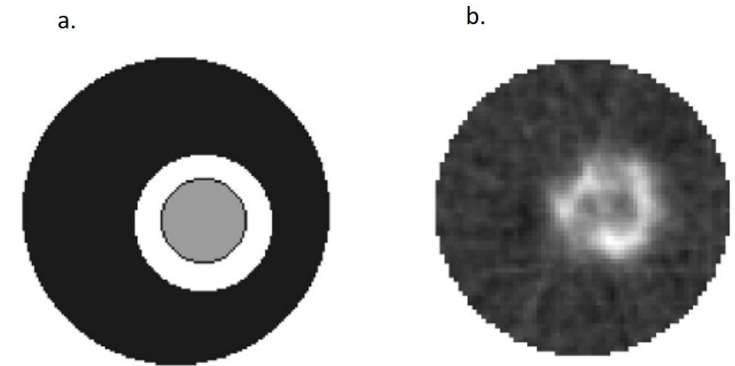


Figure 5.9: Reprinted from [153]. a. Model of the imaged media: porcine liver surrounded with porcine fat, submerged in water. b. The acquired reflection-mode tomographic image, utilizing the finite amplitude insert-substitution method.

**$\beta$  imaging in echo-mode** Reflection mode imaging poses additional challenges, compared to transmission tomography. In the latter case, the recorded signal has travelled through the whole bulk of the tissue, and therefore, the effect of varying scatterer density within the medium is averaged out. However, when utilizing echo-mode  $\beta$  imaging, the strength of the reflected echoes is, to a large extent, defined by the scatterer density at each reflection point [399], masking information about other acoustic properties. To cancel out the scatterer effect,



scientists normalized the recorded signal to a signal that is assumed to have an analogous scattering pattern. Three different reference signals have been identified in literature. One utilizes an additional signal, transmitted at the 2nd harmonic frequency. Another utilizes the second harmonic amplitude reflected from a scattering homogeneous reference medium. The last reference signal is the reflected fundamental component of the received pulse.

Akiyama [3], Fujii et al. [141] found a way to mitigate the influence of scatterers by assuming that the scatterer distribution affects a signal of a certain frequency in the same way, whether it is the generated 2nd harmonic at  $2f_0$  of the fundamental at  $f_0$ , or whether it is the transmitted fundamental at  $2f_0$ . The authors assumed that the 2nd harmonic is generated only in transmission, and not on the way back when reflected from scatterers due to low amplitudes of the reflected signal. Attenuation was taken into account in both directions of propagation, leading to the following expression for the 2nd harmonic received from distance  $z$  from the source for a transmitted signal at fundamental frequency  $f_0$ :

$$P_{2h}(z, f_0) = P_0^2(f_0) \exp\left(-2 \int \alpha(f_0, z) dz - \int \alpha(2f_0, z) dz\right) \gamma(2f_0, z) \int \frac{(B/A + 2)2\pi f_0}{4\rho c^3} dz, \quad (5.39)$$

where  $\rho$  and  $c$  are medium properties, assumed constant and  $\gamma(2f_0, z)$  is the backscattering characteristic term. The received fundamental  $P_f(z, 2f_0)$  when transmitting another pulse at  $2f_0$  is also proportional to  $\gamma(2f_0, z)$ , and  $\int \alpha(2f_0, z) dz$ . Therefore, the ratio of the generated 2nd harmonic to the fundamental at the frequency of the 2nd harmonic cancels out the backscattering and the attenuation at  $2f_0$  terms. The authors extracted  $h(z)$ , a parameter defined by  $B/A$ , speed of sound and density of the medium with the following equation

$$h(z) = \frac{A_0(0, 2f_0)}{P_0^2(0, f_0)} \frac{d}{dz} \left[ \frac{P_{2h}(z, f_0)}{P_f(z, 2f_0)} \right], \quad (5.40)$$

where  $P_0$  and  $A_0$  are pressures at the source when transmitting at  $f_0$  and  $2f_0$ , respectively. Signals  $P_{2h}(z, f_0)$  and  $P_f(z, 2f_0)$  are the received 2nd harmonic and fundamental at  $2f_0$ , correspondingly. It is important to note that the studies mentioned above retrieved one single value of  $h$ , fitting a line to the ratio  $\frac{P_{2h}(z, f_0)}{P_f(z, 2f_0)}$  observed throughout the whole sample depth. Besides a phantom study, Fujii et al. [141] conducted an *in vivo* clinical study with 41 patients, using  $h$  as a single-valued indicator of liver fat content.

A similar strategy was followed by Gong et al. [153], Liu et al. [235] who acquired C-scan images of the  $B/A$  profile, modifying Eq. (5.40):

$$\frac{B}{A}(z) = \frac{4\rho c^3}{\omega} \frac{A_0(0, 2f_0)}{P_0^2(0, f)} \frac{d}{dz} \left[ \frac{P_{2h}(z, f_0)}{P_f(z, 2f_0)} \right] - 2, \quad (5.41)$$

assessing the local slope of the ratio  $\frac{P_{2h}(z, f_0)}{P_f(z, 2f_0)}$  of the echoes reflected by tissue. The authors showed very promising discrimination capabilities, when imaging heterogeneous tissue models in the plane perpendicular to the beam propagation direction, by mechanically scanning their system point by point. No capabilities of  $B/A$  discrimination in depth of the sample were presented.

Varray et al. [393] extended the comparative method (Eq. (5.36), Eq. (5.27)) to enable imaging of heterogeneous media in echo mode. By taking several acquisition lines in the filtered 2nd harmonic image as a reference, the authors normalized the 2nd harmonic response of the whole image to construct a  $\beta$  image. The images of 2 phantoms with inclusions were

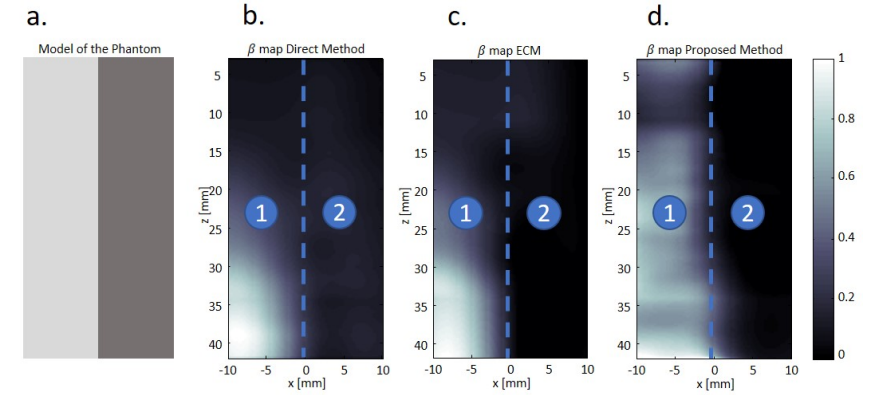


Figure 5.10: *a. Model of the imaged gelatin-based tissue-mimicking phantom with 2 layers of different oil content. Reprinted from [390], with the permission of AIP Publishing; b. Direct method. c. Extended comparative method, proposed in [393]. d. Harmonic ratio method proposed in [390].*

acquired with the ULA-OP scanner (X-Phase), transmitting a focused beam. An experimental image acquired with this strategy [390] is presented in Fig. 5.10.

van Sloun et al. [390] eliminated the influence of scatterer density, expressing  $\beta(z) = f\left(\frac{P_{2h}(z, f_0)}{P_f(z, 2f_0)}\right)$  as a function of the ratio of the received amplitudes of the 2nd harmonic to the fundamental of that signal, derived from the 1D lossy Westervelt equation (Eq. (5.8)). The proposed approach was called “the harmonic ratio method”. Simulations were performed with the iterative nonlinear contrast source approach, capable of modelling 3D fields in complex media [91]. The modelled media exhibited different  $\beta$  and  $\alpha$  values with the same constant speed of sound and density. The resulting images showed good contrast. A more realistic tissue-mimicking phantom acquisition was performed with the ULA-OP scanner, acquiring 128 RF lines. van Sloun et al. [390] compared the proposed method to the extended comparative method [394] and direct estimation of  $\beta$  from the 2nd harmonic amplitude (Sec. 5.5.2.2; Sec.5.5.2.1, Eq. 5.27-5.30). The two phantom layers had different oil content and were, therefore, expected to have different  $\beta$ . The resulting normalized  $\beta$  images of the phantom for the three studied strategies are presented in Fig. 5.10. All methods showed capable of distinguishing 2 layers with different oil content. However, the strategy proposed in [390] showed more homogeneous estimates for both layers and a better consistency over depth. Unfortunately, no follow-up experimental work further confirmed the applicability of this method in a realistic clinical setting.

Another *in silico* work Toulemonde et al. [377] proposed utilizing the extended comparative method [394] on compounded B-mode images acquired with high frame rate plane-wave imaging. Utilizing plane waves allowed imaging at various depths compared to focused beams [394], while compounding reduced the speckle. Moreover, to reduce the speckle, filtered second harmonic images were normalized by the corresponding filtered fundamental images. These normalized second harmonic signals were compared to those of the reference medium to extract the  $B/A$  distribution. This way, Toulemonde et al. [377] proposed utilizing two types of signals to reduce the influence of scatterers on  $B/A$  estimation: the fundamental of the received signal and the received 2nd harmonic of a reference medium. This approach resulted



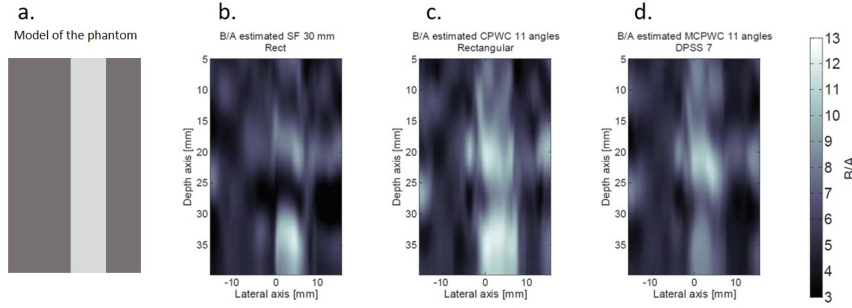


Figure 5.11: *a. Model of the imaged gelatin-based tissue-mimicking phantom with a layer of greater oil content than in the side regions. Reprinted from [378], with the permission of AIP Publishing: b. Image acquired with the extended comparative method, utilizing a focused beam [394]. c. Extended comparative method, making use of plane wave compounding [377]. d. Extended comparative method, utilizing multitaper coherent plane wave compounding [378].*

in a more accurate  $B/A$  reconstruction of a simple  $B/A$  distribution than with the original extended comparative method in [394]. Nevertheless,  $B/A$  images of a simulated medium with a complex  $B/A$  distribution were greatly degraded by the remaining speckle pattern for both methods. Further this approach was extended to multitaper coherent plane wave compounding [378], using several orthogonal apodizations for plane-wave beamforming, creating several speckle patterns for each steering angle. Toulemonde et al. [378] presented  $B/A$  images of *in silico* and experimental phantoms, showing a better  $B/A$  delineation compared to previous approaches [377, 394]. Experimental images of a three-layered tissue-mimicking phantom are presented in Fig. 5.11.

### 5.5.3 Fundamental nonlinear absorption

#### 5.5.3.1 Basic theory

When observing an increase in absorption with signal intensity [133], this was first attributed to cavitation. Later, however, it was recognized [134] to be the result of energy transfer from the fundamental to higher harmonics. Moreover, as nonlinear effects grow with the source amplitude (*e.g.*, Eq. (5.26)), nonlinear attenuation increases along with them, limiting the power that can be possibly delivered to certain depth (Fig. 5.12) [169, 195].

In the shock-free or pre-shock region ( $\sigma < 1$ ) of a lossless medium, the fundamental component of a plane wave will decrease according to Eq. (5.42) due to energy transfer to higher harmonics [140].

$$P_1(z) = P_0(1 - \frac{1}{8}\sigma^2) = P_0 \left( 1 - \frac{1}{2} \left[ \frac{(1 + \frac{1}{2}\frac{B}{A})z\pi f_0}{\rho_0 c_0^3} P_0 \right]^2 \right). \quad (5.42)$$

Additional small-signal attenuation losses can be accounted for by the Keck and Beyer solution [198] for the fundamental.

Another way to account for both effects of small-signal attenuation and nonlinear depletion of plane waves was proposed by Bartram [17], Rudnick [316], introducing spatial changes that

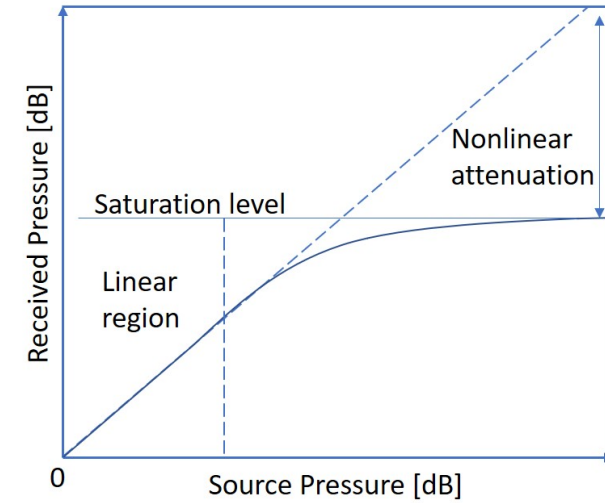


Figure 5.12: *A response curve showing the phenomenon of saturation as the source power is increased, for a lossless medium. Experimental curves can be found in [169, 195].*

are ascribed to the rate of heat production due to fluid heating by the shock fronts and energy loss between shocks:

$$\frac{dP(z)}{dz} = -\alpha P - \frac{\beta f \pi}{\rho_0 c_0^3} P^2. \quad (5.43)$$

The equation above was first introduced for weak shock theory ( $\sigma > 3$ ); however, it has also been adapted by [195] to describe the fundamental amplitude change at  $\sigma < 3$ , the proposed solution being:

$$P(z) = P(0)e^{-\alpha z} \left[ 1 + \frac{(1 - e^{-\alpha z})\beta \pi f P(0)}{\alpha \rho_0 c_0^3} \right]^{-1}. \quad (5.44)$$

When the source pressure is low, the dominating term in Eq. (5.44) is the first one on the right handside, describing small-signal attenuation, and corresponding to the linear region in Fig. 5.12. However, as the source pressure increases, the harmonics grow, depleting the fundamental harmonic as described by the 2nd term in Eq. (5.44) and corresponding to the saturating process in Fig. 5.12.

#### 5.5.3.2 $B/A$ measurement of homogeneous media

**Transmission mode** Hikata et al. [169], Kashkooli et al. [195] used the finite amplitude loss technique (FALT), based on Eq. (5.44). The authors performed a transmission measurement, where the dependence of the received signal pressure  $P(z)$  on the intensity of the transmitted signal pressure  $P(0)$  was recorded at a fixed distance. When expressing the dependence of  $P(0)/P(z)$  via  $P(0)$ , they extracted  $\beta$  from the slope of this linear dependence. The authors discuss the trend of the FALT to yield values, higher than those acquired with the thermodynamic method (Sec. 5.3) and from light diffraction (Sec. 5.5.1.1). Even though limited to homogeneous media, the method is rather simple, requiring a pair of transducers with a similar resonance frequency. The internal consistency of the measurements was stated to be 10% [195].

**Echo-mode** Byra et al. [46] applied the lossless plane wave theory (Eq. (5.42)) to determine  $B/A$  of water. Typical for echo-mode imaging, it was assumed that the backscattered waves travelled linearly. The Verasonics research scanner (Verasonics, Inc.) equipped with a linear array probe L12-5 was used to image a set of reflecting wires positioned at different depths in water. By sending progressively increasing pressure values, the authors were able to observe a portion of the fundamental saturation (Fig. 5.12) and by fitting Eq. (5.42) to this curve extract water's  $\beta$ .

### 5.5.3.3 $B/A$ imaging

All  $B/A$  imaging works, based on registration of the fundamental amplitude, were performed in echo-mode. Iinuma [181] patented the approach of detecting fundamental saturation already in 1988, when utilizing an array transducer. A simple approximate equation was used to describe the received pressure  $P_{\text{rec}}$ , depending on the transmitted pressure  $P_{\text{trans}}$ :

$$P_{\text{rec}} = \frac{P_{\text{trans}}}{1 + aP_{\text{trans}}}, \quad (5.45)$$

where  $a$  is the parameter reflecting nonlinear effects, equal to 0 if nonlinear effects are absent.

Nikoonahad and Liu [278] utilized a similar approach. However, actual  $B/A$  values were determined and a single-frequency pulse was used. The authors utilized the approximate analytical solution to a nonlinear differential equation in terms of density fluctuations [375], determining  $B/A$  from the fundamental depletion of echoes as the source pressure was progressively increased. Diffraction effects were cancelled out by taking the ratio of two signals received at different source pressures. The theory was validated with simulations and an experimental measurement in ethylene glycol after a calibration procedure in water. The authors also showed in [277] that it was possible to resolve  $B/A$  of a phantom with heterogeneous liquid layers by taking track of the pulse's history and using a recursive algorithm. Nikoonahad and Liu [277] stated that the applicability of the method to tissue still had to be investigated, since the high viscous losses in tissue may not allow for sufficient fundamental depletion at safe pressure levels.

Aiming to enable real-time  $B/A$  assessment, Fatemi and Greenleaf [122] adapted the theory in [278], limiting the number of transmissions to two: one at a low amplitude in the linear regime, and another at a high amplitude with prominent nonlinear phenomena. The authors generated images in which shadows reflected nonlinearity of preceding regions, in a manner in which attenuation manifests itself on B-mode images, as well as relative  $B/A$  images. The authors imaged nonlinearity of ethanol and water, as well as fat-muscle structures, and tissue-water and tissue-contrast agent structures, concluding that the method can effectively identify regions of elevated nonlinearity.

In conclusion, several works utilizing the depletion of the fundamental to measure  $B/A$  have been presented. Utilizing the fundamental is practical, since in most pulse-echo systems the receiving transducer has a relative bandwidth of 50% - 70%, making it challenging to detect harmonics with a good SNR [122].

## 5.6 Parametric array

The concept of the parametric array was introduced to acoustics by Westervelt [406], stating that two collimated coaxial acoustic beams, approximated by plane waves, generate the sum and difference frequency waves (secondary waves). The secondary waves represent narrow

Table 5.6: Summary of parametric array works.

Study	Type of assessment, imaged parameter	Investigated media	Uncert., %
[268]	single measurement (for homogeneous media), $\frac{\beta}{\beta_{\text{ref}}}$ , tomography, $\frac{\beta}{\beta_{\text{ref}}}$	agar gel phantom	-
[9, 269]	tomography, $\beta$	phantoms with inclusions	-
[47]	<i>in silico</i> diffraction tomography, $\beta$	simulated weakly, moderately and strongly scattering objects	-
[431]	<i>in silico</i> tomography, $\beta$	simulated fluids, biological tissues	<1 ( <i>in silico</i> experiment)
[432]	tomography, $\beta$	tissue phantoms with water, porcine liver and fat, pathologic liver; boiled egg	10 (tissue)
[401]	reflection tomography, $\beta$	normal and pathological porcine liver	5 (tissue)
[15, 16]	single measurement (for homogeneous liquid media), $\beta$	ethanol, water	2-5 (liquid)
[21, 43]	tomography (noncollinear parametric interaction), variation of $\beta$	wool fibre, hoog fat in water	-

beams, whose amplitude is proportional to the parameter of nonlinearity  $\beta$  of the propagation medium and rises linearly with distance from the probe  $z_0$ :

$$P_s(z_0) = -\frac{S_0\omega_s^2}{4\pi\rho_0c_0^4}\beta P_1(0)P_2(0) \int_0^{z_0} \frac{\exp(-(\alpha_1 + \alpha_2)z - \alpha_s(z_0 - z))}{z_0 - z} dz. \quad (5.46)$$

Eq. (5.46) is intended for homogeneous media, where  $P_s$ ,  $\omega_s$  and  $\alpha_s$  are the pressure amplitude, angular frequency and attenuation coefficient of the secondary wave,  $P_1(0)$  and  $P_2(0)$  are amplitudes of primary beams at the source and  $\alpha_1$  and  $\alpha_2$  are their attenuation coefficients, and  $S_0$  is the beam cross-sectional area of the primary beams. The difference frequency wave undergoes lower attenuation compared to the sum component. Therefore, if two source frequencies are close to each other, the difference frequency wave is simpler to detect compared to the sum component. In the contrary situation, the sum component may be more favorable since  $P_s$  is proportional to  $\omega_s$ . Detection of the difference or sum frequency component provides a means of  $\beta$  measurement, called the parametric array method. The section below summarizes the evolution and progress made regarding its application. Table 5.6 presents all the identified works, utilizing the parametric array method to measure  $B/A$ .

The possibility of  $\beta$  measurement with the parametric array was first demonstrated in [268], when the finite amplitude and thermodynamic methods were already actively used and compared [229, 230]. In a configuration when a dual-frequency voltage pulse was transmitted by a transducer and detected by a hydrophone in a transmit-mode configuration, the authors estimated  $\beta$  of an agar gel phantom by comparing the amplitude of the difference frequency wave in water to that of an agar gel phantom. Here, attenuation effects were taken into account and  $\beta$  was estimated as an average uniform value. In the same paper, Nakagawa et al. [268] extended this method to CT using a conventional system (Fig. 5.8), generating the first CT images acquired with the parametric array method. This work was further continued in [269], confirming that attenuation and  $\beta$  images could be acquired with the proposed system and discovering that the estimation of attenuation was heavily influenced by refraction, causing errors in  $\beta$  reconstruction. Nakagawa et al. [268, 269] used the Westervelt equation to model the secondary wave propagation (Eq. (5.46)). Since an accurate estimation of  $S_0$

poses a problem, the  $\beta$  value can only be estimated when comparing the secondary wave sound pressure generated in the sample to that of a medium with a known  $\beta$ . Arnold et al. [9], Nakagawa et al. [269] simplified the analysis of the parametric array method by describing it with the Burger's equation (Eq. (5.10)) rather than the Lighthill's exact equation for arbitrary fluid motion used by Westervelt [406]. The solution of the Burgers equation for homogeneous media is:

$$P_s(z_0) = -\frac{\omega_s P_1(0) P_2(0)}{\rho_0 c_0^3} \beta z_0 \int_0^{z_0} \exp(-(\alpha_1 + \alpha_2)z - \alpha_s(z_0 - z)) dz. \quad (5.47)$$

This allowed for direct  $\beta$  reconstruction from the registered primary wave amplitudes, and estimated attenuation compensation. Just as for previous studies, the source of errors in primary wave data and the attenuation correction term were attributed to diffraction or refraction effects. Diffraction tomography was proposed as a solution to this problem. The possibilities of diffraction tomography were studied based on theory and simulations in [47], where the authors had to come back to the equation initially derived by Westervelt [406] to include the diffraction effect for weakly, moderately and strongly scattering objects. The presented simulations show the ability to reconstruct the  $\beta$  profile; however, these findings, to our knowledge, were not experimentally confirmed.

Another group [431] used Eq. (5.47) to express the secondary wave amplitude. However, they used the ratio of the secondary wave pressure amplitude after and before inserting the specimen as the projection data, adapting the insert substitution method introduced for the 2nd harmonic [152] to the parametric array method. They calculated the sound field produced by a piston source, representing the primary beams as a superposition of Gaussian beams. This way the authors, for the first time, demonstrated, based on theoretical analysis, that the amplitude of the difference frequency wave is nearly proportional to the distance from the source (reducing possible diffraction errors) and has no side lobes. For these reasons, they concluded that the parametric array method provides a better source to image  $\beta$ , granting higher resolution and higher accuracy, compared to the 2nd harmonic. The authors showed the feasibility of the proposed CT method for  $\beta$  imaging with computer simulations. A follow-up with experimental results was published in [432], confirming theoretical considerations regarding the secondary wave profile. CT images of phantoms with different  $\beta$  configurations, reasonably agreeing with previous  $\beta$  measurement results of other methods, were presented. The authors did not take diffraction effects into account, considering their influence reduced due to the stable rise of the difference frequency component, and the use of the finite amplitude insert substitution method. In [401], the group extended their work in [431] to reflection mode imaging, presenting the theoretical analysis and the developed imaging system. They used a compound transducer as a transmitter and receiver, recording the signals reflected from an aluminium plate located behind the sample of interest. The images showed promise, detecting a difference between healthy, fatty and hepatocirrhosis liver tissue. The same strategy was utilized in Gong et al. [153], acquiring the image of a three-layered medium in Fig. 5.13: porcine liver surrounded by porcine fat, submerged in water.

Barrière and Royer [15], Barrière and Royer [16] introduced a new setup for  $\beta$  measurement of liquid media. They showed that the interaction of two primary beams with a high frequency ratio ( $> 10$ ) is equivalent to the phase modulation of the high-frequency wave. In a configuration where the two source transducers are on opposite sides of the sample chamber, a low frequency pulse with a velocity potential  $\psi_2$  modulates a high frequency plane wave with a velocity potential  $\psi_1$ . An important contribution of this paper is the analysis of the diffraction effects, based on plane wave expansions. The authors showed that in the case of

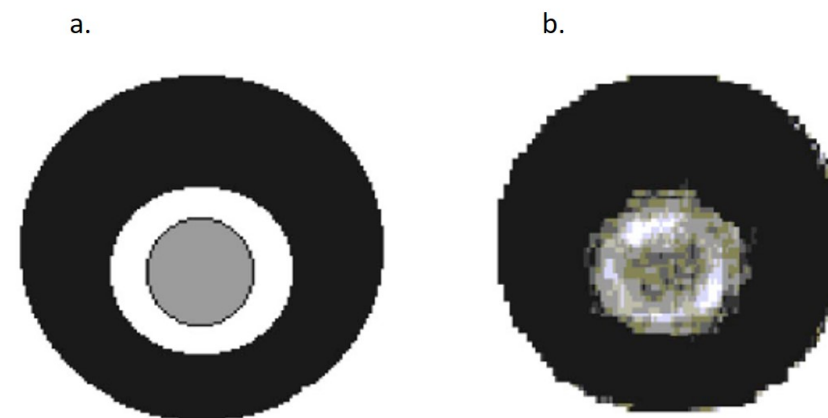


Figure 5.13: Reprinted from [153]. a. Model of the imaged media: porcine liver surrounded by porcine fat, submerged in water. b. The acquired reflection-mode tomographic image, utilizing the parametric array method.

two primary beams with a high frequency ratio ( $> 10$ ), the diffraction effect on the secondary wave is identical to that on the high frequency carrier wave. Therefore, since the presented method compares the amplitude of the secondary wave  $\psi_s(r)$  to the high frequency primary wave  $\psi_1(r)$  to extract  $\beta$ , the effect of diffraction is cancelled out. These observations were confirmed when the measured  $\beta$  values of water and ethanol showed good agreement with previously reported values. The authors also extend this methodology with a comparative method. In this case no calibration of the low frequency transducer is needed, and the relative amplitude to that in water is used. The authors state the uncertainty of their measurement to be within 5% for absolute measurements, and 2% when the comparative method is adapted.

[21, 43] is the only work, to our knowledge, that registers radiation of 2 plane waves intersecting at an angle (Fig. 5.14). The theory of such interaction is extensively treated in [165, 376]. Just as for the collinear case, nonlinearity results in generation of sum and difference frequency waves. However, in this case energy is scattered outside the region of primary wave interaction (Fig. 5.14), where it is described by the Westervelt equation. This approach allows for the reconstruction of the frequency components of the  $B/A$  distribution that depend on the orientation of the two sources and the receiver, as well as the transmit frequencies. To increase the range of reconstructed frequencies and decrease the number of required transducer configurations the authors transmit broadband signals. Moreover, these signals were encoded such that propagation delays for the coded signals were different and predictable in each coordinate of the medium. This way, each point scatterer radiated a specific coded signal proportional to  $\beta$ . The authors showed *in silico* and on *ex vivo* heterogeneous media (e.g., hog fat in water) that the high-frequency portion of  $B/A$  distribution can be reconstructed with only 3 transducers involved in the measurement (e.g., Fig. 5.14). In the case of multiple transducers where a sharp angle exists between 2 sources the reconstruction of absolute  $\beta$  values is also possible. Besides this, the system is also capable of measuring the speed of sound  $c$  distribution with no additional measurements. Differently, this work registered the sum frequency, rather than the difference frequency, since it allows for a registration of a wider band of frequency components of  $\beta$  [43]. What is more, the registered signals contain



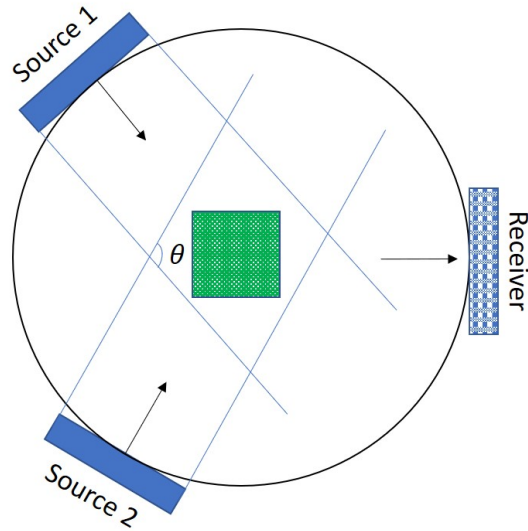


Figure 5.14: Schematic of the setup utilized in [43], registering ultrasound scattered by 2 plane waves at an angle.

information about the nonlinear parameter at a given location, unlike in case of previous parametric array works, and most FAM methods, which measure a cumulative signal.

Since the parametric array method allows generating frequencies much lower than the primary waves, most works based on Eqs. (5.46-5.47), neglect attenuation of the secondary waves  $\alpha_s$ . As demonstrated by [431, 432], when using collinear beams, the difference frequency waves rises almost linearly with distance from the source, making it easier to account for diffraction effects. Moreover, the secondary beam has no side lobes. Despite these advantages, it has been noticed in [440] that “nearly 40 dB in amplitude level difference exists between the primary waves and their difference-frequency wave”, making the SNR level rather low and its practical application difficult. Varray [392] noted that the length of the two transmitted pulses has to be sufficiently long for the generation of the secondary frequency components, setting a limitation to the resolution.

## 5.7 Pumping waves

Like the parametric array method, the pump wave method also exploits nonlinear effects produced when 2 plane waves interfere with each other. The principle of this technique is described best by the adiabatic dependence of speed of sound on  $B/A$  (Eq. (5.5)), already introduced for the thermodynamic method. Rearranging this equation with use of the linear relation between pressure and particle velocity  $P = \rho_0 c_0 u$  [165], we obtain

$$c = c_0 + \frac{B}{2A} \frac{\Delta P}{2\rho_0 c_0^2}. \quad (5.48)$$

One can now see how the speed of sound  $c$  changes with excess pressure  $\Delta P$ . Unlike in the thermodynamic method, Ichida et al. [179] created a variation in pressure  $\Delta P$  by transmitting

Table 5.7: Summary of works utilizing pumping waves to measure  $B/A$ .

Group	Study	Type of assessment, imaged parameter	Investigated media	Uncert., %
Classic pump wave technique	[179]	homogeneous, tomography, $B/A$	water; images of a fish, pig tissue in water, heated pig tissue	3 (liquid)
	[180]	tomography, $B/A$	liquid phantom with inclusions, human forearm	-
	[331]	tomography, $\frac{B/A}{2\rho_0 c_0^3}$	liquid phantom with inclusions, <i>in vivo</i> hamster	-
	[23, 200]	<i>in silico</i> tomography	heterogeneous phantoms of fluids, biological tissues	-
	[48]	theoretical basis of reflection-mode tomography, $B/A$	-	-
	[175]	<i>in silico</i> tomography, $B/A$	<i>in silico</i> phantoms with different 1D $B/A$ and attenuation profiles	-
	[49]	<i>in silico</i> reflection-mode and transmit tomography, $B/A$	<i>in silico</i> phantoms with different 1D $B/A$ profiles in lossless and attenuative media	-
	[196, 197]	homogeneous, heterogeneous 1D $B/A$ profiles	water, benzyn alcohol layer in water	-
SURF	[387]	echo-mode 2D imaging, temperature	temperature distribution in pig tissue and human abdominal tumor	20 (tissue)
	[143]	echo-mode 1D imaging, $B/A$	agar phantom, liquids, 2-layered liquid phantom	5 (liquid)
	[225]	echo-mode 2D imaging, $\beta_p = (1 + \frac{B}{A})k_s$	phantom with inclusions	-

a high-power beam (pump wave) perpendicular to the probe beam (Fig. 5.15, a.), modifying the speed of sound  $c$  and, therefore, the phase of the probe beam. By registering the modified phase of the probe wave, they extracted  $B/A$  and created the very first images of the coefficient of nonlinearity in history.

The pumping wave techniques are presented hereafter in two sections: the classic pump wave technique and the second-order ultrasound-field technique for echo-mode imaging (SURF). The main difference between these is that in the case of SURF, the probe wave has a much higher frequency than the pump wave. A summary of all the identified works in presented in Table 5.7 below. Note that pumping wave tomography corresponds to a line-by line reconstruction, where the image is formed by translating the probe transmit and receive transducers along one direction (Fig. 5.15, a). This is different from conventional tomography, used by FAM and the parametric array methods (Fig. 5.8).

### 5.7.1 Classic pump wave technique

In Ichida’s work [179], the low power narrow carrier beam (named “probe” beam) was received by another transducer after its modulation by the high-power low-frequency plane



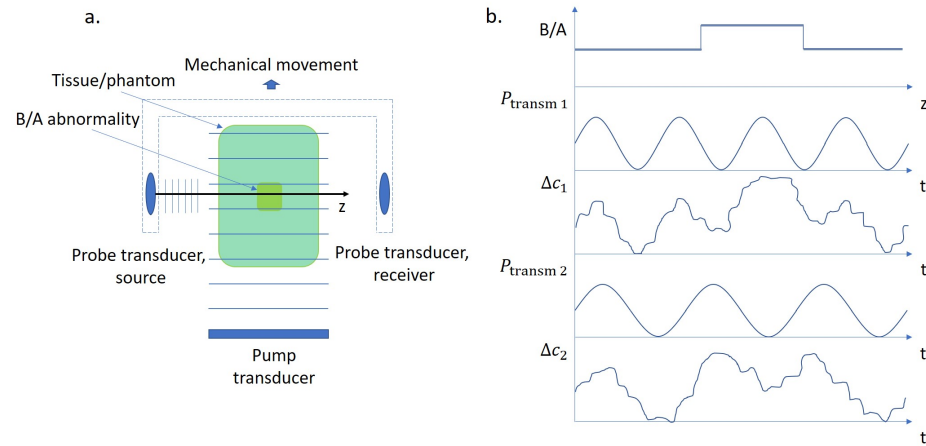


Figure 5.15: *a. Schematic of the first setup using pump waves, developed by [179]. b. A schematic illustration the speed of sound variation of the probe wave at points in space  $z$  with the given  $B/A$  when a pump wave is transmitted.  $\Delta c_1$  and  $\Delta c_2$  correspond to pump waves of different frequencies  $P_{\text{transm}1}$  and  $P_{\text{transm}2}$ , respectively.*

wave, referred to as the pump wave (Fig. 5.15, a). The pump wave was sufficiently broad to insonify the entire object. This way, assuming a homogeneous density  $\rho_0$  (Eq. (5.48)),  $B/A$  was the only parameter varying the speed of sound along the path of the probe beam. Figure 5.15, b illustrates the modulated variations of the speed of sound  $\Delta c_1$  and  $\Delta c_2$  that the probe wave experiences as it propagates through a medium with the demonstrated  $B/A$  profile when pump waves  $P_{\text{transm}1}$  and  $P_{\text{transm}2}$  of different frequencies were utilized, respectively. The authors showed that the phase shift  $\Delta\phi$  of the probe wave is the Fourier transform of the  $B/A$  distribution:

$$\Delta\phi\left(\frac{1}{\lambda_p}, z\right) = \frac{\pi}{\rho_0 c_0} \frac{P_p}{\lambda_c} \int_0^L B/A(z) \exp(j2\pi/\lambda_p) dz, \quad (5.49)$$

where  $z$  is the distance from the probe wave and  $L$  is the distance the probe wave travelled in the studied medium. Subscripts “p” and “c” indicate the pump and probe wave, correspondingly, with  $\lambda_p$  and  $\lambda_c$  the wavelengths of the pump and probe waves, respectively, and  $P_p$  the pump wave amplitude. This way, the phase shift was measured for several frequencies transmitted by the pumping wave; the corresponding Fourier coefficients were then calculated and the  $B/A$  profile was reconstructed. Mechanical movement of the carrier probe, allowed generating a 2D image line by line. Interestingly, the authors of this work observed a high  $B/A$  in muscle and bone, and low  $B/A$  of fat, contrary to the results of more recent measurements.

The previous scheme “required considerable time” [180] to acquire an image due to the frequency scanning of the pumping wave. A later modification [180] of the sinusoidal pumping wave to an impulsive pumping wave, containing many frequency components at once, allowed to make this method work in real-time. In a further modification [331], the location of the pumping wave was moved opposite the probe wave, next to the probe receiver (Fig. 5.16), allowing for a more compact and practical system. This configuration reduced  $B/A$  estimation errors due to distortion of the pumping wave’s front on the way to the probe beam due to inhomogeneous tissue attenuation. Moreover, another complementary acquisition where the probe and pump transducers were interchanged allowed for tissue attenuation compensation.

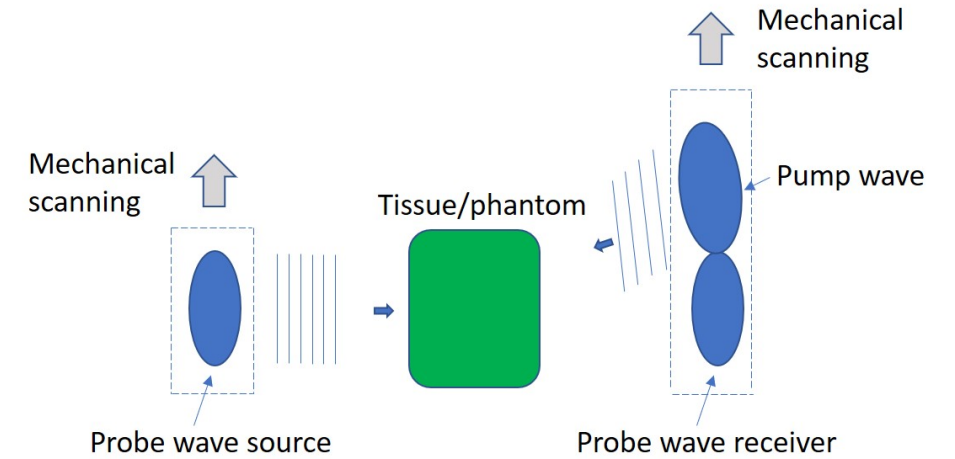


Figure 5.16: *The first setup sending the pump wave nearly coaxially to the probe beam, introduced by [331].*

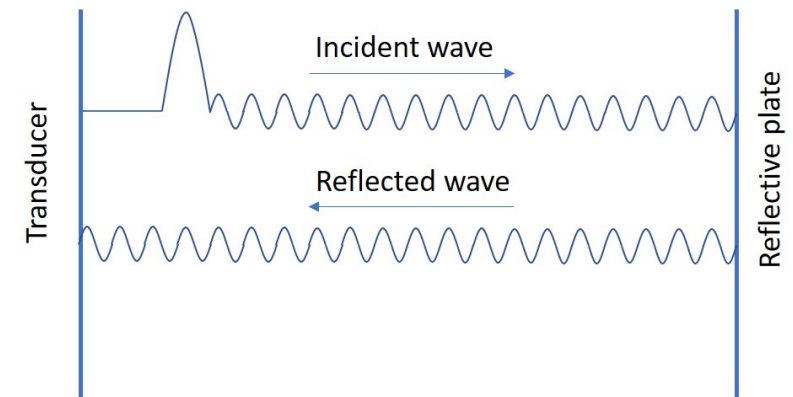


Figure 5.17: *Illustration of the pulse that enables  $B/A$  reflection imaging with the pump waves with a single transducer, presented in [48].*

Together, all the mentioned studies, performed by the same group, have acquired  $B/A$  images of phantoms, a fish, human arm, and a hamster *in vivo* [179, 180, 331].

Many further publication were devoted to improving the previously presented method in an *in silico* environment. Berkhout et al. [23], Kim et al. [200] showed that by additionally registering the frequency modulation of the signal one could also reconstruct the imaginary part of the Fourier components of the  $B/A$  distribution. These complete Fourier components acquired for a specific set of wave numbers showed superior quality of the  $B/A$  profile reconstruction. Cain [48] presented the theoretical basis for real-time  $B/A$  imaging in reflection mode, using only one transducer as a source of the probe wave, the pump wave and a receiver. The proposed transmit pulse consisted of two parts: a unipolar, high-pressure pump pulse coming right after the single-frequency, sinusoids probe wave (Fig. 5.17). The probe wave’s length equals twice the distance from the transducer to the reflector. This way, when the

pump pulse is just released from the transducer, the leading edge of the probe wave is in the same position, already back at the transducer surface, encountering the unipolar pump pulse. As the waves propagate, the pump pulse continues to interact with the reflected probe wave, producing phase changes, in other locations of the sample. Houshmand et al. [175] continued this work, and for the same configuration studied the quality of the  $B/A$  reconstruction when using different shapes of the pump pulse. Houshmand et al. [175] showed that broadband pulses provide the best estimates of the coefficient of nonlinearity, and that a chirp is a good option, providing a good  $B/A(z)$  estimate even for highly attenuating media. A following paper [49] focused on practical considerations suitable for both, reflection and transmit modes: the limitations regarding pump width and pump amplitude as well as attenuation and distortion of the pump pulse as it propagates. The authors showed that compensation for the former effects is possible for several configurations of the pump and probe wave pulses, enabling satisfactory reconstruction of  $B/A$  profiles when a single reflector is present at the end of the imaged  $B/A$  path. The authors noted that multiple reflections (*e.g.*, tissue) pose a strong challenge in reflection-mode imaging, since they interact with the pump wave, adding noise to the image. This challenge, to our knowledge, was never overcome in experimental work, with the classic pump wave technique.

Kato and Watanabe [196, 197] introduced the general case of nonlinear interaction between two plane waves intersecting at an angle  $\theta$  in a homogeneous medium [165, 376]:

$$\Delta c = u \cos \theta + \frac{P_p}{2\rho_0 c_0} \frac{B}{A}, \quad (5.50)$$

where  $u$  and  $P_p$  are the particle velocity and pressure of the pump wave, and  $\Delta c$  is the change in the probe wave's speed of sound. The equation above reduces to Eq. (5.48) in the perpendicular configuration used by the first pump wave work [179]. For the plane wave case ( $u = \frac{P_p}{\rho_0 c_0}$ ), in the phase domain we can derive

$$\Delta \phi = \frac{\omega_c}{c_0^2} \int_0^L \left( \cos \theta + \frac{1}{2} \frac{B}{A}(z) \right) u dz, \quad (5.51)$$

where  $\omega_c$  is the angular frequency of the probe wave and  $L$  is the interaction distance of the waves. Further, the authors showed that by registering the phase deviation of the probing wave  $\Delta \phi$  at intersection angles  $\theta = 0^\circ$  and  $\theta = 180^\circ$ , they were able to reconstruct the distribution of absolute  $B/A(z)$  values for a path consisting of water and benzyl alcohol layers. Kato and Watanabe [197] presents the influence of diffraction effects on the  $B/A$  measurement. The system included 2 probe sources at opposite sides of the specimen, limiting the method to tomographic applications.

It was well noted by [196] that the pump wave method exhibited a rather large number of simulation studies [23, 48, 49, 175, 200], and not so many experimental works [179, 180, 196, 331]. The authors attributed this to rather small and difficult to measure phase changes induced by the pump pulse. A broad pump pulse is favorable for inducing stronger phase changes. However, it also decreases image resolution. The current trade off poses a requirement for an intense and stable pump source.

### 5.7.2 Second order ultrasound field technique for echo-mode imaging

Second-order ultrasound field (SURF) imaging can be seen as the successor of the pump wave method. The main difference is in that the probe wave has a much higher frequency than the pump wave (*e.g.*, 2.5 MHz vs. 300 kHz [387]) and is superimposed on the probe wave at

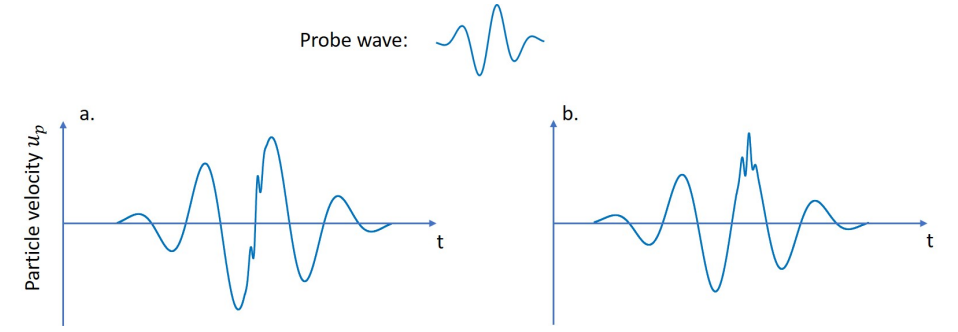


Figure 5.18: Examples of two configurations of pulse superposition used for the SURF method.

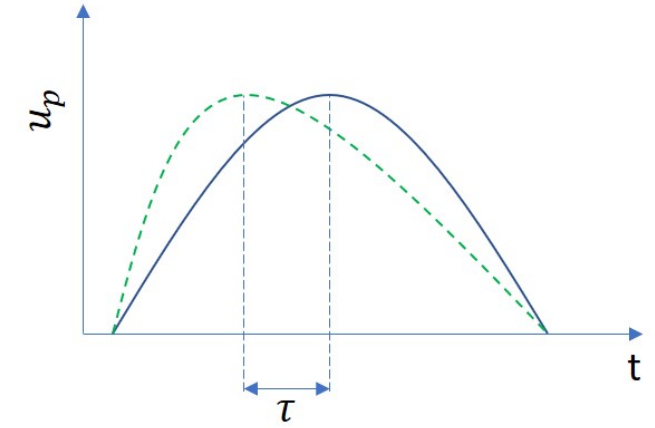


Figure 5.19: Illustration of the time delay  $\tau$  between the distorted nonlinear (dashed line) wave and the undistorted (solid line) wave.

a chosen phase interval. This requires a dual frequency source [143, 225], where the probe wave transducer also acts as a receiver in echo-mode. This technique requires two acquisitions with different configurations of the pulse superposition. For example, on Fig. 5.18, a and Fig. 5.18, b the probe wave is superimposed on the pump wave at the zero crossing of the particle velocity and at peak particle velocity, respectively. Given that the velocity at a point of an acoustic waveform can be expressed as [143, 225, 265]

$$v = c_0 + \left(\frac{B}{2A}\right)\left(\frac{\Delta P}{\rho_0 c_0}\right) + u, \quad (5.52)$$

where  $u$  is the particle velocity, a time delay  $\tau$  between the distorted and undistorted pump wave accumulates with:

$$\tau = L\left(\frac{1}{c_0} - \frac{1}{v}\right) = L\beta u / (c_0)^2, \quad (5.53)$$

proportionally to the travelled distance  $L$  (Fig. 5.19). Therefore, the high-frequency probe pulse also distorts, undergoing either compression or expansion (depending on the phase of the pump wave), resulting in a shift of its center frequency. Moreover, the pump wave profile is

affected by frequency-dependent attenuation, causing the center frequency of the pump wave to decrease with propagation. Fukukita et al. [143], Ueno et al. [387] showed that  $B/A$  and  $\alpha$  can be extracted from the ratio of the probe pulse spectra in two configurations of the probe wave superposition on the pump wave (Fig. 5.18). Moreover, since the frequencies of the detected probe pulses are close, the spectral ratio cancelled out scattering and diffraction effects. In their work, Fukukita et al. [143], Ueno et al. [387] performed  $B/A$  and  $\alpha$  measurement for several liquids, showing that  $B/A$  depth profiles for different liquid layers could be distinguished. In [387], *in vivo* images of the temperature distribution in pig tissue and a human abdominal tumor were inferred from measured  $B/A$  and attenuation. Unfortunately, no explicit images of  $B/A$  were provided.

Looking at Eq. (5.53) from another perspective, Kvam et al. [225] expressed  $v$  as

$$v = c_0(1 + (1 + \frac{B}{2A})k_s P_p) = c_0(1 + \beta k_s P_p), \quad (5.54)$$

substituting  $\frac{1}{A} = k_s = \frac{1}{\rho_0 c_0^2}$ , where  $k_s$  is the compressibility or the reverse of the bulk modulus  $1/\kappa_0$  and  $\beta k_s = \beta_p$  is the nonlinear bulk elasticity of the medium. Since in a realistic clinical setting, the density  $\rho_0$ , the compressibility  $k_s$  and speed of sound  $c_0$  are not known, the authors chose to measure the nonlinear bulk elasticity of the medium  $\beta_p$  rather than  $\beta$ . Inferring it from time delays  $\tau$ , they modified Eq. (5.53), describing the accumulated time delay  $\tau$  at point  $z_0$

$$\tau(z_0) = - \int_0^{z_0} \frac{\beta_p(z)}{c_0(z)} P_p(z) dz \quad (5.55)$$

for a plane wave probe pulse transmitted along  $z$ , superimposed with a positive phase of the pump wave, compared to that without a pump wave. The equation above neglects backward propagation delay, and is accurate for the case when signals reflected from a single scatterer are compared. However, in reality multiple scattering occurs, as well as random interference, side lobes, reverberation noise and refraction effects. Because of this, the authors chose not to infer the  $\beta_p$  variation from the derivative of  $\tau$  with respect to the receive time, which would amplify the variations, but rather fit a model based on Eq. (5.55) to estimate  $\beta_p$ . An image of the  $\beta_p$  of a tissue-mimicking phantom is demonstrated on Fig. 5.20. The estimation required knowledge of the pump wave field in space  $P_p(z)$ , inferred from a measurement in a water tank.

Since the method compares signals with similar frequency content, it is considered relatively insensitive to attenuation and diffraction effects. The contribution of this work is significant, since the method shows good contrast for an agar phantom with a corn oil inclusion *in silico* and *in vitro*, acquired with a linear 1D dual-frequency array. Besides this, Kvam et al. [224] found out that for most soft tissues the variability in  $B/A$  comes from the isentropic compressibility  $k_s = \frac{1}{A}$ .

## 5.8 Phase conjugate beams

Phase conjugate beams are time reversed beams, reradiated back to the source [81] (Fig. 5.21). An optical image of a reradiated phase-conjugate beam was presented in [39]. Phase conjugation provides the unique capability to compensate for phase distortion of the wave and achieves high-quality retrofocusing. Experimentally this was demonstrated when a focused beam was transmitted through an aberration layer with random surface variations, and in a nonlinear nondispersive medium with inhomogeneities [39, 308]. Since phase conjugation provides

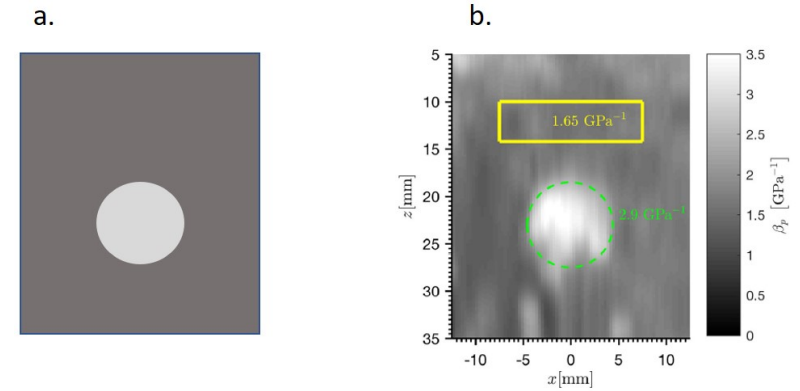


Figure 5.20: a. Schematic of an agar-based tissue-mimicking phantom with an inclusion filled with corn oil. b. Reprinted from [225]. The image of the phantom acquired with the SURF method.

amplification to the selected harmonic component (e.g., fundamental and 2nd harmonic), 2nd harmonic generation occurs during backwards propagation, allowing to register the 2nd or 4th harmonic of the transmitted signal. The registered higher harmonic amplitudes reflect  $B/A$ , and when the system is mechanically moved, it can produce C-scans (Fig. 5.21). Following this strategy, imaging of isoechogenic phantoms with heterogeneous  $B/A$  was proposed in [308], where the KZK equation was used to model wave propagation. Experimental images of isoechogenic liquid and liquid in gelatin phantoms [213, 309] provided good contrast, reflecting the  $B/A$  distribution when the 2nd and 4th harmonics were registered. The fundamental images reflected varying attenuation or reflection coefficients. No experimental images of tissues were acquired. Such a possibility remains unclear, since retrofocusing has been demonstrated for the nonlinear modes only for nondispersive media [308]. Diffraction effects can significantly deteriorate the quality of phase conjugation if the phase conjugator's diameter is too small [39].

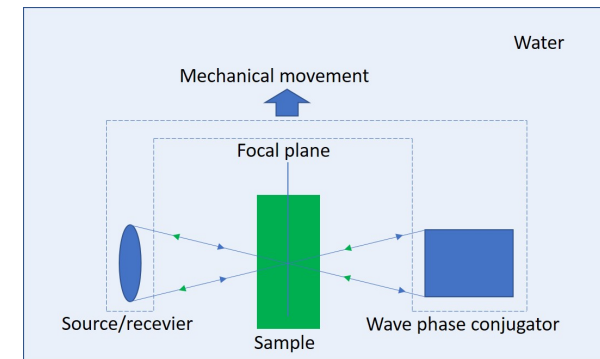


Figure 5.21: Typical phase conjugated beam setup. The arrows pointing to the right indicate the propagation of the originally transmitted signal, the arrows pointing to the left show the propagation of the phase conjugated beam.

5.9 Conclusions

The first attempts to measure  $B/A$  were made in the early sixties, when the finite amplitude [24, 350] and thermodynamic methods [24] were first proposed, almost simultaneously. The parametric array [268] and the pump wave methods [179] were developed next, making the method of aqueous solutions [329] and the phase conjugate method [308, 309] the last ones to emerge. Several papers were published, comparing the performance of some of these methods [9, 229, 230, 269, 431]. Table 5.8 summarizes the main principle of  $B/A$  measurement of all the techniques, their advantages and disadvantages, the reported range of uncertainties and whether or not experimental  $B/A$  images were acquired with the techniques. The latter possibility is particularly interesting in a clinical perspective, since visualizing heterogeneous  $B/A$  distributions gives the opportunity to localize suspicious tissue regions. It is worth mentioning that the data about measurement accuracy in Table 5.8 is rather unbalanced, since some methods were much more utilized and evaluated than others.

Table 5.8: Summary of the main  $B/A$  measurement techniques.

Method	Main principle	Advantages	Disadvantages	Uncert., %	Images
Traditional Thermo-dynamic. Sec. 5.3.1	$B/A$ is composed of 2 terms proportional to the speed of sound changes $\Delta c$ induced by an isobaric temperature change and isothermal pressure change (Eq. (5.12))	- accurate, attenuation does not pose a big problem - relatively insensitive to attenuation and diffraction effects	- requires knowledge of the isobaric volume coefficient of thermal expansion $\alpha$ and the specific heat at constant pressure $C_p$ - complicated setup	3 (liq), 5 (tis)	-
Isentropic Thermo-dynamic. Sec. 5.3.2	$B/A$ is proportional to the speed of sound changes $\Delta c$ when pressure is varied adiabatically (Eq. (5.4))	- accurate, attenuation does not pose a big problem - relatively insensitive to attenuation and diffraction effects	- requires a complicated setup	0.85-4 (liq), 7 (tis)	-
Aqueous solutions. Sec. 5.4	Differential method, measuring the influence of small concentrations on $B/A$ (Eq. (5.23))	- relatively insensitive to attenuation effects - small sample quantities - the most accurate method	- very specific, complicated setup	0.3 (liq)	-

The graph  $Uncert., \%$  states the range of errors identified in these groups of method. Looking at Tables 5.3, 5.4, 5.5, 5.6, 5.7 one can identify the works, where these uncertainties were taken from. In some cases, if the accuracy was not stated, errors were derived based on either the reference values provided in the corresponding papers, or  $B/A$  measured with the thermodynamic technique. In many cases, no information about the errors was available since the actual  $B/A$  was not known (e.g., self-made phantom,  $B/A$  images of a hamster, fish, etc).



Method	Main principle	Advantages	Disadvantages	Uncert., %	Images
Finite amplitude. Wave shape. Sec. 5.5.3	Determines $B/A$ from the US wave shape	- more accurate compared to other FAM variations	- light diffraction method: a complicated set up (a laser and an optical receiving system); - US equipment: transducer calibration and a broadband receiver required	7 - 8 (liq), 10 (tis)	-
Finite amplitude. 2nd harmonic measurements. Sec. 5.5.2	In most cases $B/A$ is determined from formulas based on the Fubini solution, modified to incorporate losses and diffraction effects Eq. (5.26 - 5.30)	- relatively low accuracy - affected by diffraction	- in some cases requires transducer calibration to estimate $P_1(0)$ - diffraction and attenuation corrections	2- 20 (liq), 3- 10 (tis)	tomography (e.g., Fig. 5.9), C-scans, echo-mode imaging (e.g., Fig. 5.10, 5.11)
Finite amplitude. Fundamental non-linear absorption. Sec. 5.5.3	Determines $B/A$ by measuring the fundamental saturation as source pressure is increased (Eq. (5.42), (5.44))	- calibration is needed only at the fundamental frequency - does not require a wide transducer bandwidth	- transducer calibration required	10 (liq), 6 (ph)	echo-mode imaging
Parametric array. Sec. 5.6	Measures the amplitude of the difference frequency wave that is proportional to $B/A$	- produces narrow, collimated beams - influenced less by diffraction effects - no side lobes	- the difference frequency beams have a low SNR - the length of source pulses has to be sufficiently long to generate secondary components	2- 5 (liq), 10 (tis)	tomography (e.g., Fig 5.13)

Method	Main principle	Advantages	Disadvantages	Uncert., %	Images
Classic pump wave. Sec. 5.7.1	Registers the phase modulation of the probe wave by the pump wave	- even in transmit mode, allows independent $B/A$ reconstruction along a single propagation line - not very sensitive to SNR since $B/A$ is inferred from phase modulation rather than pressure units	- in practice, requires a separate pump transducer	3 (liq)	tomography
Pump wave, SURF. Sec. 5.7.2	Registers the frequency shift or the time delay of the probe wave in two pulse configurations	- no diffraction correction needed - able to measure attenuation simultaneously	- in practice, requires a dual frequency transducer	5 (liq), 20 (tis)	echo-mode imaging (e.g., Fig. 5.20)
Phase conjugate beams. Sec. 5.8	Determines $B/A$ from higher harmonic amplitudes of the phase conjugated beam	- compensates for phase distortion (automatic retrofocusing) - the phase conjugator amplifies the signal	- reflects qualitative $B/A$ values - only for nondissipative/weakly dissipative media	-	C-scans

The main disadvantage of the thermodynamic method is in that it cannot be used for  $B/A$  imaging and requires an advanced and complicated setup. At the same time, it is an accurate technique, which can be considered “the golden standard”, establishing a reference to evaluate all the other methods. The method of aqueous solutions is the only technique that is more accurate [329], but it requires a specific minuscule chamber and involves more complicated calculations and more extensive knowledge about the sample parameters. Sarvazyan’s works, in line with others [342], indicated that  $B/A$  reflects the strength of solute-solvent interactions, and grants information about molecule hydration. Moreover, Sarvazyan et al. [329] observed that the replacement of an atomic group causes large changes in  $B/A$  concentration increment. These observations, together with a small sample volume, make this method a powerful option for molecular studies of biological samples. The absence of such tests may be explained by adequate alternatives currently applied in medicine, accurately detecting chemical content of human fluids [61, 90, 318]. Most of these methods have difficulty distinguishing isomers [61], while  $B/A$  is an excellent candidate for this task. Its utility for isomer distinction has already been demonstrated in [439] and may be of use when detecting early onset diabetes [61] and porphyria type [219].

In a situation when the pump wave and the probe wave propagate in the same direction, the parametric array method and pump wave method essentially merge [50]. In this review, we allot the technique to the parametric array method if  $B/A$  is inferred from the secondary wave pressure amplitude, and to the pump wave method when it is inferred through phase modulation of the probe wave. However, in the literature this allocation may be different (*e.g.*, SURF is regarded in [392] as a parametric array method). Moreover, as FAM, the parametric array, and the pump wave methods all measure cumulative nonlinear effects of US propagation, in some papers [196, 393] all three are associated to one group, referred to as FAM. In order to avoid confusion, here we refer to these three groups of methods as the extended finite amplitude methods (EFAM) for convenience. Even though the phase conjugate beam method is also based on harmonic accumulation, it is be treated separately.

The phase conjugate beam method is the most recent method, counting only a few works. Its great advantage resides in the automatic compensation for phase deviation caused by an inhomogeneous medium or irregular surface, characteristic of tissue. At the same time, it seems that phase conjugation is challenging for dissipative media like tissue, currently limiting this method to studies of liquid samples. Only qualitative characterization of the samples’ nonlinearity in conditions when the sample of interest has similar linear acoustic parameters as the reference medium, has been demonstrated at this point [213, 309].

For all EFAMS, with few exceptions, attenuation measurement at the transmitted and received frequencies is strongly linked with  $B/A$  measurement of a lossy medium. Another factor affecting wave propagation, and therefore relevant for all EFAMS, is diffraction. In transmit mode, the influence of diffraction can be mitigated by comparing the registered signal in the sample to that in a reference medium with a similar speed of sound, following the principle of the comparative method and the FAIS. Creative alternatives eliminating the need for diffraction correction also involve large source transducers (FAM) [60, 177, 184], or shifting of the diffraction pattern to the far field by attaching a steel delay line to the source [400], or measurements in the extreme near [227, 228] or far fields [76, 102, 203]. Since homogeneous EFAMS do not insonify the sample at high pressures, they can be suitable for *in vitro* assessment of organs for transplantation in transmission mode (*e.g.*, liver in [177]).

Of all EFAMS, FAM is the most extensive group with the largest number of subgroups and modifications. This is attributed to the method’s simplicity: it utilizes predominantly simple formulas within the framework of plane wave theory, and a simple setup with a source

transmitting monochromatic signals. No composite waveforms (parametric array) or additional pump wave transducers, or composite transducers (pump wave) are needed to induce the nonlinear effects. All EFAMs enable  $B/A$  tomographic imaging (Table 5.8). The first images were acquired with the pump wave method [179], reconstructing the  $B/A$  profile line-by-line. Later FAM and the parametric method were also used to obtain  $B/A$  images in transmit, based on multiple angle reconstruction tomography (Radon transform). Pump wave tomography, compared to parametric array and FAM tomography allows independent  $B/A$  reconstruction along a single propagation line without the contribution of other directions. This approach can result in real-time tomography [180], compared to reconstruction tomography. At the same time, reconstruction tomography allows improving the image resolution and quality due to numerous projections involved in the reconstruction process [51]. Parametric array tomography allows for better resolution, compared to FAM tomography (see Figs. 5.13, 5.9), since the generated beams at the sum and difference frequencies are narrower compared to the second harmonic beam [153, 401, 431]. As for pump wave tomography, the image resolution is defined by the frequency of the pump wave and the size of the probe beam [331]. This way, we expect the resolution of pump wave tomography to be lower than for the parametric array and FAM methods since the probe beam is formed by the transmitted fundamental component with a wider beam. Discrimination between healthy ( $B/A = 6.9$ ) and diseased liver ( $B/A = 8.3$ ) has been achieved with parametric array and FAM tomography [153], with even better image contrast for healthy liver and fat (Figs 5.13, 5.9). Unfortunately, all the pump wave tomographic works that we were able to identify showed rather poor quality images, dating to 1983-1985 [179, 331]. Therefore, it was difficult to compare pump wave tomography to the other types of tomography in this respect. Exceptionally, [21, 43] are the only works (the parametric array method), where  $B/A$  values were mapped to their specific locations by signal encoding.

Being a valuable asset, tomography still limits the exam to specific organs, such as the breast, and is rather time consuming for reconstruction. Paving the way for echo-mode imaging, several works have been devoted to reflection mode tomography, detecting the signals from a strong reflector on the side of the medium opposite from the source-receiver transducer (*e.g.*, [48, 153, 401]). However, this resulted in little improvement with respect to  $B/A$ ’s clinical applications.

Development to echo-mode imaging faced important challenges since the scatterer density distribution and echogenicity are the dominating factors influencing the strength of the reflected signal. Therefore, all echo-mode images were generated by limiting the scatterer effect by normalizing or comparing the signal of interest to a reference signal, assumed to have a similar scattering pattern. This strategy also has the benefit of mitigating diffraction and attenuation effects. Another common assumption in the echo-mode works is that the nonlinear effect in backwards propagation is neglected, since the amplitude of the reflected echoes is small compared to the forward propagating beam pressure (only for tissue, *e.g.*, not solids).  $B/A$  echo-mode imaging was implemented with FAM, 2nd harmonic measurements [3, 141, 153, 235, 378, 390, 394], Fundamental nonlinear absorption [122, 277, 278]) and SURF of the pump wave method [142, 143, 225, 387] (Table 5.9). Among these, Fukukita et al. [143], Nikoonahad and Liu [277, 278] were only able to image  $B/A$  of liquid layers detecting signals reflected from wires (single-point scatterers) and Akiyama [3], Fujii et al. [141], Fukukita et al. [143], Gong et al. [153], Liu et al. [235] showed average  $B/A$  tissue values only, or values detected at a fixed-depth region, limiting these works to a global, single-parameter assessment of organs (*e.g.*, fatty liver disease [141]).

The limited number of works presenting the  $B/A$  depth profile of tissue in their images

Table 5.9: Summary of the echo-mode methods implemented experimentally.

Method	Reference signal	Studied media	Probe
FAM. 2nd Harmonic measurements	- fundamental at 2 harmonic frequency $2f_0$ [3, 141, 153, 235]	- homogeneous liquids and homogeneous bovine liver [3], - homogeneous <i>in vivo</i> human liver [141] - homogeneous tissue [153, 235] <sup>1</sup>	- sector array transducer [141] - compound PZT [153, 235] - 2 transducers [3]
	- fundamental at $f_0$ [390]	- tissue-mimicking phantom with 2 layers	- Esaote LA332 commercial probe
	- 2nd harmonic in a reference medium [394]	- 2 tissue-mimicking phantoms: with an inclusion and with a contrast-agent filled cavity	- clinical probe
	- fundamental at $f_0$ and 2nd harmonic in a reference medium [377, 378]	- tissue-mimicking phantom with 3 layers	- commercial probe
FAM. Fundamental nonlinear absorption	- low amplitude signal at the same frequency	- liquid layers [277] - liquid layers and <i>in vitro</i> heterogeneous tissue [122]	- commercial Acuson linear array probe
Pumping waves. SURF	- the probe pulse superimposed at another phase of the pump wave	- liquid layers [143] - agar phantom with inclusion [225]	- dual frequency probe of 2 circular transducers [143] - dual-frequency linear array [225]

points to the observation that even the normalized signals, corrected for scatterer effects, show to be nevertheless noisy (*e.g.*, in [141],[377]). Tissue, being a structure full of point scatterers located close together, favors interference of scattered signals and multiple scattering [10], adding to the effects of grating lobes, reverberation noise [211], and electronic noise. Many presented approaches [3, 141, 153, 235, 390, 394] for assessment of the  $B/A$  depth profile involve differentiation of the normalized signal with respect to time or space, amplifying the noise. Differently, Kvam et al. [225] formulated an optimization problem, based on the expression of the measured time delay  $\tau$ , introducing penalties on the modelled process. Table 5.9 shows that the only works able to assess the in-depth profile of  $B/A$  (or of a proportional parameter) of tissue or tissue-mimicking phantoms in echo-mode are [122, 225, 378, 390, 394]. These demonstrate that current echo-mode imaging permits delineation of tissue-mimicking phantom regions with different oil content/contrast agent content [225, 378, 390, 394]. Fatemi and Greenleaf [122] were the only ones who performed  $B/A$  echo-mode imaging of heterogeneous tissues, where shadowing reflected the parameter of nonlinearity of the preceding regions. Echo-mode in-depth temperature profiles in tissue, inferred from  $B/A$ , have been demonstrated only in [387].

Interestingly, some debate regarding the utility of  $B/A$  for temperature monitoring still exists, with certain studies showing a small  $B/A$  increment when tissue is coagulated [184, 324], and others stating the contrary [66, 241]. Moreover, from another perspective, Gong et al. [153, 154] demonstrated that  $B/A$  was able to provide better discrimination of porcine liver tissue compared to attenuation, velocity  $c_0$  and density  $\rho_0$ , while Kvam et al. [224] concluded that for many soft tissues most of the estimated variability in  $B/A$  comes from variability in  $\frac{1}{A} = \rho_0 c_0$ . These controversial results indicate that more research is required to identify the boundaries of  $B/A$  applicability. Moreover, in our view, the utility of the thermodynamic technique and especially of the method for aqueous solutions may have been overlooked in biochemistry, molecular physics, and possible human fluid sample tests. Even though  $B/A$  can not be used to determine accurate and detailed chemical content of a substance, it is sensitive to structural change. Therefore, it would be particularly useful for assessment of structural

changes of the same substance [439] and has potential to diagnose diseases [61, 219] through identification of the isomer type in human fluids.

This review brings us to the conclusion that more research is required to reformulate the boundaries of  $B/A$  applicability, possibly dispelling some current hopes for clinical applications and bringing new opportunities. The thermodynamic technique and the method for aqueous solutions are the most accurate, the latter being especially useful for studies of small solute concentrations. Transmission mode EFAMS allow less accurate  $B/A$  estimation, but with a simpler setup and wider perspective clinical applications. They can be of use when assessing the condition of transplantation organs [177], or measuring  $B/A$  *in vivo* as a uniform parameter [141]. All EFAMS enable transmit tomography, limiting the exam to few clinical applications such as breast imaging. Development of an ultrasound  $B/A$  imaging modality is greatly hindered due to the fact that in echo-mode, the strength of the reflected signal is to a greater extent defined by the scatterer distribution and the variation of linear ultrasound parameters ( $c_0$ ,  $\rho_0$ ) than by  $B/A$ . Besides this, accurate imaging requires correction for diffraction effects, attenuation, various noise artifacts, and interference of signals coming from tissue scatterers. Strategies eliminating these effects would pave the way to  $B/A$  imaging in the clinic. Moreover, they may open new possibilities for imaging of the third-order nonlinear parameter  $C/A$  [44, 45, 234, 415].

# 6

## **The gFAIS method for $B/A$ measurement of tissues and liquids**

---



## 6.1 Section 1. *In – silico* validation

### Abstract:

The measurement of the parameter of nonlinearity  $B/A$  of tissues and liquids has potential to aid medical diagnosis. Therefore, accurate  $B/A$  measurement stays a relevant task. The finite amplitude insert-substitution (FAIS) method estimates  $B/A$  of biological tissues based on the measured 2nd harmonic in two configurations, (1) when only the reference medium is between the acoustic source and receiver, and (2) when the studied sample is inserted in the acoustic path with the reference medium. The generalised FAIS (gFAIS) has been previously proposed with the advantage of measuring  $B/A$  of liquids as well as ex-vivo tissues and allowing freedom in sample positioning. This simulations study validates the gFAIS method and provides insight into the practical choices for the setup that allow for an accurate measurement. Source and receiver size, distance between the source and the receiver and sample positioning have been studied on the subject of their effect on the measurement error for a homogeneous (modelling liquid) and a heterogeneous (modelling tissue) sample. Since  $B/A$  estimation also requires the measurement of the attenuation coefficients at the fundamental and 2nd harmonic frequency, practical choices for these measurements have also been studied.

From: A. Panfilova, R. J. G. Van Sloun, H. Wijkstra and M. Misch, “Simulation study on practical choices for  $B/A$  measurement by the generalized finite amplitude insert-substitution method”, *2021 IEEE International Ultrasonics Symposium (IUS)*, pp. 1-5, 2021, doi: 10.1109/IUS52206.2021.9593594

### 6.1.1 Introduction

The parameter of nonlinearity  $B/A$  reflects tissue and liquid structure and content.  $B/A$  tomographic images have shown good discrimination between hepatocarcinoma and healthy pig liver [153]. On a limited data set, it has been demonstrated that  $B/A$  of clear cell renal cell carcinoma is significantly greater than that of healthy tissue in the human kidney. From a different perspective,  $B/A$  differs among isomer types [439], granting potential to differentiate some diseases based on  $B/A$  measurement of biological liquids [219].

With several potential  $B/A$  applications only in the medical domain, accurate  $B/A$  measurement stays a relevant task. The original finite amplitude insert-substitution method (FAIS) has been used to measure  $B/A$  of *ex – vivo* tissues [152, 229]. This method requires the comparison of the 2nd harmonic amplitude generated in a reference medium (typically, water) between the acoustic source and the receiver, to that obtained when the medium under investigation is inserted in the reference medium (Fig. 6.1). Besides this, the attenuation coefficients at the fundamental frequency of the transmitted signal and at the 2nd harmonic must be measured, with the same setup. The original FAIS for lossy media was introduced for media with a nearly linear frequency dependence of attenuation, valid for tissues, but not most liquids [152]. It also assumed a sample position close to the receiver.

Recently, a new formula for  $B/A$  has been derived theoretically, suitable for media with arbitrary attenuation coefficients and sample position. In this work, we validate the proposed generalized FAIS (gFAIS) *in silico* for a homogeneous and heterogeneous sample with the k-Wave toolbox, Matlab. Besides this, we provide guidance in the practical choices that favor an accurate  $B/A$  measurement for such media, *i.e.*, source and receiver size, the distance between the source and the receiver, and sample positioning.

### 6.1.2 Methods

#### 6.1.2.1 Theoretical background and $B/A$ measurement strategy

The proposed gFAIS formula, presented in [289], reads:

$$\frac{1 + \frac{1}{2}(\frac{B}{A})_s}{1 + \frac{1}{2}(\frac{B}{A})_w} = \left( \frac{P_{2s}(f_0)}{P_{2w}(f_0)} - \frac{a}{L} D'' D' e^{-\alpha_s(2f_0)d} - e^{-2\alpha_s(f_0)d} (D'' D')^2 \frac{b}{L} \right) \times \frac{(\rho c^3)_s}{(\rho c^3)_w} \frac{2\alpha_s(f_0) - \alpha_s(2f_0)}{e^{-\alpha_s(2f_0)d} - e^{-2\alpha_s(f_0)d}} \frac{L}{D'^2 D''}, \quad (6.1)$$

where the subscripts “s” and “w” refer to the studied sample and water, respectively. Here  $D' = 2(\rho c)_w / [(\rho c)_s + (\rho c)_w]$  and  $D'' = 2(\rho c)_s / [(\rho c)_s + (\rho c)_w]$  are the pressure transmission coefficients from water to the sample and from the sample to water at normal incidence of the transmitted plane wave.  $L$  is the distance between the source and the receiver,  $a$  the distance between the source and the sample,  $d$  the sample thickness and  $b$  the distance from the sample to the receiver (Fig. 6.1).  $P_{2w}(f_0)$  and  $P_{2s}(f_0)$  are the 2nd harmonic components at frequency  $2f_0$ , generated in a pure water path between the source and the receiver (Fig. 6.1 (a)) and with the sample inserted, respectively (Fig. 6.1 (b)), when a signal at the fundamental frequency  $f_0$  is transmitted.  $\alpha_s(f_0)$  and  $\alpha_s(2f_0)$  are the medium attenuation coefficients at frequencies  $f_0$  and  $2f_0$ , respectively.

To estimate  $(B/A)_s$ , the parameters  $P_{2s}(f_0)$ ,  $P_{2w}(f_0)$ ,  $\alpha_s(f_0)$  and  $\alpha_s(2f_0)$  are measured with the acoustic setup, consisting of an aligned plane piston acoustic source and receiver (Fig. 6.1) [152, 289]. The rest of the parameters in Eq. 6.1 need to be determined separately. The

2nd harmonic amplitudes  $P_{2s}(f_0)$  and  $P_{2w}(f_0)$  are recorded when the signal at frequency  $f_0$  is transmitted, at a sufficient amplitude to induce 2nd harmonic generation, whereas harmonics higher than the 2nd are negligible [109, 290]. To measure the attenuation coefficients  $\alpha_s(f_0)$  and  $\alpha_s(2f_0)$ , the fundamental pressure amplitudes  $P_{1s}(f_0)$  and  $P_{1w}(f_0)$  at frequency  $f_0$  and  $P_{1s}(2f_0)$  and  $P_{1w}(2f_0)$  at frequency  $2f_0$  are acquired when the transmitted signal is of low acoustic pressure, in the nearly linear regime of ultrasound propagation [425].

In general, the sample attenuation coefficient at an arbitrary frequency  $f$  can be determined from

$$\alpha_s(f) = \alpha_0 f^q, \quad (6.2)$$

where  $q$  is the power law exponent, and  $\alpha_0$  is the power law prefactor, expressed in [dB/(MHz<sup>q</sup>cm)].

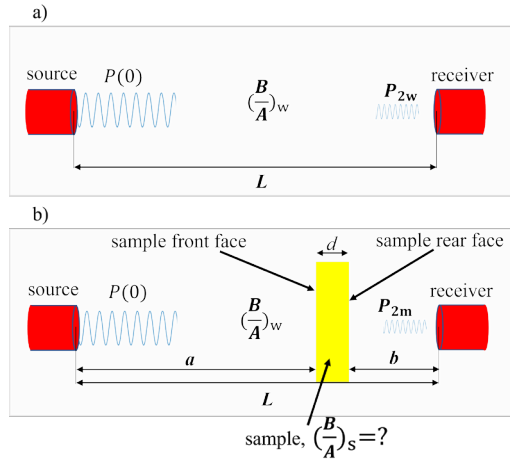


Figure 6.1: Schematic of the setup for  $B/A$  measurement with gFAIS, where  $(\frac{B}{A})_w$  and  $(\frac{B}{A})_s$  correspond to water and the studied medium, respectively;  $P(0)$  is the pressure amplitude of the transmitted monochromatic signal at the fundamental frequency  $f_0$ .  $P_{2w}(f_0)$  and  $P_{2s}(f_0)$  are the 2nd harmonic amplitudes without (a) and with (b) the sample in the acoustic path between the source and the receiver, respectively.

### 6.1.2.2 Simulations

Simulations of  $(B/A)_s$  measurement were performed in 3D space, using the open source toolbox k-Wave of Matlab [381, 402], modelling cumulative nonlinear propagation effects to the 2nd order [381].

This work simulates the measurement of  $(B/A)_s$ , and, consequently,  $\alpha_s(f_0)$  and  $\alpha_s(2f_0)$ . Other parameters in Eq. 6.1 are known (see the simulated medium properties in Table 6.2). For each of these measurements 2 simulations are needed: (1) in a reference medium, chosen to be water (Fig. 6.1 (a)), and (2) with the sample inserted in the reference medium (Fig. 6.1 (b)). This amounts to a total of 6 simulations required for  $(B/A)_s$  estimation. To measure  $\alpha_s(f_0)$  and  $\alpha_s(2f_0)$ , linear simulations were conducted, whereas the measurement of  $P_{2s}(f_0)$  and  $P_{2w}(f_0)$  required modelling of 2nd order nonlinear effects. In this work, we chose  $f_0 = 2.25$  MHz, close to that utilized in our experimental work [289].

The simulated space consisted of  $306 \times 306 \times 1320$  grid points, corresponding to dimensions of  $2.55 \times 2.55 \times 11.00$  cm<sup>3</sup>. The distance between the grid points was  $83 \mu\text{m}$ , corresponding to 8 point per wavelength (PPW) for the frequency of 2.25 MHz and 4 PPW for 4.5 MHz. A perfectly matched layer (PML) for absorbing the waves at all the edges of the simulated space was set outside of the computational grid and its thickness was fixed to 15 grid points. The number of grid points in each simulated dimension was chosen to obtain a number with small prime factors, reducing the computation time [402]. For the k-space operator, a reference speed of sound was taken by default, as the maximal speed of sound in every simulation, ensuring stability of the solution for all simulations. A temporal step of 16 ns was chosen, corresponding to a Courant-Friedrichs-Lewy (CFL) number of 0.3, advised in the k-Wave user manual as a tradeoff between the accuracy and computational speed of the solution. The simulations were run for 4731 time steps.

The circular additive pressure source was always located 120 points (1 cm) away from the border of the simulation domain (Fig. 6.2). The toneBurst and filterTimeSeries functions were utilized to create the transmitted pressure signal in time, i.e., a monochromatic 20-cycle pulse with a rectangular window and a ramp of 3 cycles, at a frequency  $f_0$  or  $2f_0$ , depending on the simulated measurement ( $\alpha_s(f_0)$  and  $P_2(f_0)$ , or  $\alpha_s(2f_0)$ ). All grid points corresponding to the source location emitted the same signal, simulating a circular piston transducer as the acoustic source. Two sources were simulated, with a radius of 6 and 12 mm, corresponding to common dimensions of single-element transducers. For both of these sources, several circular receivers with a radius of 12.5 mm were simulated parallel to the plane of the source, recording the pressure over time at the corresponding grid points. The receivers were placed 2.7 mm from each other. The receiver furthest from the source was located 120 points (1 cm) from the border of the simulation, 9 cm away from the source (Fig. 6.2).

Properties of density  $\rho$ , speed of sound  $c$ ,  $\alpha_0$ , and  $B/A$  (for the nonlinear simulations) needed to be assigned to every grid point in the simulation domain, whereas  $q$  could only be set for the whole simulation domain. No dispersion was simulated. The values for the reference medium were set to those of water (Table 6.2), assuming it lossless and setting  $q$  to 1.1, as for the simulated sample (Table 6.2). For both sources, two types of samples were simulated: homogeneous and heterogeneous. The homogeneous sample was assigned the acoustic properties of a porcine kidney (Table 6.2). The set  $\alpha_0$  and  $q$  resulted in  $\alpha_s(f_0 = 2.25 \text{ MHz}) = 1.22$  dB/cm and  $\alpha_s(2f_0 = 4.5 \text{ MHz}) = 2.61$  dB/cm. The heterogeneous sample was modelled by introducing a variation with a uniform distribution and a maximal amplitude of  $\pm 5\%$  of the homogeneous values of  $\rho_s$  and  $c_s$ , stated in Table 6.2, keeping the mean values equivalent to those of the homogeneous sample. Both  $\alpha_0$  and  $(B/A)_s$  were kept homogeneous. The thickness of the sample was always set to 1 cm, as shown in Fig. 6.2. For both sample types, 2 sample positions were simulated: (1) with the front face of the sample 1 cm away from the source, as illustrated in Fig. 6.2, and (2) 3 cm away from the source.

For all simulations, the function kspaceFirstOrder3D was utilized to simulate the pressure field. To reduce memory consumption and improve the computing speed, single precision mode was chosen (option 'Datacast' for kspaceFirstOrder3D). The computation time of one simulation consisted of about 40-42 hours, ran on a single computer server, utilizing the CPU.

For each source, 4 sample configurations were modelled (2 sample positions for both sample types), requiring a total of 12 simulations for the measurement of  $P_{2s}(f_0)$ ,  $P_{1s}(f_0)$  and  $P_{1s}(2f_0)$ . The reference measurement in water was the same for all these sample configurations, requiring 3 simulations for the measurement of  $P_{2w}(f_0)$ ,  $P_{1w}(f_0)$  and  $P_{1w}(2f_0)$ .

### 6.1.2.3 Data analysis

To retrieve the acoustic signal received by the receivers of different sizes (radii), the time-varying pressure signal at every grid point within the modelled radius was summed up in the time domain. To select the signal segment for the analysis, a threshold was set to 2% of the maximum pressure amplitude. The part of the signal between the first and last points with an amplitude closest to that of the threshold was selected and processed with the Fast Fourier Transform. Such an approach was chosen since in an experimental setting a threshold has to be set such that the signal is above the noise level. For the nonlinear simulations, the 2nd harmonic amplitudes  $P_{2w}(f_0)$  and  $P_{2s}(f_0)$  were extracted from the received signal. For the linear simulations, fundamental harmonic amplitudes were extracted:  $P_{1s}(f_0)$ ,  $P_{1w}(f_0)$  at fundamental frequency  $f_0$  and  $P_{1s}(2f_0)$ ,  $P_{1w}(2f_0)$  at fundamental frequency  $2f_0$ .

For each simulated configuration, receivers of radii 1 to 12 mm were simulated.

## 6.1.3 Results

### 6.1.3.1 Sample position 1

**Homogeneous sample** This section is devoted to the simulated measurement of  $(B/A)_s$ ,  $\alpha_s(f_0)$  and  $\alpha_s(2f_0)$  of the liquid sample in position (1), with its front face 1 cm away from the source (Fig. 6.2). The relative errors averaged over the whole simulated distance range  $L$  are

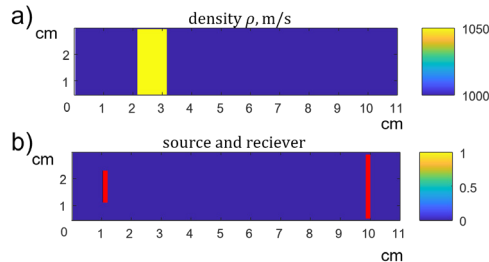


Figure 6.2: (a) The spacial distribution of density in the transverse plane of the simulated space, set for the sample in position 1, with the front face 1 cm away from the source. (b) The acoustic source, with a 12 mm diameter, and the furthest receiver from the source, with a 25 mm diameter.

Table 6.1: The simulated acoustic parameters of the reference medium (water) and of the studied medium (kidney).

Medium	$\alpha_0$ , dB/(cm MHz <sup>q</sup> )	$q$	$\rho$ , kg/m <sup>3</sup>	$c$ , m/s	$B/A$
kidney	0.5	1.1	1050	1560	7.1
water	0	1.1	1000	1500	5.2

The values of acoustic parameters were taken close to those in [428] for the kidney, and Ref. [364] for water. Water was assumed lossless and to have  $q = 1.1$  despite the true value of 2, since only one  $q$  value can be assigned to the whole computation domain in k-Wave.

referred to as  $\varepsilon_{\alpha_s(f_0)}$ ,  $\varepsilon_{\alpha_s(2f_0)}$  and  $\varepsilon_{B/A}$  for  $\alpha_s(f_0)$ ,  $\alpha_s(2f_0)$  and  $(B/A)_s$ , respectively. Figs. 6.3 (a-d) are devoted to the 6 mm-radius source, whereas Figs. 6.3 (e-g) to the 12 mm-radius source.

**6 mm radius source** Figs. 6.3 (a-c) demonstrate that when the receiver radius is 3 mm or greater, the measured parameters are close to the simulated values. Fig. 6.3 (d) shows that the accuracy of the measurement improves with the increasing receiver radius and saturates at a radius of 4 mm to around 5%, 6% and 15% for  $\alpha_s(f_0)$ ,  $\alpha_s(2f_0)$  and  $(B/A)_s$ , respectively. The smallest receiver yields the least accurate measurements of  $\alpha_s(f_0)$ ,  $\alpha_s(2f_0)$  and  $(B/A)_s$ , oscillating around the true value.

For receivers of 3 mm to 11 mm in radius, the measured attenuation coefficients  $\alpha_s(f_0)$ ,  $\alpha_s(2f_0)$  are accurate (error < 7%) at all distances  $L$ . It is of note that  $\alpha_1$  is measured with an error below 8% even for the smallest receiver when the receiver is located in the far field ( $L > \frac{fr^2}{c} = 5.4$  cm, where  $r$  is the source radius). The measurement of  $\alpha_s(2f_0)$  is limited to the near field and shows large errors for the smallest receiver, with values approaching the simulated values as  $L$  approaches the far field at 10.8 cm. The  $(B/A)_s$  measurement is more accurate in the near field, compared to the far field for all receivers. The focal point exhibits the most accurate  $(B/A)_s$  (error < 1%), whereas in the far field the errors grow with increasing  $L$ . For receivers  $\pm 3$  mm in radius, the error is below 16% in the near field.

**12 mm radius source** Figs. 6.3 (e-g) demonstrate that the measured  $\alpha_s(f_0)$ ,  $\alpha_s(2f_0)$  and  $(B/A)_s$  are more accurate and stable for larger receivers. Fig. 6.3 (j) shows a similar behavior to that of Fig. 6.3 (d), with the errors decreasing as the receiver size grows and saturating at a radius of about 6 mm with values in the range of 3-15%, 4-9%, 11-15% for  $\alpha_s(f_0)$ ,  $\alpha_s(2f_0)$  and  $(B/A)_s$ , respectively. For smaller receivers with a radius 1-3 mm, the curves in Figs. 6.3 (e-g) oscillate about the simulated values exhibiting maximal errors of 135%, 23%, and 242% for  $\alpha_s(f_0)$ ,  $\alpha_s(2f_0)$  and  $(B/A)_s$ , respectively. However, even for these receivers, the errors are smaller in the very near field at distances within 4 cm, corresponding to not more than 33%, 12% and 22% for  $\alpha_s(f_0)$ ,  $\alpha_s(2f_0)$  and  $(B/A)_s$ , respectively. All the measurements with this source were conducted in the near field.

**Heterogeneous sample** The simulated measurement of  $(B/A)_s$ ,  $\alpha_s(f_0)$  and  $\alpha_s(2f_0)$  of the heterogeneous sample, modelling tissue, is presented in Fig. 6.4 for the sample position (1). The results for the 12 mm-diameter source are presented in Figs. 6.4 (a-d) and for the 24 mm-diameter source in Figs. 6.4 (e-j).

**6 mm radius source** Figs. 6.4 (a-b) show that the measurement errors exhibit similar dependencies on receiver size and distance from the source to that for the homogeneous sample (Figs. 6.3 (a-d)). However,  $\alpha_s(f_0)$  is slightly overestimated and  $\alpha_s(2f_0)$  is greatly overestimated by all receivers.  $(B/A)_s$  starts decreasing away from the simulated value at a shorter  $L$  and a faster pace, compared to the homogeneous case. The errors  $\varepsilon_{\alpha_s(2f_0)}$  and  $\varepsilon_{B/A}$  are much greater compared to the homogeneous case (Fig. 6.3 (d)). However, at distances  $L < 4.5$  cm,  $(B/A)_s$  is measured within a 22% error for receivers  $\geq 3$  mm in radius, as for the homogeneous case.

**12 mm radius source** As for all previously described cases, the measurements presented in Figs. 6.3 (e-g) are more accurate for larger receivers.  $\alpha_s(f_0)$  and  $\alpha_s(2f_0)$  are overestimated by all receivers to essentially the same extent as the for the 6 mm source.

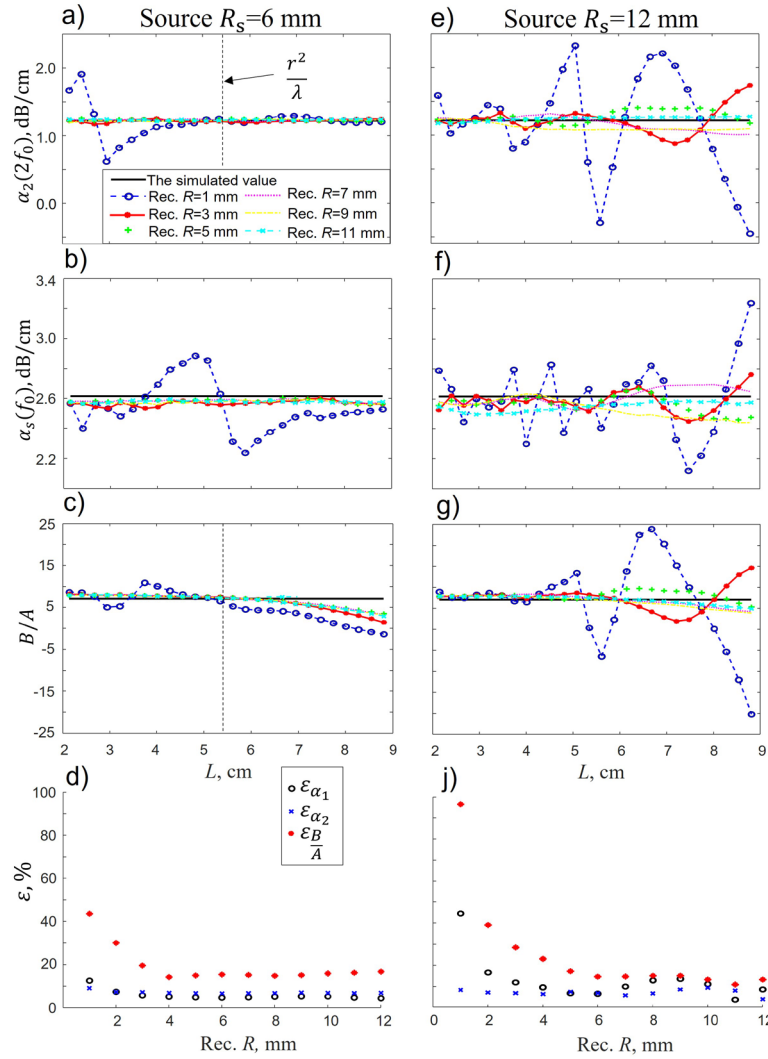


Figure 6.3: The measured acoustic parameters of the simulated liquid. Top to bottom: attenuation at the fundamental frequency  $f=2.25$  MHz  $\alpha_s(f_0)$ , attenuation at the 2nd harmonic frequency  $f=4.5$  MHz  $\alpha_s(2f_0)$ , the parameter of nonlinearity  $(B/A)_s$  and the relative errors  $\epsilon$ , averaged over the whole simulated distance range. The various markers correspond to different receiver sizes. The black horizontal thick line illustrates the simulated medium property. The vertical thin dash line indicates the focal distance for the fundamental frequency of the measurement. The plots in the left column correspond to a source radius of 6 mm, whereas in the right column to a source radius of 12 mm.

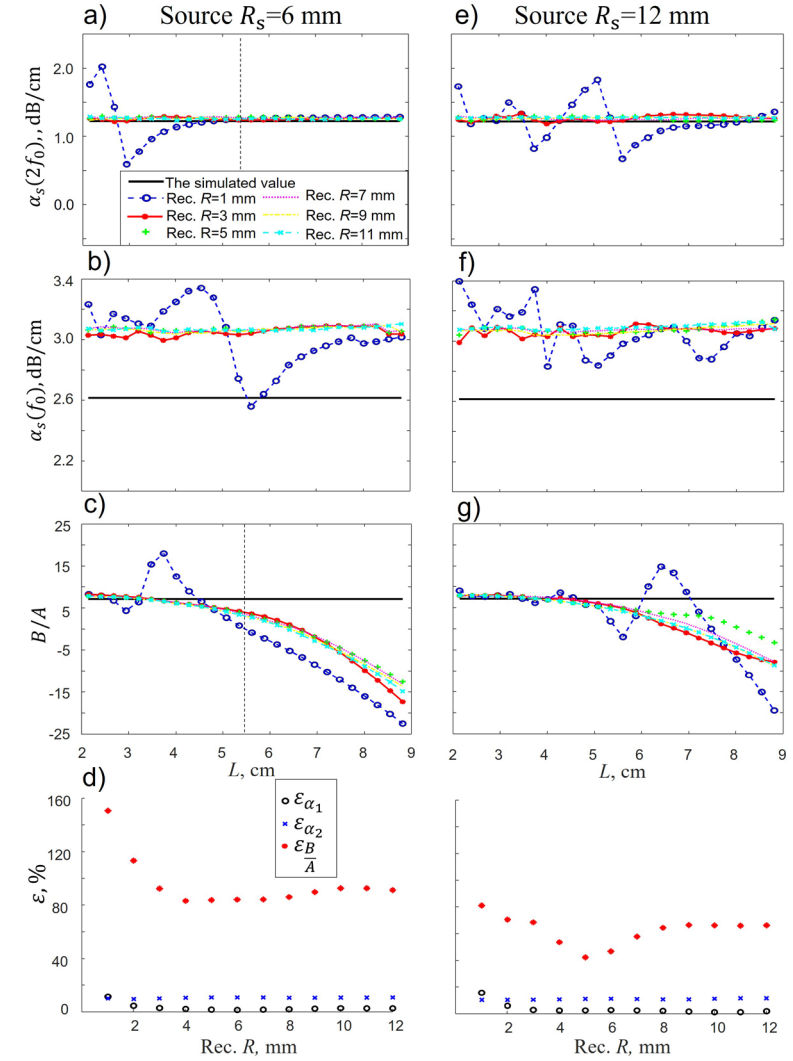


Figure 6.4: The measured acoustic parameters of the simulated tissue, top to bottom:  $\alpha_s(f_0)$ ,  $\alpha_s(2f_0)$ ,  $(B/A)_s$ , estimated based on Eq. 6.1, and  $\epsilon$ . The plots in the left column correspond to a source diameter of 12 mm, whereas in the right column to a source diameter of 24 mm.



In Fig. 6.3 (g), the measured  $(B/A)_s$  is accurate within 13% for receivers  $\geq 3$  mm in radius at  $L < 4.5$  cm. However, at further  $L$  the errors are greater than for the homogeneous medium.

Fig. 6.3 (j) shows that a larger source results in a more accurate  $B/A$  measurement, and similar errors for  $\alpha_s(2f_0)$  and  $\alpha_s(f_0)$  to those of a smaller source (Fig. 6.3 (d)).

### 6.1.3.2 Sample position 2

For both types of samples, shifting the sample results in essentially the same estimates, starting at  $L = 4$  cm.

### 6.1.4 Discussion and Conclusions

All the simulated measurements indicated that a shorter source-receiver separation distance favors a more accurate  $B/A$  measurement. A clear tendency was seen for the measurement accuracy to improve and saturate, once the receiver sizes were greater than a certain size. These observations are consistent with the plane wave approximation being valid at proximate distances to the source when larger receivers average out the diffraction pattern of the oscillating near field. A larger source provided a larger range of distances for an accurate  $B/A$  measurement, particularly appreciated for the heterogeneous tissue case, consistent with a longer near field for larger sources. Sample positioning did not affect the measurement accuracy.

Measurement accuracy for  $\alpha_s(2f_0)$  and  $\alpha_s(f_0)$  shows little dependence on source size, no dependence on sample position, and, for larger receivers, no significant dependence on the source-receiver separation distance. Small receivers ( $R < 2$  mm), *e.g.*, needle hydrophones, are not suitable for accurate measurement of the attenuation coefficient in the near field. It has been demonstrated for the heterogeneous case that the attenuation coefficient is slightly overestimated for 2.25 MHz and greatly overestimated for 4.5 MHz.

The presented results should be interpreted with care, since a heterogeneous speed of sound distribution (configuration b in Fig. 6.1) results in accumulating phase errors. Their magnitude is defined by the magnitude of the heterogeneities and the chosen time step. For the homogeneous sample, since  $\alpha_s(2f_0)$  and  $\alpha_s(f_0)$  are measured correctly (Figs. 6.3 (a-b) and (e-f)), it is unlikely that these computation phase errors significantly influenced the observed trends for the  $(B/A)_s$  measurement errors. However, in the most accurate scenario the  $(B/A)_s$  measurement the error constituted 10% in the near field, which is higher than claimed in some experimental works [152], the phase error of the nonlinear simulation and diffraction effects possibly contributing to this inaccuracy.

Since the heterogeneous sample introduces a greater range of the simulated speed of sound (1482 m/s to 1638 m/s), compared to the homogeneous sample, the phase error is expected to be greater, particularly, for the higher frequency of 4.5 MHz. To ensure validity of the derived conclusions for the heterogeneous simulations, a simulation was conducted for  $\alpha_s(2f_0)$  at a smaller time step of 12 ns, resulting in the same overestimated values. This additional result suggests that the greater  $\alpha_s(2f_0)$  is a result of phase cancellation effects concomitant to propagation through tissue with a heterogeneous speed of sound rather than computational errors. As observed in this work and in former experimental work [289], this effect grows for greater frequencies, since equivalent time delays result in greater phase delays for higher frequencies. It is of note that the  $(B/A)_s$  of tissue was estimated more accurately when the measured  $\alpha_s(2f_0)$  was utilized in Eq. 6.1, in comparison to the simulated  $\alpha_s(2f_0)$

value (results not shown). This suggests that the measured  $\alpha_s(2f_0)$  accounted for the phase cancellation effects of the accumulated 2nd harmonic.

The simulated media represented liquid and tissue in terms of homogeneity and heterogeneity, respectively. The power law exponent was equivalent in both cases, representative of tissues rather than liquids. A separate simulated experiment with corn oil in water, both given a power law exponent  $q = 2$  (results not shown) proved this aspect to be irrelevant for the conclusions derived for liquid samples. The chosen tissue model, on the other hand, was rather simple, containing no large inclusions, with randomly spread deviations from the density and speed of sound values stated in Table 6.2. Real tissue may be complex, and the conclusions of this work may not be applicable for highly heterogeneous tissue and/or with inclusions of altered acoustic properties.

The proposed work validated the gFAIS method for homogeneous and weakly heterogeneous media. It also provided practical advice on  $B/A$  measurement in aspects such as the source and receiver dimensions, their separation distance and sample positioning. In many aspects, the simulations modelled an “ideal” situation, *e.g.*, perfect angular and axial alignment of the source and the receiver, the sample faces parallel to the source and receiver faces. Care must be taken to fulfill these conditions when conducting the *ex vivo* experimental measurements.

## 6.2 Section 2. *Ex – vivo* validation

**Abstract:**  $B/A$  holds promise as a possible biomarker for tissue characterization. Moreover, measuring  $B/A$  enables identifying isomer types in biological liquids, potentially aiding diagnosis of some diseases. The standard finite amplitude insert-substitution method of measuring  $B/A$  has several limitations. It assumes a linear dependency of the attenuation coefficient on frequency, limiting it to tissue applications, and necessitates sample positioning close to the receiver. Here we propose the generalized finite amplitude insert-substitution method, which allows for  $B/A$  measurement of tissues and liquids, and gives great freedom in sample positioning. In this work, we present the derived formula and validate the experimental procedure. For this purpose,  $B/A$  measurements of corn oil, porcine fat and porcine liver were conducted. For each substance, several conditions were tested, including various distances between the source and the receiver, various sample positions and amplitudes of the transmitted pulses. A better agreement with literature data was found for lower source pressure amplitudes and distances within the near field of the source transducer. In these conditions, the measurement error was confined to 8% and 25% of the literature values of corn oil and the considered tissues, respectively. No clear indication of the influence of sample position on the measurement accuracy was found in this work.

From: A. Panfilova, X. Chen, R. J. G. van Sloun, H. Wijkstra, O. A. Sapozhnikov, and M. Mischi, “The generalized finite amplitude insert-substitution method for  $B/A$  measurement of tissues and liquids”, *Proc. Mtgs. Acoust.*, vol. 42, pp. 020001, 2020, doi: <https://doi.org/10.1121/2.0001439>

### 6.2.1 Introduction

$B/A$  has potential to provide insight for diagnostic tissue characterization [153, 401, 428]. Despite numerous works studying  $B/A$ 's utility for medical applications, multiple pathological conditions have not yet been investigated. For example, we were able to identify only two studies, measuring  $B/A$  of malignant tissues in comparison to healthy tissues [340, 341]. As for  $B/A$  of liquid biological samples, it may aid detection of early onset diabetes [61] and porphyria type [219] through identification of isomer type in human biological liquids. Therefore, development of accurate  $B/A$  measurement procedures is of clinical relevance. To facilitate this, we present the generalized finite amplitude insert-substitution method (GFAIS). Unlike the original finite amplitude insert-substitution method (FAIS), it allows measurement of samples with an arbitrary frequency dependence and gives great freedom of sample positioning between the source and receiver.

The FAIS [152, 349] method is one of the most common methods utilized for  $B/A$  measurement, since it only requires an acoustic source, a receiver and a cuvette to contain the investigated sample. It necessitates little sample volume and eliminates the need for a calibration procedure that converts received voltage signals to absolute pressure values. The method is based on the 2nd harmonic measurement in two configurations: (1) when the source and the receiver are submerged in a reference medium with a known  $B/A$  and (2) when the studied medium occupies a fraction of the acoustic path, as in Fig. 6.5. The original method developed for the measurement of  $B/A$  of lossy media [152] assumes that the investigated medium has a nearly linear frequency dependence of the attenuation coefficient. For this reason, it has been mainly utilized for  $B/A$  measurement of biological tissues. Since  $B/A$  reflects liquid content and molecular structure [329, 439], it may also be of use when analyzing biological liquid samples that can have a nearly quadratic frequency dependence of the attenuation coefficient. This motivates the development of a practical method that allows measuring  $B/A$  of liquids as well as tissues. Besides this, the original FAIS method proposes to set the sample close to the receiver, neglecting 2nd harmonic generation on the last part of the acoustic path. This imposes constraints on the cuvette geometry.

In this study, we derive a formula that takes into consideration 2nd harmonic generation on all parts of the acoustic path and makes no assumptions about the frequency dependence of the investigated specimen. The formula was validated when measuring  $B/A$  of corn oil, a slice of porcine liver and a slice of porcine fat. For this purpose, several conditions were tested, including various distances between the source and the receiver, various sample positions and amplitudes of the transmitted pulses. Such a broad spectrum of tested conditions allowed us to test the validity of the assumptions made when deriving the equation for  $B/A$  and to identify the most favorable experimental conditions for an accurate  $B/A$  derivation with the proposed equation.

### 6.2.2 Materials and methods

#### 6.2.2.1 Theoretical background

The finite amplitude insert-substitution method exploits cumulative 2nd harmonic generation [152, 349]. When an acoustic source emits a monochromatic wave at a frequency  $f$ , as this wave propagates, a signal at the 2nd harmonic frequency  $2f$  is accumulated. Its amplitude  $P_2(z)$  at a distance  $z$  from the source is proportional to the parameter of nonlinearity of the propagation medium, expressed by the lossy Fubini solution [374] for a plane wave propagating

in lossy media

$$P_2(z) = \frac{(2 + B/A)\pi f}{2\rho c^3} P_1^2(0) \frac{e^{-\alpha_2 z} - e^{-2\alpha_1 z}}{2\alpha_1 - \alpha_2}, \quad (6.3)$$

where  $B/A$  is the parameter of nonlinearity,  $\rho$  is the equilibrium density,  $c$  the small-signal speed of sound,  $P_1(0)$  the pressure amplitude at the source,  $\alpha_1$  and  $\alpha_2$  the attenuation coefficients at the fundamental  $f$  and 2nd harmonic  $2f$  frequencies, respectively [109]. This equation was derived assuming 3rd harmonic generation negligible and, therefore, is not suited for high source pressures.

If the 2nd harmonic is measured in water, whose  $B/A$  is well-known, and a second measurement is conducted when a sample with an unknown  $B/A$  is inserted in the path between the source and receiver (Fig. 6.5), one can determine the  $B/A$  of the studied medium from the ratio of the 2nd harmonics in these two configurations. Assuming that the 2nd harmonic contributions generated in various media add up linearly and assuming water to be lossless, one can derive the following formula:

$$\frac{1 + \frac{1}{2}(\frac{B}{A})_{\text{med}}}{1 + \frac{1}{2}(\frac{B}{A})_{\text{wat}}} = \left( \frac{P_{2\text{med}}}{P_{2\text{wat}}} - \frac{a}{L} D'' D' e^{-\alpha_{2\text{med}} d} - e^{-2\alpha_{1\text{med}} d} (D'' D')^2 \frac{b}{L} \right) \times \frac{(\rho c^3)_{\text{med}}}{(\rho c^3)_{\text{wat}}} \frac{2\alpha_{1\text{med}} - \alpha_{2\text{med}}}{e^{-\alpha_{2\text{med}} d} - e^{-2\alpha_{1\text{med}} d}} \frac{L}{D'^2 D''}, \quad (6.4)$$

where the subscripts “med” and “wat” refer to the studied medium and water, respectively. Here  $D' = 2(\rho c)_{\text{wat}}/[(\rho c)_{\text{med}} + (\rho c)_{\text{wat}}]$  and  $D'' = 2(\rho c)_{\text{med}}/[(\rho c)_{\text{med}} + (\rho c)_{\text{wat}}]$  are the pressure transmission coefficients from water to the sample and from the sample to water at normal incidence of the transmitted plane wave.  $L$  is the distance between the source and the receiver,  $a$  the distance between the source and the sample,  $d$  the sample thickness and  $b$  the distance from the sample to the receiver. As one can notice from Eq. 6.4, knowledge of the transmitted pressure  $P_1^2(0)$  is not necessary. Moreover, for a linear receiving system, the ratio  $P_{2\text{med}}/P_{2\text{wat}}$  is equal to the ratio of the received voltages  $V_{2\text{med}}/V_{2\text{wat}}$ .

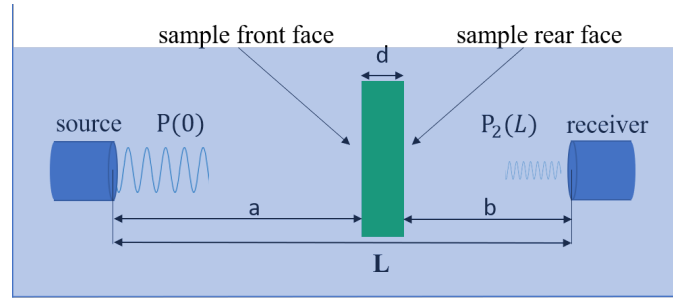


Figure 6.5: Schematic of the setup, submerged in water, utilized to measure  $\alpha_1$ ,  $\alpha_2$  and  $B/A$ . The reference measurement is conducted without the (green) sample between the source and the receiver.

### 6.2.2.2 Experimental procedure

The setup consisted of an acoustic source, a plane piston transducer 2.5 cm in diameter (C304-SU, 251 Olympus NDT Inc., Waltham, MA, USA), a receiver, a plane piston transducer 1.3

cm in diameter (V309, Panametrics-NDT, 251 Olympus NDT Inc., Waltham, MA, USA), and a cuvette that were all fixed on a rail system, ensuring their alignment. The cuvette was 3D printed (Fig. 6.6a). Its sides contained openings for rings that, when inserted, allowed to fix acoustically transparent 3-IN-1 FOLIE (Albert Hein B.V., Zaandam, The Netherlands) food film in place. The acoustically transparent film provided smooth surfaces of the investigated sample, perpendicular to the beam propagation direction.

The US acquisition was controlled via dedicated software written in Labview (National Instruments Corp., Austin, TX, USA) and implemented in a desktop. The driving signals were generated by a 33220A arbitrary wave generator (Agilent Technologies, Santa Clara, USA), further transmitted to a 50-dB 2100L RF Power amplifier (Acquitek, Massy, France). The amplified signals were transmitted to the source transducer. In all cases, these were sinusoidal 20-cycle tone bursts with a rectangular window. This pulse length provided a sufficiently narrow bandwidth of the transmitted signals and, therefore, allowed preventing overlap between the harmonics in the spectrum of the received signal. The silence period between the pulses was always set to 250 microseconds, chosen to prevent interference of any possible reflections. A total of 92-95 pulses was transmitted at every acquisition. The received signals were displayed on a TDS2014 oscilloscope (Tektronix U.K. Limited, Bracknell, UK) and sampled throughout an NI-5122 (National Instruments Corp.) acquisition board which was connected back to the desktop. The signals were recorded at a sampling frequency of 25 MHz and saved for off-line analysis.

To estimate  $B/A$ , the following parameters are required: distances  $a$ ,  $b$ ,  $d$ , densities  $\rho_{\text{med}}$  and  $\rho_{\text{wat}}$ , speed of sound  $c_{\text{med}}$  and  $c_{\text{wat}}$ , the attenuation coefficients  $\alpha_{1\text{med}}$  and  $\alpha_{2\text{med}}$ , and 2nd harmonic amplitudes  $V_{2\text{med}}$ ,  $V_{2\text{wat}}$  (see Eq. 6.4). The distances  $a$  and  $b$  were measured with a caliper, while  $d$  was always taken as 1 cm, equal to the fixed cuvette length. The densities and speed of sound were taken from the literature (Table 6.2). The rest of the parameters were measured with three through-transmission measurements, utilizing the described setup. The attenuation coefficients  $\alpha_{1\text{med}}$  and  $\alpha_{2\text{med}}$  were measured when transmitting a low-amplitude pulse of 0.01 V to the source at its center frequency (2.25 MHz) and its potential 2nd harmonic frequency (4.5 MHz), respectively. Typically, accurate attenuation measurements require low amplitude pulses to prevent energy loss at the fundamental due to higher harmonic generation [425].  $V_{2\text{med}}$ ,  $V_{2\text{wat}}$  were measured when a high-amplitude pulse was transmitted at 2.25 MHz, resulting in 2nd harmonic generation. Since the validity of Eq. 6.3 is dependant on the source pressure amplitude, several high-amplitude acquisitions were performed, transmitting signals of 0.1, 0.2, 0.3, 0.4, 0.5, 0.6 and 0.7 V to the source transducer. A  $B/A$  estimate was computed for each of these amplitudes.

For the measurement, the setup was submerged in a tank filled with degassed water at room temperature. Since the advantage of the FAIS methods is that no source calibration is required,

Table 6.2: Literature values of the acoustic parameters of the studied media.

Medium	$\alpha_{1\text{med}}$ , dB/cm	$\alpha_{2\text{med}}$ , dB/cm	$\rho_{\text{med}}$ , kg/m <sup>3</sup>	$c_{\text{med}}$ , m/s	$B/A$
Corn oil	0.3	1.2	920	1466	10.5
Por. liver	1.2	2.1	1050	1611	6.3
Por. fat	1.0	2.2	970	1460	10.8
Water	0	0	1000	1509	5.2

The values of acoustic parameters were taken from Ref. [102] for corn oil, from Ref. [152] for tissues (porcine liver and fat), and Ref. [230] for water. Water is assumed lossless.



no such procedure was performed. The distance between the source and the receiver was set to one of the four tested distances: 4, 5, 6 or 7 cm. These distances were chosen to ensure sufficient space between the source and the receiver and, therefore, a convenient positioning of the cuvette inbetween. At the same time, the plane wave approximation is valid in the proximity of the source [265], so further distances were not studied. A first acquisition without the sample registered the signals received from the transmission of 2 low-amplitude pulses and 7 high-amplitude pulses, as described above. Then the investigated sample was fixed at one of the three positions between the source and the receiver (Fig. 6.5): close to the source (with its front face 0.5 cm away from the source), in the middle between the source and the receiver, and close to the receiver (with its rear face 0.5 cm away from the receiver). Corn oil could be poured directly in the cuvette when the thin food film was still fixed on one side only. Since it was difficult to cut tissue samples with smooth side surfaces, tissue was frozen to increase its stiffness prior to the slicing procedure, and a dedicated device (Fig. 6.6b) was utilized to cut it in slices of homogeneous thickness with parallel sides. As the cuvette was 1 cm thick, the prepared tissue slices were 1 cm thick. Further, they were degassed in a degassing chamber with saline for 40 minutes. After degassing, they were fixed in the cuvette. This procedure was performed under water to avoid trapping air bubbles. The thin film provided further correction for possible thickness inhomogeneities during the slicing procedure. Once the investigated sample was positioned, the acquisition was repeated as for the pure water path. The sample was then moved to the next position between the source and the receiver and the acquisition was repeated again.

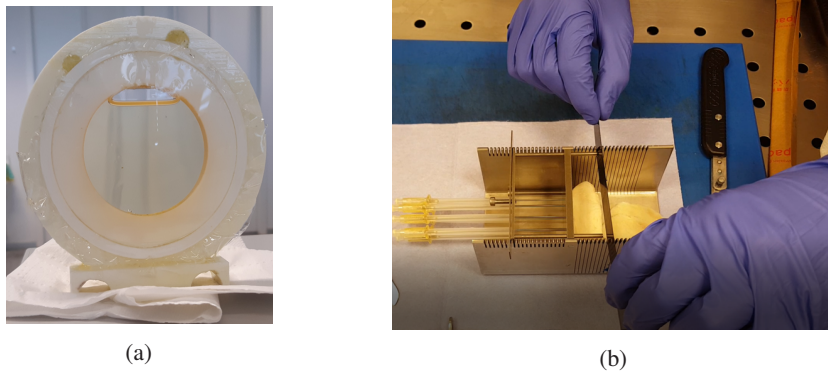


Figure 6.6: (a) The cuvette utilized for all samples. The outer rings are inserted in the cuvette opening to hold the food film tight. (b) The device utilized to cut tissue into slices with smooth parallel sides. The needles hold the tissue phantom in place, while the blade is inserted in steel openings perpendicular to the bottom of the device.

### 6.2.2.3 Data analysis

Data analysis was performed in MATLAB<sup>®</sup> (The MathWorks, Inc., Natick, MA, USA). The beginning of every pulse in each acquisition was identified, and the central segment of the pulse with a stable amplitude was selected. For attenuation measurements, the central segment of every pulse was directly processed by the Fast Fourier Transform. The average Fourier spectrum among all pulses in an acquisition was calculated and the fundamental harmonic component was extracted from it. With the amplitude of the fundamental component for

the pure water path  $V_{\text{wat},f,2f}$  and for the path with the sample  $V_{\text{med},f,2f}$ , and the pressure transmission coefficient  $T$  accounting for two transmission boundaries (water-sample, sample-water), the attenuation coefficients were calculated as

$$\alpha_{f,2f} = \frac{20}{d} \log_{10} \left( T \frac{V_{\text{wat},f,2f}}{V_{\text{med},f,2f}} \right), \quad (6.5)$$

for frequencies  $f=2.25$  MHz and  $2f=4.5$  MHz, respectively. As for the high-amplitude pulses transmitted to record 2nd harmonics  $V_{2\text{med}}, V_{2\text{wat}}$  (Eq. 6.4), a Hanning window was applied to the central part of the pulses and an average Fourier spectrum of the resulting signals was calculated. The Hanning window minimized spectral leakage from the strong fundamental component to the weaker 2nd harmonic [157]. The 2nd harmonic component of the average Fourier spectrum was extracted to compute  $V_{2\text{med}}/V_{2\text{wat}}$  for every tested amplitude.

### 6.2.3 Results

The measured  $\alpha_{1\text{med}}, \alpha_{2\text{med}}$  and  $V_{2\text{med}}/V_{2\text{wat}}$  for corn oil are presented in Fig. 6.7 for various distances between the source and the receiver  $L$ , as well as sample positions. Colors encode different transmitted amplitudes of the high-pressure pulses inducing 2nd harmonic generation. The measured parameters demonstrated in Fig. 6.7 were inserted in Eq. 6.3 to extract  $B/A$  for the tested experimental conditions. The resulting  $B/A$  estimation is demonstrated in Fig. 6.8.

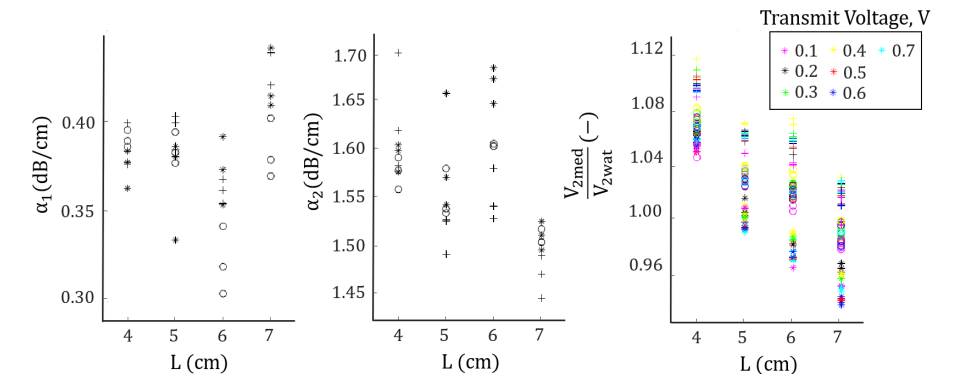


Figure 6.7: The attenuation coefficients at the fundamental  $\alpha_{1\text{med}}$  and 2nd harmonic  $\alpha_{2\text{med}}$  and the ratio of 2nd harmonic amplitudes  $V_{2\text{med}}/V_{2\text{ref}}$  for corn oil. The measurements were conducted at several distances between the source and the receiver  $L$  and various sample positions: + (close to the source: sample front face 0.5 away from the receiver), \* (close to the receiver: sample rear face 0.5 cm away from the receiver), o (in the middle). Colors for  $V_{2\text{med}}/V_{2\text{ref}}$  measurement encode different amplitudes, transmitted to the source.

From Fig. 6.7, one can see that the measured attenuation coefficients are slightly greater than the literature values for corn oil (Table 6.2), especially at the 2nd harmonic frequency. Despite this, there is good agreement between the measured  $B/A$  values and the literature value of 10.5. The standard deviation at the largest distance between the source and the receiver is appreciably greater, compared to shorter distances. We hypothesize that the plane wave approximation is no longer valid at this distance. If we assume that the effective radius of our source is equal to its geometrical radius  $r$ , the near field where the plane wave approximation is valid is up to about  $0.3 * \frac{r^2 f}{c} = 7$  cm away from the source (Fig. 9 in [265], page 354),



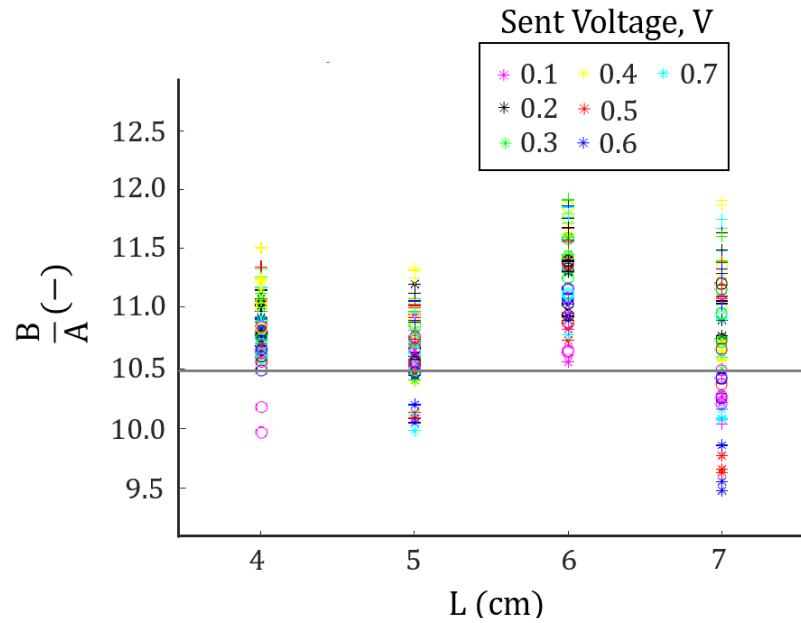


Figure 6.8: The measured  $B/A$  for corn oil at various distances between the source and the receiver  $L$ , at various amplitudes and different sample positions: + (close to the source), \* (close to the receiver), o (in the middle). The thick gray line indicates the literature value of 10.5.

making the distance of 7 cm the threshold value, less appropriate for an accurate measurement. Despite this, the error is within 6% of the literature value for the lowest transmitted amplitude of 0.1 V at all source-receiver separation distances.

No consistent influence of the amplitude of the high-amplitude pulses on  $B/A$  accuracy was noticed (Table 6.3). However, when averaged over all experimental configurations, the lowest amplitude demonstrated the best agreement with the literature values. In fact, when visually inspecting the spectra of the acquired signals in water, already at the shortest distance

Table 6.3: Mean  $B/A$  for different voltages transmitted to the source.

Medium \ Volts	0.1	0.2	0.3	0.4	0.5	0.6	0.7	Ref.
Corn oil	10.7	11.0	11.1	11.3	10.8	10.8	10.9	10.5 <sup>a</sup>
Porcine liver	-	6.4	6.7	6.8	5.3	5.9	5.9	6.3 <sup>b</sup> , 6.8 <sup>c</sup>
Porcine fat	-	11.9	12.6	13.3	13.3	13.7	13.2	9.1 <sup>b</sup> , 10.8 <sup>c</sup>

<sup>a</sup> see Ref. [116]

<sup>b</sup> Ref. [430]

<sup>c</sup> Ref. [153]

The presented  $B/A$  values were averaged among all measurements conducted at different source-receiver separation distances and sample positions. The voltage is stated in brackets, in volts.

of 4 cm and at a transmitting amplitude of 0.3 V, a 3rd harmonic component arises, constituting 25% of the 2nd harmonic amplitude. This brings us to the conclusion that sonicating amplitudes of 0.3 V and greater should already lead to an overestimation of  $B/A$ . Looking at Table 6.3, we see that the amplitudes of 0.3-0.4 V yield larger  $B/A$  values for all studied samples, compared to lower amplitudes. Interestingly, the values decrease for amplitudes higher than 0.4 V, which may indicate a nonlinear conversion factor in the receiver, i.e. in the electromechanical conversion between pressure and voltage.

Sample positions close to the source yield greater values than those close to the receiver. However, for the lowest amplitude, the estimated  $B/A$  values are nearly equivalent.

The measured  $\alpha_{1med}$ ,  $\alpha_{2med}$  and  $V_{2med}/V_{2ref}$  for porcine liver and porcine fat are shown on Fig. 6.9 and 6.10, respectively. No measurement was conducted for  $L = 7$  cm, as it was expected to yield even more variation in  $B/A$  of inherently inhomogeneous tissues. The amplitude of 0.1 V is not presented on these graphs, since the signal-to-noise ratio of the 2nd harmonic signal was too low for an accurate  $B/A$  estimation.

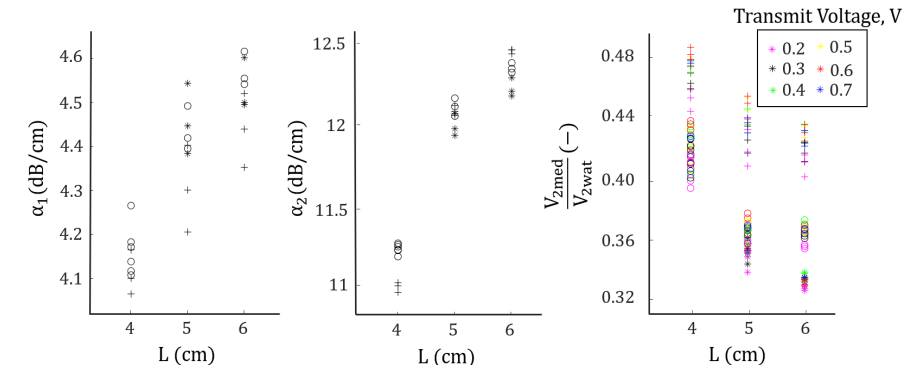


Figure 6.9: The attenuation coefficients at the fundamental  $\alpha_{1med}$  and 2nd harmonic  $\alpha_{2med}$  and the ratio of 2nd harmonic amplitudes  $V_{2med}/V_{2ref}$  for porcine fat. The measurements were conducted at several distances between the source and the receiver  $L$  and various sample positions: + (close to the source), \* (close to the receiver), o (in the middle). Colors for  $V_{2med}/V_{2ref}$  measurement encode different amplitudes, transmitted to the source.

From these graphs, one can notice that the measured attenuation coefficients are overestimated, compared to the literature values, most prominently for fat. For both tissue samples, overestimation is greater for 4.5 MHz, compared to 2.25 MHz. We hypothesize that this occurs due to greater phase-cancellation effects at higher frequencies. Phase-cancellation is much more prominent for tissues, compared to liquids, as tissues have intrinsic inhomogeneities in the speed of sound [324], leading to different arrival times for different beam portions. There is great variation in the measured attenuation coefficients of porcine liver among different source-receiver separation distances.

Despite the variation and inaccuracies in the estimation of the attenuation coefficients, we again see that the estimated  $B/A$  is close to the literature values for distances of 4 cm and 5 cm between the source and receiver and amplitudes up to 0.3 V (Fig. 6.11, Table 6.3). In case of fat, the error in the  $B/A$  measurement grows, overestimating  $B/A$ , as the sample is positioned further away from the receiver. This effect is most prominent for amplitudes in the range 0.5-0.7 V. As for porcine liver, we also see a tendency of sample positions closer to the source to overestimate  $B/A$ . However, a proper analysis of the influence of the sample

positioning on the measurement accuracy is hindered by the variability in literature data for tissues (Table 6.3). Besides this, the cuvette utilized in the measurement was not optimal for measurements with tissue. A cuvette with two separate sides, allowing to gently squeeze the tissue and measure its thickness more accurately would enable more accurate analysis.

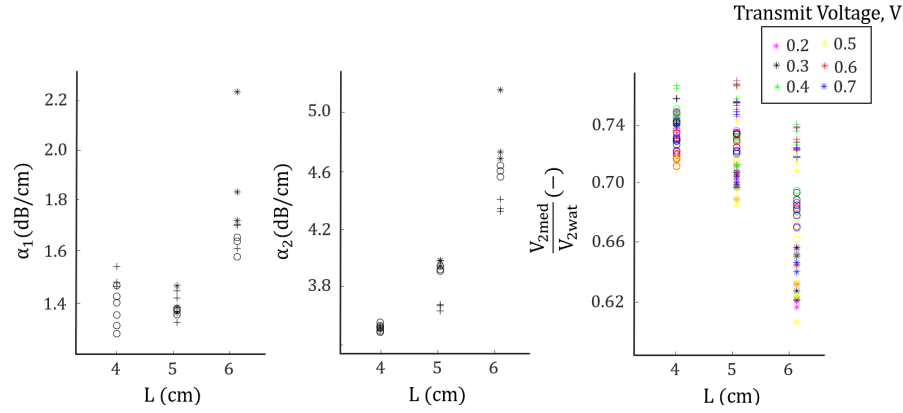


Figure 6.10: The attenuation coefficients at the fundamental  $\alpha_{1med}$  and 2nd harmonic  $\alpha_{2med}$  and the ratio of 2nd harmonic amplitudes  $V_{2med}/V_{2ref}$  for porcine liver. The measurements were conducted at several distances between the source and the receiver  $L$  and various sample positions: + (close to the source), \* (close to the receiver), o (in the middle). Colors for  $V_{2med}/V_{2ref}$  measurement encode different amplitudes, transmitted to the source.

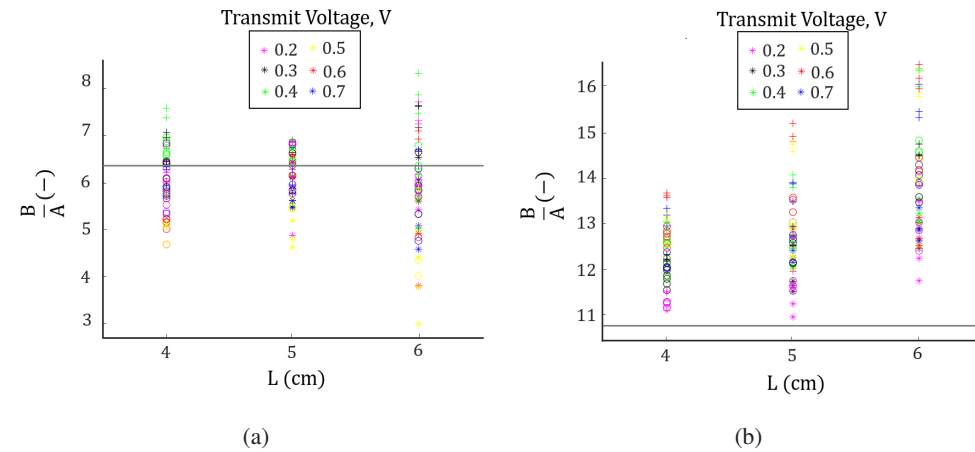


Figure 6.11: Estimated  $B/A$  for (a) Porcine liver; (b) Porcine fat. The symbols encode sample positions: + (close to the source), \* (close to the receiver), o (in the middle).

## 6.2.4 Conclusions

The current experiments demonstrated that the derived formula and the utilized setup are capable of measuring  $B/A$  of media with different frequency dependences of the attenuation

coefficient. For all media, lower amplitudes and shorter distances between the source and the receiver favored better  $B/A$  agreement with literature values. Amplitudes of 0.3 V and lower resulted in a maximum error of 25% and 8% for tissues and corn oil, respectively, for all configurations at shorter distances of 4 and 5 cm. We conclude that for tissues the utilized source transducer should not be driven at an amplitude higher than 0.3 V for a  $B/A$  estimation within 25% accuracy. At higher amplitudes, we observed nonnegligible 3rd harmonic generation and, possibly, nonlinearities in the receiving system.

The data clearly indicates more accurate  $B/A$  estimations for the liquid corn oil, compared to tissues. This is typical for FAM measurements, since tissue has an inherently heterogeneous structure, leading to greater phase-cancellation effects on the receiver. These effects are enhanced for large receivers and can contribute to great overestimation of the attenuation coefficients in tissues. Despite this, the predicted  $B/A$  values are in the range of expected values. Therefore, we conclude that the FAIS and its modification require the measurement of attenuation as a whole, including absorption, diffraction, dispersion and phase cancellation effects.

Even though overall there is a tendency for  $B/A$  to be overestimated at sample positions further away from the receiver, this effect is very limited for the lowest amplitudes, within the near field. It is difficult to draw conclusions on the generalizability of this effect, which may depend on the specific design of the cuvette and is difficult to compare to the literature due to the variability of the published estimates (Table 6.2). Yet, based on this work, we did not identify a markable influence of the sample position on the accuracy of  $B/A$  estimation. However, extensive analysis, also involving different cuvette designs and a smaller receiver, are required to derive more general conclusions on this aspect. The experiment may also benefit from a phased array source, since it may provide a closer resemblance of the field to that of a plane wave, also at further (axial) distances from the source.

This work described an improved  $B/A$  measurement method and demonstrated a validation process of the proposed approach and measurement procedure. We identified the experimental conditions that do not violate the assumptions made when deriving the proposed equation and, therefore, yield accurate  $B/A$  estimates. A smaller receiver is hypothesized to reduce phase-cancellation effects and yield more accurate  $B/A$  estimates.

## Acknowledgments

This research was funded by the eMTIC collaboration. The authors thank Anton Nikolaev for the cuvette design.

7

*B/A* measurement of clear cell renal cell carcinoma versus healthy kidney tissue

---

7

### Abstract:

The acoustic parameter of nonlinearity  $B/A$  has been shown capable of discriminating some types of pathological tissue from healthy tissue. The literature on the utility of  $B/A$  for cancer diagnostics is very limited, with measurements on the human breast and liver. This work expands the current research on cancer diagnostics by  $B/A$  assessment of 8 slices of human clear cell renal cell carcinoma (ccRCC) from two patients, and 4 slices of healthy kidney tissue from two healthy kidney samples. The Wilcoxon test identified the  $B/A$  distribution of malignant tissues to be significantly different from healthy tissue, with a median  $B/A = 8.1$  for ccRCC and  $B/A = 6.8$  for healthy tissue ( $p < 0.05$ ). Acoustic attenuation at 2.1 MHz was significantly greater ( $p < 0.05$ ) for ccRCC (1.7 dB/cm) than for healthy tissue (1.0 dB/cm). In conclusion,  $B/A$  and acoustic attenuation may represent potential diagnostic markers of ccRCC. More data and an improved experimental design are further required.

From: A. Panfilova, X. Chen, C. Widdershoven, J. E. Freund, D. S. Heijink, P. Zondervan, R. J. G. van Sloun, F. Molinari, H. Wijkstra, P. A. Dayton, and M. Mischi, “ $B/A$  measurement of clear cell renal cell carcinoma versus healthy kidney tissue”, submitted to *Ultrasound Med. Biol.*

## 7.1 Introduction

The ultrasound parameter of nonlinearity  $B/A$  has been shown to reflect water, fat and protein content of tissue [8, 341]. At the same time,  $B/A$  is also influenced by tissue structure: at equivalent chemical content,  $B/A$  has been shown to decrease when cell-to-cell adhesion bonds are destroyed [435]. Cancerous tissue often demonstrates altered water [293], glycogen and lipid [264] content compared to healthy tissue, as is reported for ccRCC. Moreover, cancerous tissue structure is characterized by increased cellularity [264] and lack of cell-to-cell adhesion [186]. Therefore,  $B/A$  may be a useful diagnostic parameter for cancer detection. Although in animal tissue  $B/A$  showed good differentiation between healthy and diseased tissue [401, 428],  $B/A$  measurements in human cancerous tissue has only been performed in liver and breast tissue [340, 341]. To further investigate the utility of  $B/A$  for cancer diagnostics, we measure  $B/A$  in an *ex-vivo* setting of two healthy kidney specimens and two specimens of clear cell renal cell carcinoma (ccRCC), being the most frequent renal carcinoma [264].

## 7.2 Materials and Methods

### 7.2.1 Theoretical background

As a monochromatic wave propagates, energy is transferred from the fundamental to the 2nd harmonic, whose amplitude is proportional to the nonlinear parameter  $B/A$  of the propagation medium [152]. If the 2nd harmonic is measured in water, whose  $B/A$  is well-known, and another measurement is conducted with the investigated sample inserted in the path between the source and receiver, the  $B/A$  of the studied sample can be determined from the ratio of the second harmonics in these two configurations [152]. In this work, we utilize the generalized finite amplitude insert-substitution method presented in [289], which utilizes the plane-wave approximation but makes no assumptions either about sample attenuation or about its position. To estimate  $B/A$  it is also necessary to measure the density  $\rho$ , the speed of sound  $c$ , and the attenuation coefficients at the fundamental and 2nd harmonic frequency  $\alpha_1$  and  $\alpha_2$  of the sample. All the quantities measured with the generalized finite amplitude insert-substitution method [289] represent one single average value corresponding to the region of the sample through which the acoustic beam propagated and was, subsequently, received from [152, 289]. This region is defined by the dimensions of the source and receiver.

### 7.2.2 Experimental Procedure

### 7.2.3 Patient selection and sample preparation

Two patients diagnosed with ccRCC, and scheduled for radical nephrectomy, provided oral consent to utilize the resected tissue for scientific purposes. After surgery, part of the cancerous tissue was selected by the histopathologist for the  $B/A$  measurement. After the measurement, the studied tissue was fixated and underwent histopathological analysis, confirming the diagnosis of ccRCC (sample 1: WHO grade 4, sample 2: WHO grade 3). Due to the smaller size of one of the tumors, a sample of healthy tissue was also available from one of the patients. To acquire more data for the healthy kidney, a specimen was selected at an autopsy of a subject who donated his/her organs to science. An additional measurement on 2 porcine fat slices was performed for validation purposes.



The tissue was frozen for an hour at  $-20\text{ }^{\circ}\text{C}$  to increase its stiffness and allow for an easier slicing procedure. To cut the kidney into slices with flat parallel sides, a dedicated device was utilized, described in [289]. All slices were cut to have a thickness of 4-7 mm. The two tumor samples provided 3 and 5 slices, respectively. Two healthy slices were available from one of the resected kidneys, and 2 more from the kidney extracted at autopsy.

### 7.2.3.1 Measurement procedure

The setup consisted of two acoustic circular piston transducers, the source C304-SU (251 Olympus NDT Inc., Waltham, MA, USA) and the receiver V309 (Panametrics-NDT, 251 Olympus NDT Inc., Waltham, MA, USA), separated by a distance of 4.5 cm (Fig. 7.1). Their alignment was provided with a railsystem, previously utilized in [289]. A steel cuvette fixing the tissue slices consisted of 2 parts, one attached to the receiver holder, and another fixed on the rails. Both sides of the cuvette had circular openings of 30 mm in diameter, allowing the acoustic beam to pass. A system of rings inserted in both of the cuvette sides fixed acoustically-transparent thin film (3-IN-1 FOLIE, Albert Hein B.V., Zaandam, The Netherlands) which gently squeezed the tissue from both sides and ensured smooth surfaces.

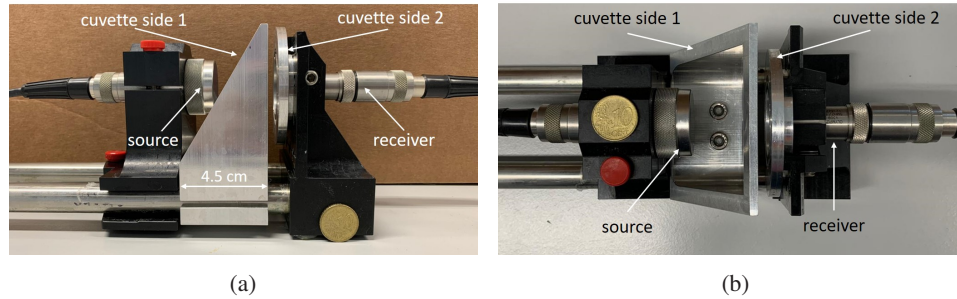


Figure 7.1: (a) Side view of the measurement setup. (b) Top view of the measurement setup.

The signal transmission and acquisition was controlled by LabVIEW (National Instruments Corp., Austin, TX, USA) software as previously described in [289]. The driving signals were 20-cycle pulses with a rectangular window, generated by 33220A arbitrary wave generator (Agilent Technologies, Santa Clara, USA) and amplified by a 50-dB 2100L RF Power amplifier (Acquitek, Massy, France) before transmission to the source transducer. For every acquisition, a total of 92-95 pulses was transmitted, received and saved.

The setup was submerged in a degassed water bath. The tissue slice was fixed between the cuvette sides under water, to avoid trapping of air bubbles. Four through-transmission measurements were performed. Two measurements involved the transmission of low-amplitude signals ( $\leq 0.02\text{ V}$ ) to the source at  $f = 2.1\text{ MHz}$  and  $2f = 4.2\text{ MHz}$ , aimed at determining  $\alpha_1$  and  $\alpha_2$ . Two high-amplitude measurements, transmitting 0.15 and 0.2 V to the source at  $f$  were conducted to achieve 2nd-harmonic generation and register a 2nd-harmonic signal with a signal-to-noise ratio above 30, yielding two  $B/A$  estimations. Then the tissue was flipped and the acquisition was performed again. Finally, the tissue was gently removed, keeping the sides of the cuvette in place, and the measurements were repeated without the sample. As a result, each tissue slice was measured in two orientations at two pressure amplitudes. Homogeneous slices are expected to produce similar  $B/A$  values in both slice orientations.

Sample density  $\rho$  was measured by weighing the slices on a H4J Pocket Weegschaal scale,

and measuring their volume by the amount of displaced water in a Fisherbrand graduated cylinder.

### 7.2.4 Data analysis

The data was analysed with MATLAB<sup>®</sup> (The MathWorks, Inc., Natick, MA, USA). The speed of sound  $c$  was determined based on the delay of the arrival time of the signal caused by the inserted sample with respect to water, determined by the maximum of the cross-correlation of the signals without and with the sample.

The Fast Fourier Transform was utilized to extract the amplitude of the fundamental frequency components of the low amplitude pulses. The attenuation coefficients  $\alpha_1$  and  $\alpha_2$  were estimated based on the damping of the signal introduced by the sample, as in [289].

When extracting the 2nd-harmonic amplitudes of the high-amplitude acquisitions, a Hanning window was used on all pulses fed to the Fast Fourier Transform to reduce spectral leakage from the strong fundamental component to the weaker 2nd harmonic, as in [289].

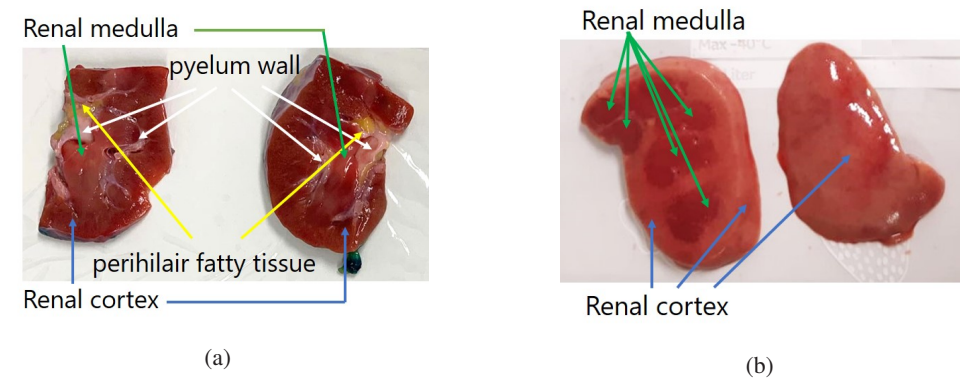


Figure 7.2: (a) Slices of the remaining healthy kidney tissue from the first excised kidney. (b) Slices of the healthy kidney tissue taken at autopsy.

It was observed that the measured  $B/A$  values of heterogeneous slices exhibited high variation between two slice orientations and values uncommon for biological tissue. We hypothesized that the slice heterogeneity leads to invalidity of the plane wave approximation, necessary for an accurate  $B/A$  estimation. Therefore, a threshold was set to the variability of the measured  $B/A$  of a slice in the 2 configurations. When the difference between the medians of  $B/A$  in 2 orientations exceeded 50% of the mean of the measured  $B/A$  at both slice orientations and both pressures, these values were disregarded from statistical analysis. This threshold was chosen somewhat arbitrarily, to constitute twice the deviation from the literature  $B/A$  value observed for homogeneous animal tissue at distances 4-5 cm away from the utilized source [289]. The plane wave approximation is not critical for the measurement of  $c$ ,  $\alpha_1$  and  $\alpha_2$  in tissue with acoustic impedance close to that of water and receivers as large as 6 mm in diameter, as in this work [19, 259]. Therefore, all data was included in the statistical analysis of  $c$ ,  $\alpha_1$  and  $\alpha_2$ .

The Wilcoxon nonparametric test was performed on  $B/A$ ,  $c$ ,  $\alpha_1$  and  $\alpha_2$  distributions to identify if the difference between the median values of cancer and healthy tissue were significant.

	Slice 1, orient. 1	Slice 1, orient. 2	Slice 2, orient. 1	Slice 2, orient. 2
$B/A$	11.5, 11.9	11.4, 11.4	9.8, 9.6	9.7, 9.5

Table 7.1: The measured  $B/A$  of two homogeneous slices of porcine fat. Two  $B/A$  values in each column correspond to two high-amplitude acquisitions.

Healthy kidney sample	$B/A$	$c$	$\alpha_1$ , dB/cm	$\alpha_2$ , dB/cm
Kidney 1, slice 1, orientation 1	2.1, 1.6	<b>1606</b>	<b>4.5</b>	<b>12.7</b>
Kidney 1, slice 1, orientation 2	19.2, 18.3	<b>1636</b>	<b>0.7</b>	<b>5.4</b>
Kidney 1, slice 2, orientation 1	12.0, 10.3	<b>1618</b>	<b>1.1</b>	<b>4.0</b>
Kidney 1, slice 2, orientation 2	2.7, 3.2	<b>1583</b>	<b>0.9</b>	<b>2.6</b>
Kidney 2, slice 1, orientation 1	<b>7.3, 7.4</b>	<b>1565</b>	<b>1.3</b>	<b>2.0</b>
Kidney 2, slice 1, orientation 2	<b>7.8, 8.1</b>	<b>1544</b>	<b>1.3</b>	<b>2.0</b>
Kidney 2, slice 2, orientation 1	<b>5.8, 6.3</b>	<b>1592</b>	<b>0.8</b>	<b>2.1</b>
Kidney 2, slice 2, orientation 2	<b>5.4, 5.2</b>	<b>1538</b>	<b>0.5</b>	<b>1.2</b>

Table 7.2: The measured acoustic parameters of the healthy tissue slices. The bold font highlights the acquisitions that were included in the statistical analysis.

### 7.3 Results

The measured  $B/A$  for the 2 porcine fat slices are presented in Table 7.1, showing a maximum deviation of 12% from the literature value of 10.8 [152]. The studied human healthy kidney slices are shown in Fig. 7.2, while the measured  $B/A$  for these slices are presented in Table 7.2. The white pyelum wall structures on Fig. 7.2a (a) are stiff, owing to the higher stromal and the muscular composition of the tissue, and may be expected to have different acoustic properties from the surrounding tissue. The yellow perihilar fatty tissue, is expected to have a  $B/A$  close to 10.8, almost twice as high as that of the kidney parenchyma [152], as typical for fatty tissue. In fact, the  $B/A$  variability threshold for these slices is above 50%, reaching a maximum of 170%. Therefore, these values were disregarded from the statistical analysis and only healthy data from the kidney taken at autopsy was included (Fig. 7.2b). These samples were more homogeneous and show more consistent  $B/A$  value for both slice orientations.

Figures 7.3a and 7.3b present examples of the slices of the 2 tumor samples, showing that tumor tissue is heterogeneous. Table 7.3 contains the measured acoustic parameters of all investigated slices. The data included in the statistical analysis is presented in bold for these slices.  $B/A$  variations between the slice sides are within the set threshold. Figure 7.4 illustrates the distributions of all the measured parameters of cancer and healthy slices included in the statistical analysis. The speed of sound and attenuation at the 2nd harmonic of 2.1 MHz are not significantly different, while  $B/A$  and attenuation at the fundamental frequency are significantly different ( $p < 0.05$ ). The median  $B/A$  of cancer is 8.1 versus 6.8 of healthy kidney tissue. The median  $\alpha_2$  of cancer is 3.9 dB/cm versus 2.1 dB/cm of healthy kidney tissue.

### 7.4 Discussion

In this work, we follow the same measurement strategy as in [289] but the tissue cuvette is out of steel and has a long 4.5 cm base (Fig. 7.1), fixed on the rails, ensuring a stable position with

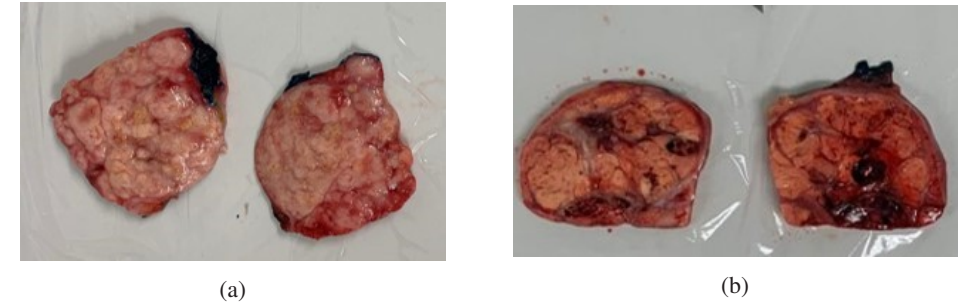


Figure 7.3: Tumor slices of kidney sample 1 (a) and kidney sample 2 (b), exhibiting a macroscopic and microscopic heterogeneous tumor composition with degenerative, fibrotic and edematous changes.

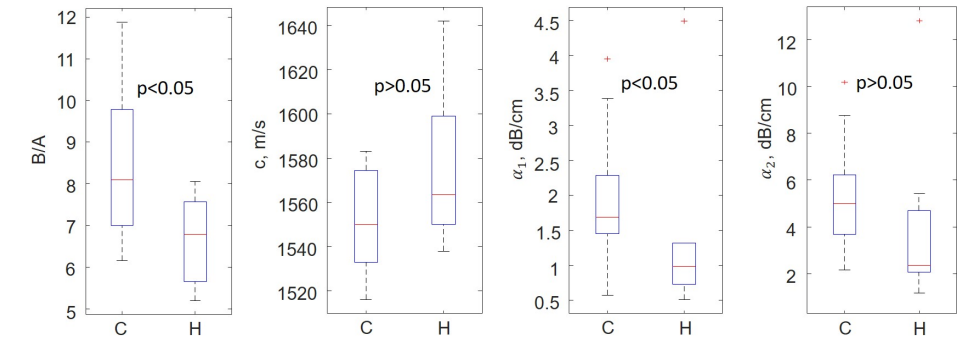


Figure 7.4: Acoustic parameters of the cancerous tissue slices (C) versus healthy tissue slices (H).

cuvette sides strictly perpendicular to the beam propagation direction. This resulted in a more accurate  $B/A$  measurement, as demonstrated for homogeneous porcine fat samples. On the other hand, when tissue consists of several tissue types with different acoustic properties, as the kidney slices in Fig. 7.2a, the method proves inaccurate, due to the violation of the plane wave approximation. Cancerous tissue is often heterogeneous, with fibrotic, degenerative and necrotic changes, confirmed by histology for both samples of ccRCC that exhibited cellular as well as edemous and sclerotic regions. As a result, the wave front travels at different speeds of sound, and its amplitude depends on the specific path travelled. Therefore, to improve confidence in the measurement results, we selected samples with consistent  $B/A$  values for both slice orientations; this way, we expect the more homogeneous slices to be included in the analysis.

The median  $B/A$  value of the healthy homogeneous slices is close to the literature value of 6.9 for porcine healthy kidney [152], bringing confidence in our findings. The greater  $B/A$  of ccRCC samples may be ascribed to the high lipid and glycogen content, characteristic for this tumor [264], since fatty tissue has been reported to have high  $B/A$  of 10.8-11.0 [152]. The highly cellular regions of ccRCC also exhibit a significantly lower apparent diffusion coefficient, possibly indicating higher cellular density and lower water content [357]. The latter would also contribute to higher  $B/A$ . At the same time, edemous regions of ccRCC

Tumor sample	$B/A$	$c$	$\alpha_1$ , dB/cm	$\alpha_2$ , dB/cm
Tumor 1, slice 1, orientation 1	<b>7.7, 8.1</b>	<b>1517</b>	<b>0.9</b>	<b>2.5</b>
Tumor 1, slice 1, orientation 2	<b>11.9, 11.4</b>	<b>1516</b>	<b>0.8</b>	<b>2.2</b>
Tumor 1, slice 2, orientation 1	<b>6.7, 6.7</b>	<b>1565</b>	<b>1.7</b>	<b>4.2</b>
Tumor 1, slice 2, orientation 2	<b>7.3, 8.0</b>	<b>1574</b>	<b>2.0</b>	<b>5.1</b>
Tumor 1, slice 3, orientation 1	7.3, 7.5	<b>1575</b>	<b>1.5</b>	<b>3.6</b>
Tumor 1, slice 3, orientation 2	0.8, 0.7	<b>1783</b>	<b>2.2</b>	<b>6.1</b>
Tumor 2, slice 1, orientation 1	<b>10.1, 10.5</b>	<b>1577</b>	<b>1.4</b>	<b>4.0</b>
Tumor 2, slice 1, orientation 2	<b>9.0, 9.4</b>	<b>1551</b>	<b>0.6</b>	<b>2.4</b>
Tumor 2, slice 2, orientation 1	<b>8.4, 8.0</b>	<b>1549</b>	<b>2.4</b>	<b>5.6</b>
Tumor 2, slice 2, orientation 2	<b>6.2, 6.6</b>	<b>1560</b>	<b>1.5</b>	<b>3.8</b>
Tumor 2, slice 3, orientation 1	6.8, 6.5	<b>1536</b>	<b>2.3</b>	<b>8.3</b>
Tumor 2, slice 3, orientation 2	17.7, 17.9	<b>1535</b>	<b>1.6</b>	<b>6.3</b>
Tumor 2, slice 4, orientation 1	9.6, 9.3	<b>1535</b>	<b>1.7</b>	<b>4.9</b>
Tumor 2, slice 4, orientation 2	-4.9, -5.4	<b>1583</b>	<b>3.9</b>	<b>10.2</b>
Tumor 2, slice 5, orientation 1	-0.6, -0.5	<b>1528</b>	<b>3.4</b>	<b>8.7</b>
Tumor 2, slice 5, orientation 2	6.4, 5.9	<b>1531</b>	<b>2.2</b>	<b>6.2</b>

Table 7.3: The measured acoustic parameters of the cancerous tissue slices. The bold font highlights the acquisitions that were included in the statistical analysis.

could have a lower  $B/A$  than healthy kidney due to the greater water content in those regions.

The greater median values of  $\alpha_1$  and  $\alpha_2$  for ccRCC compared to healthy tissue are in line with the attenuation observed in optical coherence tomography signals [135]. We attribute this to greater composition and structure heterogeneity of malignant tissue that causes scattering and varying phase delays for different acoustic paths within the tissue [259]. The difference in attenuation is expected to increase with frequency, since for smaller wavelengths the phase cancellation effects due to inhomogeneities grow, as observed in our data and in [259]. The majority of tissue slices disregarded from  $B/A$  statistical analysis demonstrate greater attenuation than those included in this analysis. This finding supports our hypothesis that heterogeneous slices show greater  $B/A$  variation. The measured speed of sound distributions showed no significant difference.

When flipping the slice, the exact investigated area may have been shifted, contributing to the variability of  $B/A$  in the two slice orientations. More data and one-to-one histopathologic correlation [266] are needed to confirm our findings. The measurement accuracy may improve with a smaller region of investigation, leading to less heterogeneity within this region. It may also be beneficial to perform histopathological quantification of the volumes of edemous and cellular regions of the studied slices and correlate them to the measured  $B/A$ .

## 7.5 Conclusion

This work demonstrates that  $B/A$  and acoustic attenuation may be potential diagnostic indicators of ccRCC due to the rich lipid and glycogen content of this tumor and its heterogeneity in composition and structure. It also provides guidance to further experimental studies investigating the utility of  $B/A$  for cancer diagnostics. In some animal studies,  $B/A$  has been shown to provide better tissue discrimination, compared to linear parameters, attenuation and density [432], opening new possibilities for cancer diagnostics with ultrasound. However,

$B/A$  echo-mode tissue imaging is a very challenging task [290]. Therefore, it is important to prove the clinical value of  $B/A$  on simpler *ex vivo* experiments before further developing this imaging modality.

## Acknowledgements

This research was supported by the eMTIC collaboration and in part by the Russian Science Foundation (RSF) under Grant No. 19-12-00148 (OAS).

**Part IV**  
**Epilogue**

**8**

**Discussion and future prospects**

---



US has the advantages of being a real-time, portable, widely available and cost-effective modality. Adequate cancer diagnostics with US would have a global impact, giving access to clinical diagnostics even in low-income countries. However, currently the use of US in cancer diagnostics is limited to some organs and cancer types, often requiring additional imaging and histopathology for definitive diagnosis. This thesis aimed at improving cancer diagnostics with US, focusing on two nonlinear US modalities: CE-US and nonlinear parameter  $B/A$  imaging. Below is a detailed discussion on the posed research questions.

- **What is the relationship between vascular features and DCE-US dispersion and perfusion?**

Malfunctional tumor vasculature results in abnormal blood flow that can be visualized with CE-US. This modality is part of routine clinical practice in many clinics across the globe [98, 100]. Typically the diagnosis is based on real-time assessment of perfusion-related features. Therefore, isoperfused tumors may be missed and the diagnosis is operator-dependent. DCE-US [95] analysis has the ability to quantify perfusion and dispersion-related features, enabling the detection of more tumors and making the analysis more accurate and less operator-dependent. These features reflect angiogenic vascular alterations characteristic for tumor. Several studies [215, 217, 391] have shown dispersion to have a higher discrimination capability between malignant and healthy tissue than perfusion. Currently, it is still not completely understood which altered features of the vascular architecture are reflected by the estimated perfusion and dispersion.

To shed light on the connection between DCE-US and vascular features, implanted fibrosarcoma tumors were imaged in their largest cross section with DCE-US and their whole volume was captured with AA in a longitudinal study at 4 time points. The extracted DCE-US perfusion and dispersion features were correlated to vascular features derived from AA images and similar longitudinal trends were identified. Moreover, in some cases it was possible to locate the DCE-US plane in the 3D AA volumes: it was discovered that large vessels were clearly highlighted on perfusion maps and could be identified in the AA volume. This enabled a qualitative comparison of the spatial distributions of DCE-US and AA-derived features. Correlation analysis of longitudinal trends of the DCE-US and AA features showed MVD to correlate with perfusion; the spatial distribution map confirmed this and showed large vessels to be highly perfused, as well as regions with high MVD. No link between dispersion and vascular features was identified. It was hypothesized that dispersion reflects properties of smaller vessels than those visible with AA.

The main limitation of the study design is that features extracted from 2D DCE-US images were correlated with AA features extracted from the whole tumor volume. More meaningful analysis could be achieved if both imaging modalities were performed in 3D mode, or if AA captured a volume mainly containing the same cross-section as the DCE-US plane. The latter would also allow to compare the spatial distributions of the studied features. Another improvement would involve a reference technique capable of imaging vessels below the 100  $\mu\text{m}$  resolution of AA. Superresolution imaging [67], with a resolution of several micrometers, may be a good candidate for this purpose. Immunohistology also enables visualizing the microvasculature and deriving MVD [418].

- **Do antibubbles exhibit augmented nonlinear behavior compared to current-generation UCAs?**

Diagnosis based on both CE-US and DCE-US may be challenging in some cases where the weak signal coming from small vessels with low UCA concentration is masked by the nonlinear

tissue signal [125]. This problem could be mitigated by refining the existing contrast-specific imaging schemes or by utilizing a UCA with a stronger nonlinear behavior than that of the current generation UCAs. In this work, we investigate the latter option since most contrast-specific imaging schemes are based on eliminating the linear signal scattered by tissue but do not eliminate the nonlinear tissue signal. An alternative UCA would allow imaging at lower pressures, where the nonlinear tissue signal is negligible.

Antibubbles, *i.e.*, encapsulated gas bubbles with incompressible cores, have been proposed as a UCA prototype with augmented nonlinear behavior, due to their asymmetric radial oscillation under exposure to the sonic field [214]. Moreover, antibubbles with liquid cores would allow delivering large quantities of medication locally, without damping the bubble oscillation, unlike other therapeutic UCAs [302, 344], offering clinicians a traceable and highly effective therapeutic agent. Experimental characterization of antibubbles is scarce [306]. In this work, an acoustic characterization of endoskeleton antibubbles was performed in the diagnostic frequency range of 1.0 MHz to 3.5 MHz at low acoustic pressures, and compared to that of reference bubbles with an analogous shell and analogous mean bubble size, and a commercial UCA SonoVue<sup>TM</sup>. Scatter measurements were conducted to record the nonlinear signal amplitude scattered by the studied UCAs in an acoustically transparent cuvette. Moreover, UCA attenuation was measured to assess shadowing, and a vascular phantom was imaged with DCE-US, simulating clinical images. Endoskeleton antibubbles were shown to generate stronger or comparable nonlinear signal to that of the reference UCA and to that of the clinically approved UCA SonoVue<sup>TM</sup>. Antibubbles exhibited the highest attenuation among the studied UCAs. These results indicate that the addition of an incompressible core inside a gas bubble may augment the bubble's nonlinear behavior and that antibubbles have potential to become a traceable therapeutic agent.

Solid proof that the incompressible inclusions in the gas phase augment the nonlinear signal generated by UCA bubbles could not be provided in this work, since the utilized reference bubbles, unlike endoskeleton antibubbles, had no endoskeleton inside them, and had a different size distribution. The high attenuation values suggest that alternative antibubbles, with a more compliant shell would be more suitable for imaging purposes. Future work involves manufacturing a reference UCA with bubbles which, except for the absence of the inner core(s), present not only the same shell properties and inner gas as the corresponding antibubbles, but also the same inner structure and size distribution. Investigation of antibubbles properties like shell material and type of gas is necessary to optimize antibubbles performance and to bring them to the clinic.

- **Which are the most promising  $B/A$  measurement and imaging strategies and what are the challenges on the way to  $B/A$  imaging?**

$B/A$  measurement and, to a greater extent,  $B/A$  imaging are challenging tasks. The conducted literature review demonstrated the FAM group of methods to be most commonly utilized for single-parameter  $B/A$  assessment due to its relative simplicity.  $B/A$  tomography has been achieved with several strategies, *e.i.*, FAM, pump wave and parametric array methods, each of these strategies with their strengths and weaknesses. Pump wave tomography grants the possibility to obtain real-time images but is expected to have a lower resolution compared to FAM and parametric array methods. The parametric array method grants the highest resolution, whereas FAM is the simplest in implementation. Echo-mode imaging is of greatest interest in a clinical setting, since it is not limited to a few organs in its application. Several strategies succeeded in  $B/A$  imaging of tissue-mimicking phantoms, and only one work presented echo-mode images of tissue, where shadowing served as an indication of high  $B/A$ .

These strategies were able to correct for the effect of the scatter distribution by normalizing to a reference signal assumed to be influenced by the scatter distribution in the same manner as the signal of interest, the latter being the 2nd harmonic (FAM), the fundamental harmonic (FAM) or a time the delay (SURF or the pump wave family of methods).

Development of echo-mode  $B/A$  imaging modalities is hindered due to the fact that in echo-mode, the strength of the reflected signal is to a greater extent determined by the scatterer distribution and the variation of linear US parameters rather than by  $B/A$ , with diffraction, attenuation, multiple scattering and noise artifacts also affecting the signal. This poses the need to correct for all effects unrelated to  $B/A$ . Normalization by/comparison to a reference signal produced by the same source and propagated through the same medium is currently the most promising strategy to correct for the combination of these effects, eliminating the need in estimating these corrections as separate entities. In practice, separating nonlinear effects from the rest may be challenging, since the reference signal may not be free of nonlinear effects itself, particularly, in applications requiring greater image depth and, therefore, a sufficiently high source pressure. Moreover, the necessity of a reference signal hinders the clinical implementation since, in practice, motion artifacts are always present, altering the spatial distribution of acoustic parameters and making a reference signal acquired at a different time point no longer appropriate for an accurate correction. Besides this, as the observed nonlinear effects are cumulative,  $B/A$  was typically extracted through differentiation of the normalized signal in time, amplifying the noise components. Differently from the others, SURF does not differentiate the signal of interest and was modelled to extract the bulk modulus distribution, related to  $B/A$ . The latter strategy may be the most promising for eliminating noise components.

The limitation of the conducted work involves no simulation/experimental work. The derived conclusions were solely based on the results acquired by multiple research groups.

#### • Can a more practical and applicable version of the FAIS method be developed?

The gFAIS method was developed as a more practical version of one of the simplest  $B/A$  measurement methods, the FAIS method [152]. It estimates  $B/A$  from the 2nd harmonic amplitudes in two configurations: (1) generated in a reference medium with a known  $B/A$  and (2) when the sample of interest is inserted in the reference medium. A measurement of the attenuation coefficients at the fundamental and 2nd harmonic frequency is also required. Theoretical derivation of  $B/A$  dependency on the 2nd harmonic amplitude is based on the plane wave approximation and the assumption of weak nonlinear effects, with negligible 3rd and higher harmonics. Differently from the original FAIS, an arbitrary sample position is assumed as well as an arbitrary frequency dependence of attenuation, making gFAIS applicable to a broader range of tissues and liquids.

An *in-silico* and an experimental validation of the gFAIS were performed. The *in-silico* validation of the method was conducted in k-Wave of Matlab that enables modelling 2nd order cumulative nonlinear effects. k-Wave was chosen since it is capable of modeling nonlinear waves travelling in arbitrary directions through heterogeneous media and requires fewer grid points compared to the alternative full-wave methods [92]. The Iterative Nonlinear Contrast Source method is also characterized by these advantages [92, 396]; however, to our knowledge, it is not implemented in an openly available toolbox as k-Wave. Several experimental configurations were studied: two sources with different radii, twelve receiver sizes and two sample positions, all of these configurations simulated at source-receiver separation distances from 2 to 9 cm. To simulate a  $B/A$  measurement, three through-transmission measurements were simulated in 3D space: one inducing 2nd harmonic generation (nonlinear

simulations) and 2 low pressure amplitude measurements of the attenuation coefficients at the fundamental and 2nd harmonic frequency (linear simulations). The simulated studied samples were a homogeneous medium mimicking liquid and a medium with weakly heterogeneous density and speed of sound mimicking weakly heterogeneous tissue. All the simulated measurements indicated that shorter source-receiver separation distances and larger receivers favor a more accurate  $B/A$  measurement. The larger source provided a wider range of distances where  $B/A$  could be measured, due to a longer near field. In the most favorable setup configuration, the  $B/A$  measurement error was 10% for the studied substances. From a different perspective, it was observed that attenuation of the heterogeneous medium was overestimated compared to the simulated value. This can be ascribed to phase cancellation effects occurring in media with a heterogeneous speed of sound distribution. Nevertheless, the “measured” attenuation value rather than the simulated one yielded much more accurate  $B/A$  estimation, indicating that the actual attenuation of the harmonics, including phase cancellation effects, needs to be accounted for in the equation.

Limitations of this work involve possible computational phase errors in the nonlinear simulations due to an insufficiently small timestep and a simplistic model of weakly heterogeneous tissue. Besides this, in a realistic situation only the particle velocity component perpendicular to the receiver face is registered by the acoustic receiver. However, the current work made the assumption that the particle velocity projections in the other two spatial dimensions are negligible and utilized the absolute pressure amplitudes to estimate  $B/A$ . For a plane wave field, this would yield the same results; however, in practice, wave propagation also occurs in other directions, albeit to a smaller extent. Future work involves simulating more realistic tissue models, registration of particle velocity perpendicular to the receiver face and simulations with smaller time steps, ensuring higher accuracy of the simulation.

The experimental validation of the method was performed with a setup including a rail-system that ensured alignment of the acoustic source and the receiver and allowed fixing a sample holder for the investigated sample. Based on simulation results, a source with the dimensions of the largest simulated source was chosen, and a sufficiently big receiver. This work measured  $B/A$  of corn oil, pig fat and pig liver at source-receiver separation distances of 4 to 7 cm, several amplitudes of the transmitted pulses, and three sample positions: close to the source, close to the receiver, and in the middle between the source and the receiver. As in the *in-silico* experiments, shorter distances between the source and the receiver favored a more accurate  $B/A$  measurement, whereas the sample position did not influence the accuracy of the measurement. A range of transmit amplitudes suitable for the source transducer was identified, yielding a 2nd harmonic amplitude with a sufficient SNR and yet a negligible 3rd harmonic component. At lower source pressure amplitudes and shorter distances within the near field of the source transducer, the measurement error was confined to 8% and 25% of the values reported in the literature for corn oil and the considered tissues, respectively.

The main limitation of this work is that the plastic sample holder was not robust to tilting and, therefore, introduced errors to the measurement. Besides this, the chosen tissue slices were of the same tissue type, visually uniform and homogeneous, making it difficult to extrapolate the accuracy of the measurement to highly heterogeneous cancer tissue.

#### • Does $B/A$ differ for healthy kidney tissue and ccRCC?

The utility of  $B/A$  has been poorly studied for cancer diagnostics. The parameter of nonlinearity  $B/A$  reflects tissue water, fat and protein content [435]. Moreover, it is influenced by the tissue structure, *e.g.*, cellular adhesion [435] and molecular water state [342]. Since cancerous tissue exhibits structural and chemical content alterations,  $B/A$  may be a suitable cancer marker.

To broaden the scope of our knowledge about  $B/A$  of cancerous tissue and assess its utility for cancer diagnostics, the  $B/A$  of human ccRCC and healthy kidney tissue were measured and compared for the first time. Kidney tissue was extracted from two patients scheduled for nephrectomy and, to provide more healthy tissue samples, one patient at autopsy. The tissue was frozen to increase its stiffness and cut with a histocutter, providing homogeneous in thickness slices. For the  $B/A$  measurement, the *ex-vivo* validation results of gFAIS allowed to utilize the same source and receiver at the optimal conditions, and refine the cuvette design, resulting in a steel stable cuvette robust to tilting. Despite the improved setup and a refined experimental procedure, to further improve  $B/A$  measurement accuracy,  $B/A$  of every tissue slice was measured in 2 orientations, interchanging the front and back face of the slice, and at two transmitted amplitudes in the identified suitable range. On a limited data set, it was demonstrated that  $B/A$  of ccRCC is greater than that of healthy tissue, presumably, due to high lipid content in ccRCC. The study also provided insight into the effect of heterogeneity on the applicability of the method. It was shown that heterogeneous slices, unlike homogeneous tissue slices, yielded abnormal  $B/A$  values, or values greatly differing in the 2 measured slice orientations. Such slices also exhibited high attenuation, supporting the hypothesis that the method failed due to tissue heterogeneity.

The main limitation of this study was the small sample size. Moreover, the measured  $B/A$  provided single-value assessment of a tumor slice. With tumor known to be a heterogeneous tissue mass, the studied sample can include edematous regions, with large quantities of water and few cells, as well as highly cellular regions. The former is expected to have a lower  $B/A$  compared to healthy tissue, whereas the latter, for high fat content tissue, exhibits a greater  $B/A$ . Furthermore, in some cases, when the sample was very heterogeneous, the method was no longer accurate since the acoustic field did not correspond to a plane wave after propagating through such tissue. This suggests that investigation of smaller tissue regions with less variation, with one-to-one histopathologic correlation, would give more insight into how sensitive  $B/A$  is to tissue state, and emphasizes the need in  $B/A$  imaging rather than single-parameter assessment. From the implementation point of view, it may have been beneficial to choose a clinical phase-array probe as the acoustic source rather than a circular transducer, possibly ensuring better compliance to the plane wave approximation and facilitating an easier transition to  $B/A$  imaging. *In-silico* experiments may help elucidate what type of source is beneficial for this measurement and how various types of heterogeneity (randomly distributed/inclusion within a homogeneous medium) affect the accuracy of the method and identify the practical choices for the experimental methodology that favor a more accurate measurement.

# 9

## Conclusions

---

This thesis provided insight to the link between vascular features and DCE-US features and showed that antibubbles have potential to become a therapeutic UCA and, possibly, a new generation UCA. It identified the most promising  $B/A$  measurement and imaging strategies and highlighted the challenges on the way to  $B/A$  imaging. It also introduced a more practical version of the FAIS method, the gFAIS method, and provided guidance on practical choices for the setup that favor an accurate  $B/A$  measurement. Finally, this PhD work also broadened our knowledge on  $B/A$  of biological tissues and its utility for cancer diagnostics, demonstrating  $B/A$  to be a promising imaging marker for the detection of ccRCC.

## Bibliography

- [1] L. Adler and E.A. Hiedemann. Determination of the nonlinearity parameter  $B/A$  for water and m-xylene. *J. Acoust. Soc. Am.*, 34(4):410–412, 1962.
- [2] R. E. Airley and A. Mobasheri. Hypoxic regulation of glucose transport, anaerobic metabolism and angiogenesis in cancer: novel pathways and targets for anticancer therapeutics. *Chemother.*, 53(4):233–256, 2007.
- [3] I. Akiyama. Reflection mode measurement of nonlinearity parameter  $B/A$ . In *AIP Conference Proceedings*, volume 524, pages 321–324. American Institute of Physics, 2000.
- [4] N. S. Anavekar and J. K. Oh. Doppler echocardiography: a contemporary review. *J. Cardiol.*, 54(3):347–358, 2009.
- [5] N. Anderton. *Acoustic properties of antibubbles*. Dissertation, University of the Witwatersrand, Johannesburg, 2020.
- [6] A. Anvari, F. Forsberg, and A. E. Samir. A primer on the physical principles of tissue harmonic imaging. *Radiographics*, 35(7):1955–1964, 2015.
- [7] R. E. Apfel. The effective nonlinearity parameter for immiscible liquid mixtures. *J. Acoust. Soc. Am.*, 74(6):1866–1868, 1983.
- [8] R. E. Apfel. Prediction of tissue composition from ultrasonic measurements and mixture rules. *J. Acoust. Soc. Am.*, 79(1):148–152, 1986.
- [9] N. Arnold, A. Cai, Y. Nakagawa W. Hou, and G. Wade. Acoustic tomography for imaging the nonlinear parameter. *Pattern Recogn. Acoust. Imag.*, 768:93–99, 1987.
- [10] A. Aubry and A. Derode. Multiple scattering of ultrasound in weakly inhomogeneous media: Application to human soft tissues. *J. Acoust. Soc. Am.*, 129(1):225–233, 2011.
- [11] M. A. Averkiou. Tissue harmonic imaging. volume 2, pages 1563–1572. IEEE, 2000.
- [12] M. A. Averkiou, D. N. Roundhill, and Jeffry E. Powers. A new imaging technique based on the nonlinear properties of tissues. In *1997 IEEE Ultrasonics Symposium Proceedings. An International Symposium (Cat. No. 97CH36118)*, volume 2, pages 1561–1566. IEEE, 1997.



- [13] J. Banchet and J. D. N. Cheeke. Measurement of the acoustic nonlinearity parameter  $B/A$  in solvents: Dependence on chain length and sound velocity. *J. Acoust. Soc. Am.*, 108(6):2754–2758, 2000.
- [14] J. Banchet, J. Cancian, and J. D. N. Cheeke. Measurement of the acoustic nonlinearity parameter in 1-alkanols. *Ultrasonics*, 38:301–304, 2000.
- [15] C. Barrière and D. Royer. Nonlinear parameter measurement and transient acoustic field imaging using the parametric interaction in liquids. In *2000 IEEE Ultrasonics Symposium. Proceedings. An International Symposium*, volume 1, pages 603–606. IEEE, 2000.
- [16] C. Barriere and D. Royer. Diffraction effects in the parametric interaction of acoustic waves: Application to measurements of the nonlinearity parameter  $B/A$  in liquids. *Ultrasound Med. Biol.*, 48(6):1706–1715, 2001.
- [17] J. F. Bartram. A useful analytical model for the parametric acoustic array. *J. Acoust. Soc. Am.*, 52:1042–1044, 1972.
- [18] K. W. Beekman, A. D. Colevas, K. Cooney, R. DiPaola, R. L. Dunn, M. Gross, E. T. Keller, K. J. Pienta, C. J. Ryan, D. Smith, et al. Phase ii evaluations of cilengitide in asymptomatic patients with androgen-independent prostate cancer: scientific rationale and study design. *Clin. Genitourin. Cancer*, 4(4):299–302, 2006.
- [19] K. Beissner. Exact integral expression for the diffraction loss of a circular piston source. *Acta Acustica united with Acustica*, 49(3):212–217, 1981.
- [20] P. Belitsos, D. Papoutsis, A. Rodolakis, S. Mesogitis, and A. Antsaklis. Three-dimensional power doppler ultrasound for the study of cervical cancer and precancerous lesions. *Ultrasound Obstet. Gynecol.*, 40(5):576–581, 2012.
- [21] S. A. Bereza, V. A. Burov, and S. N. Evtukhov. Model experiments on acoustic tomography of the nonlinear parameter. *Acoust. Phys.*, 54(4):449–459, 2008.
- [22] W. A. Berg, J. D. Blume, J. B. Cormack, E. B. Mendelson, D. Lehrer, M. Böhm-Vélez, E. D. Pisano, R. A. Jong, W. P. Evans, M. J. Morton, et al. Combined screening with ultrasound and mammography vs mammography alone in women at elevated risk of breast cancer. *JAMA*, 299(18):2151–2163, 2008.
- [23] A. J. Berkhout, J. Ridder, and L. F. van der Wal. *Acoustical imaging*. Plenum press, New York, 1991.
- [24] R. T. Beyer. Parameter of nonlinearity in fluids. *J. Acoust. Soc. Am.*, 32(6):719–721, 1960.
- [25] R. T. Beyer. Nonlinear acoustics. *Am. J. Phys.*, 41:1060–1067, 1973.
- [26] S. S. Bhat, T. T. Fernandes, P. Poojar, M. da Silva Ferreira, P. C. Rao, M. C. Hanumantharaju, G. Ogbole, R. G. Nunes, and S. Geethanath. Low-field MRI of stroke: Challenges and opportunities. *J. Magn. Reson. Imaging*, page e27324, 2020.
- [27] L. Bjørnø. Characterization of biological media by means of their non-linearity. *Ultrasonics*, 24:254–259, 1986.
- [28] L. Bjørnø. Contemporary aspects of the theory and application of nonlinear acoustics. *Arch. Acoust.*, 30(1):73–85, 2005.
- [29] L. Bjørnø. Introduction to nonlinear acoustics. *Phys. Proc.*, 3:5–16, 2010.
- [30] D. T. Blackstock. Generalized burgers equation for plane waves. *J. Acoust. Soc. Am.*, 77(6):2050–2053, 1985.
- [31] D.T. Blackstock. Convergence of the Keck-Beyer perturbation solution for plane waves of finite amplitude in a viscous fluid. *J. Acoust. Soc. Am.*, 39(2):411–413, 1966.
- [32] H. J. Bleeker, K. K. Shung, and J. L. Barnhart. Ultrasonic characterization of Albunex, a new contrast agent. *J. Acoust. Soc. Am.*, 87(4):1792–1797, 1990.
- [33] R. Boellaard, Roberto D.-B., Wim J. G. Oyen, F. Giammarile, K. Tatsch, W. Eschner, F. J. Verzijlbergen, S. F. Barrington, L. C. Pike, W. A. Weber, et al. FDG PET/CT: EANM procedure guidelines for tumour imaging: version 2.0. *Eur. J. Nucl. Med. Mol. Imaging*, 42(2):328–354, 2015.
- [34] A. Boukaz, B. J. Krenning, W. B. Vletter, F. J. ten Cate, and N. de Jong. Contrast superharmonic imaging: A feasibility study. *Ultrasound Med. Biol.*, 29(4):547–553, 2003.
- [35] A. Boukaz, N. de Jong, and C. Cachard. Standard properties of ultrasound contrast agents. *Ultrasound Med. Biol.*, 24(3):469–472, 1998.
- [36] M. Brock, T. Eggert, J. P. Rein, F. Roghmann, K. Braun, L. Björn, F. Sommerer, Noldus J., and C. Bodman. Multiparametric ultrasound of the prostate: Adding contrast enhanced ultrasound to real-time elastography to detect histopathologically confirmed cancer. *J. Urol*, 189(1):93–98, 2013.
- [37] G. A. Brock-Fisher, M. D. Poland, and P. G. Rafter. Means for increasing sensitivity in non-linear ultrasound imaging systems, November 26 1996. US Patent 5,577,505.
- [38] M. J. Brown and A. J. Giaccia. The unique physiology of solid tumors: opportunities (and problems) for cancer therapy. *Cancer Res.*, 58(7):1408–1416, 1998.
- [39] A. P. Brysev, L. M. Krutyansky, P. Pernod, and V. L. Preobrazhensky. Nonlinear ultrasonic phase-conjugate beams and their application in ultrasonic imaging. *Acoust. Phys.*, 50(6):623–640, 2004.
- [40] E. Bullitt, G. Gerig, S. M. Pizer, W. Lin, and S. R. Aylward. Measuring tortuosity of the intracerebral vasculature from mra images. *IEEE Trans. Med. Imag.*, 22(9):1163–1171, 2003.
- [41] J. M. Burgers. A mathematical model describing the theory of turbulence. In R. von Mises and T. von Karman, editors, *Advances in Applied Mechanics*, volume 1, pages 171–199. Academic Press NY, 1948.
- [42] P. N. Burns, D. H. Simpson, and M. A. Averkiou. Nonlinear imaging. *Ultrasound Med. Biol.*, 26(S1):S19–S22, 2000.
- [43] V. A. Burov, S. N. Evtukhov, A. M. Tkacheva, and O. D. Romyantseva. Acoustic tomography of the nonlinear parameter by a small number of transducers. *Akust. Zh.*, 52(6):760–776, 2006.
- [44] V. A. Burov, A. A. Shmelev, and D. I. Zotov. A prototype for a tomography system using third-order acoustic nonlinear effects. *Akust. Zh.*, 59(1):27–44, 2013.
- [45] V. A. Burov, A. A. Shmelev, R. V. Kryukov, and O. D. Romyantseva. Role of nonlinear interactions in third-order acoustic tomography. *Akust. Zh.*, 61(6):636–650, 2015.
- [46] M. Byra, J. Wójcik, and A. Nowicki. Ultrasound nonlinearity parameter assessment using plane wave imaging. In *2017 IEEE International Ultrasonics Symposium (IUS)*, pages 1511–1516. IEEE, 2017.

- [47] A. Cai, J. Sun, and G. Wade. Imaging the acoustic nonlinear parameter with diffraction tomography. *IEEE Trans. Ultrason. Ferroelectr. Freq. Control*, 39(6):708–715, 1992.
- [48] C. A. Cain. Ultrasonic reflection mode imaging of the nonlinear parameter  $B/A$ : I. a theoretical basis. *J. Acoust. Soc. Am.*, 80(28):28–32, 1986.
- [49] C. A. Cain and H. Houshmand. Ultrasonic reflection mode imaging of the nonlinear parameter  $B/A$ : II: Signal processing. *J. Acoust. Soc. Am.*, 86(1):28–32, 1989.
- [50] C. A. Cain, H. Nishiyama, and K. Katakura. On ultrasonic methods for measurement of the nonlinear parameter  $B/A$  in fluid-like media. *J. Acoust. Soc. Am.*, 80(2):685–688, 1986.
- [51] A. Caponnetto and M. Bertero. Tomography with a finite set of projections: singular value decomposition and resolution. *Inverse problems*, 13:1191–1205, 1997.
- [52] A. Carovac, F. Smajlovic, and D. Junuzovic. Application of ultrasound in medicine. *Acta Informatica Medica*, 19(3):168, 2011.
- [53] P. H. Carroll and J. L. Mohler. NCCN guidelines updates: prostate cancer and prostate cancer early detection. *J. Natl Compr. Canc. Netw.*, 16(5S):620–623, 2018.
- [54] E. L. Carstensen, W. K. Law, N. D. McKay, and T. G. Muir. Demonstration of nonlinear acoustical effects at biomedical frequencies and intensities. *Ultrasound Med. Biol.*, 6:359–368, 1980.
- [55] E.L. Cartersen. Nonlinearities in the bioeffects of ultrasound. *J. Acoust. Soc. Am.*, 103:3079, 1998.
- [56] T. V. Chalikian, A. P. Sarvazyan, Th. Funck, V. N. Belonenko, and F. Dunn. Temperature dependences of the acoustic nonlinearity parameter  $B/A$  of aqueous solutions of amino acids. *J. Acoust. Soc. Am.*, 52:52–58, 1992.
- [57] A. Challapalli, L. Carroll, and E. O. Aboagye. Molecular mechanisms of hypoxia in cancer. *Clin. Transl. Imaging*, 5(3):225–253, 2017.
- [58] R. Chanamai and D. J. McClements. Ultrasonic attenuation of edible oils. *J. Am. Oil Chem. Soc.*, 75(10):1447–1448, 1998.
- [59] R. Chanamai and D. J. McClements. Ultrasonic attenuation of edible oils. *Journal of the American Oil Chemists’ Society*, 75(10):1447–1448, 1998.
- [60] F. Chavrier, C. Lafon, and A. Birer. Determination of the nonlinear parameter by propagating and modeling finite amplitude plane waves. *Phys. Med. Biol.*, 119(5):2639–2644, 2006.
- [61] J. Chen, X. Zhao, J. Fritsche, P. Yin, P. Schitt-Kopplin, W. Wang, X. Lu, H. U. Harling, E. D. Schleicher, R. Lehmann, and G. Xu. Practical approach for the identification and isomer elucidation of biomarkers detected in a metabonomic study for the discovery of individuals at risk for diabetes by integrating the chromatographic and mass spectric information. *Anal. Chem.*, 80:1280–1289, 2008.
- [62] P. Chen, S. Turco, R. J. G. van Sloun, A. Pollet, J. den Toonder, H. Wijkstra, and M. Mischi. In-vitro investigation of the relationship between microvascular structure and ultrasound contrast agent dynamics. In *2019 IEEE Int. Ultrason. Symp.*, pages 403–406, 2019.
- [63] W. Chen and S. Holm. Fractional laplacian time-space models for linear and nonlinear lossy media exhibiting arbitrary frequency power-law dependency. *J. Acoust. Soc. Am.*, 115:1424–1430, 2004.
- [64] Wen-Shiang Chen, Thomas J Matula, Andrew A Brayman, and Lawrence A Crum. A comparison of the fragmentation thresholds and inertial cavitation doses of different ultrasound contrast agents. *J. Acoust. Soc. Am.*, 113(1):643–651, 2003.
- [65] A. Chitnalah, D. Kourtiche, H. Jakjoud, and Mustapha Nadi. Pulse echo method for nonlinear ultrasound parameter measurement. *Techn. Acoust.*, 13:1–8, 2007.
- [66] M. J. Choi, S. R. Guntur, J. M. LEE, D. G. Paeng, K. I. Lee, and A. Coleman. Changes in ultrasonic properties of liver tissue in vitro during heatin-cooling cycle concomitant with thermal coagulation. *Ultrasound Med. Biol.*, 37(12):2000–2012, 2011.
- [67] K. Christensen-Jeffries, O. Couture, P. A Dayton, Y. C. Eldar, K. Hynynen, F. Kiessling, M. O’Reilly, G. F. Pinton, G. Schmitz, M.-X. Tang, et al. Super-resolution ultrasound imaging. *Ultrasound Med. Biol.*, 46(4):865–891, 2020.
- [68] S. H. Chung, A. E. Cerussi, C. Klifa, H. M. Baek, O. Birgul, G. Gulsen, S. I. Meritt, D. Hsiang, and B.J. Tromberg. In vivo water state measurements in breast cancer using broadband diffuse optical spectroscopy. *Phys. in Med. Biol.*, 53:6713–6727, 2008.
- [69] C. C. Church. The effects of an elastic solid surface layer on the radial pulsations of gas bubbles. *J. Acoust. Soc. Am.*, 97(3):1510–1521, 1995.
- [70] C. C. Church. Frequency, pulse length, and the mechanical index. *Acoust. Res. Lett. Online-Arlo*, 6(3):162–168, 2005.
- [71] T. R. Church, M. Wandell, C. Lofton-Day, S. J. Mongin, M. Burger, S. R. Payne, E. Castaños-Vélez, B. A. Blumenstein, T. Rösch, N. Osborn, D. Snover, R. W. Day, and D. F. Ransohoff. Prospective evaluation of methylated SEPT9 in plasma for detection of asymptomatic colorectal cancer. *Gut*, 63(2):317–325, 2014.
- [72] R. O. Cleveland and J. A. McAteer. *The Physics of Shock Wave Lithotripsy*. BC Decker Inc, London, second edition edition, 2007.
- [73] W. N. Cobb. Finite amplitude method for the determination of the acoustic nonlinearity parameter  $B/A$ . *J. Acoust. Soc. Am.*, 73(5):1525–1531, 1983.
- [74] A. B. Coppens, R. T. Beyer, M. B. Seiden, J. Donohue, F. Guepin, R. H. Hodson, and C. Townsend. Parameter of nonlinearity in fluids 2. *J. Acoust. Soc. Am.*, 38:797–804, 1965.
- [75] Jean-Michel Correas, Lori Bridal, Amélie Lesavre, Arnaud Méjean, Michel Claudon, and Olivier Hélénon. Ultrasound contrast agents: properties, principles of action, tolerance, and artifacts. *Eur. Radiol.*, 11(8):1316–1328, 2001.
- [76] G. A. Cortela, C. A. Negreira, and W. C. A. Pereira. Durability study of a gellan gum-based tissue-mimicking phantom for ultrasonic thermal therapy. *J. Acoust. Soc. Am.*, 147(3):1531–1545, 2020.
- [77] D. Cosgrove. Ultrasound contrast agents: An overview. *Eur J. Radiol.*, 60(3):324–330, 2006.
- [78] D. Cosgrove and N. Lassau. Imaging of perfusion using ultrasound. *Eur. J. Nucl. Med. Mol. Imaging*, 37:65–85, 2010.
- [79] B. Cox and P. Beard. Super-resolution ultrasound. *Nature*, 527:451–452, 2015.
- [80] M. J. Crocker, editor. *Encyclopedia of Acoustics*, volume 1, pages 193–202. John Wiley and Sons, Inc., New York, NY, 1997.

- [81] K. B. Cunningham, M. F. Hamilton, A. P. Brysev, and L. M. Krutyansky. Time-reversed sound beams of finite amplitude. *J. Acoust. Soc. Am.*, 109(6):2668–2674, 2001.
- [82] V. Daeichin, J. G. Bosch, A. Needles, F. S. Foster, A. van der Steen, and N. de Jong. Subharmonic, non-linear fundamental and ultraharmonic imaging of microbubble contrast at high frequencies. *Ultrasound Med. Biol.*, 41(2):486–497, 2015.
- [83] J. R. Davies, J. Tapson, and B. J. P. Mortimer. A novel phase locked cavity resonator for  $B/A$  measurements in fluids. *Ultrasonics*, 38:284–291, 2000.
- [84] L. A. Dawson and M. B. Sharpe. Image-guided radiotherapy: rationale, benefits, and limitations. *Lancet Oncol.*, 7(10):848–858, 2006.
- [85] N. de Jong and L. Hoff. Ultrasound scattering properties of Alunex microspheres. *Ultrasonics*, 31(3):175–181, 1993.
- [86] N. de Jong, L. Hoff, T. Skotland, and N. Bom. Absorption and scatter of encapsulated gas filled microspheres: theoretical considerations and some measurements. *Ultrasonics*, 30(2):95–103, 1992.
- [87] N. de Jong, R. Cornet, and C. T. Lancée. Higher harmonics of vibrating gas-filled microspheres. Part two: measurements. *Ultrasonics*, 32(6):455–459, 1994.
- [88] N. de Jong, P. J. A. Frinking, A. Bouakaz, and F. J. ten Cate. Detection procedures of ultrasound contrast agents. *Ultrasonics*, 38(1-8):87–92, 2000.
- [89] N. de Jong, M. Emmer, A. van Wamel, and M. Versluis. Ultrasonic characterization of ultrasound contrast agents. *Med. Biol. Eng. Comput.*, 47:861–873, 2009.
- [90] J. Delanghe. New screening diagnostic techniques in urinalysis. *Acta Clinica Belgica*, 62(3):155–161, 2007.
- [91] L. Demi, K. W. A. van Dongen, and M.D. Verweij. A contrast source method for nonlinear acoustic wave fields in media with spatially inhomogeneous attenuation. *J. Acoust. Soc. Am.*, 129(3):1221–1230, 2011.
- [92] L. Demi, B. E. Treeby, and M. D. Verweij. Comparison between two different full-wave methods for the computation of nonlinear ultrasound fields in inhomogeneous and attenuating tissue. *Proc. IEEE Int. Ultrason. Symp.*, pages 1464–1467, 2014.
- [93] A. J. Devaney. Quasi-plane waves and their use in radiation and scattering problems. *Optics communications*, 35:1–3, 1980.
- [94] C. F. Dietrich, J. C. Mertens, B. Braden, G. Schuessler, M. Ott, and A. Ignee. Contrast-enhanced ultrasound of histologically proven liver hemangiomas. *Hepatology*, 45(5):1139–1145, 2007.
- [95] C. F. Dietrich, M. A. Averkiou, J.-M. Correas, N. Lassau, E. Leen, and F. Piscaglia. An EFSUMB introduction into dynamic contrast-enhanced ultrasound (DCE-US) for quantification of tumour perfusion. *Ultraschall Med.*, 33(04):344–351, 2012.
- [96] C. F. Dietrich, J. Bamber, A. Berzigotti, S. Bota, V. Cantisani, L. Castera, D. Cosgrove, G. Ferraioli, M. Friedrich-Rust, O. H. Gilja, et al. EFSUMB guidelines and recommendations on the clinical use of liver ultrasound elastography, update 2017 (short version). *Ultraschall Med.*, 38(04):377–394, 2017.
- [97] C. F. Dietrich, R. G. Barr, A. Farrokh, M. Dighe, M. Hocke, C. Jenssen, Y. Dong, A. Saftoiu, and R. F. Havre. Strain elastography-how to do it? *Ultrasound Int. Open*, 3(4):E137, 2017.
- [98] C. F. Dietrich, M. Averkiou, M. B. Nielsen, R. G. Barr, P. N. Burns, F. Calliada, V. Cantisani, B. Choi, M. C. Chammas, D. A. Clevert, M. Claudon, J. M. Correas, X. W. Cui, D. Cosgrove, M. D’onofrio, Y. Dong, J. Eisenbrey, T. Fontanilla, O. H. Gilja, A. Ignee, C. Jenssen, Y. Kono, M. Kudo, N. Lassau, A. Lyshchik, M. F. Meloni, F. Moriyasu, C. Nolsøe, F. Piscaglia, M. Radzina, A. Saftoiu, P. S. Sidhu, L. Sporea, D. Schreiber-Dietrich, C. B. Sirlin, M. Stanczak, H. P. Weskott, S. R. Wilson, J. K. Willmann, T. K. Kim, H. J. Jang, A. Veziridis, and S. Westerway. How to perform contrast-enhanced ultrasound (CEUS). *Ultrasound Int. Open*, 4(1):E2, 2018.
- [99] C. F. Dietrich, E. Bibby, C. Jenssen, A. Saftoiu, J. Iglesias-Garcia, and R. F. Havre. Eus elastography: How to do it? *Endosc. Ultrasound*, 7(1):20–28, 2018.
- [100] C. F. Dietrich, C. Pállson Nolsøe, R. G. Barr, A. Berzigotti, P. N. Burns, V. Cantisani, M. C. Chammas, N. Chaubal, B. I. Choi, D.-A. Clevert, et al. Guidelines and good clinical practice recommendations for contrast-enhanced ultrasound (ceus) in the liver—update 2020 WFUMB in cooperation with EFSUMB, AFSUMB, AIUM, and FLAUS. *Ultrasound Med. Biol.*, 2020.
- [101] A. A. Doinikov, A. Novell, P. Calmon, and A. Bouakaz. Simulations and measurements of 3-d ultrasonic fields radiated by phased-array transducers using the westervelt equation. *J. Acoust. Soc. Am.*, 61(9):1470–1477, 2014.
- [102] F. Dong, E.L. Madsen, M.C. Macdonald, and J.A. Zagzebski. Nonlinearity parameter for tissue-mimicking materials. *Ultrasound Med. Biol.*, 25(5):831–838, 1999.
- [103] Z. Dong, K. Junichi, and Z. Wei. Model equation for acoustic nonlinear measurement of dispersive specimens at high frequency. *J. Acoust. Soc. Am.*, 23(10):2807–2810, 2006.
- [104] K. W. Van Dongen and M. D. Verweij. Sensitivity study of the acoustic nonlinearity parameter for measuring temperatures during high intensity focused ultrasound treatment. *J. Acoust. Soc. Am.*, 123(5):3225, 2008.
- [105] Stéphane Dorbolo, Hervé Caps, and Nicolas Vandewalle. Fluid instabilities in the birth and death of antibubbles. *New J. Phys.*, 5(1):74–77, 2003.
- [106] F. A. Duck. *Physical Properties of Tissue: a Comprehensive Reference Book*. Academic Press, London, 1990.
- [107] F. A. Duck. Nonlinear acoustics in diagnostic ultrasound. *Ultrasound Med. Biol.*, 28(1):1–18, 2002.
- [108] F. A. Duck and H. C. Starrit. Acoustic shock generation by ultrasonic imaging equipment. *Br. J. Radiol.*, 57:231–240, 1983.
- [109] F. Dunn, W. K. Law, and L. A. Frizzell. Nonlinear ultrasonic wave propagation in biological materials. *Ultrasonics symposium*, pages 527–532, 1981.
- [110] R. J. Eckersley, C. T. Chin, and P. N. Burns. Optimising phase and amplitude modulation schemes for imaging microbubble contrast agents at low acoustic power. *Ultrasound Med. Biol.*, 31(2):213–219, 2005.
- [111] F. Eggers and Th. Funck. Ultrasonic measurements with milliliter liquid samples in the 0.5-100 mhz range. *Am. Inst. Phys.*, 44:969–977, 1973.
- [112] J. R. Eisenbrey, J. K. Dave, V. G. Halldorsdottir, D. A. Merton, P. Machado, J. B. Liu, C. Miller, J. M. Gonzalez, S. Park, S. Dianis, et al. Simultaneous grayscale and subharmonic ultrasound imaging on a modified commercial scanner. *Ultrasonics*, 51(8):890–897, 2011.

[113] C. W. Elston and I. O. Ellis. Pathological prognostic factors in breast cancer. i. the value of histological grade in breast cancer: experience from a large study with long-term follow-up. *Histopathol.*, 19(5):403–410, 1991.

[114] J. Emery, S. Gassea, and C. Dugue. Coefficient de nonlinearite acoustique dans les melanges eau-methanol et eau-ethanol. *J. Phys.*, 11(40):231–234, 1979.

[115] M. Emmer, H. J. Vos, D. E. Goertz, A. van Wamel, M. Verluis, and N. de Jong. Pressure-dependent attenuation and scattering of phospholipid-coated microbubbles at low acoustic pressures. *Ultrasound Med. Biol.*, 35(1):102–111, 2009.

[116] R. L. Errabolu, C. M. Sehgal, and J. F. Greenleaf. Dependence of ultrasonic nonlinear parameter  $B/A$  on fat. *Ultrasonic Imag.*, 9:180–194, 1987.

[117] R. V. Errabolu, C. M. Sehgal, R. C. Bahn, and J. F. Greenleaf. Measurement of ultrasonic nonlinear parameter in excised fat tissues. *Ultrasound Med. Biol.*, 14(2):137–146, 1988.

[118] C. Errico, J. Pierre, S. Pezet, Y. Desailly, Z. Lenkei, O. Couture, and Tanter M. Ultrafast ultrasound localization microscopy for deep super-resolution vascular imaging. *Nature*, 527:499–502, 2015.

[119] E. C. Everbach and R. E. Apfel. An interferometric technique for  $B/A$  measurement. *J. Acoust. Soc. Am.*, 98(6):3428–3438, 1995.

[120] E. C. Everbach, Z. Zhu, P. Jiang, B. T. Chu, and R. E. Apfel. A corrected mixture law for  $B/A$ . *J. Acoust. Soc. Am.*, 89(1):446–447, 1991.

[121] T. Faez, D. Goertz, and N. de Jong. Characterization of Definity™ ultrasound contrast agent at frequency range of 5–15 mhz. *Ultrasound Med. Biol.*, 37(2):338–342, 2011.

[122] M. Fatemi and J. F. Greenleaf. Real-time assessment of the parameter of nonlinearity in tissue using the “nonlinear shadowing”. *Ultrasound Med. Biol.*, 22(9):1215–1228, 1996.

[123] O. Faust, U. R. Acharya, K. M. Meiburger, F. Molinari, J. E. Koh, C. H. Yeong, P. Kongmebhol, and K. H. Ng. Comparative assessment of texture features for the identification of cancer in ultrasound images: a review. *Biocybern. Biomed. Eng.*, 38(2):275–296, 2018.

[124] E. C. Fear, S. C. Hagness, P. M. Meaney, M. Okoniewski, and M. A. Stuchly. Breast tumor detection with near-field imaging. *IEEE microwave magazine*, 3(1):48–56, 2002.

[125] D. T. Fetzter, V. Rafailidis, C. Peterson, E. G. Grant, P. Sidhu, and R. G. Barr. Artifacts in contrast-enhanced ultrasound: a pictorial essay. *Abdom. Radiol.*, 43(4):977–997, 2018.

[126] E. A. Filonenko and V. A. Khokhlova. Effect of acoustic nonlinearity on heating of biological tissue by high-intensity focused ultrasound. *Ultrasound Med. Biol.*, 47(4):541–549, 2001.

[127] J. W. Fletcher, B. Djulbegovic, H. P. Soares, B. A. Siegel, V. J. Lowe, G. H. Lyman, R. E. Coleman, R. Wahl, J. C. Paschold, N. Avril, et al. Recommendations on the use of 18F-FDG PET in oncology. *J. Nucl. Med.*, 49(3):480–508, 2008.

[128] F. P. Fliedner, T. B. Engel Trine, H. H. El-Ali, A. E. Hansen, and A. Kjaer. Diffusion weighted magnetic resonance imaging (DW-MRI) as a non-invasive, tissue cellularity marker to monitor cancer treatment response. *BMC Cancer*, 20(1):1–9, 2020.

[129] I. Fogelman, G. Gnanasegaran, and H. van der Wall. *Radionuclide and hybrid bone imaging*. Springer, 2013.

[130] J. Folkman. Tumor angiogenesis: theraputic implications. *N. Engl. J. Med.*, 285(21):1182–1186, 1971.

[131] J. Folkman. The role of angiogenesis in tumor growth. In *Semin. Cancer Biol.*, volume 3, pages 65–71, 1992.

[132] F. Forsberg, W. T. Shi, and B. B. Goldberg. Subharmonic imaging of contrast agents. *Ultrasonics*, 38(1-8):93–98, 2000.

[133] F. E. Fox and G. D. Rock. Ultrasonic absorption in water. *J. Acoust. Soc. Am.*, 12:505–510, 1941.

[134] F. E. Fox and W. A. Wallace. Absorption of finite amplitude sound waves. *J. Acoust. Soc. Am.*, 26:994–1006, 1954.

[135] J. E. Freund, M. Buijs, C. D. Savci-Heijink, D. M. de Bruin J. J. M. C. H. de la Rosette, T. G. van Leeuwen, and M. P. Laguna. Optical coherence tomography in urologic oncology: a comprehensive review. *SN Compr. Clin. Med.*, 1:67–84, 2019.

[136] P. Frinking, T. Segers, Y. Luan, and F. Tranquart. Three decades of ultrasound contrast agents: a review of the past, present and future improvements. *Ultrasound Med. Biol.*, 46(4):892–908, 2020.

[137] P. J. A. Frinking and N. de Jong. Acoustic modeling of shell-encapsulated gas bubbles. *Ultrasound Med. Biol.*, 24(4):523–533, 1998.

[138] P. J. A. Frinking, A. Bouakaz, J. Kirkhorn, F. J. T. Cate, and N. de Jong. Ultrasound contrast imaging: current and new potential methods. *Ultrasound Med. Biol.*, 26(6):965 – 975, 2000.

[139] K. Froyso. Weakly nonlinear propagation of a pulsed sound beam. *J. Acoust. Soc. Am.*, 95(1):123–130, 1993.

[140] E. Fubini-Ghiron. Absorption of finite amplitude sound waves. *Alta Frequenza*, 4:530–581, 1935.

[141] Y. Fujii, N. Taniguchi, I. Akiyama, J. Tsao, and K. Itoh. A new system for in vivo assessment of the degree of nonlinear generation using the second harmonic component in echo signals. *Ultrasound Med. Biol.*, 30(11):1511–1516, 2004.

[142] H. Fukukita, S. Ueno, and T. Yano. Application of nonlinear effect to ultrasonic pulse reflection method-modulation characteristics of received pulse. *Jpn. J. Appl. Phys.*, 26:49–51, 1987.

[143] H. Fukukita, S. Ueno, and T. Yano. Ultrasound pulse reflection mode measurement of nonlinearity parameter  $B/A$  and attenuation coefficient. *J. Acoust. Soc. Am.*, 99(5):2775–2782, 1996.

[144] Jr. G. W. Ficken and E. A. Hiedemann. Simple form of the sing-around method for the determination of sound velocities. *J. Acoust. Soc. Am.*, 28(5):921–923, 1956.

[145] J.-L. Gennisson, T. Defieux, M. Fink, and M. Tanter. Ultrasound elastography: principles and techniques. *Diagn. Interv. Imaging*, 94(5):487–495, 2013.

[146] L. Germain, R. Jacques, and J. D. N. Cheeke. Acoustic microscopy applied to nonlinear characterization of biological media. *J. Acoust. Soc. Am.*, 86(4):1560–1565, 1989.

[147] R. C. Gessner, C. B. Frederick, F. S. Foster, and P. A. Dayton. Acoustic angiography: a new imaging modality for assessing microvasculature architecture. *Int. J. Biomed. Imaging*, 2013:1–9, 2013.

[148] S. Ginter, M. Liebler, E. Steiger, T. Dreyer, and R. E. Riedlinger. Full-wave modeling of therapeutic ultrasound: Nonlinear ultrasound propagation in ideal fluids. *J. Acoust. Soc. Am.*, 111:2049–2059, 2002.



- [149] D. E. Goertz, N. de Jong, and A. F. W. van der Steen. Attenuation and size distribution measurements of definit<sup>TM</sup> and manipulated definit<sup>TM</sup> populations. *Ultrasound Med. Biol.*, 33(9):1376–1388, 2007.
- [150] X. Gong, L. K. Zarembo, and V. A. Krasilnikov. Measurement of the acoustic nonlinear parameter of liquid nitrogen. *Akust. Zh.*, 9:382–383, 1963.
- [151] X. Gong, R. Feng, C. Zhu, and T. Shi. Ultrasonic investigation of the nonlinearity parameter  $B/A$  in biological media. *J. Acoust. Soc. Am.*, 76(3):949–950, 1984.
- [152] X. Gong, Z. Zhu, T. Shi, and J. Huang. Determination of the acoustic nonlinearity parameter in biological media using FAIS and ITD methods. *J. Acoust. Soc. Am.*, 86(1):1–5, 1989.
- [153] X. Gong, D. Zhang, J. Liu, H. Wang, Y. Yan, and X. Xu. Study of acoustic nonlinearity parameter imaging methods in reflection mode for biological tissues. *J. Acoust. Soc. Am.*, 116(3):1819–1825, 2004.
- [154] X. F. Gong, X. Z. Liu, and D. Zhang. Influences of tissue composition and structural features of biological media on the ultrasonic nonlinearity parameter. *Chin. J. Acoust.*, 12(3):265–270, 1993.
- [155] J. M. Gorce, M. Arditì, and M. Schneider. Influence of bubble size distribution on the echogenicity of ultrasound contrast agents. *Invest. Radiol.*, 35(11):661–671, 2000.
- [156] S. A. Goss and F. J. Fry. Nonlinear acoustic behavior in focused ultrasonic fields: observations of intensity dependent absorption in biological tissue. *IEEE Trans. Sonics Ultrason.*, SU-28, 1981.
- [157] T. Grandke. Interpolation algorithms for discrete fourier transforms of weighted signals. *IEEE Trans. Instrum. Meas.*, 32(2):350–355, 1983.
- [158] R. T. Greenlee, M. B. Hill-Harmon, T. Murray, and M. Thun. Cancer statistics, 2001. *CA: a cancer journal for clinicians*, 51(1):15–36, 2001.
- [159] M. Greenspan and C. E. Tschiegg. Speed of sound in water by a direct method. *J. Research Natl. Bur. Standards*, 59(4):249–254, 1957.
- [160] M. Greenspan and C. E. Tschiegg. Tables of the speed of sound in water. *J. Acoust. Soc. Am.*, 31:75–76, 1959.
- [161] C. Greis. Quantitative evaluation of microvascular blood flow by contrast-enhanced ultrasound (CEUS). *Clin. Hemorheol. Microcirc.*, 49(1-4):137–149, 2011.
- [162] T. E. Gureyev, D. M. Paganin, G. R. Myers, Y. I. Nesterets, and S. W. Wilkins. Phase-and-amplitude computer tomography. *Appl. Phys. Lett.*, 89(3):034102, 2006.
- [163] M. P. Hagelberg, G. Holton, and S. Kao. Calculation of  $B/A$  for water from measurements of ultrasonic velocity versus temperature and pressure to 10 000 kg/cm<sup>2</sup>. *J. Acoust. Soc. Am.*, 41(3):564–567, 1967.
- [164] A. Hall. The cytoskeleton and cancer. *Cancer and Metastasis Rev.*, 28(1-2):5–14, 2009.
- [165] M. F. Hamilton and D. T. Blackstock. On the coefficient of nonlinearity in nonlinear acoustics. *J. Acoust. Soc. Am.*, 83(1):74–77, 1987.
- [166] M. F. Hamilton and D. T. Blackstock, editors. *Nonlinear Acoustics*. Academic Press, 1998.
- [167] G. R. Harris, Y. Liu, S. Maruvada, and P. M. Gammell. Finite amplitude method for measurement of nonlinearity parameter  $B/A$  using plane-wave tone bursts. In *2007 IEEE Ultrasonics Symposium Proceedings*, pages 2072–2074, 2007.
- [168] L. Haumesser and F. V. Meulen. Reduced propagation path for  $B/A$  nonlinear parameter evaluation. *Proc. Mtgs. Acoust.*, 38:045023, 2019.
- [169] A. Hikata, H. Kwun, and C. Elbaum. Finite amplitude wave propagation in solid and liquid he. *J. Acoust. Soc. Am.*, 21(9):3932–3939, 1980.
- [170] S. N. Histed, M. L. Lindenberg, E. Mena, B. Turkbey, P. L. Choyke, and K. A. Kurdziel. Review of functional/anatomic imaging in oncology. *Nucl. Med. Commun.*, 33(4):349, 2012.
- [171] L. Hoff, P. C. Sontum, and B. Hoff. Acoustic properties of shell-encapsulated, gas-filled ultrasound contrast agents. *IEEE Ultrasonics Symposium*, pages 1441–1444, 1996.
- [172] Lars Hoff. *Acoustic characterization of contrast agents for medical ultrasound imaging*. Springer, Heidelberg, 2001.
- [173] T. Hofmarcher, P. Lindgren, N. Wilking, and B. Jönsson. The cost of cancer in Europe 2018. *Eur. J. Cancer*, 129:41–49, 2020.
- [174] G. Holton, M. P. Hagelberg, S. Kao, and Jr W. H. Johnson. Ultrasonic-velocity measurements in water at pressures to 10 000 kg/cm<sup>2</sup>. *J. Acoust. Soc. Am.*, 43(1):102–107, 1968.
- [175] H. Houshmand, R. J. McGough, E. Ebbini, H. Lee, and C. A. Cain. Ultrasonic transmission mode imaging of the nonlinear parameter  $B/A$ : a simulation study. *1988 Ultrasonics symposium*, pages 979–983, 1988.
- [176] S. Hu, J. Zhang, C. Cheng, Q. Liu, G. Sun, and C. Zuo. The role of 18 F-FDG PET/CT in differentiating malignant from benign portal vein thrombosis. *Abdom. imaging*, 39(6):1221–1227, 2014.
- [177] C. Hunter, O. A. Sapozhnikov, A.D. Maxwell, V. A. Khokhlova, Y-N Wang, B. MacConaghy, and W. Kreider. An ultrasonic caliper device for measuring acoustic nonlinearity. *Physics Procedia*, 87:93–98, 2016.
- [178] J.-J. Hwang and D. H. Simpson. Two pulse technique for ultrasonic harmonic imaging, September 14 1999. US Patent 5,951,478.
- [179] N. Ichida, T. Sato, and M. Linzer. Imaging the nonlinear ultrasonic parameter of a medium. *Ultrasonic Imaging*, 5:295–299, 1983.
- [180] N. Ichida, T. Sato, and M. Linzer. Real-time nonlinear parameter tomography using impulsive pumping waves. *IEEE Trans. Sonics Ultrason.*, 31(5):635–641, 1984.
- [181] K. Iinuma. Ultrasonic method and apparatus for tissue characterization and imaging of nonlinear parameter, September 20 1988. US Patent 4,771,786.
- [182] F. Ingenito and A. O. Williams Jr. Calculation of second-harmonic generation in a piston beam. *J. Acoust. Soc. Am.*, 49:319–328, 1971.
- [183] E. Jackson, R. O. Cleveland, and C. C. Coussios. The origins of nonlinear enhancement in ex vivo tissue during high intensity focused ultrasound (HIFU) ablation. In *Proc. Mtgs Acoust.*, volume 19, page 075067. Acoustical Society of America, 2013.
- [184] E.J. Jackson, C.C. Coussios, and R.O. Cleveland. Nonlinear acoustic properties of ex vivo bovine liver and the effects of temperature and denaturation. *Phys. Med. Biol.*, 59:3223–3238, 2014.
- [185] R. K. Jain, S. A. Shah, and P. L. Finney. Continuous noninvasive monitoring of ph and temperature in rat walker 256 carcinoma during normoglycemia and hyperglycemia. *J. of the National Cancer Institute*, 73(2):429–436, 1984.

- [186] M. Janiszewska, M. C. Primi, and T. Izard. Cell adhesion in cancer: Beyond the migration of single cells. *J. Biolog. Chem.*, 295(8):2495–2505, 2020.
- [187] M. Jayson and H. Sanders. Increased incidence of serendipitously discovered renal cell carcinoma. *Urology*, 51(2):203–205, 1998.
- [188] H. Jeong, S. Zhang, D. Barnard, and X. Li. Significance of accurate diffraction corrections for the second harmonic wave in determining the acoustic nonlinearity parameter. *AIP Advances*, 5(9):097179, 2015.
- [189] H. Jeong, S. Zhang, and X. Li. A novel method for extracting acoustic nonlinearity parameters with diffraction corrections. *J. Mech. Sci. Technol.*, 30(2):643–652, 2016.
- [190] H. Jeong, D. Barnard, S. Cho, S. Zhang, and X. Li. Receiver calibration and the nonlinearity parameter measurement of thick solid samples with diffraction and attenuation corrections. *Ultrasonics*, 81:147–157, 2017.
- [191] P. Ji, E. Tan, W. Gan, and J. Yang. A comparative analysis of preprocessing methods for the parametric loudspeaker based on the Khokhlov–Zabolotskaya–Kuznetsov equation for speech reproduction. In *IEEE Trans. Audio Speech Lang. Process.*, volume 19, pages 937–946, 2011.
- [192] K.-T. Jin, J.-Y. Yao, X.-L. Fang, H. Di, and Y.-Y. Ma. Roles of lncRNAs in cancer: focusing on angiogenesis. *Life Sci.*, page 117647, 2020.
- [193] M. E. Kamphuis, M. J. W. Greuter, R. H. J. A Slart, and C. H. Slump. Quantitative imaging: systematic review of perfusion/flow phantoms. *Eur. Radiol. Exp.*, 4(1):1–13, 2020.
- [194] O. F. Kaneko and J. K. Willmann. Ultrasound for molecular imaging and therapy in cancer. *Quant. Imaging Med. Surg.*, 2(2):87–97, 2012.
- [195] H. A. Kashkooli, P. J. Dolan, and C. W. Smith. Measurement of the acoustic nonlinearity parameter in water, methanol, liquid nitrogen, and liquid helium-2 by two different methods: A comparison. *J. Acoust. Soc. Am.*, 82(6):2086–2089, 1987.
- [196] A. Kato and Y. Watanabe. Measurement method of spatial distribution of nonlinearity parameter  $B/A$  using nonlinear interaction of two sound waves. *Jpn. J. Appl. Phys.*, 32:2274–2278, 1993.
- [197] A. Kato and Y. Watanabe. Diffraction effect on phase deviation caused by nonlinear interaction between two sound waves in measuring spatial distribution of nonlinearity parameter  $B/A$ . *Jpn. J. Appl. Phys.*, 33:2922–2928, 1994.
- [198] W. Keck and R. T. Beyer. Frequency spectrum of finite amplitude ultrasonic waves in liquids. *Phys. Fluids*, 3(3):346–352, 1960.
- [199] H. Khelladi, F. Plantier, J. L. Daridon, and H. Djelouah. Measurement under high pressure of the nonlinearity parameter  $B/A$  in glycerol at various temperatures. *Ultrasonics*, 49(8):668–675, 2009.
- [200] D. Kim, J. F. Greenleaf, and C. M. Sehgal. Ultrasonic imaging of the nonlinear parameter  $B/A$ : Simulation studies to evaluate phase and frequency modulation methods. *Ultrasound Med. Biol.*, 16(2):175–181, 1990.
- [201] H. J. Kim, L. S. Schmerr, and A. Sedov. Generation of the basis sets for multi-gaussian ultrasonic beam models—an overview. *J. Acoust. Soc. Am.*, 119(4):1971–1978, 2006.
- [202] T. K. Kim, H. J. Jang, P. N. Burns, J. Murphy-Lavallee, and S. R. Wilson. Focal nodular hyperplasia and hepatic adenoma: differentiation with low mechanical-index contrast-enhanced sonography. *Am. J. Roentgenol.*, 190(1):58–66, 2008.
- [203] R. L. King, Y. Liu, S. Maruvada, B. A. Herman, and K. A. Wear. Development and characterization of a tissue-mimicking material for high-intensity focused ultrasound. *IEEE Trans. Ultrason. Ferroelectr. Freq. Control*, 58(7):1397–1405, 2011.
- [204] I.-C. Jr. Kiricuta and V. Simplăceanu. Tissue water content and nuclear magnetic resonance in normal and tumor tissues. *Cancer Res.*, 35(5):1164–1167, 1975.
- [205] Jonathan A Kopechek, Kevin J Haworth, Jason L Raymond, T Douglas Mast, Stephen R Perrin Jr, Melvin E Klegerman, Shaoling Huang, Tyrone M Porter, David D McPherson, and Christy K Holland. Acoustic characterization of echogenic liposomes: frequency-dependent attenuation and backscatter. *J. Acoust. Soc. Am.*, 130(5):3472–3481, 2011.
- [206] S. Kotopoulis, K. Johansen, O. H. Gilja, A. T. Poortinga, and M. Postema. Acoustically active antibubbles. *Acta Phys. Pol. A*, 127(1):99–102, 2015.
- [207] P. Koumoutsakos, I. Pivkin, and F. Milde. The fluid mechanic of cancer and its therapy. *Annu. Rev. Fluid Mech.*, 45:325–355, 2013.
- [208] D. Kourtiche, L. Allies, A. Chitnalah, and M. Nadi. Harmonic propagation of finite amplitude sound beams: comparative method in pulse echo measurement of nonlinear  $B/A$  parameter. *Meas. Sci. and Technol.*, 12:1990–1995, 2001.
- [209] S. M. Kramer, S. L. McBride, and H. D. Mair. Characteristics of wide-band planar ultrasonic transducers using plane and edge wave contributions. *IEEE Trans. Ultrason. Ferroelectr. Freq. Control*, 35(2):253–263, 1988.
- [210] V. A. Krasilnikov, V. V. Shklovskaya-kordy, and L. K. Zarembo. On the propagation of ultrasonic waves of finite amplitude in liquids. *J. Acoust. Soc. Am.*, 29:642–647, 1957.
- [211] F. W. Kremkau and K. J. W. Taylor. Artifacts in ultrasound imaging. *J. Ultrasound Med.*, 5:227–237, 1986.
- [212] W. H. Kruskal and W. A. Wallis. Use of ranks in one-criterion variance analysis. *J. Am. Stat. Assoc.*, 47(260):583–621, 1952.
- [213] L. M. Krutyansky, V. L. Preobrazhensky, Ph. Pernod, and O. B. Matar. Nonlinear imaging of isoechogenic phantoms using phase conjugation of the second acoustic harmonic. *Physics of wave phenomena*, 15(3):186–190, 2007.
- [214] N. Kudo, R. Uzbekov, R. Matsumoto, R. Shimizu, C. S. Carlson, N. Anderton, A. Deroubaix, C. Penny, A. T. Poortinga, D. M. Rubin, A. Bouakaz, and M. Postema. Asymmetric oscillations of endoskeletal antibubbles. *Jpn. J. Appl. Phys.*, 59:SKKE02, 2020.
- [215] M. P. J. Kuenen, M. Mischi, and H. Wijkstra. Contrast-ultrasound diffusion imaging for localization of prostate cancer. *IEEE Trans. Med. Imag.*, 30:1493–1502, 2011.
- [216] M. P. J. Kuenen, T. A. Saidov, H. Wijkstra, and M. Mischi. Spatiotemporal correlation of ultrasound-contrast-agent dilution curves for angiogenesis localization by dispersion imaging. *IEEE Trans. Ultrason. Ferroelectr. Freq. Control*, 60(12):2665–2669, 2013.
- [217] M. P. J. Kuenen, T. A. Saidov, H. Wijkstra, and M. Mischi. Contrast-ultrasound dispersion imaging for prostate cancer localization by improved spatiotemporal similarity analysis. *Ultrasound Med Biol*, 39(9):1631–1641, 2013.
- [218] M. P. J. Kuenen, I. H. F. Herold, H. H. M. Korsten, J. J. M. C. H. de la Rosette, and H. Wijkstra. Maximum-likelihood estimation for indicator dilution analysis. *IEEE Trans. Biomed. Eng.*, 61(3):821–831, 2014.

- [219] A. Kuhnel, U. Grob, K. Jacob, and M. O. Doss. Studies on coproporphyrin isomers in urine and feces in the porphyrias. *Clin. Chim. Acta*, 282:45–58, 1999.
- [220] T. Kujawska, J. Wojcik, L. Filipczyński, and J. Etienne. A new method for determination of the acoustic nonlinearity parameter  $B/A$  in multilayer biological media. *WCU 2003*, pages 81–84, 2003.
- [221] H. L. Kuntz, E. L. Hixson, and W. W. Ryan. The rayleigh distance and geometric nearfield size of nonplane sound radiators. *J. Acoust. Soc. Am.*, pages S82–S83, 1983.
- [222] J. Kushibiki, M. Ishibashi, N. Akashi, T. Sannomiya, N. Chubachi, and F. Dunn. Measurement of the acoustic nonlinearity parameter  $B/A$  in solvents: Dependence on chain length and sound velocity. *J. Acoust. Soc. Am.*, 102(5):3038–3044, 1997.
- [223] V. P. Kuznetsov. Equations of nonlinear acoustics. *Sov. Phys. Acoust.*, 16(4):548–553, 1970.
- [224] J. Kvam, S. Holm, and B. A. J. Angelsen. Exploiting ballou’s rule for better tissue classification. *J. Acoust. Soc. Am.*, 145(4):2103–2112, 2019.
- [225] J. Kvam, S. Solberg, O. F. Myhre, A. Rodriguez-Molares, and B. A. J. Angelsen. Nonlinear bulk elasticity imaging using dual frequency ultrasound. *J. Acoust. Soc. Am.*, 146(4):2492–2500, 2019.
- [226] M. Lampaskis and M. Averkiou. Investigation of the relationship of nonlinear backscattered ultrasound intensity with microbubble concentration at low MI. *Ultrasound Med. Biol.*, 36(2):306–312, 2010.
- [227] W. K. Law, L. A. Frizzell, and F. Dunn. Ultrasonic determination of the nonlinearity parameter  $B/A$  for biological media. *J. Acoust. Soc. Am.*, 69(4):1210–1212, 1981.
- [228] W. K. Law, L. A. Frizzell, and F. Dunn. Nonlinear ultrasonic propagation in biological media. *J. Acoust. Soc. Am.*, 45:55–58, 1982.
- [229] W. K. Law, L. A. Frizzell, and F. Dunn. Comparison of thermodynamic and finite amplitude methods of  $B/A$  measurement in biological materials. *J. Acoust. Soc. Am.*, 74:1295–1297, 1983.
- [230] W. K. Law, L. A. Frizzell, and F. Dunn. Determination of the nonlinearity parameter  $B/A$  of biological media. *Ultrasound Med. Biol.*, 11(2):307–318, 1985.
- [231] J. H. Lee, H. Cheong, S. S. Lee, C. K. Lee, Y. S. Sung, J.-W. Huh, J.-A. Song, and H. Choe. Perfusion assessment using intravoxel incoherent motion-based analysis of diffusion-weighted magnetic resonance imaging: validation through phantom experiments. *Invest. Radiol.*, 51(8):520–528, 2016.
- [232] L. Leenhardt, M. F. Erdogan, L. Hegedus, S. J. Mandel, R. Paschke, T. Rago, and G. Russ. 2013 european thyroid association guidelines for cervical ultrasound scan and ultrasound-guided techniques in the postoperative management of patients with thyroid cancer. *Eur. Thyroid J.*, 2(3):147–159, 2013.
- [233] X. Li, S. Zhang, H. Jeong, and S. Cho. Calibration of focused ultrasonic transducers and absolute measurements of fluid nonlinearity with diffraction and attenuation corrections. *J. Acoust. Soc. Am.*, 142:984–990, 2017.
- [234] X. Liu, J. Li, X. Gong, Z. Zhu, and D. Zhang. Theoretical and experimental study of the third-order nonlinearity parameter  $C/A$  for biological media. *Physica S*, 228:172–178, 2007.
- [235] X. Liu, X. Gong, C. Yin, J. Li, and D. Zhang. Noninvasive estimation of temperature elevations in biological tissues using acoustic nonlinearity parameter imaging. *Ultrasound Med. Biol.*, 34(3):414–424, 2008.
- [236] B. Ljungberg, K. Bensalah, A. Bex, S. Canfield, S. Dabestani, F. Hofmann, M. Hora, M. A. Kuczyk, T. Lam, L. Marconi, et al. Renal cell carcinoma. *Eur. Assoc. Urol.*, 2015.
- [237] A. Lopatzidis and R. K. Millard. Empirical estimators of gamma fits to tracer dilution curves and their technical basis and practical scope. *Phys. Meas.*, 22(4):N1 – N5, 2001.
- [238] T. Lorentzen, C. P. Nolsøe, C. Ewertsen, M. B. Nielsen, E. Leen, R. F. Havre, N. Gritzmann, B. Brkljacic, D. Nürnberg, A. Kabaalioglu, D. Strobel, C. Jessen, F. Piscaglia, O. H. Gilja, P. S. Sidhu, and C. F. Dietrich. EFSUMB guidelines on interventional ultrasound (INVUS), part i—general aspects (long version). *Ultraschall Med.*, 36(05):E1–E14, 2015.
- [239] T. Lorentzen, CP Nolsøe, C. Ewertsen, MB Nielsen, E. Leen, RF Havre, N. Gritzmann, B. Brkljacic, D. Nürnberg, A. Kabaalioglu, D. Strobel, C. Jessen, F. Piscaglia, O. H. Gilja, P. S. Sidhu, and C. F. Dietrich. EFSUMB guidelines on interventional ultrasound (invus), part i—general aspects (long version). *Ultraschall Med.*, 36(05):E1–E14, 2015.
- [240] K. H. Lu. Screening for ovarian cancer in asymptomatic women. *JAMA*, 319(6):557–558, 2018.
- [241] Y. Lu, X. Liu, X. Gong, and D. Zhang. Relationship between the temperature and the acoustic nonlinearity parameter in biological tissues. *Chinese Science Bulletin*, 49(22):2360–2363, 2004.
- [242] Z. Lu, J. L. Daridon, B. Lagourette, and S. Ye. A phase-comparison method for measurement of the acoustic nonlinearity parameter  $B/A$ . *Meas. Sci. Technol.*, 9:1699–1705, 1998.
- [243] Z. Lu, B. Lagourette, and J. L. Daridon. Acoustic nonlinearity parameter of liquid alkanes as a function of temperature, chain length and isomerism. *Physics and Chemistry of Liquids*, pages 255–266, 2001.
- [244] Q. Ma, Y. Ma, X. Gong, and D. Zhang. Improvement of tissue harmonic imaging using the pulse-inversion technique. *Ultrasound Med. Biol.*, 31:889–894, 2005.
- [245] W. M. Madigosky, I. Rosenbaum, and R. Lucas. Sound velocities and  $B/A$  in fluorocarbon fluids and in several low density solids. *J. Acoust. Soc. Am.*, 38:1639–1643, 1981.
- [246] H. B. Mann and D.R. Whitney. On a test of whether one of two random variables is stochastically larger than the other. *Ann. Math. Stat.*, 18(1):50–60, 1947.
- [247] C. K. Mannaerts, R. R. Wildeboer, A. W. Postema, J. Hagemann, L. Budäus, D. Tilki, M. Mischi, H. Wijkstra, and G. Salomon. Multiparametric ultrasound: evaluation of greyscale, shear wave elastography and contrast-enhanced ultrasound for prostate cancer detection and localization in correlation to radical prostatectomy specimens. *BMC Urology*, 18(1):1–10, 2018.
- [248] C. K. Mannaerts, M. R. W. Engelbrecht, A. W. Postema, R. A. A. van Kollenburg, C. M. A. Hoeks, C. D. Savci-Heijink, R. J. G. van Sloun, R. R. Wildeboer, T. M. de Reijke, M. Mischi, et al. Detection of clinically significant prostate cancer in biopsy-naïve men: direct comparison of systematic biopsy, multiparametric mri-and contrast-ultrasound-dispersion imaging-targeted biopsy. *BJU Int.*, 126(4):481–493, 2020.
- [249] G. Mariani, L. Bruselli, T. Kuwert, E. E. Kim, A. Flotats, O. Israel, M. Dondi, and N. Watanabe. A review on the clinical uses of spect/ct. *Eur. J. Nucl. Med. Mol. Imaging*, 37(10):1959–1985, 2010.
- [250] P. Marmottant, S. van der Meer, M. Emmer, Mi. Versluis, N. de Jong, S. Hilgenfeldt, and D. Lohse. A model for large amplitude oscillations of coated bubbles accounting for buckling and rupture. *J. Acoust. Soc. Am.*, 118(6):3499–3505, 2005.

- [251] H. Maruyama, M. Takashi, H. Ishibashi, H. Okugawa, S. Okabe, M. Yoshikawa, and O. Yokosuka. Ultrasound-guided treatments under low acoustic power contrast harmonic imaging for hepatocellular carcinomas undetected by B-mode ultrasonography. *Liver. Int.*, 29:708–714, 2008.
- [252] K. M. Meiburger, S. Y. Nam, E. Chung, L. J. Suggs, S. Y. Emelianov, and F. Molinari. Skeletonization algorithm-based blood vessel quantification using in vivo 3D photoacoustic imaging. *Phys. Med. Biol.*, 61(22):7994–8009, 2016.
- [253] C. S. Melincovici, A. B. Bosca, S. Susman, M. Marginean, C. Mihu, M. Istrate, J.-M. Moldovan, A. L. Roman, and C. M. Mihu. Vascular endothelial growth factor (VEGF)-key factor in normal and pathological angiogenesis. *Rom. J. Morphol. Embryol.*, 59(2):455–467, 2018.
- [254] U. Menon, A. Gentry-Maharaj, R. Hallett, A. Ryan, M. Burnell, A. Sharma, S. Lewis, S. Davies, S. Philpott, A. Lopes, K. Godfrey, D. Oram, J. Herod, K. Williamson, M. W. Seif, I. Scott, T. Mould, R. Woolas, J. Murdoch, S. Dobbs, N. N. Asmo, S. Leeson, D. Cruickshank, A. McGuire, S. Campbell, L. Fallowfield, N. Singh, A. Dawney, S. J. Skates, M. Parmaer, and I. Jacobs. Sensitivity and specificity of multimodal and ultrasound screening for ovarian cancer, and stage distribution of detected cancers: results of the prevalence screen of the uk collaborative trial of ovarian cancer screening (UKCTOCS). *Lancet Oncol.*, 10(4):327–340, 2009.
- [255] F. V. Meulen and L. Haumesser. Evaluation of  $B/A$  nonlinear parameter using an acoustic self-calibrated pulse-echo method. *Applied Phys. Letters*, 92:214106, 2008.
- [256] I. G. Mikhailov and V. A. Shutilov. Diffraction of light on harmonics of ultrasound waves, distorted in the process of propagation in liquid. *Soviet Phys.-Acoustics*, 5:75–78, 1959.
- [257] I. G. Mikhailov and V. A. Shutilov. About the distortion of the shape of finite amplitudes ultrasound waves in various liquids. *Akust. Zh.*, 5:340–346, 1960.
- [258] R. K. Millard. Indicator-dilution dispersion models and cardiac output computing methods. *Am. Physiol. Soc.*, 272(4):H2004–H2012, 1997.
- [259] J. G. Miller, D. E. Yuhas, J. W. Mimbs, S. B. Dierker, L. J. Busse, J. J. Laterra, A. N. Weiss, and B. E. Sobel. Ultrasonic tissue characterization: Correlation between biochemical and ultrasonic indices of myocardial injury. In *1976 Ultrasonics Symposium*, pages 33–43. IEEE, 1976.
- [260] M. Mischi, T. Kalker, and E. Korsten. Videodensitometric methods for cardiac output measurements. *EURASIP J. Adv. Signal Process.*, page 2003 862083, 2003.
- [261] M. Mischi, M. P. J. Kuenen, and H. Wijkstra. Angiogenesis imaging by spatiotemporal analysis of ultrasound-contrast-agent dispersion kinetics. *IEEE Trans. Ultrason. Ferroelectr. Freq. Control*, 59(4):621–629, 2012.
- [262] M. Mischi, M. P. J. Kuenen, and H. Wijkstra. Angiogenesis imaging by spatiotemporal analysis of ultrasound contrast agent dispersion kinetics. *IEEE Trans. Ultrason. Ferroelectr. Freq. Control*, 59(4):621–629, 2012.
- [263] M. Mischi, N. G. Rognin, and M. A. Averkiou. *Ultrasound imaging modalities*. Elsevier, 2014.
- [264] H. Moch, P. A. Humphrey, and T. M. Ulbright. Who classification of tumours of the urinary system and male genital organs. In *WHO classification of tumours of the urinary system and male genital organs*. Lyon: IARC Press, 2016.
- [265] T. G. Muir and E. L. Carstensen. Prediction of nonlinear acoustic effects at biomedical frequencies and intensities. *Ultrasound Med. Biol.*, 6:345–357, 1980.
- [266] BG Muller, A Swaan, DM de Bruin, W van den Bos, AW Schreurs, DJ Faber, ECH Zwartkruis, L Rozendaal, AN Vis, JA Nieuwenhuijzen, et al. Customized tool for the validation of optical coherence tomography in differentiation of prostate cancer. *Technol. Cancer Res. Treat.*, 16(1): 57–65, 2017.
- [267] J. M. Munson and A. C. Shieh. Interstitial fluid flow in cancer: implications for disease progression and treatment. *Cancer Manag. Res.*, 6:317, 2014.
- [268] Y. Nakagawa, M. Nakagawa, M. Yoneyama, and M. Kikuchi. Nonlinear parameter imaging computed tomography by parametric acoustic array. In *IEEE 1984 Ultrasonics Symposium*, pages 673–676. IEEE, 1984.
- [269] Y. Nakagawa, W. Hou, A. Cai, N. Arnold, and G. Wade. Nonlinear parameter imaging with finite-amplitude sound waves. In *IEEE 1986 Ultrasonics Symposium*, pages 901–904. IEEE, 1986.
- [270] A. S. Narang and S. Varia. *Role of tumor vascular architecture in drug delivery*, volume 63. Elsevier, 2011.
- [271] K. Naugolnykh. Nonlinear acoustics: from research in physics to application (historical incidents). *Acoust. Phys.*, 55(3):338–344, 2009.
- [272] K. Naugolnykh and L. Ostrovskii. *Nonlinear Wave Processes in Acoustics*, chapter 1, pages 1–11. Cambridge University Press, Cambridge, 1998.
- [273] P. G. Newman and G. S. Rozycki. The history of ultrasound. *Surg. Clin. North Am.*, 78(2): 179–195, 1998.
- [274] B. Nicholson and D. Theodorescu. Angiogenesis and prostate cancer tumor growth. *J. Cell. Biochem.*, 91(1):125–150, 2004.
- [275] B. Nico, V. Benagiano, D. Mangieri, N. Maruotti, A. Vacca, and D. Ribatti. Evaluation of microvascular density in tumors, pro and contra. *Histol. Histopathol.*, 23(5):601–607, 2008.
- [276] C. Nikolini, P. Carlo, and S. Ridella. The physical state of intranuclear water and ions: Changes during cell proliferation and chemically induced carcinogenesis. *Cancer Res.*, 15(2):184–189, 1987.
- [277] M. Nikoonahad and D. C. Liu. Pulse-echo  $B/A$  measurement using variable amplitude excitation. In *1989 IEEE Ultrasonics Symposium*, pages 1047–1051. IEEE, 1989.
- [278] M. Nikoonahad and D. C. Liu. Pulse-echo single frequency acoustic nonlinearity parameter ( $B/A$ ) measurement. *IEEE Trans. Ultrason. Ferroelectr. Freq. Control*, 37(2):127–134, 1990.
- [279] O. Nomoto and K. Negishi. Diffraction of light by ultrasonic waves of finite amplitude. *Acta Acustica united with Acustica*, 15(4):223–235, 1965.
- [280] A. Novell, J. M. Escoffre, and A. Bouakaz. Ultrasound contrast imaging in cancer –technical aspects and prospects. *Curr. Mol. Imaging*, 2:77–88, 2013.
- [281] Anthony Novell, Jean-Michel Escoffre, and Ayache Bouakaz. Second harmonic and subharmonic for non-linear wideband contrast imaging using a capacitive micromachined ultrasonic transducer array. *Ultrasound Med. Biol.*, 39(8):1500–1512, 2013.
- [282] S. A. Ooss, L. A. Frizell, and F. Dunn. Ultrasonic absorption and attenuation in mammalian tissues. *Ultrasound Med. Biol.*, 5:181–186, 1979.
- [283] Maija-Riitta Ordén, Jukka S Jurvelin, and Pertti P Kirkinen. Kinetics of a us contrast agent in benign and malignant adnexal tumors. *Radiol.*, 226(2):405–410, 2003.



- [284] A. R. Padhani. Dynamic contrast-enhanced MRI in clinical oncology: current status and future directions. *J. Magn. Reson. Imaging*, 16(4):407–422, 2002.
- [285] A. R. Padhani, G. Liu, D. Mu-Koh, T. L. Chenevert, H. C. Thoeny, T. Takahara, A. Dzik-Jurasz, B. D. Rossand, M. van Cauteren, D. Collins, D. A. Hammoud, G. J. S. Rustin, B. Taouli, and P. L. Choyke. Diffusion-weighted magnetic resonance imaging as a cancer biomarker: consensus and recommendations. *Neoplasia*, 11(2):102–125, 2009.
- [286] A. Panfilova, S. Shelton, R. J. G. Sloun, L. Demi, H. Wijkstra, P. A. Dayton, and M. Mischi. Does contrast ultrasound dispersion imaging reveal changes in tortuosity? a comparison with acoustic angiography. *2016 IEEE Int. Ultrason. Symp.*, 2016.
- [287] A. Panfilova, R. J. G. van Sloun, R. Wildeboer, H. Wijkstra, , and M. Mischi. A fixed-distance plane wave method for estimating the ultrasound coefficient of nonlinearity. In *Proc. Mtgs. Acoust.*, volume 34, page 020001. Acoustical Society of America, New York, 2018.
- [288] A. Panfilova, S. E. Shelton, C. Caresio, R. J. G. van Sloun, F. Molinari, H. Wijkstra, P. A. Dayton, and M. Mischi. On the relationship between dynamic contrast-enhanced ultrasound parameters and the underlying vascular architecture extracted from acoustic angiography. *Ultrasound Med. Biol.*, 45(2):539–548, 2019.
- [289] A. Panfilova, X. Chen, R. J. G. van Sloun, H. Wijkstra, O. A. Sapozhnikov, and M. Mischi. The generalized finite amplitude insert-substitution method for  $B/A$  measurement of tissues and liquids. *Proc. Mtgs. Acoust.*, 42(1):020001, 2020.
- [290] Anastasiia Panfilova, R. J. G. van Sloun, Hessel Wijkstra, Oleg A. Sapozhnikov, and Massimo Mischi. A review on  $B/A$  measurement methods with a clinical perspective. *J. Acoust. Soc. Am.*, 149(4):2200–2237, 2021.
- [291] C. Pantea, C. F. Osterhoudt, and D. N. Sinha. Determination of acoustical nonlinear parameter of water using the finite amplitude method. *Ultrasonics*, 53:1012–1019, 2013.
- [292] D. M. Patterson, A. R. Padhani, and D. J. Collins. Technology insight: water diffusion MRI—a potential new biomarker of response to cancer therapy. *Nat. Clin. Pract. Oncol.*, 5(4):220–233, 2008.
- [293] M.-F. Penet, S. Kakkad, F. Wildes, and Z. M. Bhujwalla. Water and collagen content are high in pancreatic cancer: Implications for quantitative metabolic imaging. *Front. Oncol.*, 10:3189, 2021.
- [294] F. Plantier, J. L. Daridon, and B. Lagourette. Nonlinear parameter ( $B/A$ ) measurements in methanol, 1-butanol and 1-octanol for different pressures and temperatures. *J. Phys. D: Appl. Phys.*, 35:1063–1067, 2002.
- [295] F. Plantier, J. L. Daridon, and B. Lagourette. Measurement of the  $B/A$  nonlinearity parameter under high pressure: Application to water. *J. Acoust. Soc. Am.*, 111(2):707–715, 2002.
- [296] F. Plantier, J. L. Daridon, and B. Lagourette. Measurement of the acoustic nonlinearity parameter in liquid alkanes under pressure and comparison with the Lee - Kesler correlation. *J. Acoust. Soc. Am.*, 35:109–116, 2003.
- [297] M. S. Plesset and A. Prosperetti. Bubble dynamics and cavitation. *Annual review of fluid mechanics*, 9(1):145–185, 1977.
- [298] D. B. Plewes and W. Kucharczyk. Physics of MRI: a primer. *J. Magn. Reson. Imag.*, 35(5):1038–1054, 2012.
- [299] A. M. Ponce, B. L. Viglianti, D. Yu, P. S. Yarmolenko, C. R. Michelich, J. Woo, M. B. Bally, and M. W. Dewhirst. Magnetic resonance imaging of temperature-sensitive liposome release: Drug dose painting and antitumor effects. *J. Natl. Cancer Inst.*, 99(1):53–63, 2007.
- [300] A. T. Poortinga. Micron-sized antibubbles with tunable stability. *Colloids and Surf A*, 419:15–20, 2013.
- [301] M. Postema and O. H. Gilja. Contrast-enhanced and targeted ultrasound. *World J. Gastroenterol.*, 17(1):28–41, 2005.
- [302] M. Postema and O. H. Gilja. Ultrasound-directed drug delivery. *Curr. Pharm. Biotechnol.*, 8(6):355–361, 2007.
- [303] M. Postema and G. Schmitz. Bubble dynamics involved in ultrasonic imaging. *Expert Rev. Mol. Diagn.*, 6(3):493–502, 2006.
- [304] M. Postema and G. Schmitz. Ultrasonic bubbles in medicine: Influence of the shell. *Ultrason. Sonochem.*, 14:438–444, 2007.
- [305] M. Postema, F. J. ten Cate, G. Schmitz, N. de Jong, and A. van Wamel. Generation of a droplet inside a microbubble with the aid of an ultrasound contrast agent: first result. *Lett. Drug. Des. Discov.*, 4(1):74–77, 2007.
- [306] M. Postema, A. Novell, C. Sennoga, A. T. Poortinga, and A. Bouakaz. Harmonic response from microscopic antibubbles. *Appl. Acoust.*, 137:148–150, 2018.
- [307] M. Postema, R. Matsumoto, R. Shimizu, A. T. Poortinga, and N. Kudo. High-speed footage shows transient nucleation of different hydrophobic particles in suspension. *Jpn. J. Appl. Phys.*, 59:1–3, 2020.
- [308] V. Preobrazhensky and Ph. Pernod. Nonlinear acoustics of phase conjugate waves in heterogeneous media. *WCU 2003*, 53:875–878, 2003.
- [309] V. Preobrazhensky, Y. Pyl’nov Ph. Pernod, L. Krutyansky, and N. Smagin. Nonlinear acoustic imaging of isoechogenic objects and flows using ultrasound wave phase conjugation. *ACTA Acustica united with Acustica*, 95:36–45, 2009.
- [310] R. D. Purrington and G. V. Norton. A numerical comparison of the westervelt equation with viscous attenuation and a causal propagation operator. *Math Comp Sim*, 82:1287–1297, 2012.
- [311] M. I. Qamar, A. E. Read, R. Skidmore, J. M. Evans, and P. N. Wells. Transcutaneous doppler ultrasound measurement of superior mesenteric artery blood flow in man. *Gut*, 27(1):100–105, 1986.
- [312] E. Quaia. Assessment of tissue perfusion by contrast-enhanced ultrasound. *Eur. Radiol.*, 21(3):604–615, 2011.
- [313] S.R. Rao, S.E. Shelton, and P.A. Dayton. The ‘fingerprint’ of cancer extends beyond solid tumor boundaries: assessment with a novel ultrasound imaging approach. *IEEE Trans Biomed Eng*, 63(5), 2016.
- [314] P. Ricci, A. Laghi, V. Cantisani, P. Paolantonio, S. Pacella, E. Pagliara, F. Arduini, V. Pasqualini, F. Trippa, M. Filpo, and R. Passariello. Contrast-enhanced sonography with SonoVue: enhancement patterns of benign focal liver lesions and correlation with dynamic gadobenate dimeglumine-enhanced MRI. *Am. J. Roentgenol.*, 184(3):821–827, 2005.

- [315] N. G. Rognin, P. Frinking, M. Costa, and M. Arditì. In-vivo perfusion quantification by contrast ultrasound: Validation of the use of linearized video data vs. raw rf data. In *2008 IEEE Int. Ultrason. Symp. Proceedings*, pages 1690–1693. Piscataway:IEEE, 2008.
- [316] I. Rudnick. Theory of the attenuation of very high amplitude sound waves. Technical Report 1, Soundrive Engine Company, Los Angeles, CA, 1952.
- [317] I. Rudnick. On the attenuation of finite amplitude waves in a liquid. *J. Acoust. Soc. Am.*, 30: 564–567, 1958.
- [318] C. S. Saatkamp, M. L. Almeida, J. A. M. Bispo, A. L. B. Pinheiro, A. B. Fernandes, and L. Silveira Jr. Quantifying creatinine and urea in human urine through raman spectroscopy aiming at diagnosis of kidney disease. *J. Biomed. Optics*, 21(3):1–7, 2016.
- [319] A. Săftoiu, O. H. Gilja, P. S. Sidhu, C. F. Dietrich, V. Cantisani, D. Amy, M. Bachmann-Nielsen, F. Bob, J. Bojunga, M. Brock, et al. The EFSUMB guidelines and recommendations for the clinical practice of elastography in non-hepatic applications: update 2018. *Ultraschall Med.*, 40 (04):425–453, 2019.
- [320] T. Saidov, C. Heneweer, M. Keunen, J. Broich-Oppert, H. Wijkstra, J. Rosette, and M. Mischi. Fractal dimension of tumor microvasculature by dce-us: preliminary study in mice. *Ultrasound Med. Biol.*, 42(12):2852–2863, 2016.
- [321] S. Saito. Measurement of the acoustic nonlinearity parameter  $B/A$  in liquid media using focused ultrasound. *J. Acoust. Soc. Am.*, 93(1):162–172, 1993.
- [322] S. Saito. Measurement of acoustic nonlinearity parameter using focused ultrasound detected by a concave receiver. *J. Acoust. Soc. Jpn.*, 16(4):239–246, 1993.
- [323] S. Saito. Finite amplitude method for measuring the nonlinearity parameter  $B/A$  in small-volume samples using focused ultrasound. *J. Acoust. Soc. Am.*, 127(1):51–61, 2010.
- [324] S. Saito and J. H. Kim. Two-dimensional measurement of the nonlinearity parameter  $B/A$  in excised biological samples. *Rev. Scientific Instruments*, 82(6):1–9, 2011.
- [325] S. Saito, A. Yamamoto, and K. Nakamura.  $B/A$  measurement for liquid media using an ln transducer with inverted-domain layer. *Jpn. J. Appl. Phys.*, 44(6B):4431–4435, 2005.
- [326] O. A. Sapozhnikov. High-intensity ultrasonic waves in fluids: nonlinear propagation and effects. In J. A. Gallego-Juárez and K. F. Graff, editors, *Power Ultrasonics. Applications of High-Intensity Ultrasound*, chapter 2, pages 9–35. Woodhead Publishing, Cambridge, UK, Chap, 2015.
- [327] A. P. Sarvazyan. Development of methods of precise ultrasonic measurements in small volumes of liquids. *Ultrasonics*, pages 151–154, 1982.
- [328] A. P. Sarvazyan. Ultrasonic velocity of biological compounds. *Annu. Rev. Biophys. Biophys. Chem.*, 20:321–342, 1991.
- [329] A. P. Sarvazyan, T. V. Chalikian, and F. Dunn. Acoustic nonlinearity parameter  $B/A$  of aqueous solutions of some amino acids and proteins. *J. Acoust. Soc. Am.*, 88:1555–1561, 1990.
- [330] T. Sato and Y. Yamakoshi. Nonlinear tissue imaging. *1986 Ultrason. symposium*, pages 890–900, 1986.
- [331] T. Sato, A. Fukusima, N. Ichida, H. Ishikawa, H. Miwa, Y. Igarashi, T. Shimura, and K. Murakami. Nonlinear parameter tomography system using counterpropagating probe and pump waves. *Ultrason. Imaging*, 7(1):49–59, 1985.
- [332] S. G. Schalk, L. Demi, M. Smeenge, D. M. Millis, K.D. Wallace, J.J.M.C.H. de la Rosette, H. Wijkstra, and M. Mischi. 4d spatiotemporal analysis of ultrasound contrast agent dispersion for prostate cancer localization: a feasibility study. *IEEE Trans. Ultrason. Ferroelectr. Freq. Control*, 62(5):839–851, 2015.
- [333] S. G. Schalk, L. Demi, N. Bouhouch, M. P. J. Kuenen, A. W. Postema, J. J. de la Rosette, H. Wijkstra, T. J. Tjalkens, and M. Mischi. Contrast-enhanced ultrasound angiogenesis imaging by mutual information analysis for prostate cancer localization. *IEEE Trans. Biomed. Eng.*, 64(3): 661–670, 2016.
- [334] S.G. Schalk, J. Huang, J. Li, L. Demi, H. Wijkstra, and M. Mischi. 3d quantitative contrast ultrasound for prostate cancer localization. *Eur. J. Ultrasound (in press)*, 2018.
- [335] M. Schneider. Characteristics of SonoVue™. *Echocardiography*, 16:743–746, 1999.
- [336] J. C. V. Schwarz, M. G. J. T. B. van Lier, J. P. H. M. van den Wijngaard, M. Siebes, and E. van Bavel. Topologic and hemodynamic characteristics of the human coronary arterial circulation. *Front. Physiol.*, 10:1611, 2020.
- [337] J. P. M. Sedelaar, G. J. L. H. Leenders, C. A. Hulsbergen-van de Kaa, H. G. Poel, J. A. W. M. Laak, F. M. J. Debruyne, H. Wijkstra, and J. J. Rosette. Microvessel density: Correlation between contrast ultrasonography and histology of prostate cancer. *Eur. Urol.*, 40(3):285–293, 2001.
- [338] T. Segers, N. de Jong, and M. Versluis. Uniform scattering and attenuation of acoustically sorted ultrasound contrast agents: modeling and experiments. *J. Acoust. Soc. Am.*, 140(4):2506–2517, 2016.
- [339] T. Segers, P. Kruizinga, M. P. Kok, G. Lajoinie, N. de Jong, and M. Versluis. Monodisperse versus polydisperse ultrasound contrast agents: non-linear response, sensitivity, and deep tissue imaging potential. *Ultrasound Med. Biol.*, 44(7):1482–1492, 2018.
- [340] C. M. Sehgal, R. C. Bahn, and J. F. Greenleaf. Measurement of the acoustic nonlinearity parameter  $B/A$  in human tissues by a thermodynamic method. *J. Acoust. Soc. Am.*, 76:1023–1029, 1984.
- [341] C. M. Sehgal, G. M. Brown, R. C. Bahn, and J. F. Greenleaf. Measurement and use of acoustic nonlinearity and sound speed to estimate composition of excised livers. *Ultrasound Med. Biol.*, 12(11):865–874, 1986.
- [342] C. M. Sehgal, B. R. Porter, and J. F. Greenleaf. Ultrasonic nonlinear parameters and sound speed of alcohol–water mixtures. *J. Acoust. Soc. Am.*, 79(2):566–570, 1986.
- [343] Taner Şen, Omac Tüfekcioğlu, Sen2015mechanically, and Yavuzer Koza. Mechanical index. *Anatolian journal of cardiology*, 15(4):334, 2015.
- [344] C. A. Sennoga, E. Kanbar, L. Auboire, P. A. Dujardin, D. Fouan, J. M. Escoffre, and A. Bouakaz. Microbubble-mediated ultrasound drug-delivery and therapeutic monitoring. *Expert Opin. Drug Deliv.*, 14(9):1031–1043, 2017.
- [345] S. Sfoungaristos and P. Perimenis. PSA density is superior than PSA and gleason score for adverse pathologic features prediction in patients with clinically localized prostate cancer. *Can. Urol. Assoc. J.*, 6(1):46, 2012.
- [346] P. M. Shankar, P. D. Krishna, and V. L. Newhouse. Advantages of subharmonic over second harmonic backscatter for contrast-to-tissue echo enhancement. *Ultrasound Med. Biol.*, 24(3): 395–399, 1998.

- [347] S. E. Shelton, Y. Z. Lee, M. Lee, E. Cherin, F. S. Foster, S. R. Aylward, and P. A. Dayton. Quantification of microvascular tortuosity during tumor evolution utilizing acoustic angiography. *Ultrasound Med. Biol.*, 41(7):1869–1904, 2015.
- [348] C. Shen and P. Li. Tissue harmonic image analysis based on spatial covariance. *IEEE Trans. Ultrason. Ferroelectr. Freq. Control*, 48:1648–1656, 2001.
- [349] V. V. Shklovskaya-Kordi. Acoustical methods for determining internal pressure in liquids. *Sov. Phys. Acoust.*, 9:107–111, 1963.
- [350] V. A. Shutilov. Optical studies of the shape of ultrasonic waves of large amplitude in liquids. *Soviet Phys.-Acoustics*, 5(2):231–240, 1959.
- [351] P. S. Sidhu, V. Cantisani, C. F. Dietrich, O. H. Gilja, A. Saftoiu, E. Bartels, M. Bertolotto, F. Calliada, D.-A. Clevert, D. Cosgrove, et al. The EFSUMB guidelines and recommendations for the clinical practice of contrast-enhanced ultrasound (CEUS) in non-hepatic applications: update 2017 (long version). *Ultraschall Med.*, 39(02):e2–e44, 2018.
- [352] R. M. S. Sigrist, J. Liau, A. E. Kaffas, M. C. Chammas, and J. K. Willmann. Ultrasound elastography: review of techniques and clinical applications. *Theranostics*, 7(5):1303, 2017.
- [353] R. J. G. Sloun, L. Demi, A. W. Postema, J. J. Rosette, H. Wijkstra, and M. Mischi. Entropy of ultrasound-contrast-agent velocity fields for angiogenesis imaging in prostate cancer. *IEEE Trans. Med. Imag.*, 36(3):826–837, 2017.
- [354] M. Smeenge, F. Tranquart, C. K. Mannaerts, T. M. de Reijke, M. J. van de Vijver, M. P. Laguna, S. Pochon, J. J. de la Rosette, and H. Wijkstra. First-in-human ultrasound molecular imaging with a VEGFR2-specific ultrasound molecular contrast agent (BR55) in prostate cancer: a safety and feasibility pilot study. *Invest. Radiol.*, 52(7):419–427, 2017.
- [355] R. A. Smith, K. S. Andrews, D. Brooks, S. A. Fedewa, D. Manassaram-Baptiste, D. Saslow, O. W. Brawley, and R. C. Wender. Cancer screening in the united states, 2017: a review of current american cancer society guidelines and current issues in cancer screening. *CA: a cancer journal for clinicians*, 67(2):100–121, 2017.
- [356] G. Sölétormos, M. J. Duffy, S. O. A. Hassan, R. H. M. Verheijen, B. Tholander, R. C. Bast, K. N. Gaarenstroom, J. M. Bonfrer C. M. Sturgeon, P. H. Petersen, H. Troonen, G. CarloTorre, J. K. Kulpa, M. K. Tuxen, and R. Molina. Clinical use of cancer biomarkers in epithelial ovarian cancer: updated guidelines from the european group on tumor markers. *Int. J. Gynecol. Cancer*, 26(1), 2016.
- [357] E. Squillaci, G. Manenti, F. Di Stefano, R. Miano, L. Strigari, and G. Simonetti. Diffusion-weighted mr imaging in the evaluation of renal tumours. *J. Exp. Clin. Cancer Res.*, 23(1):39–46, 2004.
- [358] P. R. Srinivas, B. S. Kramer, and S. Srivastava. Trends in biomarker research for cancer detection. *Lancet Oncol.*, 2(11):698–704, 2001.
- [359] S. Stapleton, H. Goodman, Z. Yu-Qing, E. Cherin, R.M. Henkelman, P.N. Burns, and F.S. Foster. Acoustic and kinetic behavior of definity in mice exposed to high frequency ultrasound. *Ultrasound Med. Biol.*, 35(2):296–307, 2009.
- [360] J. E. Streeter, R. C. Gessner, J. Tsuruta, S. Feingold, and P. A. Dayton. Assessment of molecular imaging of angiogenesis with three-dimensional ultrasonography. *Mol. Imaging*, 10(6):460–468, 2011.
- [361] E. P. Stride and C. C. Coussios. Cavitation and contrast: the use of bubbles in ultrasound imaging and therapy. *Proc. Inst. Mech. Eng H*, 224:171–191, 2009.
- [362] C. Strouthos, M. Lampaskis, V. Sboros, A. McNeilly, and M. Averkiou. Indicator dilution models for the quantification of microvascular blood flow with bolus administration of ultrasound contrast agents. *IEEE Trans. Ultrason. Ferroelectr. Freq. Control*, 57(6):1296–1310, 2010.
- [363] M. G. Sullivan and R. Feinn. Using effect size - or why the p-value is not enough. *J. Grad. Med. Educ.*, 4(3):279–282, 2012.
- [364] Visa Suomi, Jiri Jaros, Bradley Treeby, and Robin Cleveland. Nonlinear 3-D simulation of high-intensity focused ultrasound therapy in the kidney. *Engineering in Medicine and Biology Society (EMBC)*, pages 5648–5651, 2016.
- [365] S. Suresh. Biomechanics and biophysics of cancer cells. *Acta biomaterialia*, 3(4):413–438, 2007.
- [366] T. L. Szabo. Time domain equations for lossy media obeying a frequency power law. *J. Acoust. Soc. Am.*, 96(1):491–500, 1994.
- [367] T. L. Szabo. Causal theories and data for acoustic attenuation obeying a frequency power law. *J. Acoust. Soc. Am.*, 97(1):14–24, 1994.
- [368] S. Takahashi. Measurement of acoustic nonlinearity parameter by observation waveforms. *Jpn. J. Appl. Phys.*, 34:2790–2792, 1995.
- [369] M. Takenouchi, M. S. H. Suzuki, and H. Tagami. Hydration characteristics of pathologic stratum corneum-evaluation of bound water. *the society for investigative dermatology*, 87(5):574–576, 1986.
- [370] M. X. Tang and R. J. Eckersley. Frequency and pressure dependent attenuation and scattering by microbubbles. *Ultrasound Med. Biol.*, 33(1):164–168, 2007.
- [371] M. X. Tang, R. J. Eckersley, and J. A. Noble. Pressure-dependent attenuation with microbubbles at low mechanical index. *Ultrasound Med. Biol.*, 31(3):377–384, 2005.
- [372] U. Techavipoo, T. Varghese, Q. Chen, T. A. Stiles, J. A. Zagzebski, and G. R. Frank. Temperature dependence of ultrasonic propagation speed and attenuation in excised canine liver tissue measured using transmitted and reflected pulses. *J. Acoust. Soc. Am.*, 115(6):2859–2865, 2004.
- [373] G. ter Haar. Ultrasonic imaging: safety considerations. *Interface Focus*, 1(4):686–697, 2011.
- [374] A. L. Thuras, K. T. Jenkins, and H. T. O’Neil. Extraneous frequencies generated in air carrying intense waves. *J. Acoust. Soc. Am.*, 6:173–180, 1935.
- [375] J. N. Tjotta and S. Tjotta. Nonlinear equations of acoustics, with application to parametric acoustic arrays. *J. Acoust. Soc. Am.*, 69:1644–1652, 1981.
- [376] J. N. Tjotta and S. Tjotta. Interaction of sound waves. part 1: basic equations and plane waves. *J. Acoust. Soc. Am.*, 82(4):1425–1428, 1987.
- [377] M. Toulemonde, F. Varray, O. Basset, P. Tortoli, and C. Cachard. High frame rate compounding for nonlinear  $B/A$  parameter ultrasound imaging in echo mode - simulation results. In *2014 IEEE International Conference on Acoustics, Speech and Signal Processing*, pages 5153–5157. IEEE, 2014.
- [378] M. Toulemonde, F. Varray, O. Basset, P. Tortoli, and C. Cachard. Nonlinearity parameter  $B/A$  of biological tissue ultrasound imaging in echo mode. In *AIP Conference Proceedings*, volume 1685, page 040016, 2015.

- [379] G. M. Tozer, S. Lewis, A. Michalowski, and V. Aber. The relationship between regional variations in blood flow and histology in a transplanted rat fibrosarcoma. *Br. J. Cancer*, 61:250–257, 1990.
- [380] B. E. Treeby and B. T. Cox. k-wave: Matlab toolbox for the simulation and reconstruction of photoacoustic wave fields. *J. Biomed Opt.*, 15(2):021214, 2010.
- [381] Bradley E Treeby, Jiri Jaros, Alistair P Rendell, and BT Cox. Modeling nonlinear ultrasound propagation in heterogeneous media with power law absorption using a k-space pseudospectral method. *J. Acoust. Soc. Am.*, 131(6):4324–4336, 2012.
- [382] L. D. True and C. D. Jordan. The cancer nuclear microenvironment: interface between light microscopic cytology and molecular phenotype. *J. Cell. Biochem.*, 104(6):1994–2003, 2008.
- [383] J. Tu, J. Guan, Y. Qiu, and T. J. Matula. Estimating the shell parameters of SonoVue® microbubbles using light scattering. *J. Acoust. Soc. Am.*, 126(6):2954–2962, 2009.
- [384] S. Turco, I. Tardy, P. Frinking, H. Wijkstra, and M. Mischi. Quantitative ultrasound molecular imaging by modeling the binding kinetics of targeted contrast agent. *Phys. Med. Biol.*, 62(6):2449, 2017.
- [385] S. Turco, H. Wijkstra, and M. Mischi. Mathematical models of contrast transport kinetics for cancer diagnostic imaging: a review. *IEEE Rev. Biomed. Eng.*, 9:121–147, 2017.
- [386] S. Turco, P. Frinking, R. Wildeboer, M. Arditi, H. Wijkstra, J. R. Linder, and M. Mischi. Contrast-enhanced ultrasound quantification: from kinetic modeling to machine learning. *Ultrasound Med. Biol.*, 46:518–543, 2020.
- [387] S. Ueno, M. Hashimoto, H. Fukukita, and T. Yano. Ultrasound thermometry in hyperthermia. In *IEEE Ultrasonics Symposium*, pages 1645–1651. IEEE, 1990.
- [388] H. J. Vala and A. Baxi. A review on otsu image segmentation algorithm. *Int J Adv Res Comput Sci Softw Eng*, 2:387–389, 2013.
- [389] P. LMJ van Neer, G. Matte, M. G. Danilouchkine, C. Prins, F. van den Adel, and N. de Jong. Super-harmonic imaging: development of an interleaved phased-array transducer. *IEEE Trans. Ultrason. Ferroelectr. Freq. Control*, 57(2):455–468, 2010.
- [390] R. van Sloun, L. Demi, C. Shan, and M. Mischi. Ultrasound coefficient of nonlinearity imaging. *IEEE Trans. Ultrason. Ferroelectr. Freq. Control*, 62(7):1331–1341, 2015.
- [391] R. J. G. van Sloun, L. Demi, A. W. Postema, J. J. de la Rosette, H. Wijkstraa, and M. Mischi. Ultrasound-contrast-agent dispersion and velocity imaging for prostate cancer localization. *Med. Im. Analysis*, 48:1648–1656, 2001.
- [392] F. Varray. *Simulation in nonlinear ultrasound : application to nonlinear parameter imaging in echo mode configuration*. Ph.D. dissertation, Université Claude Bernard, Lyon I, 2011.
- [393] F. Varray, O. Basset, P. Tortoli, and C. Cachard. Extensions of nonlinear  $B/A$  parameter imaging methods for echo mode. *IEEE Trans. Ultrason. Ferroelectr. Freq. Control*, 58(6):1232–1244, 2011.
- [394] F. Varray, J. Chenot, O. Basset, P. Tortoli, D. Melodelima, and C. Cachard. Nonlinear parameter imaging to characterize HIFU ablation: Preliminary in vitro results in porcine liver. In *2011 IEEE International Ultrasonics Symposium Proceedings*, pages 1361–1363. IEEE, 2011.
- [395] E. Verboven. *Development of ultrasound contrast agent based radiotherapy*. Ph.D. dissertation, Arenberg doctoral school, KU Leuven, 2017.
- [396] M. D. Verweij, B. E. Treeby, K. W. A. Van Dongen, and L. Demi. Simulation of ultrasound fields. *Comprehensive biomedical physics*, pages 465–499, 2014.
- [397] M. Veta, J. P. W. Pluim, P. J. van Diest, and M. A. Viergever. Breast cancer histopathology image analysis: a review. *IEEE Trans. Biomed. Eng.*, 61(5):1400–1411, 2014.
- [398] B. L. Viglianti, S. A. Abraham, C. R. Michelich, P. S. Yarmolenko, J. R. MacFall, M. B. Bally, and M. W. Dewhirst. In vivo monitoring of tissue pharmacokinetics of liposome/drug using MRI: Illustration of targeted delivery. *Magnet. Reson. Med.*, 51(6):1153–1162, 2004.
- [399] R. C. Waag. A review of tissue characterization from ultrasonic scattering. *IEEE Transact. Biomed. Eng.*, 31:884–893, 1984.
- [400] K.D. Wallace, C.W. Lloyd, M.R. Holland, and J. G. Miller. Finite amplitude measurements of the nonlinear parameter  $B/A$  for liquid mixtures spanning a range relevant to tissue harmonic mode. *Ultrasound Med. Biol.*, 33(4):620–629, 2007.
- [401] H. Wang, X. Zhu, X. Gong, and D. Zhang. Computed tomography of the acoustic nonlinearity parameter  $B/A$  for biological tissues via difference frequency wave from a parametric array in reflection mode. *Chinese Sci. Bull.*, 48(22):2427–2430, 2003.
- [402] Kejia Wang, Emily Teoh, Jiri Jaros, and Bradley E Treeby. Modelling nonlinear ultrasound propagation in absorbing media using the k-Wave toolbox: experimental validation. *Proc. IEEE Int. Ultrason. Symp.*, pages 523–526, 2012.
- [403] K. Wei, A. R. Jayaweera, S. Firoozan, A. Linka, D. M. Skyba, and S. Kaul. Quantification of myocardial blood flow with ultrasound-induced destruction of microbubbles administered as a constant venous infusion. *Circulation*, 97(5):473–483, 1998.
- [404] H. K. Weir, T. D. Thompson, A. Soman, B. Møller, and S. Leadbetter. The past, the present, the future of cancer incidence in the united states: 1975 through 2020. *Cancer*, 121(11):1827–1837, 2015.
- [405] J. J. Wen and M. A. Breazeale. A diffraction beam field expressed as the superposition of gaussian beams. *J. Acoust. Soc. Am.*, 83(5):1752–1756, 1988.
- [406] P. J. Westervelt. Parametric acoustic arrays. *J. Acoust. Soc. Am.*, 53(1):535–537, 1963.
- [407] C. Whatmough and C. R. Lamb. Computed tomography: principles and applications. *Compendium*, 2006.
- [408] A. O. Williams. The piston source at high frequencies. *J. Acoust. Soc. Am.*, 23(1):1–6, 1951.
- [409] R. Williams, J. M. Hudson, B. A. Lloyd, A. R. Sureshkumar, Go. Lueck, L. Milot, M. Atri, G. A. Bjarnason, and P. N. Burns. Dynamic microbubble contrast-enhanced us to measure tumor response to targeted therapy: a proposed clinical protocol with results from renal cell carcinoma patients receiving antiangiogenic therapy. *Radiol.*, 260(2):581–590, 2011.
- [410] J. K. Willmann, L. Bonomo, A. C. Testa, P. Rinaldi, G. Rindi, K. S. Valluru, G. Petrone, M. Martini, A. M. Lutz, and S. S. Gambhir. Ultrasound molecular imaging with br55 in patients with breast and ovarian lesions: first-in-human results. *J. Clin. Oncol.*, 35(19):2133, 2017.
- [411] W. D. Wilson. Speed of sound in distilled water as a function of temperature and pressure. *J. Acoust. Soc. Am.*, 31:1067–1072, 1959.
- [412] J. Wu and J. Tong. Measurements of the nonlinearity parameter  $B/A$  of contrast agents. *Ultrasound Med. Biol.*, 24(1):153–159, 1998.



- [413] L. Xia. Analysis of acoustic nonlinearity parameter  $B/A$  in liquids containing ultrasound contrast agents. *J. Acoust. Soc. Am.*, 146(2):1394–1403, 2019.
- [414] H. X. Xu, M. D. Lu, G. J. Liu, X. Y. Xie, Z. F. Xu, Y. L. Zheng, and J. Y. Liang. Imaging of peripheral cholangiocarcinoma with low-mechanical index contrast-enhanced sonography and Sonovue. *J. Ultrasound Med.*, 25(1):23–33, 2006.
- [415] X. Xu, F. Mao, X. Gong, and D. Zhang. Theoretical calculation and experimental study on the third-order nonlinearity parameter  $C/A$  for organic liquids and biological fluids. *J. Acoust. Soc. Am.*, 113(3):1743–1748, 2003.
- [416] W. T. Yang, J. Chang, and C. Metreweli. Patients with breast cancer: differences in color doppler flow and gray-scale us features of benign and malignant axillary lymph nodes. *Radiol.*, 215(2): 568–573, 2000.
- [417] T. E. Yankeelov and J. C. Gore. Dynamic contrast enhanced magnetic resonance imaging in oncology: theory, data acquisition, analysis, and examples. *Curr. Med. Imaging Rev.*, 3(2):91–107, 2007.
- [418] D. Yilmazer, Ü. Han, and B. Önal. A comparison of the vascular density of vegf expression with microvascular density determined with cd34 and cd31 staining and conventional prognostic markers in renal cell carcinoma. *Int. Urol. Nephrol.*, 39:691–698, 2007.
- [419] K. Yoshizumi, T. Sato, and N. Ichida. A physicochemical evaluation of the nonlinear parameter  $B/A$  for media predominantly composed of water. *J. Acoust. Soc. Am.*, 82(1):302–305, 1987.
- [420] H. Yu, J. K. Mouw, and V. M. Weaver. Forcing form and function: biomechanical regulation of tumor evolution. *Trends in cell Biol.*, 21(1):47–56, 2011.
- [421] J. Yu, X. Cai, Y. Wang, and Y. Ma. Simulation and phantom study of the acoustic nonlinear  $B/A$  parameter for biological tissues by using comparative method. *Int. J. Biosci. Biochem. Bioinf.*, 4: 438–447, 2014.
- [422] E. A. Zabolotskaya and R. V. Khokhlov. Quasi-plane waves in the nonlinear acoustics of confined beams. *Sov. Phys. Acoust.*, 15(1):40–47, 1969.
- [423] P. Zanzonicot. Principles of nuclear medicine imaging: planar, SPECT, PET, multi-modality, and autoradiography systems. *Radiat. Res.*, 177(4):349–364, 2012.
- [424] B. Zelhof, M. Pickles, G. Liney, P. Gibbs, G. Rodrigues, S. Kraus, and L. Turnbull. Correlation of diffusion-weighted magnetic resonance data with cellularity in prostate cancer. *BJU Int.*, 103(7): 883–888, 2009.
- [425] B. Zeqiri. Errors in attenuation measurements due to nonlinear propagation effects. *J. Acoust. Soc. Am.*, 91(5):258–2593, 1992.
- [426] B. Zeqiri, A. Cook, L. Retat, and J. Civalé. On measurement of the acoustic nonlinearity parameter using the finite amplitude insertion substitution (FAIS) technique. *Metrologia*, 52:406–422, 2015.
- [427] D. Zhang and X. Gong. Computer simulation of acoustic nonlinear parameter tomography. *Chin. J. Acoust.*, 13(2):169–175, 1994.
- [428] D. Zhang and X. Gong. Experimental investigation of the acoustic nonlinearity parameter tomography for excised pathological biological tissues. *Ultrasound Med. Biol.*, 25(4):593–599, 1999.
- [429] D. Zhang and X. Gong. Acoustic nonlinear imaging and its application in tissue characterization. In *Ultrasonic And Advanced Methods For Nondestructive Testing And Material Characterization*, pages 139–153. World Scientific, New Jersey, 2006.
- [430] D. Zhang, X. Gong, and S. Ye. Acoustic nonlinearity parameter tomography for biological specimens via measurements of the second harmonics. *J. Acoust. Soc. Am.*, 99(4):2397–2402, 1996.
- [431] D. Zhang, X. Chen, and X. Gong. Acoustic nonlinearity parameter tomography for biological tissues via parametric array from a circular piston source—theoretical analysis and computer simulations. *J. Acoust. Soc. Am.*, 109(3):1219–1225, 2001.
- [432] D. Zhang, X. Gong, and X. Chen. Experimental imaging of the acoustic nonlinearity parameter  $B/A$  for biological tissues via a parametric array. *Ultrasound Med. Biol.*, 27(10):1359–1365, 2001.
- [433] J. Zhang and F. Dunn. In vivo  $B/A$  determination in a mammalian organ. *J. Acoust. Soc. Am.*, 81 (5):1635–1637, 1987.
- [434] J. Zhang and F. Dunn. A small volume thermodynamic system for  $B/A$  measurement. *J. Acoust. Soc. Am.*, 89(1):73–79, 1991.
- [435] J. Zhang, M. S. Kuhlenschmidt, and F. Dunn. Influences of structural factors of biological media on the acoustic nonlinearity parameter  $B/A$ . *J. Acoust. Soc. Am.*, 89(1):80–91, 1991.
- [436] H. Zhao, R. Xu, Q. Ouyang, L. Chen, B. Dong, and Y. Huihua. Contrast-enhanced ultrasound is helpful in the differentiation of malignant and benign breast lesions. *Eur J Radiol*, 73(2):288–293, 2010.
- [437] J. Zhao, X. Li, J. Yu, and Y. Wang. Nonlinear ultrasound simulation based on full-wave model and comparisons with kzk. *Int. J. Biosci. Biochem. Bioinf.*, 4(5):322–325, 2014.
- [438] X. Zhao and R. J. McGough. The Khokhlov-Zabolotskaya-Kuznecov equation with power law attenuation. In *2014 IEEE International Ultrasonics Symposium Proceedings*, pages 2225–2228, 2014.
- [439] Z. Zhe, C. Gong, and Z. Dong. Molecular structure dependence of acoustic nonlinearity parameter  $B/A$  for silicone oils. *Chin. Phys. B*, 23(5):1–6, 2014.
- [440] Y. Zheng, R. Gr. Maev, and I. Yu. Solodov. Nonlinear acoustic applications for material characterization: a review. *Can. J. Phys.*, 77:927–967, 1999.
- [441] Z. Zhu, M. S. Roos, W. N. Cobb, and K. Jensen. Determination of the acoustic nonlinearity parameter  $B/A$  from phase measurements. *Am. J. Phys.*, 74:1518–1520, 1983.
- [442] E. Zorebski and M. Zorebski. Acoustic nonlinearity parameter  $B/A$  determined by means of thermodynamic method under elevated pressures for alkanediols. *Ultrasonics*, 49:668–675, 2009.
- [443] E. Zorebski, M. Zorebski, and S. Ernst. Speed of ultrasound in liquids measured at a constant acoustic pathlength. comparison and discussion of errors. *J. Phys. IV France*, 129:79–82, 2005.
- [444] E. Zorebski, M. Zorebski, and M. Dzida. Acoustic nonlinearity parameter  $B/A$ , internal pressure, and acoustic impedance determined at pressures up to 100 mpa for 1-ethyl-3-methylimidazolium bis[(trifluoromethyl)sulfonyl]imide. *Archives of Acoustics*, 41(1):59–66, 2016.

# Acknowledgements

Many people contributed to this work, and directly, or indirectly helped me graduate.

I would like to thank my first promotor **prof. dr. ir. M. Mischi**, second promotor **prof. dr. ir. H. Wijkstra**, and my copromotor **dr. ir. R.J.G. van Sloun** for their guidance during this project. **Massimo**, you have helped me develop a more practical and efficient approach to solving problems. Thank you for your advice and feedback. You were often the first one to provide it, replying even on weekends. I have always been impressed by how hard-working and dedicated to the field you are. **Hessel**, I am grateful to you for the experience of collaborating with the hospital and for giving me the opportunity to conduct my last experiments in a clinical environment. **Ruud**, besides valuable practical advice, at difficult times your support was priceless and kept me going without losing hope.

I am sincerely grateful to the committee members **dr. ir. M.D. Verweij**, **dr. ir. R.G.P. Lopata**, **dr. L. Demi**, **prof. dr. M. Postema**, MD, **dr. P.J. Zondervan** for critically assessing my work and taking the time for my defence.

I thank my coauthors **prof. dr. O.A. Sapozhnikov**, **prof. dr. M. Postema**, **dr. A.T. Poortinga**, **prof. dr. ir. P.A. Dayton**, **dr. S.E. Shelton**, **prof. dr. F. Molinari**, **dr. C. Caresio**, MD, Msc. **J.E. Freund**, MD, **dr. P. Zondervan**, MD, **dr. D.S. Heijink**, MD, Msc. **C. Widdershoven**, Msc. **P. Chen**, Msc. **X. Chen**, **dr. L. Demi**, **dr. M. Kuenen**, **dr. R.R. Wildeboer** for our fruitful collaboration.

I am particularly indebted to **prof. dr. O.A. Sapozhnikov**, **prof. dr. M. Postema**, **dr. A. Poortinga**, **dr. L. Demi** and **dr. M. Kuenen**.

I thank **prof. dr. O.A. Sapozhnikov** for his help with designing a proper experiment measuring  $B/A$ . Oleg Anatolievich, when I expressed that I was having difficulty measuring  $B/A$ , you were so eager to help that you even missed a few talks at the conference where we met, to listen to me and help me figure out where the problem may lay. Your advice put me on the right path of designing a proper experiment for tissue measurements and gave so much insight on the reasons for previous failures. It was my honour working with someone so knowledgeable in the field and, at the same time, kind and patient. We met at a true turning point in my PhD. If not for you, I do not know if I would have had the strength to continue.

I would like to express my gratitude to **prof. dr. M. Postema**, who has provided as much support to my antibubble research as one could possibly imagine. We have shared many fruitful scientific discussions and your excellent sense of humour made them even more entertaining. It has been an honour and my true pleasure working with you.

I thank **dr. A. Poortinga** who was helpful to my work even before we had a mutual project to work on. It is wonderful that we kept in touch after meeting at a conference and, later on, got to work together. It is a pleasure working with someone so knowledgeable and kind as you.

I would like to thank **dr. L. Demi** for the (helaas) short time he was my supervisor. You were my lab guru and when you left I had no idea what I would do without you.

I would like to express my gratitude to **dr. M. Kuenen** for his guidance in the first years of my PhD and helping me understand CUDI.

A big thank you to **dr. D. Pustakhod**, Msc. **R. Pajkovic**, **dr. D. Vakulov**, Msc. **A. Lichauco** and **dr. A. Nikolaev** for helping me with some practical issues, like weighing contrast agent material on sufficiently accurate scales, designing cuvettes, etc.

Last but not least, I thank **C. Schaafstra**, **M. van Riet** and **J. de Vos** for their help with administrative tasks. It was a pleasure working with my colleagues **X. Chen**, **L. Bogatu**, **N. Chennakeshava**, **R.**

**Maximidis**, **P. Chen**, **S. Turco**, **N. Kuijsters**, **E. Fotiadou**, **M. Bester**, **M. Nano**, **F. Sammali**, **L. van Knippenberg**, **Y. Huang**, **R.R. Wildeboer**, **B. Luijten**, **C. Rabotti**, **T. Bakkes**, **A. van Diepen**, **B. Oei**, **E. Peri**, **L. Eerikainen**, **S. Schalk**.

This work could never have been finalized without the support of **my family**. I felt so vulnerable without you next to me. Learning to live without you by my side was the true challenge of these years. Nevertheless, even when miles apart you found numerous ways to support me. **Mother**, **grandmother Alexandra**, **Aldo**, **Juan**, aunt **Sveta**, I am endlessly grateful to you! **Папа, Татьяна, бабушка Энна Николаевна, тетя Света, Татьяна**, спасибо вам за поддержку! **Aldo**, my love, you have given me a sense of home and companionship that I missed for so long and have made me a happier person. **Els**, **Jeroen**, **Enzo**, **Vito**, **Nino** thank you for the cosy evenings spent together, with board games and plenty of tasty food.

A big thank you to my friends. **Kirill** and **Elena**, you both are very special people to me and we go a long way back together. During my bachelor, besides my family, you were the strong shoulders I could lean on if I needed support. I am so grateful that we have not lost touch over the years and I still see you both as very dear friends. **Alisa**, you and I have known each other for more than 15 years. What a number! We encountered similar problems when moving abroad and now, when getting old =))) It has brought us even closer together.

**Arturo** and **Hanna**, thank you for the political/historical discussions, the games, the catsitting and your companionship in general! **Anna**, my dear, I am so grateful to have a friend like you. We both shared a similar burden for years and, luckily, have both overcome it and moved on to a happier stage of our lives. **Laura**, thank you so much for the dance parties that we attended together, for our breaks and lunches and tons of loud laughs. I am happy I have someone like you who understands me so well in some aspects that few people do. **Hongie**, you are so positive and active that whenever I am around you, you make me happier as well! I hope Switzerland treats you well! **Dijana**, you are my favorite follower and such a positive person. Never change the latter! **Niko**, thank you for the drawing sessions, the dances and your companionship (particularly during corona times). **Vadim**, thank you for teaching me how to lead, the conversations, the catsitting, your (sometimes very particular (stupid?=))) jokes and your support. **Xufei** and **Nish**, I am glad that we have become friends so fast, it was so easy to get along, talk about almost anything and become close to both of you. An extra thank you for being my paranimfs! I heard, it is going to be entertaining... =) **Alex**, it is great to have a Master's buddy and to share how our life evolves since then. **Veronika**, I am happy to have such an easy-going and understanding friend. **Awital**, **Kelly**, **Murtuza** and **Davide**, **Daniel**, **Oleg**, **Anton** thank you for the fun times we have together when we meet!

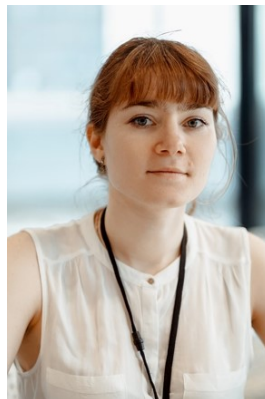
Lastly, I would like to express my gratitude to the whole **MBSE team at Philips Engineering Solutions** and the **Bright Society team** that have welcomed me and made me feel at home. This has allowed me to finalize this work in a good state of mind. A special thank you to **Sonja** and **Eric** for giving me the opportunity to join the team and to **Patric** and **Wouter** for our fruitful conversations, the friendly atmosphere and helping me advance in this new domain.

# Curriculum Vitae

Anastasiia Panfilova was born on 19-08-1991 in Ussuriysk, Russia. She received her Bachelor's degree in Applied Physics (track Medical Physics) *cum laude* in 2013 at Peter the Great St. Petersburg Polytechnic University in Saint Petersburg, Russia. Subsequently, she was granted a scholarship to pursue a Master at the Vrije Universiteit Amsterdam in Amsterdam, the Netherlands. At this university, she graduated *cum laude* from the research Master in Medical Natural Sciences, track Medical Physics. During her MSc curriculum she worked on two research projects. One project focused on modelling arteriolar network adaptation of healthy and diseased vessels and was based at the Amsterdam University Medical Centers, location AMC. The other was devoted to estimating the dim-light melatonin onset from subject-specific data and phenotyping of melatonin secretors, based at Philips Research.

In 2016, Anastasiia started her PhD project within the IMPULS2-program (currently referred to as e/MTIC), hosted by the Eindhoven University of Technology in collaboration with Philips Research and the Jeroen Bosch Hospital in 's-Hertogenbosch. During her PhD, she worked on further developing nonlinear ultrasound for cancer diagnostics, featuring contrast-enhanced ultrasound and the nonlinear parameter  $B/A$  measurement.

In 2021, she joined Philips Engineering Solutions and is currently involved in the implementation of Model-Based Systems Engineering.



# List Of Authors's publications

## Journal papers

-2022

A. Panfilova, X. Chen, C. Widdershoven, J. E. Freund, D. S. Heijink, P. Zondervan, R. J. G. van Sloun, F. Molinari, H. Wijkstra, P. A. Dayton, and M. Mischi, " $B/A$  measurement of clear cell renal cell carcinoma versus healthy kidney tissue", submitted to *Ultrasound Med. Biol.*

P. Chen, A. M. A. O. Pollet, A. Panfilova, M. Zhou, S. Turco, J. M. J. den Toonder and M. Mischi, "Acoustic characterization of tissue-mimicking materials for ultrasound perfusion imaging research", *Ultrasound Med. Biol.*, vol. 48, no. 1, pp. 124-142, 2022

-2021

A. Panfilova, P. Chen, R. J. G. van Sloun, H. Wijkstra, M. Postema, A. T. Poortinga, and M. Mischi, "Experimental acoustic characterisation of an endoskeletal antibubble contrast agent: first results", *Med. Phys.*, vol. 48, no. 11, pp. 6765-6780, 2021

A. Panfilova, R. J. G. van Sloun, H. Wijkstra, O. Sapozhnikov, and M. Mischi, "A review on  $B/A$  measurement methods with a clinical perspective", *J. Acoust. Soc. Am.*, vol. 149, no. 4, pp. 2200-2237, 2021

-2019

A. Panfilova, S. E. Shelton, C. Caresio, R. J. G. van Sloun, F. Molinari, H. Wijkstra, P. A. Dayton, and M. Mischi, "On the relationship between dynamic contrast - enhanced ultrasound parameters and the underlying vascular architecture extracted from acoustic angiography", *Ultrasound Med. Biol.*, vol. 45, no. 2, pp. 539-548, 2019

-2016

R. R. Wildeboer, A. Panfilova, M. Mischi and H. Wijkstra, "Imaging Modalities in Focal Therapy: Multiparametric Ultrasound", *Archivos Espanoles de Urologia*, vol. 69, pp. 281-290, 2016

## Conference proceedings

-2021

A. Panfilova, R. J. G. Van Sloun, H. Wijkstra and M. Mischi, “Simulation study on practical choices for  $B/A$  measurement by the generalized finite amplitude insert-substitution method”, *2021 IEEE International Ultrasonics Symposium (IUS)*, pp. 1-5, 2021, *Poster presentation at IEEE IUS 2021 Virtual Symposium*

-2020

A. Panfilova, X. Chen, R. J. G. van Sloun, H. Wijkstra, O. A. Sapozhnikov, and M. Mischi, “The generalized finite amplitude insert-substitution method for  $B/A$  measurement of tissues and liquids”, *Proc. Mtgs. Acoust.*, vol. 42, pp. 020001, 2020, *Oral presentation at The 179th Meeting of the Acoustical Society of America 2020: Acoustics Virtually Everywhere*

-2018

A. Panfilova, R. J. G. van Sloun, R. R. Wildeboer, H. Wijkstra, and M. Mischi, “A fixed-distance plane wave method for estimating the ultrasound coefficient of nonlinearity”, *Proc. Mtgs. Acoust.*, vol. 34, pp. 020001, 2018, *Oral presentation at 21st International Symposium on Nonlinear Acoustics, Santa Fe, New Mexico, USA*

-2017

A. Panfilova, S. Shelton, R. J. G. van Sloun, C. Caresio, H. Wijkstra, P. Dayton and M. Mischi, “Which properties of the vascular architecture are reflected by dynamic contrast-enhanced ultrasound imaging of dispersion and wash-in rate? A comparison with acoustic angiography”, *2017 IEEE International Ultrasonics Symposium (IUS)*, pp. 1-4, 2017, *Poster presentation at IEEE IUS 2017, Washington, D.C., USA*

-2016

A. Panfilova, S. Shelton, R. J. G. van Sloun, L. Demi, H. Wijkstra, P. Dayton and M. Mischi, “Does contrast ultrasound dispersion imaging reveal changes in tortuosity? : a comparison with acoustic angiography”, *2016 IEEE International Ultrasonics Symposium (IUS)*, pp. 1-4, 2016, *Poster presentation at IEEE IUS 2016, Tours, France*

## Conference abstracts

-2022

P. Chen, A. M. A. O. Pollet, A. Panfilova, M. Zhou, S. Turco, J. M. J. den Toonder and M. Mischi, “Investigating microvascular phantom and case materials for ultrasound perfusion imaging”, *The 27th European symposium on Ultrasound Contrast Imaging, Rotterdam, The Netherlands, 2022, Submitted*

-2020

A. Panfilova, P. Chen, R. J. G. van Sloun, H. Wijkstra, M. Postema, A. T. Poortinga, and M. Mischi, “Acoustic characterization of antibubbles”, *The 25th European symposium on Ultrasound Contrast Imaging, Rotterdam, The Netherlands, 2020, Poster presentation*

-2019

A. Panfilova, P. Chen, R. J. G. van Sloun, H. Wijkstra, M. Postema, A. T. Poortinga, and M. Mischi, “Acoustic characterization of antibubbles for quantitative imaging”, *2019 International Congress on Ultrasonics, Leuven, Belgium, 2019, Poster presentation*

A. Panfilova, P. Chen, R. J. G. van Sloun, H. Wijkstra, M. Postema, A. T. Poortinga, and M. Mischi, “Acoustic characterization of antibubbles for contrast-enhanced ultrasound imaging”, *Annual IEEE EMBS Benelux Chapter Symposium: Artificial Intelligence In Healthcare, Leuven, Belgium, 2019, Poster presentation*

-2018

A. Panfilova, S. E. Shelton, C. Caresio, R. J. G. van Sloun, F. Molinari, H. Wijkstra, P. A. Dayton, and M. Mischi, “On what dynamic contrast-enhanced ultrasound tells us about the underlying vascular architecture”, *23rd European symposium on Ultrasound Contrast Imaging, Rotterdam, The Netherlands, 2018, Oral presentation*

A. Panfilova, S. E. Shelton, R. J.G. van Sloun, C. Caresio, H. Wijkstra, P. A. Dayton, M. Mischi, “What dynamic contrast-enhanced ultrasound tells us about the underlying vascular architecture”, *Catharina Wetenschapsavond, Eindhoven, The Netherlands, 2018, Poster presentation*

-2017

A. Panfilova, S. E. Shelton, R. J. G. van Sloun, C. Caresio, H. Wijkstra, P. A. Dayton, M. Mischi, “On the relation between contrast-ultrasound kinetic features and microvascular density by acoustic angiography”, *IEEE Poster Contest, Eindhoven, The Netherlands, 2017, Poster presentation*